Extended $p_{3/2}$ neutron orbital and the N=32 shell closure in ^{52}Ca

Das vergrößerte $p_{3/2}$-Neutronenorbital und der N=32-Schalenabschluss in ^{52}Ca
Zur Erlangung des Grades eines Doktors der Naturwissenschaften (Dr. rer. nat.)
Genehmigte Dissertation von Mădălina Enciu aus Sibiu, Romania
Tag der Einreichung: 09.06.2023, Tag der Prüfung: 19.07.2023

1. Gutachten: Prof. Dr. Alexandre Obertelli
2. Gutachten: Prof. Dr. Thomas Aumann
Darmstadt, Technische Universität Darmstadt

TECHNISCHE UNIVERSITÄT DARMSTADT

Physics Department
Institut für Kernphysik
AG Obertelli

Extended $p_{3/2}$ neutron orbital and the N=32 shell closure in ^{52}Ca
Das vergrößerte $p_{3/2}$-Neutronenorbital und der N=32-Schalenabschluss in ^{52}Ca

Accepted doctoral thesis by Mădălina Enciu

Date of submission: 09.06.2023
Date of thesis defense: 19.07.2023

Darmstadt, Technische Universität Darmstadt

For *M* & *A*

Erklärungen laut Promotionsordnung

§ 8 Abs. 1 lit. c PromO

Ich versichere hiermit, dass die elektronische Version meiner Dissertation mit der schriftlichen Version übereinstimmt.

§ 8 Abs. 1 lit. d PromO

Ich versichere hiermit, dass zu einem vorherigen Zeitpunkt noch keine Promotion versucht wurde. In diesem Fall sind nähere Angaben über Zeitpunkt, Hochschule, Dissertationsthema und Ergebnis dieses Versuchs mitzuteilen.

§ 9 Abs. 1 PromO

Ich versichere hiermit, dass die vorliegende Dissertation selbstständig und nur unter Verwendung der angegebenen Quellen verfasst wurde.

§ 9 Abs. 2 PromO

Die Arbeit hat bisher noch nicht zu Prüfungszwecken gedient.

Darmstadt, 09.06.2023

M. Enciu

Abstract

The nuclear shell structure is not universal across the nuclear landscape. The standard shell closures, 2, 8, 20, 28, 50, 82, and 126 can weaken and fade away, while new ones can appear [1]. The numbers of nucleons that correspond to a shell closure are commonly named as *magic* numbers. An example is the appearance of the N=32 and 34 new neutron magic numbers in the neutron-rich calcium isotopes region [2, 3]. Moreover, experimental measurements show an increase of charge radii [4, 5] and matter radii [6] as one starts filling the $2p_{3/2}$ neutron orbital in potassium and calcium isotopes. One hypothesis is that the p neutron orbitals have a large size relative to the f neutron orbitals [7], and this would explain the measured large charge and matter radii values.

The first part of the thesis presents the results of ^{52}Ca(p,pn)^{51}Ca cross section measurements, supporting the N=32 shell closure in ^{52}Ca. It focuses also on the determination of the size of the single-particle neutron orbitals in the pf-shell via (p,pn) reactions and momentum distribution analysis. The quasi-free neutron scattering reaction was measured during an experimental campaign at the Radioactive Isotope Beam Factory (RIBF), at the SAMURAI fragment spectrometer, in inverse kinematics at an energy of ∼230 MeV/nucleon in a 15-cm long liquid hydrogen target and using the MINOS TPC [8]. Inclusive and exclusive cross sections to bound states of ^{51}Ca were evaluated using γ-ray spectroscopy measurements, as well as the momentum distributions corresponding to the removal of $1f_{7/2}$ and $2p_{3/2}$ neutrons were measured. The cross sections, interpreted within the distorted-wave impulse approximation (DWIA) reaction framework, are consistent with a shell closure at the neutron number N=32, found as strong as at N=28 and N=34 in Ca isotopes. The analysis of the momentum distributions leads to a difference of the root-mean-square radii of the $1f_{7/2}$ and $2p_{3/2}$ neutron orbitals of 0.61(23) fm [9], in agreement with the modified-shell-model prediction of 0.7 fm [7] suggesting that the large root-mean-square (rms) radius of the $2p_{3/2}$ orbital in neutron-rich Ca isotopes is responsible for the unexpected linear increase of the charge radius with the neutron number.

The method for determining the rms radii of the single-particle neutron orbitals via momentum distribution measurements in (p,pn) reactions was further applied for the neighbouring isotopes, ^{53}Ca and ^{54}Ca. The size of the $1f_{7/2}$, $2p_{3/2}$, $2p_{1/2}$, and $1f_{5/2}$ neutron orbitals was obtained and showed consistency with the results from ^{52}Ca. The p orbitals show indeed a larger spatial extension compared to the f neutron orbitals (>0.5 fm difference) as a result of this study.

The second part of this thesis presents the research and development of a new particle tracker, STRASSE [10] combined with a long liquid hydrogen target, aimed for the study of proton induced quasi-free scattering reactions such as (p,2p) and (p,3p). Despite the improved luminosity, the MINOS system [8] was used only for tracking the reaction vertex inside the liquid hydrogen target. A similar setup allowing particle spectroscopy in addition to γ-ray spectroscopy could provide missing mass information. STRASSE is designed to be used together with CATANA [11], which is an array of CsI(Na) crystals aimed for measuring the total energy of the protons from the (p,2p) and (p,3p) reactions, as well as to perform γ-ray spectroscopy. This new experimental setup will be able to reconstruct the reaction vertex with sub-mm resolution and to perform missing mass measurements with a resolution of below 2 MeV [10]. The production and testing of the liquid hydrogen target cell for STRASSE will be presented in this thesis, as well as offline and in-beam testing of the readout electronics aimed for STRASSE, using the prototype silicon tracker PFAD.

Abstract

Die Struktur der Kernhülle ist in der gesamten Kernlandschaft nicht universell. Die bekannten Schalenabschlüsse 2, 8, 20, 28, 50, 82 und 126 können verschwinden, während neue erscheinen können [1]. Die Anzahl an Nukleonen, die einem Schalenabschluss entsprechen, werden üblicherweise als *magische* Zahlen bezeichnet. Ein Beispiel ist das Auftreten der neuen magischen Neutronenzahlen N=32 und 34 in der neutronenreichen Calciumisotopenregion [2, 3]. Darüber hinaus zeigen experimentelle Messungen eine Zunahme der Ladungsradien [4, 5] und Massenradien [6], wenn das $2p_{3/2}$-Neutronenorbital in Kalium- und Calciumisotopen befüllt wird. Eine Hypothese besagt, dass die p-Neutronenorbitale im Vergleich zu den f-Neutronenorbitalen größer sind [7]. Dies würde die gemessenen Ladungs- und Massenradien erklären.

Der erste Teil der Arbeit präsentiert die Ergebnisse der Messungen des Wirkungsquerschnittes von ^{52}Ca(p,pn)^{51}Ca, welche den Schalenabschluss für N=32 in ^{52}Ca unterstützen. Ein weiterer Schwerpunkt der Arbeit liegt auf der Bestimmung der Größe der Einteilchen-Neutronorbitale in der pf-Schale mittels (p,pn)-Reaktionen und Impulsverteilungsanalyse. Die quasifreie Neutronenstreuungsreaktion wurde während einer experimentellen Kampagne in der Radioactive Isotope Beam Factory (RIBF) am SAMURAI-Fragmentspektrometer in inverser Kinematik bei einer Energie von $\sim$230 MeV/Nukleon in einem 15 cm langen Flüssigwasserstoff-Target unter Verwendung des MINOS TPC [8] gemessen. Inklusive und exklusive Wirkungsquerschnitte zu gebundenen Zuständen von ^{51}Ca wurden mithilfe von γ-Strahlenspektroskopiemessungen ausgewertet. Außerdem wurden die Impulsverteilungen gemessen, die der Entfernung von $1f_{7/2}$- und $2p_{3/2}$- Neutronen entsprechen. Die Wirkungsquerschnitte, die im Rahmen der DWIA interpretiert werden, stimmen mit einem Schalenabschluss bei der Neutronenzahl N=32 überein, der bei Ca-Isotopen genauso stark ist wie bei N=28 und N=34. Die Analyse der Impulsverteilungen führt zu einer Differenz der quadratisch gemittelten Ladungsradien der $1f_{7/2}$- und $2p_{3/2}$- Neutronenorbitale von 0,61(23) fm [9] und stimmt mit der Vorhersage von 0,7 fm des modifizierten Schalenmodells überein [7]. Das deutet darauf, dass der große quadratisch gemittelten Radius des $2p_{3/2}$-Neutronenorbitals in neutronenreichen Ca-Isotopen für den unerwarteten linearen Anstieg des Ladungsradius, in Abhängigkeit von der Neutronenzahl, verantwortlich ist. Die Methode zur Bestimmung der quadratisch gemittelten Radien der Einteilchen-Neutronenorbitale über Impulsverteilungsmessungen in (p,pn) Reaktionen wurde weiterhin auf die benachbarten Isotope ^{53}Ca und ^{54}Ca angewendet. Die Größe der $1f_{7/2}$-, $2p_{3/2}$-, $2p_{1/2}$- und $1f_{5/2}$- Neutronenorbitale wurde ermittelt und stimmte mit den Ergebnissen von ^{52}Ca überein. Als Ergebnis dieser Studie zeigen die p-Orbitale tat-

sächlich eine räumlich größere Ausdehnung im Vergleich zu den f-Neutronenorbitalen (>0,5 fm Unterschied).

Der zweite Teil dieser Arbeit stellt die Forschung und Entwicklung eines neuen Teilchen-Trackers, STRASSE [10], in Kombination mit einem langen Flüssigwasserstoff-Target vor. Dieser zielt auf die Untersuchung protoneninduzierter quasifreier Streureaktionen wie (p,2p) und (p,3p) ab. Trotz der verbesserten Zählrate wurde das MINOS-System [8] nur zur Verfolgung des Reaktionsscheitelpunkts innerhalb des Flüssigwasserstoff-Targets verwendet. Ein ähnlicher Aufbau, der zusätzlich zur γ-Strahlenspektroskopie auch Teilchenspektroskopie ermöglicht, könnte fehlende Masseninformationen liefern. STRASSE ist für die Verwendung zusammen mit CATANA [11] konzipiert, einer Anordnung von CsI(Na)-Kristallen zur Messung der Gesamtenergie der Protonen aus den (p,2p)- und (p,3p)- Reaktionen sowie um eine γ-Strahlenspektroskopie durchzuführen. Dieser neue Versuchsaufbau wird in der Lage sein, den Reaktionsscheitelpunkt mit einer Auflösung im sub-mm-Bereich zu rekonstruieren und fehlende Massenmessungen mit einer Auflösung von unter 2 MeV durchzuführen [10]. In dieser Arbeit wird die Herstellung und Erprobung der Flüssigwasserstoffzelle für STRASSE sowie Offline- und In-Beam-Tests der für STRASSE vorgesehenen Ausleseelektronik unter Verwendung des Prototyps des Silizium-Trackers PFAD vorgestellt.

Contents

1 Introduction

1.1 Atomic nuclei and the driving mechanism for shell evolution

A nucleus is composed of interacting nucleons, i.e., neutrons and protons. The nucleons are in turn composed out of quarks and gluons, sketched in Figure 1.1, left side. Quantum chromodynamics (QCD) describes the strong interactions between the quarks and gluons. According to QCD, the colored objects such as quarks interact weakly at low distances (<1 fm) and strongly at larger distances. This behavior is known as the asymptotic freedom. Also this is why quarks carrying color are bound and form colorless systems, the protons and neutrons [12]. The typical energies at play in nuclear structure are low compared to the masses of nucleons and therefore, the nucleon-nucleon (NN) interactions can be described effectively with nucleons and pions as degrees of freedom, without the need to resolve the energy scale of the constituting quarks and gluons. The nuclear forces can be considered as a residual of the strong force, which is acting between the constituents of the nucleons and which is "leaking" outside the nucleons [13]. This approach is taken by the chiral effective field theory (ChEFT). In ChEFT the different contributions of the NN interactions are ordered according to a power counting scheme, in powers of $\mu = Q/\Lambda$, with Q being the typical nucleon momenta in the nucleus or the pion mass (soft scale) and Λ being the breakdown scale (hard scale) of the theory ($\sim$0.5-1 GeV) [12, 13]. The NN interactions are given mainly in the leading order (LO) and next-to leading (NLO) order terms of the expansion and, additionally, three-nucleon (3N) interactions appear at next-to-next-to leading order (N^2LO) terms [12]. Modern ChEFT calculations are performed up to N^3LO or even N^4LO terms [14]. The results of ChEFT should be independent from the chosen breakdown scale and the accuracy should increase by considering higher order terms; this is achieved using renormalization techniques [12]. Traditionally, the coupling constants entering into the ChEFT interactions are fitted on nucleon-nucleon scattering phase shifts and binding energies of 3-body nuclei [13]. Interactions derived from ChEFT can describe pp and pn scattering data with high precision ($\chi^2\sim$1) [15] and can nowadays be used in ab initio nuclear structure calculations [14]. The alternative for the nucleon-nucleon interactions commonly used in ab initio calculations are the semi-phenomenological interactions (such as Argonne $v18$ [16], CD-Bonn [17] and the soft interaction $V_{low\,k}$ [18]).

Historically, the nucleons in the nucleus were described in analogy to the electrons in the atoms; they were considered to occupy discrete energy levels in the nuclei, obeying the Pauli principle, with the difference that the electrons are bound by the external electrical potential produced by the positively charged nucleus, while the *mean field* in which nucleons are bound

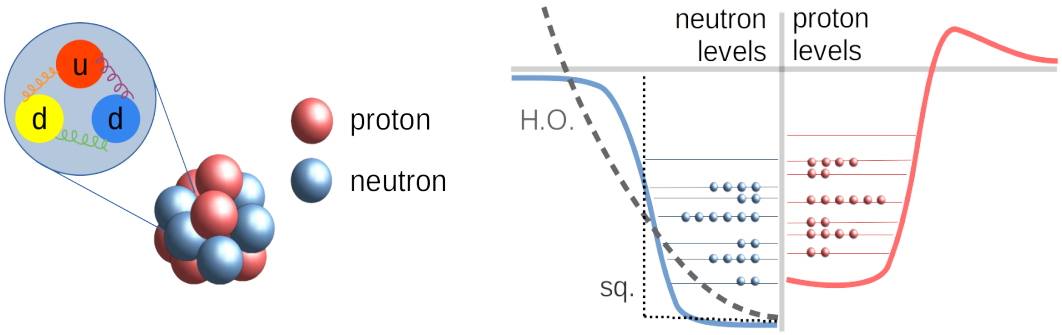

Figure 1.1: A simplified view of a nucleus with protons and neutrons and the constituting quarks and gluons of a nucleon (left). A nuclear potential well with a sketch of the neutron and proton levels (right). Aside from a potential of the Woods-Saxon type, the harmonic oscillator (H.O.) and the square well (sq.) potentials are also sketched for the neutrons side.

is produced by themselves. In this picture, which is the *Shell Model*, the discrete energy levels are grouped into shells and when a shell is complete or fully occupied, the system is energetically stabilized compared to the neighbouring nuclei. These stable configurations appear for certain numbers of nucleons and these numbers are called *magic numbers* [19]. The shell model was developed more than 70 years ago, by several physicists independently (M. Goeppert Meyer, O. Haxel, J. H. D. Jensen, and H. E. Sues) [20, 21] and it was a Nobel-Prize-worthy achievement in nuclear physics.

Figure 1.1 shows in the right side a sketch of protons and neutrons potential wells, the vertical dimension representing the energy of the nuclear potentials and the horizontal dimension representing the radial coordinate in space. The first magic numbers: 2, 8, 20, 40 where already obtained by M. Goeppert Meyer and J. H. D. Jensen by considering the independent nucleons in a harmonic oscillator potential or a square well potential [20, 21]. By adding a centrifugal (l^2) term and a spin-orbit $(\vec{s} \cdot \vec{l})$ term, they obtained the further empirically observed magic numbers 28, 50, 82, 126 [20, 21]. The harmonic oscillator (H.O.) and the square well potentials are depicted with a grey dashed line and a black dotted line, respectively, in Figure 1.1. The energy levels and their ordering obtained with the modified harmonic oscillator are shown in Figure 1.2. The signature of the shell structure can be found in observables such as the energy of the first excited state in even-even nuclei, E(2^+). In doubly-magic nuclei E(2^+) is high, while the transition probability B(E2; $0^+ \rightarrow 2^+$) is low. Additionally, the separation energy for neutrons or protons for closed shell nuclei is high compared to the neighbouring nucleus with A+1.

The independent-particle shell model provides a good description especially for the stable, closed-shell atomic nuclei [22]. For nuclei with valence nucleons (nucleons outside of a closed shell), one needs to include the two-body residual interactions. Since 1954 it was suggested that the spin-orbit term is in fact more complicated and that there must be a tensor force or

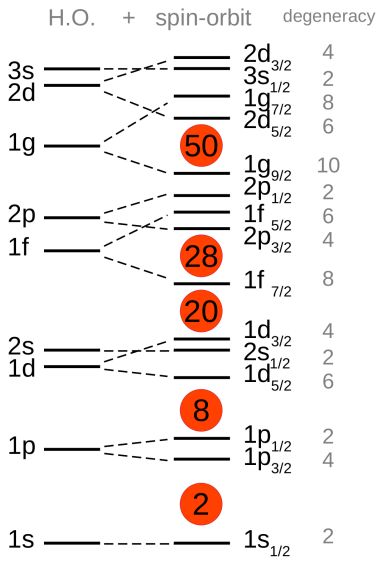

Figure 1.2: The first energy levels in a single-particle shell model. The left side shows the levels using an harmonic oscillator potential and the right side shows the levels with the addition of the spin-orbit interaction. The numbers in the boxes indicate the magic numbers.

a two-body spin-orbit force [23]. The impact of these two-body residual interactions on the *shell evolution* was discussed by Talmi and Unna in 1960 [1] giving as an example the relative energy shift of the $1p_{1/2}$, $1d_{5/2}$, and $2s_{1/2}$ neutron orbitals. The energy levels ordering is not kept throughout the whole nuclear chart; they can shift and change their ordering as a result of the monopole drift and this can lead to the weakening or the disappearance of some conventional magic numbers or to the emergence of new magic numbers. Some examples of magic numbers disappearing are: $N = 8$ which disappears in the Be isotopes [24], $N = 20$ disappearing in Na [25, 26] and Mg [27] isotopes or $N = 28$ disappearing in Si [28]; on the other hand $N = 16$ can appear in the oxygen isotopes [29–31] making $^{24}_{8}O_{16}$ doubly magic and the $N = 32$ and $N = 34$ emerge in the calcium isotopes region. References [32–34] provide extensive reviews on the shell evolution and the change of magic numbers away from stability.

Focusing on the case of the $N = 32$ and $N = 34$ new magic numbers in the calcium isotopes, they have been explained within the interacting shell model as steaming mostly from the shift in energy of the $1f_{5/2}$ neutron orbital, represented in Figure 1.3. How is the residual interaction responsible for the shell evolution?

The nucleus is a many-body system, the Hamiltonian of an A-nucleus system being given by: $H = \sum_k^A T(k) + \sum_{j<k}^A V(j,k)$, with $T(k)$ the kinetic energy and $V(j,k)$ the two-body nucleon-nucleon interaction considering here two-body forces only. Alternatively, one can use a single-particle effective potential, $U(k)$, and consider the rest to be a *residual interaction* among the nucleons in the considered valence space:

$$H = \sum_k^A [T(k) + U(k)] + \left[\sum_{j<k}^A V(j,k) - \sum_k^A U(k) \right] \tag{1.1}$$

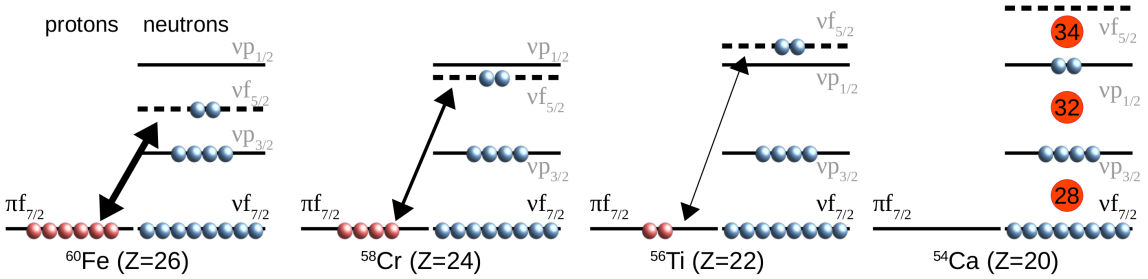

Figure 1.3: Schematics of the shell evolution towards the neutron-rich calcium isotopes. The $f_{5/2}$ neutron orbitals shifts in energy as the protons are removed from the $f_{7/2}$ proton orbital. Two new neutron shell closures at $N = 32$ and $N = 34$ emerge due to this shift in energy. Figure adapted after [3].

which can be written as:

$$H = H^{(0)} + H^{(1)} = \sum_{k}^{A} \epsilon_k^{(0)} + \sum_{j,k}^{A} \hat{\epsilon}_{j,k}^{(1)} \tag{1.2}$$

with $H^{(0)}$ describing the ensemble of independent particles moving in a *mean field* and the $H^{(1)}$ part containing the *residual interactions* [35]. $H^{(1)}$ can be an effective Hamiltonian in a reduced valence space around the Fermi surface, or in an extended valence space with all nucleons active (no-core shell model, NCSM). One can also divide the full Hamiltonian into a *monopole* part plus higher-grade multipole terms, $H = H_{mono} + H_M$. In the interacting shell model, $H^{(0)}$ gives the single-particle energies (SPE), $\epsilon_k^{(0)}$, to which we need to add the effect of the monopole part of the residual interaction in order to obtain the *effective* single-particle energies (ESPE), as in equation 1.2. The monopole interaction between two nucleons contains the central force, spin-orbit terms and tensor terms. The spin-isospin term, $V_{\sigma\tau}(r)\,(\vec{\sigma_1}\cdot\vec{\sigma_2})(\vec{\tau_1}\cdot\vec{\tau_2})$, produces an attractive interaction. Moreover, the spin-isospin part favours the spin-flip, via $\vec{\sigma}$, being the main contributor to the central part of the monopole interaction and mainly coupling pairs of nucleons in the same orbit l. At the same time, it favours the isospin-flip (or charge-exchange) processes via $\vec{\tau}$ [34]. In other words, it is the most attractive for pairs such as $\pi\,\mathrm{j}_<$ and $\nu\,\mathrm{j}_>$ or $\nu\,\mathrm{j}_<$ and $\pi\mathrm{j}_>$ ($\mathrm{j}_> = l + 1/2$ and $\mathrm{j}_< = l - 1/2$). The values for the matrix element of the tensor force for various pairs of orbitals is plotted Ref. [34]. Another major term responsible for the shell evolution is the tensor force, $f(r)\,S_{12}(r)$, with $S_{12}(r) = \frac{3}{r^2}(\vec{\sigma_1}\cdot\vec{r})(\vec{\sigma_2}\cdot\vec{r}) - \vec{\sigma_1}\cdot\vec{\sigma_2}$ being the tensor operator and $f(r)(<0)$ being the coupling strength of the tensor interaction. The tensor force is the most attractive for spin-flip, isospin-flip pairs $\nu\,\mathrm{j}_<$ and $\pi\mathrm{j'}_>$ and repulsive for $\mathrm{j}_>$ and $\mathrm{j'}_>$ type of pairs. The impact of the tensor force on the shell evolution is evaluated in Refs. [36, 37] and the values for the matrix element of the tensor force for various pairs of orbitals are plotted Ref. [34].

The SPE is independent on the occupancy of the orbitals, but the monopole part of the residual interaction depends on the occupation of the orbitals. The effective single-particle energy shift, as a result of the interaction of the $\pi f_{7/2}$ orbital with the $p_{1/2}$, $p_{3/2}$, and $f_{5/2}$

neutron orbitals, changes the order of the single-particle orbitals when one removes protons from the $\pi f_{7/2}$ orbital. The strong attraction between the $\pi f_{7/2}$ orbital and the $\nu f_{5/2}$ orbital, which were νj$_<$ and πj'$_>$, is now weakening and the new magic numbers at $N = 32$ and $N = 34$ are created, as depicted in Figure 1.3.

1.2 New shell closures at N = 32 and N = 34 in Ca isotopes

The calcium isotopes have the proton magic number, Z=20, and the two well-established neutron magic numbers, $N = 20$ and $N = 28$. Moreover, 6 of the calcium isotopes with A=40, 42, 43, 44, 46, and 48, have a natural abundance and are stable[1]. In the neutron-rich side of the calcium isotopes, new shell closures at $N = 32$ and 34 were revealed, as well as on the proton-rich side, the new $N = 16$ shell closure was recently observed [44]. The first experimental observation of the $N = 32$ in the calcium isotopes dates back to 1985 [2]. From the γ-ray decay spectrum of ^{52}Ca populated via the β-decay of ^{52}K, the energy of the 2^+ excited state in ^{52}Ca was established at a value of 2.563 MeV [2]. From the E(2^+) systematics in the Ca isotopes chain, showing a local maximum for $N = 32$, similar to $N = 20$ and $N = 28$, it was concluded that $N = 32$ becomes a magic number. Moreover, in the same paper, shell-model calculations for pf-shell nuclei with the valence space including the $1f_{7/2}$, $2p_{3/2}$, $1f_{5/2}$

[1] ^{148}Ca has a long half-life of >2·10^{19}y

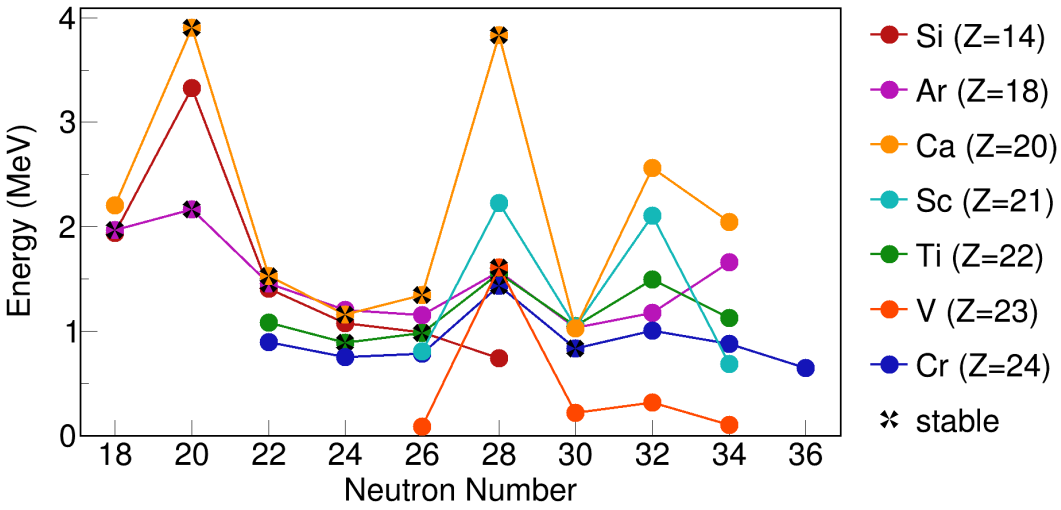

Figure 1.4: The systematics for the energy of the first excited state in Si, Ar, Ca, Sc, Ti, V and Cr isotopes. From this figure one can observe the emergence of the $N = 32$ and $N = 34$ shell closures, being the strongest in the Ca isotopes, and on the other hand, the disappearance of the $N = 28$ shell closure for the Si isotopes. The stable (or with very large half-life) isotopes are marked as indicated by the legend. Data from Refs. [2, 3, 28, 38–43].

and $2p_{1/2}$ predict the 2^+ excited state at 2.28 MeV and the ground state 0^+ configuration of $0.94\left|f_{7/2}^8 p_{3/2}^4\right\rangle + 0.29\left|f_{7/2}^8 p_{3/2}^3 p_{1/2}^1\right\rangle + 0.10\left|f_{7/2}^8 p_{3/2}^3 f_{5/2}^1\right\rangle + ...$ further confirming the neutron shell closure at $N = 32$.

For the next even-even neighbouring nucleus, ^{54}Ca, the value of E(2^+) was later pinned down experimentally at 2.043 MeV [3]. This measurement is supporting the $N = 34$ shell closure as well in the calcium isotopes. The E(2^+) systematics of even Ca isotopes are plotted in Figure 1.4 in comparison to the even-even Si, Ar, Ti and Cr isotopes and the energy of the first excited state for the Sc and V even-N isotopes. The 2^+ energy states correspond to the excitation of a neutron pair to the next valence neutron orbital [45]. In the calcium isotopic chain, the E(2^+) value for $N = 34$ is 0.5 MeV lower than for $N = 32$. Shell model calculations show [3, 46] that for ^{52}Ca, this value reflects the energy gap E($p_{1/2}$) - E($p_{3/2}$). On the other hand, for ^{54}Ca, the E(2^+) value is lowered as a result of the correlation energy, but the energy gap E($f_{5/2}$) - E($p_{1/2}$) is in fact comparable to E($p_{1/2}$)-E($p_{3/2}$), making the two shell closures, $N = 32$ and $N = 34$, of comparable strengths. The $\sim$0.5 MeV energy difference is coming from the relative strengths of the $\left\langle p_{3/2}p_{3/2}\right| V \left|p_{1/2}p_{1/2}\right\rangle_{J=0}$ and $\left\langle p_{1/2}p_{1/2}\right| V \left|f_{5/2}f_{5/2}\right\rangle_{J=0}$ pairing-matrix elements [3]. Moreover, based on Ref. [46], the shell-model calculated spectroscopic factor for the neutron removal of the $\nu p_{1/2}$ neutron orbital from ^{54}Ca (g.s.) is 91% of the maximum value, while for the $\nu p_{3/2}$ neutron orbital from ^{52}Ca (g.s.) and $\nu f_{7/2}$ neutron orbital from ^{48}Ca (g.s.) the values of 89% and 92% (experimental value [47]), respectively, are reported further supporting the similarity in strength between the $N = 32$ and $N = 34$ shell closures.

Going to lighter nuclei, in the argon isotopes one finds a weakening of the $N = 32$ shell closure with an E(2^+) of only 1.1 MeV [48, 49], but the persistence of the $N = 34$ shell closure with an E(2^+) value of 1.656 MeV [39], higher even than at $N = 28$. This can be seen in Figure 1.3. Towards larger Z values, experimental measurements show that the $N = 32$ and $N = 34$ shell closures are declining after the chromium [40] and scandium [42] isotopes, respectively.

From mass measurements on isotopes from potassium to titanium we get additional evidence for the energy gap at $N = 32$ [50–53], as well as from the mass measurement on ^{54}Ca [54] and the one-neutron knock-out cross section measurement [46], supporting the $N = 34$ shell closure. Moreover, transition probability measurements also confirm the existence of a shell closure at $N = 32$ in titanium [41, 55] and chromium [56] isotopes.

The Ca isotopes benefit from having a robust $Z = 20$ proton core, making them ideal for studying their characteristics along the neutron number. The robustness of the $Z = 20$ proton core was investigated and confirmed by many experiments for the neutron-rich potassium and calcium isotopes [45, 57–59]. All the above experimental evidences based on 2^+ energy, mass, transition probability and cross section measurements of ^{54}Ca(p,pn) reveal the new and non-standard $N = 32$ and $N = 34$ neutron shell closures in the neutron-rich region of nuclei. The neutron structure of ^{52}Ca was not directly probed so far, and this is one of the objectives of this thesis.

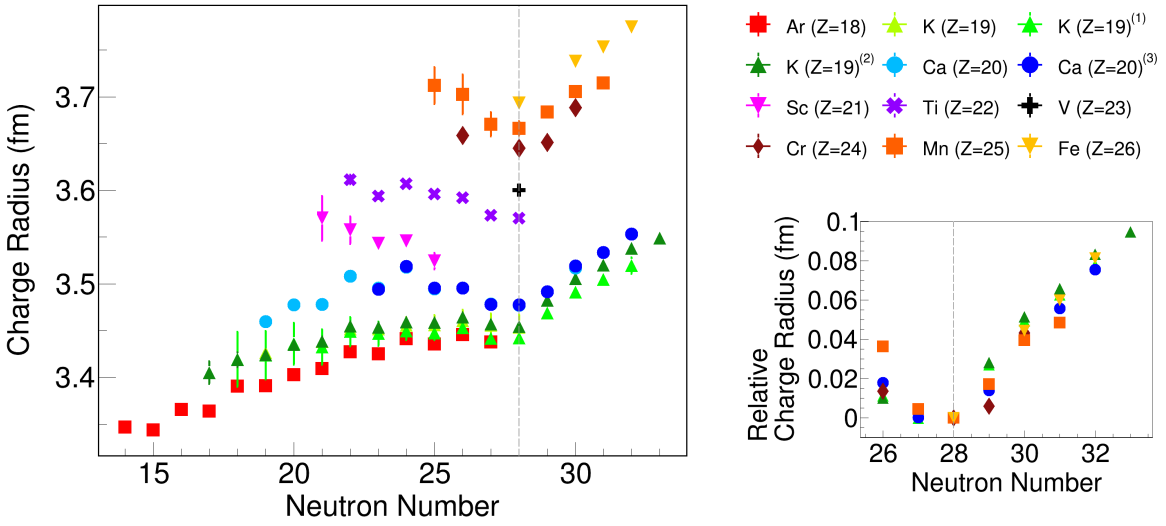

Figure 1.5: Absolute (left) and relative (right) charge radii for isotopes with $Z = 18 - 26$. The dashed-grey vertical line marks $N = 28$. Sources: [60], [61](1), [5](2), and [4](3).

1.3 Charge radii of neutron-rich Ca isotopes

Aside from the experimental measurements mentioned in the previous section used for supporting the $N = 32$ neutron shell closure, charge radii measurements are also used as experimental evidences for the magic numbers [4]. The isotope shift method provides differential charge radii values [62, 63]. It is a tool from atomic physics giving us precise information on the nuclear structure. As its name suggests, the method is based on the shift in the electronic energy levels between the different isotopes of the same element [64]. The isotope shift has two components, one is the *mass shift* and the second one is the *field shift* or the *volume shift*. The mass shift has two components, the normal mass shift (NMS) and the specific mass shift (SMS). NMS is arising from the fact that the nucleus has finite mass and therefore does not coincide with the center of mass of the atom as the electrons orbit around it, while the SMS is concerning the multi-electron spatial correlations and involves knowledge of the electron wavefunction. The second component of the isotope shift is sensitive to the *size* of the nucleus. The Coulomb field that the electron(s) "feel" is different for a point-like source or for a finite-size nucleus as a source. The potential changes its shape and it is sensitive to the charge radius of the nucleus. The effect is stronger for the electrons in the S orbital as their wavefunction does not vanish at $r = 0$. The mass shift is proportional to the inverse squared mass of the nucleus and is dominating the light nuclei region, while the filed shift is dominating the heavy nuclei region. [65]. The method consists in measuring an S→P transition of the selected ionization state of the element. If a hyperfine structure exists, the centroid frequency is typically considered. In a simplified picture, the change in the transition energy is proportional to the change in total electron probability density at the origin, $\delta \langle \Psi | \Psi \rangle^2_{r=0}$, times the mean-square charge radius difference, $\delta \langle r^2 \rangle$. As a result, the isotope shift, or the

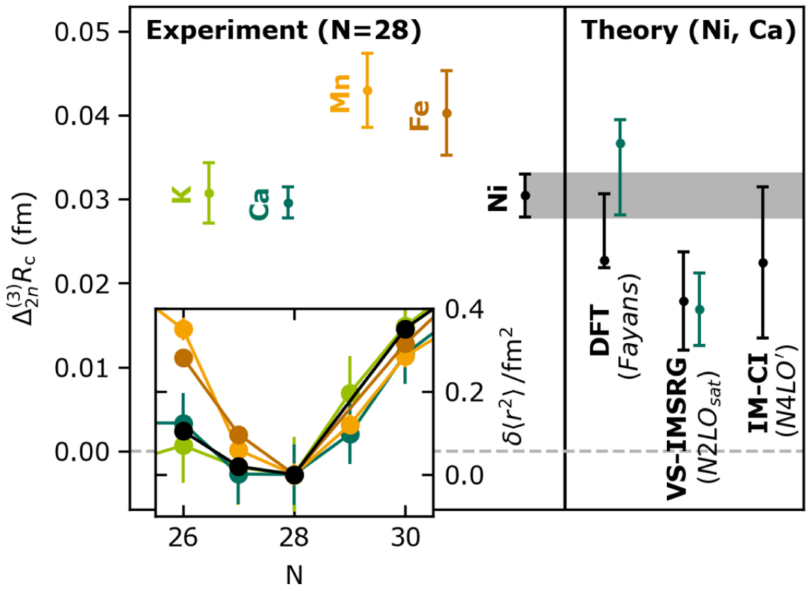

Figure 1.6: The two-neutron three-point indicator for the charge radii. Experimental values (left) and theoretical calculations (right). The inset shows the charge radii relative to the value at $N = 28$. Figure reprinted with the permission from [66] ©2023 by American Physical Society.

difference in the frequency of the selected transition between the isotopes A and A', $\delta\nu^{A,A'}$, will be the sum between a mass term and a volume shift term, the later one being sensitive to the difference between rms charge radii of the two isotopes [62], $\delta\langle r^2\rangle^{A,A'} = \langle r^2\rangle^{A'} - \langle r^2\rangle^{A}$ with the masses $M_{A'}$ and M_A.

$$\delta\nu^{A,A'} = K_{MS}\frac{M_{A'} - M_A}{M_{A'}M_A} + F\delta\langle r^2\rangle^{A,A'}$$

with K_{MS} the mass shift term containing the normal mass and specific mass effects and F being the field shift term. Both can be calculated theoretically as well as determined experimentally.

$$\delta\langle r^2\rangle^{A,A'} = \frac{1}{F}\left(\delta\nu^{A,A'} - K_{MS}\frac{M_{A'} - M_A}{M_{A'}M_A}\right)$$

This is a differential measurement, so we need a reference charge radius value for the isotope A in order to obtain the rms charge radius of the isotope A' of the same element. Although the isotope shift measurements have a very high accuracy, typically the theoretical calculations are the dominant source of errors for the charge radii determination. The reference value comes with an additional source of uncertainties.

Charge radii measurements were conducted in several isotopic chains [4, 5, 60, 61]. In Figure 1.5 the absolute values (left) for the charge radii as well as the values relative to the $N = 28$ (right) are plotted as a function of the neutron number for isotopes from $Z = 18$ to $Z = 26$. Although the charge radii reflect the distribution of the protons inside the nucleus,

they are also affected greatly by the neutrons inside the nucleus; an extended distribution of the neutrons, neutron skins or halos would attract and extend the proton distribution as well. In all isotopic chains we notice a local minimum at the magic number $N = 28$ and a sharp increase after it and this is generally seen as an experimental evidence for magic numbers. No such behavior is observed at $N = 32$ for the potassium and calcium isotopic chains. The charge radii of the most neutron-rich potassium and calcium isotopes ($N = 32$) were recently measured by Koszorús *et al.* [5] and Garcia Ruiz *et al.* [4], respectively.

Local minimum or kink in the charge radii trend as evidence for the magic numbers?

In the trend of the charge radii across magic numbers, one usually expects to see a local minimum or a kink. Sommer *et al.* [66] measured the charge radii in the nickel isotopic chain showing surprising results from the comparison of the charge radii behaviour across the $N = 28$ shell closure in the two doubly magic nuclei ^{48}Ca and ^{56}Ni.
The experimental charge radii values for the K, Ca, Mn and Ni isotopes are presented in the Figure 1.6 (inset) relative to their value at $N = 28$. The two-neutron three-point indicator is used for comparing the strength of the "kink" in the various isotopic chains (left). The two-neutron three-point indicator was calculated as follows:

$$\Delta^{(3)}_{2n} R_c(N) = \frac{1}{2}\left[R_c\left(N+2\right) - 2R_c\left(N\right) + R_c\left(N-2\right)\right]$$

with $R_c(N)$ being the measured charge radius value for N neutrons.
What was noticed by Sommer *et al.* [66] is that the "kink" strength is similar for the potassium, calcium and nickel isotopes around the neutron magic number 28. The similarity in the charge radii trends between calcium and nickel isotopes despite the differences between ^{48}Ca

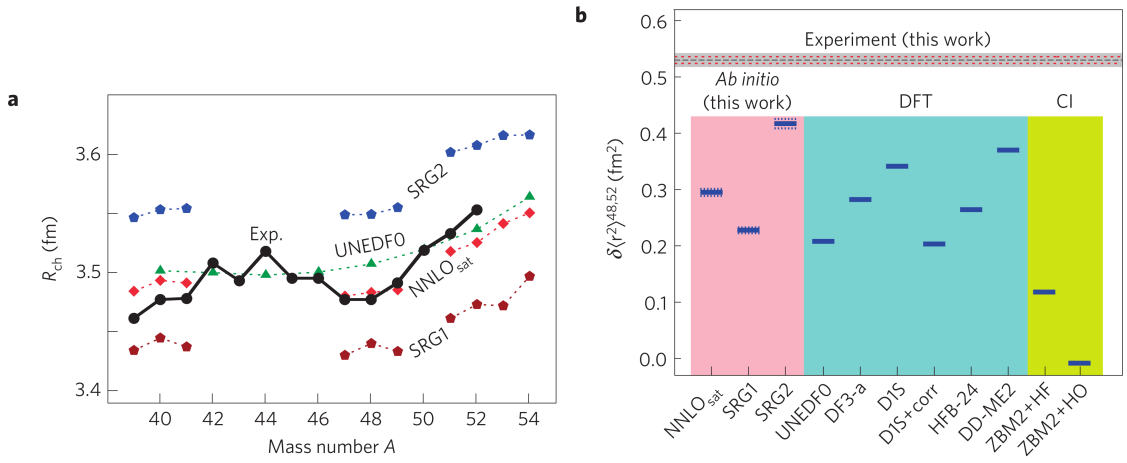

Figure 1.7: Left: Charge radii of the Ca isotopes as a function o the neutron number, experimental values (black) and theoretical calculations (colors). Right: the differential charge radius value from the experiment (brown) and from the theoretical calculations (blue). Figure reprinted with the permission from [4] ©2023 by Springer Nature.

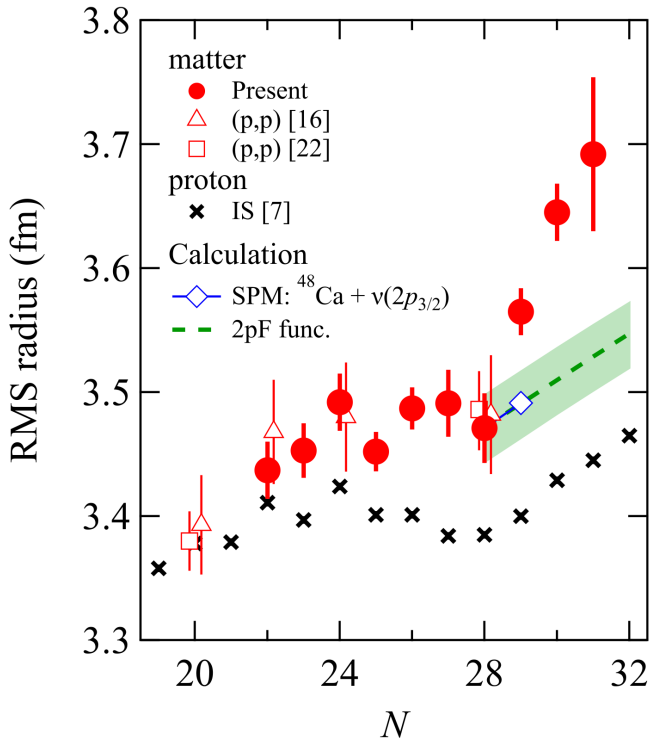

Figure 1.8: Matter radii (red circles) and proton radii (black crosses) of Ca isotopes as a function of the neutron number N. Figure reprinted with the permission from [6] ©2023 by American Physical Society.

and ^{56}Ni is surprising; ^{56}Ni is known to be a much softer core than ^{48}Ca. The two nuclei have a different proton occupancy, $Z = 20$ and $Z = 28$, respectively, and thus a different ordering of the neutron single-particle energy levels. A strong evidence for the shell-closure is a low B(E2) value. The B(E2) value for ^{56}Ni is more than 4 times larger than that of ^{48}Ca. In the right side plot of the same figure, one can see how the nuclear density functional theory (DFT) and *ab initio* calculations can well reproduce the experimental two-neutron tree-point value, more details can be found in the original text [66]. The conclusion of Sommer *et al.* [66] is that the "kink" in the charger radii is not reflecting the strength of a shell closure.

Going back to the Figure 1.5, for $N = 32$, the fact that one does not observe a "kink" in the charge radii trend of the calcium isotopes is not necessarily a sign of the lack of magicity at $N = 32$. Moreover, in the right side plot, the relative charge radii reveal how the slope after $N = 28$ is nearly the same between the isotopes of all elements. This large slope is not reproduced by most of the theoretical models including ab initio and this can be seen for the case of calcium isotopes in Figure 1.7, with the exception being DFT models such as Fy(Δr,HFB) [5, 67]. The left side plot is showing with black dots the experimental charge radii values in fm units and the colored dots are calculations with different theoretical models indicated in the figure. The right side plot is showing with the brown horizontal line the

experimental value for the differential charge radius $\delta\langle r^2\rangle^{48,52}$ and the calculated values with the blue lines. More details about the theoretical calculations and the comparison to the experimental values are found in the original paper [4]. Nevertheless, the measured charge radius for ^{52}Ca turned out to be surprisingly large for a doubly magic nucleus as the authors of the paper state, "The large and unexpected increase of the size of the neutron-rich calcium isotopes beyond N = 28 challenges the doubly-magic nature of ^{52}Ca" [4].

The same trend with the large slope after $N = 28$ is observed in the matter radii values obtained from interaction cross section measurements for the Ca isotopes in the paper *Swelling of Doubly Magic ^{48}Ca Core in Ca Isotopes beyond $N = 28$* [6]. The matter radii values are plotted with red circles in Figure 1.8 and the proton radii, obtained from the charge radii [4] via the isotope shift method, are also shown with black crosses. The diamond represents the radius obtained by adding a $p_{3/2}$ valence neutron to a ^{48}Ca core. The matter radii data is pointing towards a sudden increase of the neutron density distribution after $N = 28$ and it represents a challenge for theory, if confirmed.

Swollen *p* neutron orbitals explaining the large charge radii?

The large value for the charge radius of ^{52}Ca, with no kink at $N = 32$ and the large slope after $N = 28$ are thought to challenge the doubly-magic character of ^{52}Ca [4]. A modified shell-model by Bonnard *et al.* [7] manages to reproduce the trend of the charge radii of Ca- and K isotopes by proposing the population of some enlarged p neutron orbitals in these neutron-rich nuclei. At the addition of an extra neutron to the system, the isoscalar monopole polarizability is responsible with the overall increase of the matter radius, while the isovector monopole polarizability is trying to equalize the neutron and the proton rms

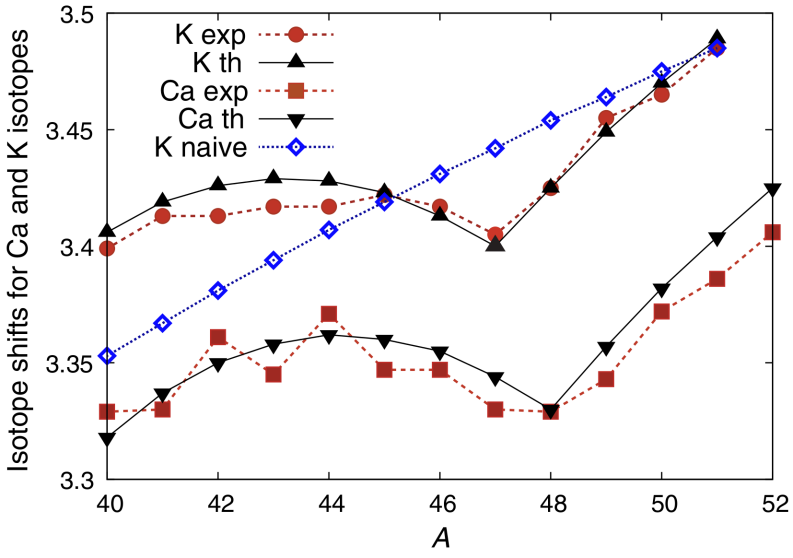

Figure 1.9: The charge radii in K and Ca isotopes: experimental values with red and theoretical calculations with black. See the original paper for more details [7]. Figure reprinted with the permission from [7] ©2023 by American Physical Society.

radii. The addition of the term in the interaction responsible for this effect is *ad hoc* and no explanation is given for it by Ref. [7]. Figure 1.9 from Ref [7] shows that the experimental values and the slope of the charge radii for Ca and K isotopes are well reproduced by these calculations assuming an extended $p_{3/2}$ neutron orbital which would produce an increase in the proton distribution as well. This model predicts a 0.7 fm difference between the huge $p_{3/2}$ and the $f_{7/2}$ neutron orbital in the Ca and K neutron-rich nuclei. So far, no experimental data corroborate this prediction. This is addressed by the work presented in this manuscript.

These being said, the large value for the charge radius of ^{52}Ca is predicted to be due to the filling of a large spatially distributed $p_{3/2}$ neutron orbital and it does not imply a lack of magicity of $N = 32$, but on the contrary. The extension of the charge distribution as one increases the neutron radius is due to an effect of equalization of the proton and neutron radii as suggested by Ref. [7]. The large charge radius value implies that the valence nucleons have a large occupation of the $p_{3/2}$ neutron orbital as opposed to the $f_{5/2}$, in which case it would have had a smaller radius. This qualifies ^{52}Ca for having a shell closure at $N = 32$.

1.4 Methods for determining the charge, matter and neutron radii of nuclei

1.4.1 Charge radii measurements

Electronic and muonic X-ray transitions coupled with laser spectroscopy

There are various methods explored by the experimental nuclear physics for obtaining information about the size of the nuclear matter, protons and neutrons. One of the methods is the isotope shift method, which is an well-established and powerful tool in the study of the nuclear size and was already discussed in this chapter. It is measuring the shift in certain atomic transitions caused by the size of the nucleus. Here a distinction is made between the optical transitions and the X-ray transitions; the theoretical interpretation of X-ray transitions is simpler than that of optical transitions and the variation from element to element is smooth and gradual, but the measurements using the X-ray transitions are not as precise as with the optical ones [64]. The isotope shift method is used for probing the charge radii of the atomic nuclei [62, 63, 68]. Nonetheless, it does not offer absolute values for the charge radii, but rather relative values, so one needs a reference nucleus with a very well known charge radius. On the positive side, the isotope shift method using laser spectroscopy is not limited to stable nuclei, but it can be used for studying exotic nuclei, far from stability [69]. Also, it's important to note that the determination of charge radii using the isotope shift method is independent from nuclear models. By precisely measuring the transition energy and not the shift in the transition, one could obtain absolute values as well, although for the moment it is only possible for hydrogen-like systems [62]. A more sensitive probe are the muonic X-rays. The muon is more than 200 times heavier than the electron and has a larger overlap with the nucleus. As a result, the associated muonic X-ray transitions are affected more by the size of

the nucleus than the electronic X-ray transitions [70–72].

Electron scattering experiments

For obtaining absolute charge radius values one can perform electron elastic scattering measurements [73]. The electron elastic scattering differential cross section is the product of the Mott differential cross section and the square of the form factor, $F(q)$. The form factor is the Fourier transform of the charge distribution $\rho_{ch}(r)$:

$$F(q) = \frac{1}{Z}\int \rho_{ch}(r)\frac{sin(q\cdot r)}{qr}4\pi r^2 dr$$

The Mott differential cross section, which is the relativistic version of the Rutherford scattering, considers the nucleus to be point-like, while in reality is has an extended charge distribution. Thus, the form factor adds the effect of the charge distribution to the scattering differential cross section. The density is written as a two-parameter Fermi-type distribution and the two parameters are found from the experimental data from a χ^2 minimization procedure. The electron elastic scattering experiments are limited to stable nuclei, but can offer a high accuracy for the charge rms radii determination.

1.4.2 Measurement of single-particle rms radii of proton orbitals

The rms radii of the single-particle proton orbitals were obtained so far form (e,e'p) measurements as in Ref. [74]. The measured the momentum distributions from the (e,e'p) reaction were fitted to momentum distribution curves obtained from DWIA calculations. In the DWIA calculations, the single-particle wavefunction of the proton bound state was calculated with a Wood-Saxon potential, with the depth adjusted for the separation energy and the excitation energy of the final states, fixed diffuseness parameter, and the radial parameter left as a free fitting parameter. To be noted is that (e,e'p) measurements can be performed on stable nuclei only. In Ref. [74] the ^{51}V(e,e'p)^{50}Ti reaction was measured and the size of the $\pi f_{7/2}$ orbital was obtained with a value of 4.20(14)fm.
Another method for accessing the proton single-particle orbital size is by measuring the charge radii of pairs of nuclei of same neutron number, but proton numbers differing by one unit. From the difference one can extract the rms radius of the last valence single-particle proton orbital. This novel method is demonstrated in Ref. [75, 76] for the $3s_{1/2}$ proton single-particle orbital of ^{206}Pb, from the difference of the charge distributions of the ^{206}Pb and ^{205}Tl nuclei measured by electric scattering.

1.4.3 Matter radii measurements

Interaction cross section measurements

The interaction cross section measurements are mainly used for the determination of matter radii [77]. The reaction cross section for a target and projectile, ${}^{A_T}\mathrm{Z}_T + {}^{A_P}\mathrm{Z}_P$, can be expressed as a sum of all reaction processes except the elastic scattering. The reaction cross section includes the interaction cross section (σ_I), where the fragment is different from the projectile (${}^{A_F}\mathrm{Z}_F \neq {}^{A_P}\mathrm{Z}_P$) as well as the inelastic scattering contribution in which the fragment or the target are left in an excited state but have the same identity. Typically the interaction cross section is measured by the transmission technique, counting the unreacted nuclei after passing through the target. Often times the inelastic scattering contribution is neglected. In many cases it is indeed negligible, but in some cases it can lead to errors if it is not evaluated [78]. The interaction cross section can be further divided into the sum of all interactions with the protons that reduce the atomic number (Z) and the sum of all interactions with the neutrons that reduce the neutron number (N) of the nucleus. The first part is called charge changing cross section (σ_{CC}) and the second is called neutron removal cross sections ($\sigma_{\Delta N}$): $\sigma_I = \sigma_{CC} + \sigma_{\Delta N}$. From the charge changing cross section one can evaluate the charge radius of a nucleus and from the neutron removal cross section one can evaluate the neutron radius of a nucleus. The matter, charge and neutron radii obtained via cross section measurements are model-dependent, which can be a downside. The Glauber model is typically used for describing the cross sections for the production of a fragment ${}^{A_F}_{N_F}\mathrm{Z}_F$ from a projectile ${}^{A_P}_{N_P}\mathrm{Z}_P$ [78]:

$$\sigma = C_{Z_P}^{Z_F} C_{N_P}^{N_F} \int d^2b [1 - P_p(b)]^{Z_P - Z_F} P_p^{Z_F}(b) [1 - P_n(b)]^{N_P - N_F} P_n^{Z_N}(b)$$

with b being the impact parameter, C_n^k are binomial coefficients counting all possible combinations to select k particles out of the total of n particles. P_p and P_n are the survival probabilities for a single nucleon, proton or neutron [78]:

$$P_p(b) = \int dz d^2s \rho_p^P(\vec{s}, z) exp[-\sigma_{pp} Z_T \int d^2s \rho_p^T(\vec{b} - \vec{s}, z) - \sigma_{pn} N_T \int d^2s \rho_n^T(\vec{b} - \vec{s}, z)]$$

a similar relation holds for P_n; σ_{pp} and σ_{pn} are the proton-proton and proton-neutron total cross sections obtained by fitting to experimental data on a wide energy range. From these relations, one accesses the proton and neutron densities of the target and of the projectile, and the matter density is: $\rho_m(r) = \rho_p(r) + \rho_n(r)$, and the rms radii are:

$$\langle r^2 \rangle_i^{1/2} = \left(\frac{\int r^4 \rho_i(r) dr}{\int r^2 \rho_i(r) dr} \right)^{1/2}$$

where i stands for the protons, neutrons or matter. The interaction cross section method can be applied for studying a wide variety of stable and unstable nuclei [79, 80]. Similarly the elastic proton and alpha scattering reactions can be used for determining the matter radii.

Antiprotons for probing the nuclear matter size

Antiprotons are as well a suitable probe for the nuclear density. One method of using antiprotons is by measuring the level widths and shifts of antiprotonic X-rays induced by the strong interaction, which gives information on the matter distribution at the periphery [81]. The second method is by measuring the annihilation cross section for one neutron or for one proton of the target nucleus. The annihilation cross section is also sensitive to the periphery of the nuclear matter [81] or to the density ratio ρ_n/ρ_p and can be used for determining the halo factor. An example of such experimental setup for probing the nuclear matter using antiprotons is PUMA [82].

1.4.4 Neutron radii and neutron skin thickness measurements

Polarized electron scattering and parity violation cross section asymmetry

For the neutron radii determination, one can perform electron scattering measurements using *polarized* electron beams. Because the weak charge of the neutrons is larger than that of the protons, polarized electron elastic scattering experiments for parity violation cross section asymmetry (A_{PV}) measurements become a electroweak probe for the neutron densities [83, 84]:

$$A_{PV} = \frac{\sigma_R - \sigma_L}{\sigma_R + \sigma_L} \propto \frac{G_F Q^2 |Q_W| F_W(Q^2)}{4\sqrt{2}\pi\alpha Z F_{ch}(Q^2)}$$

where $\sigma_{R/L}$ is the cross section for the scattering of right/left-handed electrons from the target nucleus, G_F is the Fermi coupling constant, F_{ch} is the charge form factor, Q_W is the weak charge of the target nucleus. In this kind of experiment, one obtains the form factor of the weak charge of the nucleus, $F_W(Q^2)$, which is related to the neutron density, but one needs complete information about the proton, or charge density of the nucleus. The difficulty of these measurements is that the parity violating asymmetry is very small ($\sim$1 ppm [83]). The PREX-1 [85] and PREX-2 [84] experiments achieved a very high precision using polarized electron scattering for the ^{208}Pb neutron skin thickness value. The coherent π^0 photoproduction cross section measurements [86] were also used for determining the neutron skin thickness of ^{208}Pb. These measurements of the neutron skin thickness of ^{208}Pb have implications in understanding the EOS of nuclear matter and the structure and stability of neutron stars.

This list of experiments probing the nuclear matter is not exhaustive, but shows the diversity of methods used in nuclear physics for the matter, charge, and neutron rms radii determination. Some of the methods provide better accuracy than the others. In this thesis the use quasi-free neutron knock-out reactions are used for accessing the size of the *single-particle neutron orbitals* in the $pf-$ shell for calcium isotopes. This method is similar to the method using the (e,e'p) reaction for determining the size of the proton single-particle orbitals.

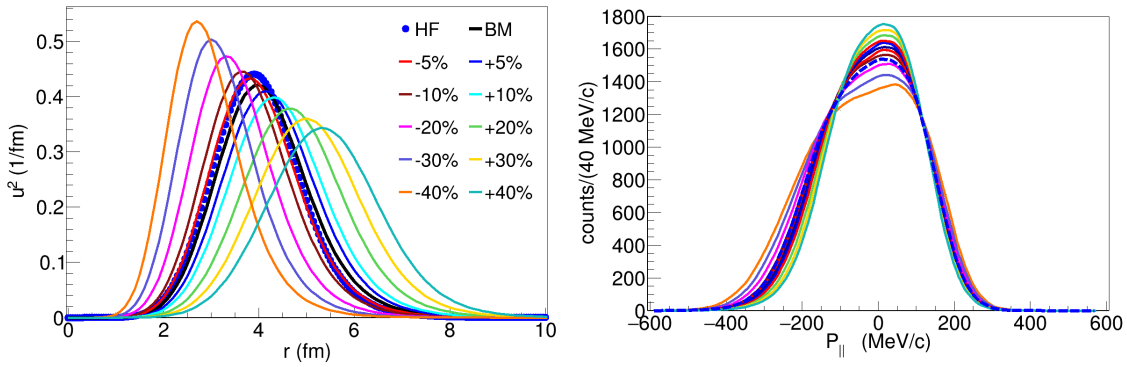

Figure 1.10: Examples of single-particle radial wavefunctions (left) and the produced parallel momentum distributions (right) for the $f_{7/2}$ neutron orbital of ^{52}Ca. The different colors correspond to calculations performed for orbitals of different sizes.

1.4.5 Studying the neutron single-particle orbitals radii via the quasi-free knock-out (p,pn) reaction

It is an well-established method to use the width of the parallel momentum distribution for extracting the angular momentum l. But the momentum distributions for a given l are sensitive to the size of the neutron orbital in a neutron knock-out reaction as well. The determination of the size of the neutron single-particle orbitals via (p,pn) reactions is based on the link between the spatial extension and the momentum distribution of the neutron inside the studied nucleus due to the Heisenberg uncertainty principle. The method is model-dependent. The experimental momentum distribution data is fitted with theoretical momentum distribution curves and using a χ^2 minimisation criterion one determines the size of the neutron wavefunction with which the theoretical calculations describe the experimental data the best. The accuracy depends on the case; one needs to be able to deconvolute the total momentum distribution into the component corresponding to the neutron knock-out from the studied single-particle orbitals and also one can apply this method only if the theoretical momentum distribution curves are sensitive enough to the orbital size. Examples of calculated single-particle wavefunctions for an f neutron orbital and the corresponding parallel momentum distribution are shown in Figure 1.10. The different colored curves correspond to calculations for different sizes for the single-particle neutron orbitals and the variation of the rms radius results in a variation of the shape of the momentum distribution. Details and results of the study of the pf-shell single-particle neutron orbitals of ^{52,53,54}Ca isotopes are presented in chapters 2 and 3 of this thesis.

1.5 Nuclear reactions with radioactive ion beams

For obtaining radioactive ion (RI) beams, one has two main production methods. One can shoot with light projectiles on heavy targets, producing the spallation and fission of the target, or one can shoot with an accelerated heavy ion on a light target, producing a sec-

ondary cocktail beam by the fragmentation of the projectile. The first production method, the ISOL technique, results in secondary beams of low energy (a few tens of keV), but of good quality (low energy spread). Examples of facilities using this method are ISOLDE at CERN, Switzerland, GANIL in France or TRIUMF in Canada. The ISOL technique is needed for exact measurements at low energies such as mass measurement or laser spectroscopy.
The second production method, the in-flight production, gives high-energy beams, but of worse quality than with the ISOL technique. The secondary cocktail beams obtained using this method are separated and identified event-by-event before being used for nuclear reactions on a secondary target. Examples of facilities producing high-energy RI beams are GSI in Germany, RIBF (RIKEN) in Japan, or FRIB in USA.

For the study of direct nuclear reactions, we are interested in high-energy radioactive ion beams. The production of a certain rare isotope depends on the fragmentation cross section of the primary beam. Going further from stability means working with lower intensity secondary beams. For increasing the measured yield one would like to use thicker targets. An example of experimental setup composing of a thick target is MINOS [8], which was used at RIBF experiments.
MINOS is using a 15-cm long liquid hydrogen target which allows to study proton-induced knock-out reactions. With a thick target, we now face an uncertainty in the reaction vertex position, which is usually needed for the Doppler-shift correction if one performs γ-ray spectroscopy, as well as for the precise determination of the momentum of the fragments. For this, MINOS has a TPC placed around the thick liquid hydrogen target. The TPC tracks the protons resulting from the quasi-free scattering reactions and can reconstruct the reaction vertex using these tracks. The study presented in chapters 2 and 3 are based on experimental data acquired at the RIBF facility using high-energy neutron-rich cocktail beams and the MINOS experimental setup.

Chapter 4 of this thesis presents the research and development of a new particle tracker combined with a liquid hydrogen target, STRASSE [10]. STRASSE aims to achieve a better resolution for the reaction vertex position determination using two layers of double-sided silicon strip sensors. Also, STRASSE will be used together with CATANA [11], a detector array of CsI crystals, which will measure the total energy of the protons and the γ-rays. With STRASSE and CATANA one will be able to perform missing mass measurements, complementary to γ-ray spectroscopy, and explore the nuclear structure far from stability.

2 Extended $p_{3/2}$ neutron orbital and the $N = 32$ shell closure in ^{52}Ca

2.1 Overview

The first part of the study presented in this chapter is the measurement of the inclusive and exclusive cross-sections for the ^{52}Ca(p,pn)^{51}Ca reaction. The experimental exclusive cross-sections to remove a neutron from the $f_{7/2}$, $p_{3/2}$ and $p_{1/2}$ orbital are obtained via in-beam γ-ray spectroscopy. An evaluation of the neutron-evaporation cross-section was also needed in order to be subtracted and to obtain the pure (p,pn) quasi-free scattering cross-section values. The subtraction was done individually for each final-state tagged by its decay γ-ray transition.

The second part of the study involves a momentum distribution analysis. The momenta of the beam and fragment particles were obtained using the velocities at the reaction vertex position and their directions. All these quantities were measured and allowed for a precise momentum distribution analysis. From the parallel and perpendicular momenta of the ^{51}Ca fragment particles relative to the ^{52}Ca beam particles corresponding to the removal of a neutron from the $f_{7/2}$ and $p_{3/2}$ neutron orbitals, one could gain information about the spatial distribution and the rms radii of single-particle these orbitals. In the next section of this chapter the data analysis method is described step-by-step, followed by a description of the theoretical models used for the two studies and their results.

2.2 Experimental Setup

The experiment was carried out at the Radioactive Isotope Beam Factory (RIBF) at the RIKEN Nishina Center operated jointly with the Center for Nuclear Study of the University of Tokyo. The full beam line schematics of the RIBF facility is shown in Figure 2.1. Three modes for primary beam production available at the RIBF facility are shown schematically in Figure 2.2. The first mode uses the azimuthally varying field (AVF) injector together with the RIKEN Ring Cyclotron (RRC) and the Superconductiong Ring Cyclotron (SRC) and a charge stripper located between AVF and RRC. This mode is used for the acceleration of light beams. The second mode uses the RILAC (RIKEN Heavy-ion Linac) together with the RRC, the Intermediate-stage Ring Cyclotron (IRC) and SRC. In this acceleration mode two charge strippers are placed, before and after the RRC. The energy obtained after SRC in the first

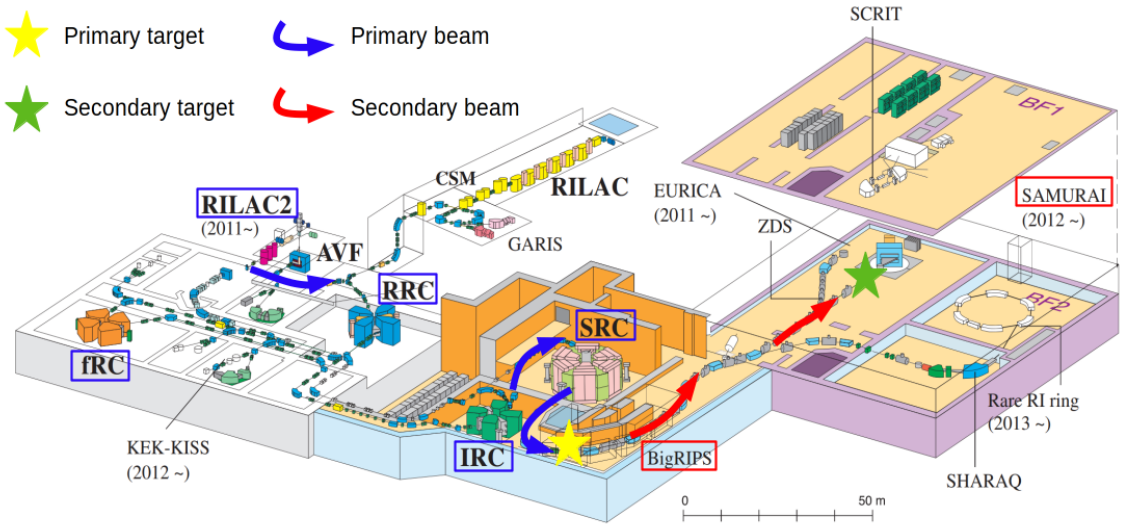

Figure 2.1: Schematics of the RIBF facility. The ^{70}Zn primary beam was obtained using the RILAC2 injector and further accelerated using RRC, fRC, IRC and SRC cyclotrons. After SRC, the primary beam enters the BigRIPS area where the secondary beam (cocktail beam including ^{52}Ca) is produced using a ^{9}Be primary target, then it is separated and identified. The ^{52}Ca(p,pn)^{51}Ca reaction was studied in the SAMURAI area. Figure adapted from [87] under CC-BY.

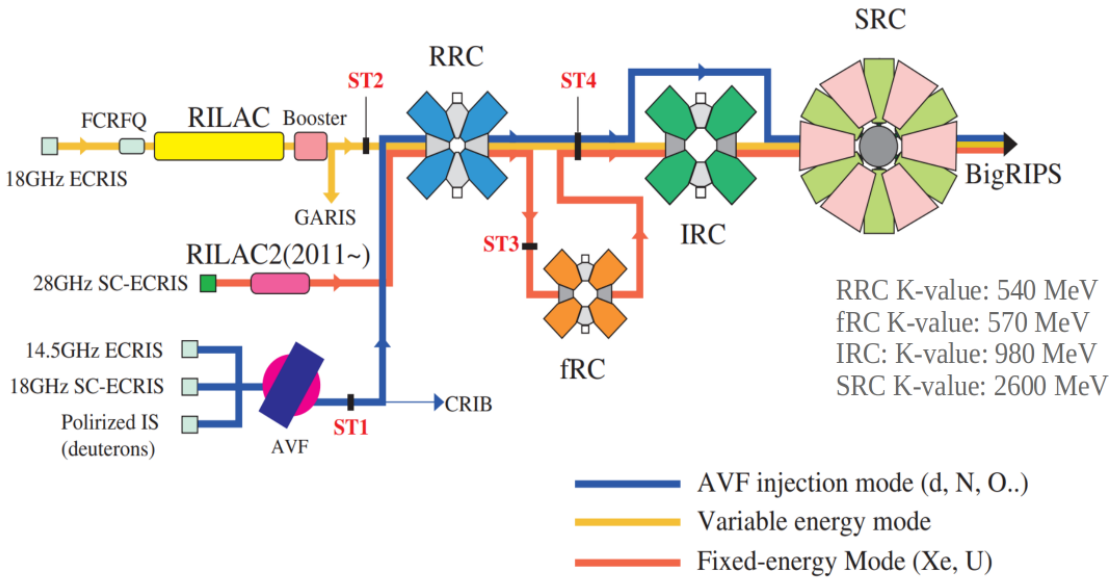

Figure 2.2: The three acceleration modes using SRC provided at the RIBF facility. The characteristics of the cyclotrons are shown on the figure. Figure adapted from [87] under CC-BY.

Dipole	Brho (Tm)
D1	7.3000
D2	7.0954
D3	7.0621
D4	7.0621
D5	6.8540
D6	6.8540

Focal plane	Slit position (mm)	Degrader
F1	Slit L = 64.2 Slit R = 64.2	Al 3 mm
F2	Slit U = 120.0 Slit D = 120.0 Slit L = 18.0 Slit R = 6.0	
F5	Slit L = 110.0 Slit R = 110.0	Al 2 mm
F7	Slit U = 120.0 Slit D = 120.0 Slit L = 20.0 Slit R = 20.0	

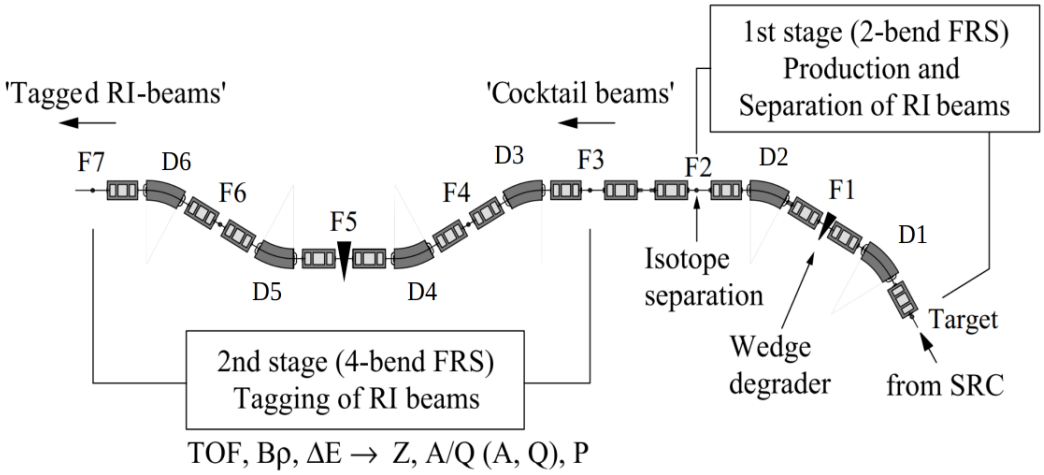

Figure 2.3: Sketch of the BigRIPS area from F0 to F7 focal planes. It has two stages, in the first stage the cocktail beam is produced and separated and the in the second stage the beam can be identified and tagged. The BigRIPS settings are shown in the table above. Figure reprinted with the permission from [88] ©2023 by Elsevier.

two modes can be varied in a wide range up to 400 MeV/u by varying the RF frequency. The third mode uses RILAC2 coupled with RRC, fixed-frequency Ring Cyclotron (fRC), IRC and SRC. Two charge strippers are used in this mode, placed before and after fRC. In this mode the energy of the primary beam after SRC is fixed at the value of 345 MeV/u due to the fixed frequency operation of the fRC. The characteristics of each cyclotron are shown in Figure 2.2. The ^{70}Zn primary beam was obtained at the energy of 345 MeV/u and with a beam intensity of 240-pnA using the RILAC2 injector and the third acceleration mode.

After SRC, the ^{70}Zn primary beam entered the BigRIPS area sketched in Figure 2.3. The primary beam impinged on a 10-mm-thick Be target (at F0 focal plane of BigRIPS) for the production of the secondary beam cocktail of radioactive isotopes. The production and the separation of the secondary beam was done in the first stage of the BigRIPS. The identifi-

cation of the beam particles was done event-by-event using the second stage of the BigRIPS separator [89] via the magnetic rigidity (Bρ), time-of-flight (TOF) and energy loss (ΔE) measurements [90] with parallel plate avalanche counters (PPACs), plastic scintillators at the focal planes F3, F5 and F7, and an ionization chamber (IC) at F7. The secondary beam passes through 2 dipoles with a bending angle of 30° in the first stage and 4 dipoles in the second stage of BigRIPS, labeled in Figure 2.3. A degrader was placed at F5 for allowing a better separation of the different species of the cocktail beam. The BigRIPS settings are shown in the table of Figure 2.3. There were two PPACs (PPAC1 and PPAC2) placed at each of the F3, F5 and F7, giving the X-Y position of the secondary cocktail beam in 4 planes (1A, 1B, 2A, 2B). The PPACs have a sensitive area of $240\times150\,\mathrm{mm}^2$ with a position resolution of 0.25 mm [91]. Plastic scintillators used for TOF measurements have an active area of 120 mm$\times$100 mm (used for F3 and F7) or 240 mm$\times$100 mm (for F5) and a time resolution of $\sim$40 ps [90]. The timestamp information of all detectors was measured with respect to the plastic scintillator detector for Beam Trigger (SBT) placed at F13 focal plane, at 2737 mm before the secondary target. The ΔE measurement is given by the MUSIC detector placed at F7. The MUSIC ionization chamber consists of twelve anodes and thirteen cathodes aligned alternately, the neighboring anodes being electrically connected in pairs. The 6 pairs of anodes are readout and averaged for obtaining the ΔE value. The correlation between the neighbouring anode readings is used for removing inconsistent events. The ^{52}Ca beam particles were obtained with an intensity of 4.41 pps and purity of 2.31 % in BigRIPS. The ^{52}Ca beam had an energy of $\sim$265 MeV/nucleon (FWHM=3 MeV/nucleon) before the secondary target.

The tagged secondary cocktail beam from BigRIPS enters the SAMURAI experimental area. The secondary target position at F13 focal plane is marked in Figure 2.1 with a green star and the SAMURAI experimental area is shown in Figure 2.4. After the reaction at the secondary target, the reaction fragments pass through the large acceptance SAMURAI analyzer magnet [93] with a central magnetic field of 2.7 T. The fragment particle identification is done by trajectory reconstruction using two multi-wire drift chambers (FDC1&2) placed before and after the SAMURAI magnet for the magnetic rigidity information, while the TOF and ΔE were provided by a 24-segment plastic scintillator hodoscope. The FDC1 and FDC2 are composed of several wire planes oriented at -30°, 0° and +30°. They have a hexagonal cell structure and are operated with He + 60% CH_4 gas at 1 atm. The active area for FDC1 is 620 mm$\times$340 mm and for FDC2 the active area is 2296mm$\times$836mm. The FDC1 detector is placed at 2720 mm distance before the center of the SAMURAI magnet and the FDC2 detector is placed at 3684 mm distance after the center of the SAMURAI magnet, at 59.93° deflection angle. The hodoscope detector for the fragments (HODOF) is composed of 24 plastic scintillator bars (BC408) each having the the dimension of 1200 mm(V)$\times$100 mm(H)$\times$10 mm(T). The HODOF is placed at 59.93° deflection angle as FDC2, at a distance of 5146 mm from the center of the SAMURAI magnet.

The (p,pn) reaction was studied using MINOS [8], a 151(1) mm liquid hydrogen target with a density of 73 mg/cm^3 surrounded by a time projection chamber (TPC) allowing a vertex reconstruction with the resolution of 5 mm (FWHM) [95]. The Figure 2.5 shows a drawing

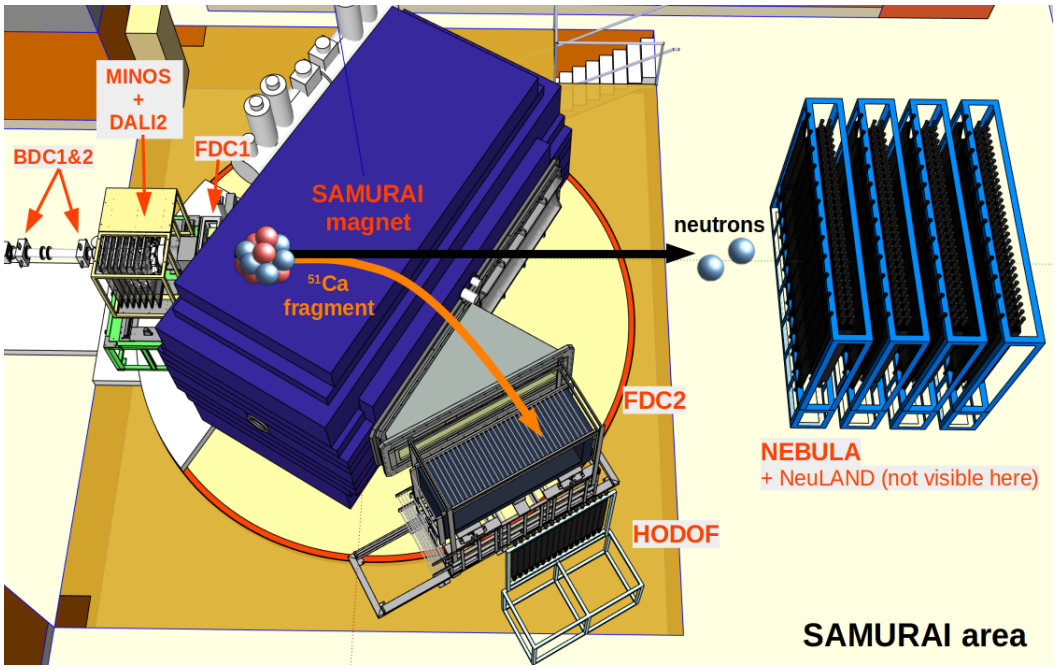

Figure 2.4: Scheme of the SAMURAI area. Source: [92]. BDC1 and BDC2 are used for tracking (X-Y position and θ angle) the beam before entering the reaction chamber. MINOS+DALI2 are used for this experiment for tracking protons and detecting the γ rays. The fragments are tracked (X-Y position) before (FDC1) and after (FDC2) being bent in the SAMURAI magnet. The timing and energy measurement of the fragments is done with the hodoscope detectors (HODOF). Neutrons can as well be detected in this setup with the NeuLAND and NEBULA detectors.

of the liquid hydrogen target and the TPC. The MINOS TPC has a cylindrical shape with the length of 300 mm, inner diameter of 80 mm and with an outer diameter of 193 mm. It is filled with a gas mixture of argon (82%), CF_4 (15%) and isobutane (3%) chosen for increasing the drift velocity of the electrons. The charge collection at the anode is done with a Micromegas pad detection plane [95] with 128 μm amplification gap. There are 4608 pads arranged in 18 rings of Δr=2 mm, containing 256 pads each. This geometry results in larger pad size in the outer region of the TPC compared to the inner region. The readout electronics of the MINOS TPC is based on AGET chips [8]. The X-Y position of the proton track is obtained from the Micromegas pads position. The third dimension, Z, is obtained from the drift time information. The time resolution of MINOS of $\sim$20 ns leads to a spatial resolution along the drift field (Z-axis) of about 1 mm [8].

The reaction chamber with the MINOS TPC and the liquid hydrogen target were placed at F13 focal plane at 4228 mm distance before the center of the SAMURAI magnet. The reaction takes place in the target volume and the vertex position is reconstructed using the proton tracked in the TPC and the initial beam tracked by BDC1 and BDC2 (beam drift chambers). The velocities of the beam and fragment particles were corrected for the energy loss in the materials along their trajectories from BigRIPS and SAMURAI, respectively, up to the reac-

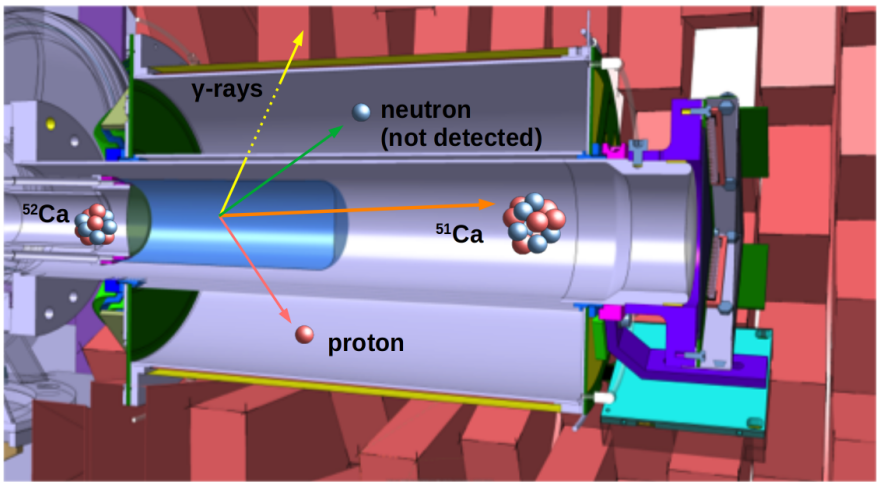

Figure 2.5: Drawing of the liquid hydrogen target (blue) and the MINOS TPC (purple). The DALI crystals (red) are placed around MINOS. A schematics of the (p,pn) reaction on ^{52}Ca within the liquid hydrogen target is also shown. Source: [94].

tion vertex, while their directions before and after the reaction were reconstructed using the position information from the beam and fragment drift chambers (BDC1, BDC2 and FDC1) (See their position in Figure 2.4). The beam drift chambers BDC1 and BDC2 are composed of X and Y wires oriented perpendicularly on each other and filled with with He + 60% CH_4 gas at 1 atm. They have an active area of 80 mm×80 mm and are positioned at a distance of 1235 mm and 2235 mm, respectively, before the target.

The γ-rays for tagging the final states of ^{51}Ca fragment were measured with DALI2$^+$ [96], a high-efficiency array of 226 NaI(Tl) scintillation detectors placed around MINOS. There are three types of crystals used for DALI2$^+$ with sizes of $45\times80\times160\,\text{mm}^3$, $40\times80\times160\,\text{mm}^3$ and $60\times60\times120\,\text{mm}^3$, each encapsulated in 1-mm thick Al housing. The energy resolution for photons at 662 keV is about 9% (FWHM) [96]. The crystals are arranged in layers perpendicular to the beam axis together with one layer of crystals along the beam axis covering the forward angles. The layers have a "sunflower" geometry, optimized for having a maximum efficiency. In this configuration the angular size of a crystal positioned at 60° seen from the mid-target position is 6° [96]. The DALI2$^+$ detectors were calibrated individually using γ-ray sources of ^{60}Co, ^{137}Cs and ^{88}Y. The response functions of the detector array were obtained using the GEANT4 framework [97]. The GEANT4 simulations for the γ-ray spectra were benchmarked using the source measurements and discrepancies between the measured and simulated spectra are included in the systematic errors of the results of the study. The DALI2$^+$ crystals are shown with red in Figure 2.5. The particles produced in the reaction are sketched in the figure as well. The knocked-out neutron is not detected because of the kinematics of the (p,pn) reaction. The neutron from the (p,pn) reaction is emitted at angles similar to the proton angle and there is no neutron detection coverage for these angles in the setup.

Two plastic scintillator arrays, NeuLAND [98] demonstrator and NEBULA [99] were present at this experiment. They were placed after the SAMURAI magnet at zero-degree deflection angle. The NeuLAND detector array consists of 400 segments of 5 $\times$ 5 $\times$ 250 cm^3 each arranged in 8 layers. The 8 layers were having alternating orientations, 4 layers with horizontal segments and 4 layers with vertical segments. The NeuLAND detector was placed at a distance of 1165 mm (first layer) and 11515 mm (last layer) from the center of the SAMURAI magnet. NEBULA is composed of 120 vertical segments of 12 $\times$ 12 $\times$ 180 cm^3 arranged in 4 layers. The 4 layers were placed at distances of 13895 mm, 14026 mm, 14714 mm, and 14871 mm from the center of the SAMURAI magnet.
The typical low neutron separation energies for the neutron-rich isotopes allow for the population of unbound states via (p, p'), inelastic scattering, followed by neutron-evaporation. Via the neutron-evaporation process, the neutrons are emitted from ^{52}Ca (found in an excited state $E_x > S_n$) isotropically in the center of mass (or forwards in the laboratory frame). In this case, one has the ^{52}Ca nucleus as a beam, ^{51}Ca as a fragment and one detects one proton in MINOS, exactly as in the case of the (p,pn) reaction. The two neutron detectors could detect and track the neutrons from (p,p') events, helping to discard the neutron-evaporation events and obtain clean (p,pn) reaction events.

2.3 Data Analysis

2.3.1 Beam PID

The beam particle identification (PID) is done event-by-event using the second stage of BigRIPS consisting of the focal planes from F3 to F7 dedicated to the separation of the cocktail beam. The position information of the PPACs and time information of the plastic scintillators are measured at F3, F5 and F7 focal planes together with the energy loss measurement, ΔE, at F7. A Bρ - ΔE - TOF method is implemented [90]. The following set of equations allows the determination of β and A/Q (mass number/charge state) value of the beam particles:

$$TOF_{37} = \frac{L_{35}}{\beta_{35}c} + \frac{L_{57}}{\beta_{57}c} \tag{2.1}$$

$$\left(\frac{A}{Q}\right)_{35} = \frac{(B\rho)_{35}\, c}{(\gamma\beta)_{35}\, m_u} \tag{2.2}$$

$$\left(\frac{A}{Q}\right)_{57} = \frac{(B\rho)_{57}\, c}{(\gamma\beta)_{57}\, m_u} \tag{2.3}$$

with $\beta = v/c$ and $\gamma = \sqrt{1-\beta^2}$, c is the speed of light, m_u is the atomic mass unit, and $(B\rho)$ is the magnetic rigidity of particles at the dipoles. Various combinations of the available observables can be used for the beam particle identification, but the chosen method, combining the two stages F3-F5 and F5-F7, gives the best resolution.

The magnetic rigidity $B\rho$ is deduced via trajectory reconstruction up to 1^{st} order in position and angle from PPACs positioned upstream and downstream of each dipole. Out of the 4 planes (1A, 1B, 2A and 2B) of each PPAC, the requirement is that at least one of the first pair and at least one of the second pair fires. For the events with no PPAC position information, the x-position was reconstructed using the time difference registered in each plastic scintillator detector. The percentage of events with missing position for the each run number for F3, F5 and F7 are shown in Figure 2.6. For most of the runs, the percentage of missing position information is below 5%, but some runs are completely missing the F3 position information (F3 PPACs tripped for these runs). The arrows for the F3 data (magenta line) in the plot show that for those sets of runs the percentage of events with missing position information went up to 100, which is out of the plot's scale. The position reconstruction using the time difference is performed using the existing valid events and the calibration was done with a linear fit for the F3 position. For F5, which covers a wider position range, a 5^{th} order polynomial was used for reproducing the correlation with fidelity. The final percentage of invalid events (missing time, position or energy information) after the position recovery for F3 and F5 goes down to 3% for all runs.

It is considered that there is no charge change in the degrader at F5 focal plane, $(A/Q)_{35} = (A/Q)_{57}$ but the values β_{35} and β_{57} are different because of the energy lost in the degrader material. The term TOF_{37} contains a time of flight offset which is adjusted so that the obtained A/Q values are correct. The time of flight offset arises from the time delay existing in

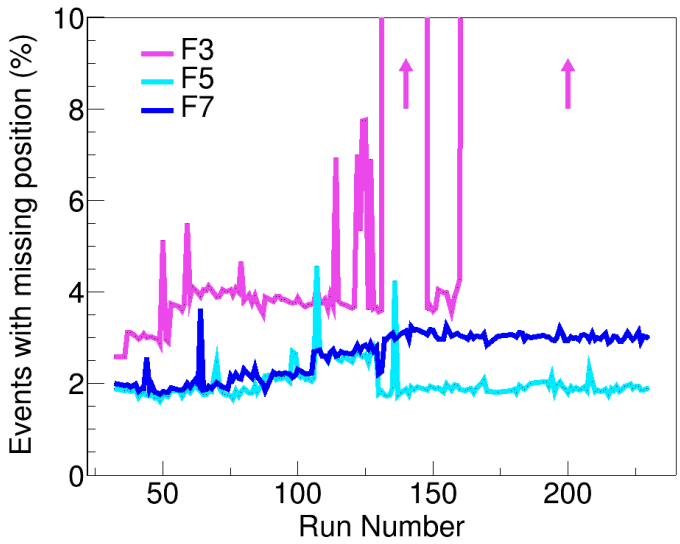

Figure 2.6: Percentage of events with missing position information in BigRIPS F3, F5 and F7 focal planes along the run number (32 - 230).

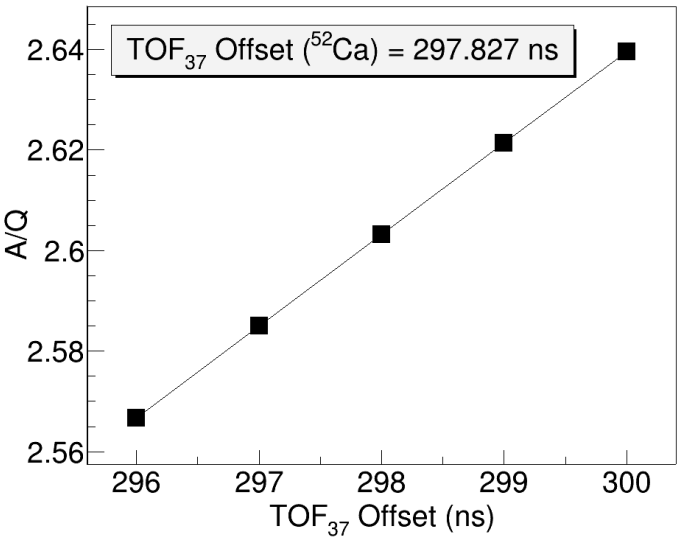

Figure 2.7: Time of flight offset (TOF_{37}Offset) tuning for the ^{52}Ca beam in BigRIPS.

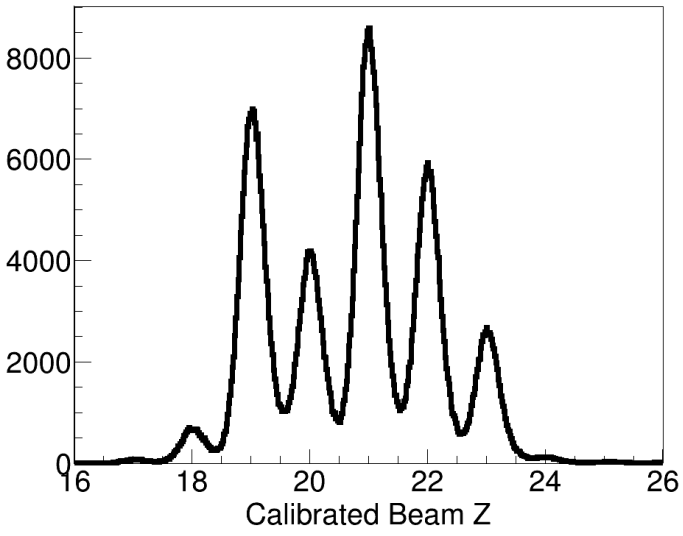

Figure 2.8: Histogram with the distribution of the calibrated atomic number Z for the cocktail beam detected in BigRIPS.

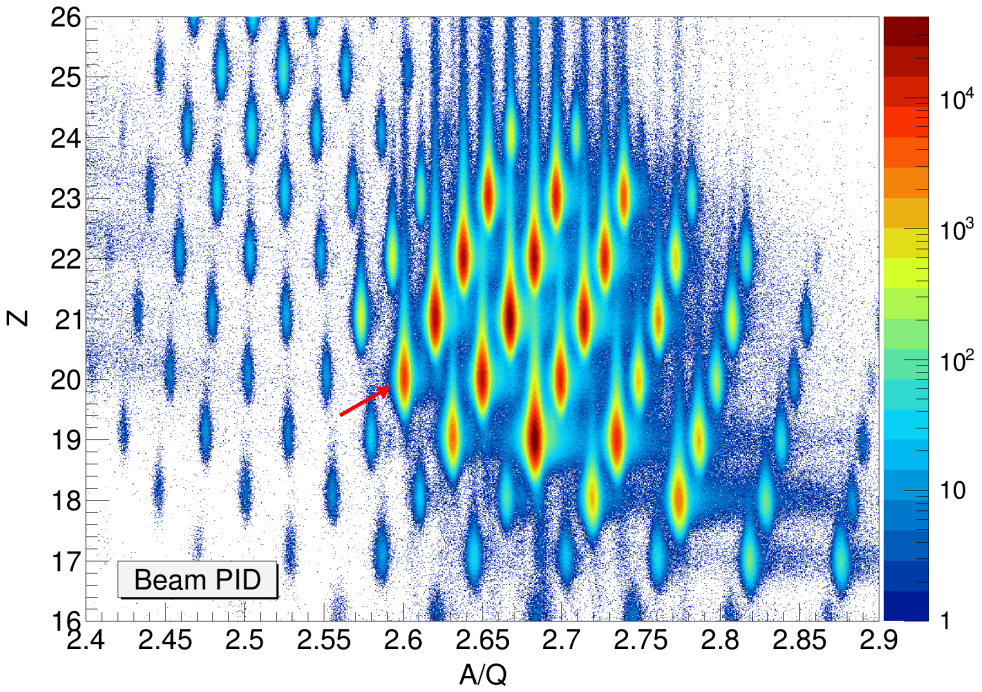

Figure 2.9: Beam particle identification (PID) plot in BigRIPS. The ^{52}Ca isotope is marked with a red arrow.

the electronics between the F3 and F7 plastic scintillation detectors and also it accounts for the flight difference along the beam line through the degrader at F5 for the different beam species. As a result it is dependent on the isotope. The Figure 2.7 shows the values of the A/Q for the ^{52}Ca beam particles for a range of TOF_{37} offset values. The offset value of 297.827 ns corresponding to an A/Q equal to 2.60 for ^{52}Ca will be further used in the analysis.

The determination of Z (atomic number) of the particles is done using the ΔE information at F7 together with the velocity of the particle, β_{57}, between F5 and F7 are used as follows:

$$\Delta E \propto \frac{Z^2}{\beta_{57}^2}\left[ln\left(\frac{2m_e c^2\beta_{57}^2}{I}\right) - ln\left(1-\beta_{57}^2\right) - \beta_{57}^2\right] \tag{2.4}$$

The constant of proportionality contains the detector material information and the integration along its thickness. The full expression of the Bethe-Bloch formula in the differential form is the following:

$$\frac{dE}{dx} = \left(\frac{e^2}{4\pi\epsilon_0}\right)^2\left(\frac{4\pi Z_p^2}{m_p c^2\beta_p^2}\right)\left(\frac{\rho_t Z_t N_A}{A_t}\right)\left[ln\left(\frac{2m_p c^2\beta_p^2}{I}\right) - ln\left(1-\beta_{57}^2\right) - \beta_{57}^2\right] \tag{2.5}$$

where the p and t subscripts referring to the projectile and the target, respectively, N_A is the Avogadro's number and ϵ_0 is the electrical permittivity of the vacuum. The Z value obtained

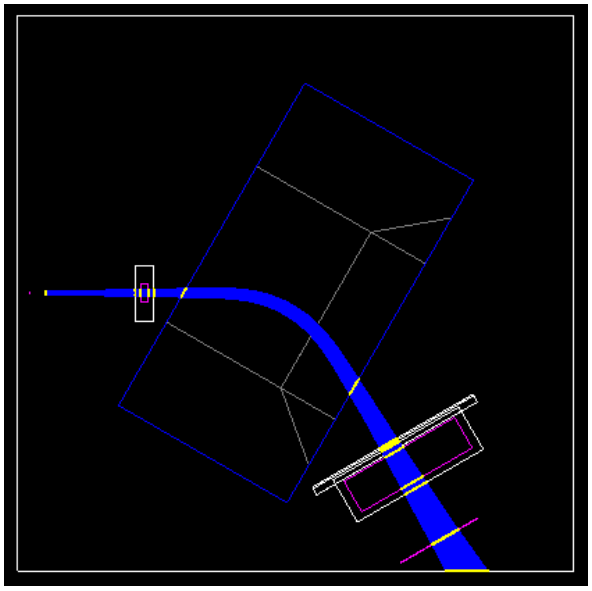

Figure 2.10: Simulated tracks (blue) of fragments in the SAMURAI magnet starting from the target and passing through FDC1, FDC2 and HODO detectors (active areas marked with magenta boxes).

from the equation (2.4) is then calibrated and the Z distribution of the cocktail beam is shown in Figure 2.8.

The two values for β between F3-F5 and F5-F7 are different due to energy losses in the material along the beam line. The velocity determined between F5-F7 will be further corrected for the energy losses along the beam line up to the entrance to the target for each event. This correction is done using the Bethe-Bloch formula 2.5 knowing the list of materials along the beam line. The beam position measured with BDC1 and BDC2 can be extrapolated for obtaining the position of the beam at the entrance of the target cell. The beam spot for this reaction channel had a 2D Gaussian profile with σ_X =4.6 mm and σ_Y =4.1 mm. A cut of 15 mm radius was imposed for valid events at the entrance window of the target cell throughout the calculations of the reaction cross sections.

The beam PID plot is shown in Figure 2.9 as Z versus A/Q. The ^{52}Ca isotope is marked with a red arrow on this plot. A beam particle identification with 4.76 σ separation in Z and 31.44 σ separation in A/Q was achieved for beam Ca isotopes, comparable to the PID obtained by Ref. [39]. The ^{52}Ca beam had an intensity of 4.41 pps and purity of 2.31 %. A number of 2.5 10^6 events were identified as ^{52}Ca beam within 4 σ's on both Z and A/Q axes and arriving in a valid position range on the liquid hydrogen target entrance window.

2.3.2 Fragment PID

After the reaction, the fragments are separated and identified with the large acceptance SAMURAI analyzer magnet having a central magnetic field of 2.7 T and the hodoscope detectors. A time-of-flight measurement is obtained between the plastic scintillators at the focal plane F13 (SBT) localized before the target and the hodoscope detectors. The trajectory in the SAMURAI magnet is reconstructed using the position and angles measured before and after the analyzing magnet in the fragment drift chambers (FDC1 and FDC2).

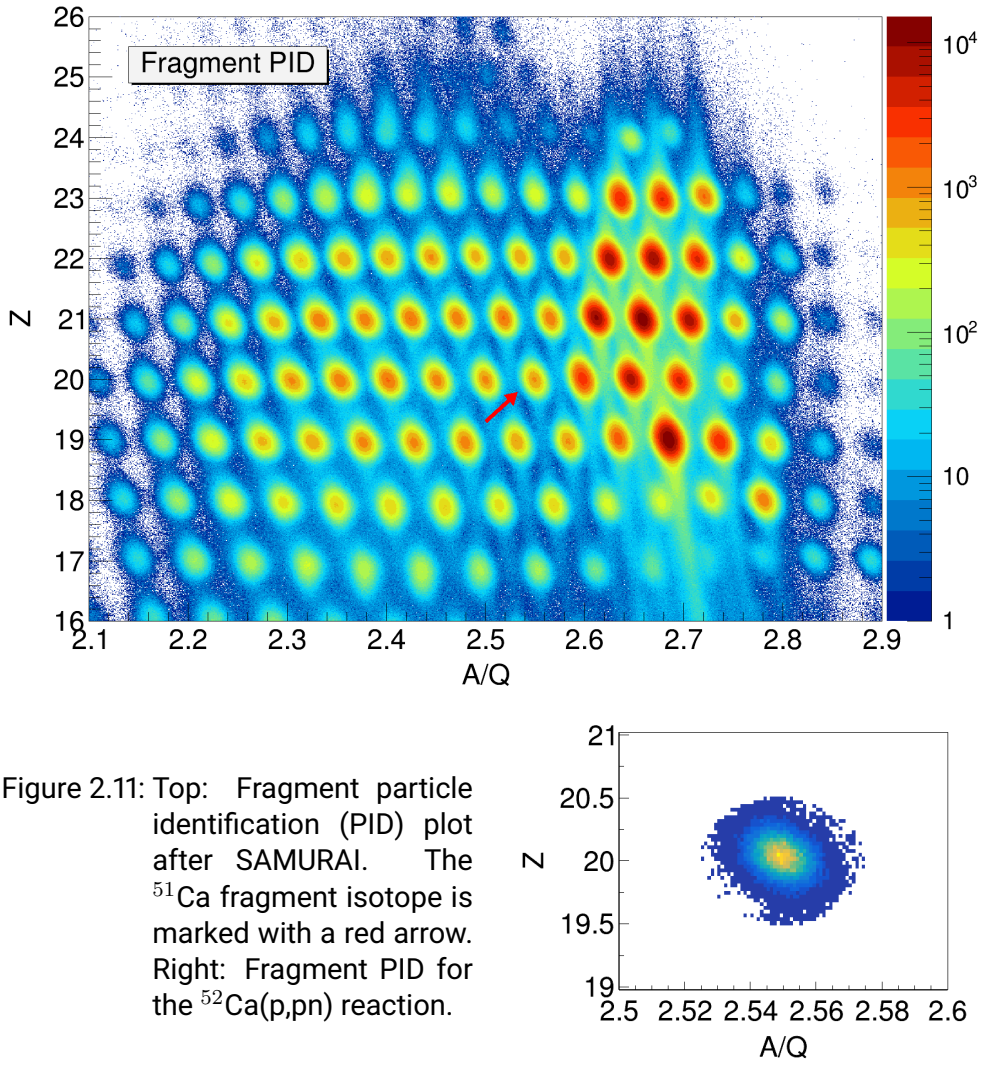

Figure 2.11: Top: Fragment particle identification (PID) plot after SAMURAI. The ^{51}Ca fragment isotope is marked with a red arrow. Right: Fragment PID for the ^{52}Ca(p,pn) reaction.

Because of the large spatial range covered by the magnet, the flight-length (FL) and the magnetic rigidity (Bρ) in the magnet are obtained as functions of the positions and angles in FDC1 and FDC2 detectors from a GEANT4 simulation for charged fragments in the SAMURAI magnet (NEBULA simulator - smsimulator5.4 [100]). The simulation is performed only for ^{52}Ca (direct, unreacted beam) and ^{51}Ca (fragment of the ^{52}Ca(p,pn) reaction), using the experimental position and velocity profiles as input. The FL and Bρ functions are fitting functions of the simulated events. Fragment tracks through the SAMURAI magnet from simulation are shown in Figure 2.10. Having the TOF, FL and Bρ information, the mass-to-charge ratio (A/Q) for the fragments was obtained while the charge measured in the hodoscopes allowed for the determination of Z, the charge of the fragments.

The corrections that needed to be applied for the fragment analysis were the following: correction for charge drift for some hodoscopes along run number (because of gain fluctu-

ations), correction for the time drift of the plastic scintilator at F13 along run number, TOF offsets for the hodoscopes relative to the F13 plastic scintilator tuned individually, charge calibration of each hodoscope and an energy loss correction for the beta value of the fragment between the target and the SAMURAI magnet (the FDC1 detector material). After the fragment particle identification and isotope tagging are done, an alternative and more precise way to calculate the velocity of the fragment is implemented. This method is using the rigidity and mass-to-charge ratio (Bρ and A/Q) instead of the flight-length and time-of-flight (FL and TOF) :

$$\beta = \frac{FL}{TOF \cdot c} \tag{2.6}$$

$$\gamma\beta = \frac{(B\rho) \cdot c}{(A/Q) \cdot m_u} \tag{2.7}$$

The fragment particle identification plot, Z vs. A/Q is shown in the top plot of Figure 2.11 with the ^{51}Ca fragment marked with a red arrow. The right plot of the same figure shows the selection of the ^{51}Ca fragment. The SAMURAI magnet, the fragment drift chambers and hodoscopes following along the fragment track are able to cover a large range of isotopes with Z ranging from below 16 to just over 24 and with a mass-to-charge ratio ranging between 2 and 3. The PID, Z and A/Q, for both the beam and the fragment prove to be stable over the entire experiment. All the calibrations fit the best in the range of the Ca isotopes and small distortions may appear for isotopes further from this region. Vertical traces appear around some of the isotopes as for the case of ^{51}K because of incomplete charge detection in the hodoscope detector material. Fortunately, these long tails from other isotopes did not interfere with the selection of the ^{51}Ca fragment. For the fragment Ca isotopes, a 7.21 σ separation in Z and 8.12 σ separation in A/Q was obtained and, as in the case of the beam, the isotope tagging was done within 4 σ's cuts.

2.3.3 Vertex reconstruction with MINOS

For each proton track, several events are registered in the MINOS TPC. The X and Y coordinates of each event is given by the Micromegas grid, while the Z-coordinate is determined using the drift time information:

$$Z = (t_{drift} - t_0) \cdot v_{drift} \tag{2.8}$$

with t_{drift} being the drift time, t_0 is a time offset and v_{drift} is the drift velocity in the TPC. The drift time will be longer as the ionization in the drift chamber takes place further from the Micromegas plane. It is obtained for each event by fitting the collected charge as a function of time with the analytical formula [95]:

$$q(t) = A * exp\left(-3\frac{t - t_{drift}}{\tau}\right) sin\left(\frac{t - t_{drift}}{\tau}\right)\left(\frac{t - t_{drift}}{\tau}\right)^3 + q_b \tag{2.9}$$

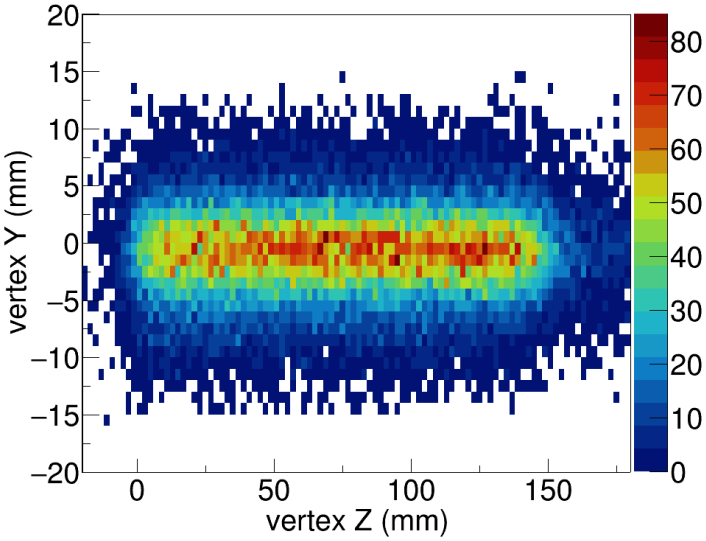

Figure 2.12: The reaction vertex reconstructed with MINOS (Y vs Z) for the ^{52}Ca (p,pn) ^{51}Ca reaction.

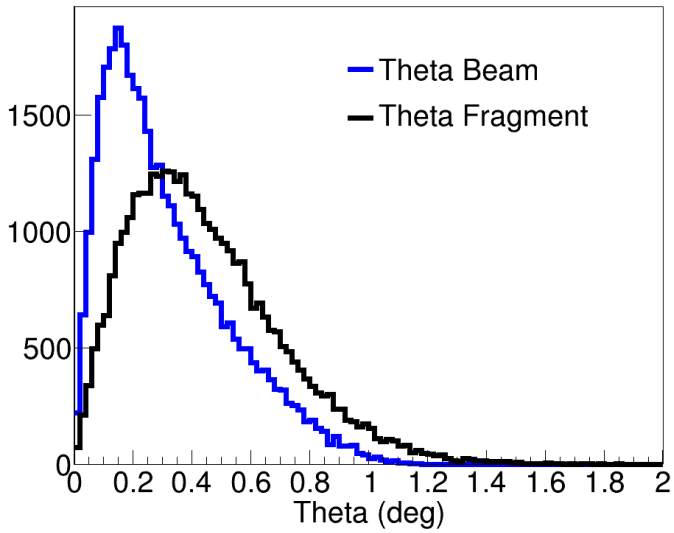

Figure 2.13: Beam incident angle before the reaction (blue) and the fragment angle after the reaction (black) with respect to the symmetry axis along beam line.

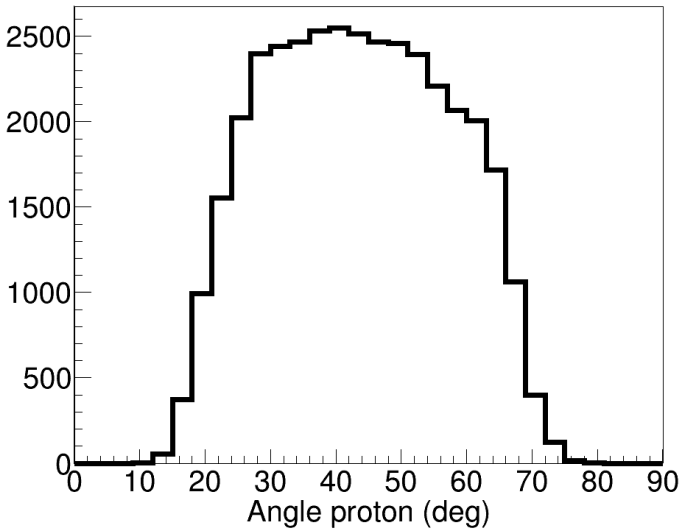

Figure 2.14: The angular distribution of the proton tracked with the MINOS TPC for the ^{52}Ca (p,pn) ^{51}Ca reaction channel.

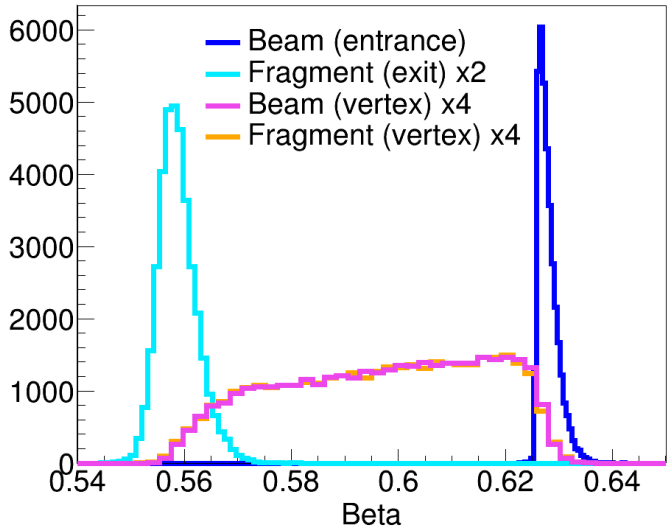

Figure 2.15: The beta distributions for the beam at the entrance to the target, for the beam and fragment at the reaction vertex and for the fragment at the exit from the target.

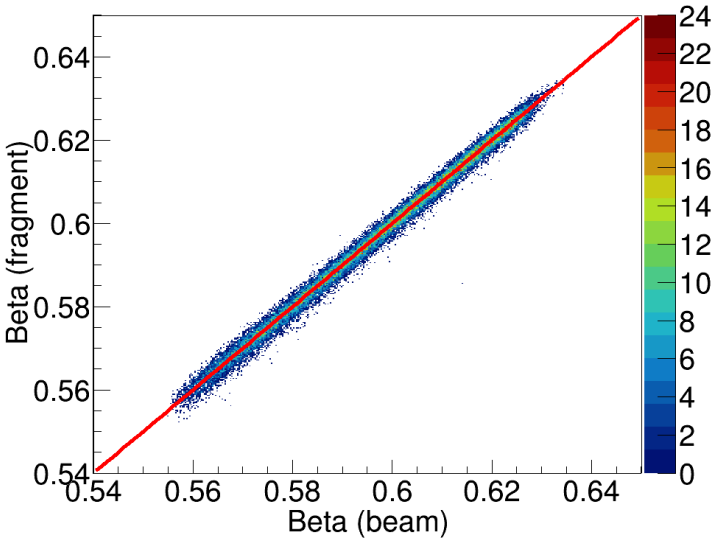

Figure 2.16: The correlation between the fragment beta distribution and the beam beta corrected for the velocity change at the reaction. For guidance the line y=x is also shown (red solid line).

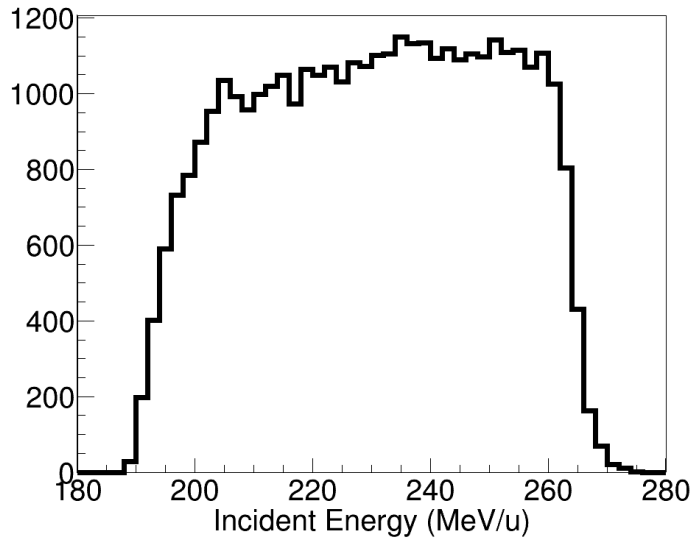

Figure 2.17: The distribution of the incoming energy at reaction vertex ranges between 190 and 270 MeV/u for the ^{52}Ca (p,pn) ^{51}Ca reaction channel.

the electronic signal q(t) is a function of the shaping time (τ), the signal amplitude (A), the signal baseline (q_b) and the drift time (t_{drift}). The drift velocity in the TPC was determined using the TPC length, the minimum and maximum drift time registered by MINOS:

$$v_{drift} = \frac{L_{TPC}}{t_{max} - t_{min}} \tag{2.10}$$

v_{drift} was determined for each run individually for better accuracy.

The event filtering is done in two stages. The first stage is a Hough filter in 2D, in the (X,Y) plane of the Micromegas and in the second stage the third dimension is considered for another Hough filter in 3D [95]. The used algorithm filters off the noise contributions to the tracks. If the number of obtained tracks is one, as in (p,pn) reactions, the proton track together with the beam track will give the vertex position. If the number of tracks is two, as in (p,2p) reactions, the two tracked protons will give the vertex position.

By requesting ^{52}Ca as beam, ^{51}Ca as fragment and the detection of one particle in the TPC, the distribution of the vertex position shown in the Figure 2.12 is obtained. From the experimental data from various (p,pn) and (p,2p) reactions, the target length was found to be 151(1) mm.

A number of 36k events were measured in the ^{52}Ca (p,pn) ^{51}Ca reaction channel. The imposed conditions were: beam tagged as ^{52}Ca, fragment tagged as ^{51}Ca, 1 proton detected in the MINOS TPC and the reaction vertex to be found within the target region. This number of events is further corrected by the MINOS efficiency. The MINOS efficiency is determined using the γ-ray spectrum with and without the vertex position information used for the Doppler-shift correction, as described in section 2.3.4. The angle of the ^{52}Ca beam before the reaction is obtained from the BDC detectors and reaction vertex position information. The fragment trajectory after the reaction is determined with the FDC1 position information together with the vertex position are used. The angular distributions for both beam and fragment (theta angle) are given in the Figure 2.13 as well as for the proton tracked by MINOS (relative to the beam line direction) in the Figure 2.14.

The velocities of the beam and fragment can now be corrected for the energy loss in the liquid hydrogen target until the reaction vertex. The resulting β-distributions before, after the target and at the reaction vertex for the beam and the fragment are plotted in Figure 2.15. The fragment distribution after the target are shown with a factor of 2 on the vertical axis while the beta distributions for the beam and the fragment at the reaction vertex got a factor of 4 on the vertical axis for an optimal visualisation on the plot. In Figure 2.16 the velocity of the fragment is plotted against the velocity of the beam at the reaction vertex, corrected for the change in velocity after the knock-out reaction, together with the function y=x shown with a red line which proves the good match of the reconstructed velocities. The velocity β of the fragment is later used in the Doppler correction for the measured γ-ray spectrum. Finally, the incident energy for the reaction is obtained and is plotted in Figure 2.17. The incident energy takes values between 190 and 270 MeV/u for the ^{52}Ca (p,pn) ^{51}Ca reaction channel.

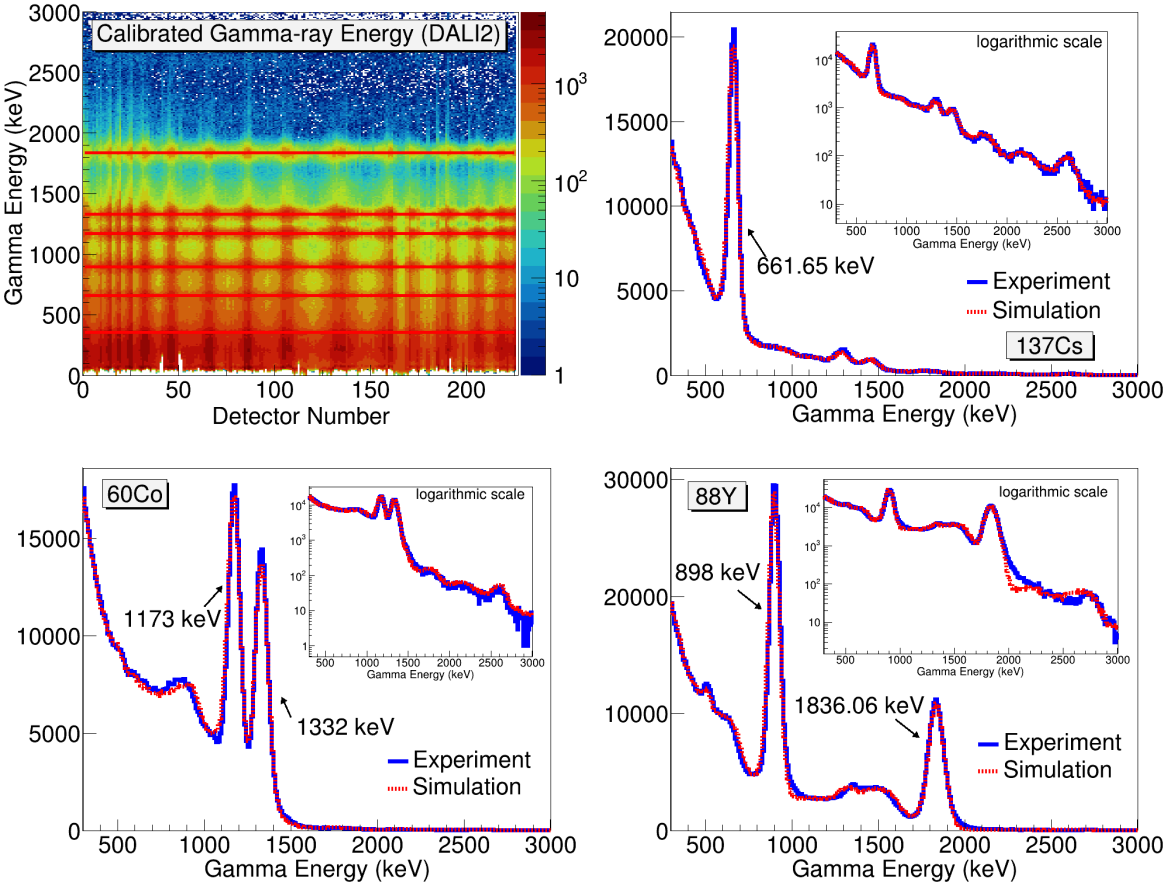

Figure 2.18: Gamma spectra of the calibration sources (see details in text).

2.3.4 DALI2$^+$ γ-ray detection array

Calibration of DALI2$^+$

The final states of the fragment after the (p,pn) reaction can de-excite via γ-ray emission measured with the DALI2$^+$ detector array. DALI2$^+$ was calibrated using the following γ-ray sources: ^{137}Cs, ^{60}Co and, ^{88}Y emitting at 661.65 keV, 898 keV, 1173.22 keV, 1332.49 keV, and 1836.06 keV. The two-dimensional plot shown in Figure 2.18 (top-left) gives the gamma-ray energy spectra with the source measurements for each crystal. The above-mentioned peaks are clearly visible and calibrated. The literature energy values are marked by red horizontal lines on the plot. The source measurements were performed before the experiment, as well as at the end and two times during the experiment. The γ-ray background was monitored and measured. The scintillator detectors are sensitive to the residual magnetic fields of the surrounding dipoles and to the beam intensity, as a result, the gain varied throughout the experimental runs. The 4 sets of source measurements were applied over the experimental runs divided in 4 groups for a minimum γ-ray energy variation. Measurements with a ^{133}Ba source were also performed. The ^{133}Ba peaks are present at energies lower than 500 keV: 80.99 keV, 302.85 keV and 356.01 keV. The line at 356.02 keV is also marked with an horizontal red

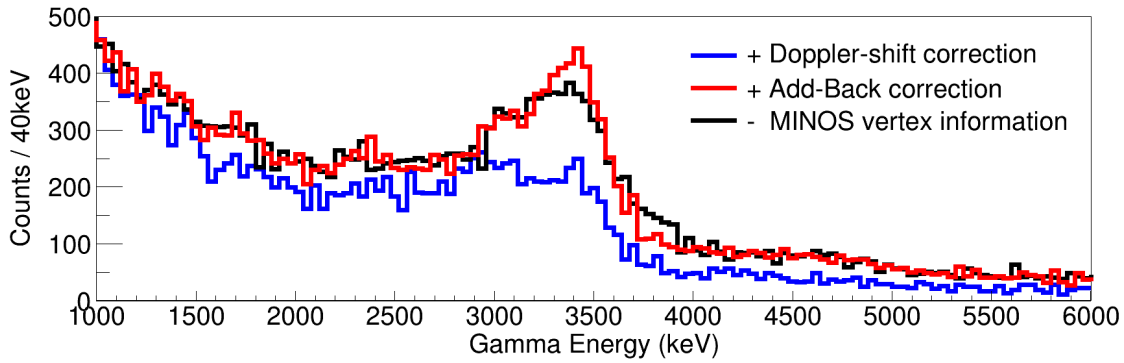

Figure 2.19: Gamma spectra in coincidence with the ^{52}Ca (p,pn) ^{51}Ca reaction channel after the energy calibration and the Doppler - shift correction (blue), after the Add - Back correction (red) and with no vertex position information from the MINOS TPC (black) used for the efficiency evaluation of MINOS. The spectrum is shown starting with 1000 keV because there is no visible structure and the count is too high for this scale below this value.

line in Figure 2.18, but these peaks were not used for the calibration because in some cases they were not clean or well separated. The low-energy peak from ^{133}Ba at 352 keV and the weak high-energy peak from ^{88}Y at 2734 keV were used for cross-checking the linearity of the energy calibration, which showed energy shifts below 1% in the extrapolation regions.

The response functions of the DALI2^{+} detector array for the source measurements were simulated within GEANT4 framework. The detection resolution of each crystal determined from the source measurements was considered in the simulation as a two-parameters function of the form $a \cdot E^{b}$ along the energy range. The simulated spectrum was added on top of the normalized natural background γ-ray spectrum. The overlapping simulated and experimental spectra for the ^{137}Cs, ^{60}Co and, ^{88}Y γ-ray sources are also shown in Figure 2.18. Each figure shows the spectrum in linear scale with the energy measured in keV together with an inset with the same spectrum in the logarithmic scale for the visualisation of the small peaks. The main peaks of each calibration source are labeled in the figures. The plots show how the simulations (dotted red curves) reproduce very well the measured spectra (solid blue line). The simulated and measured spectra agree within 5% (relative difference). After the calibration of the DALI2^{+} detector-array both in time and energy and the validation of the simulation for the response functions, one can move with the analysis to the γ-ray spectra for the in-beam reactions. For the efficiency of the DALI2^{+} detectors we fully rely on the GEANT4 simulations for the experimental runs.

Doppler - shift correction of the γ-ray spectrum

In the raw γ-ray spectrum for the ^{52}Ca (p,pn) ^{51}Ca reaction channel, the peak that can be easily identified is the 511 keV annihilation peak, while no other recognizable peaks are seen. Further corrections are needed until the peaks structure of the ^{51}Ca γ-rays spectrum becomes visible. The emitted γ rays are detected with a Doppler - shift. The shift in energy

is dependent on the velocity of the fragment at the emitting moment and on the angle under which the detectors see the γ-ray relative to the fragment. The detected energy needs then to be corrected as follows:

$$E_{Doppler} = E_{\gamma} \cdot \gamma_{fragment} \cdot (1 - \beta_{fragment} \cdot cos\,\theta_{\gamma}) \tag{2.11}$$

with

$$\gamma_{fragment} = \frac{1}{\sqrt{1 - \beta^2_{fragment}}} \tag{2.12}$$

where $E_{Doppler}$ is the energy corrected for the Doppler - shift, E_{γ} is the detected gamma energy, with the energy calibration already applied, $\beta_{fragment}$ is the β value of the fragment at the vertex position, and θ_{γ} is the angle of the vertex-detector direction relative to the fragment direction.

The velocity of the fragment is obtained from the SAMURAI analysing magnet rigidity together with the known mass-to-charge ratio value with high accuracy. The velocity is then corrected for the energy loss in the materials along the beam line up to the exit point of the liquid hydrogen target. From this point, together with the vertex position information, the flight length in the target is calculated and an additional correction for the energy loss in the target material is applied up to the reaction vertex. The correction is done in steps of 1 mm inside the target material with a linear interpolation for fractions of 1 mm. The uncertainty on the $\beta_{fragment}$ due to the vertex position uncertainty is 0.0011 (sigma value). The uncertainty of the fragment velocity due to the vertex position uncertainty impacts the Doppler-shift corrected γ-ray energy as well as the determination of the momentum of the fragment relative to the beam. The later is used in the momentum distribution analysis discussed in section 2.3.9.

The mean interaction point in each crystal is obtained from the GEANT4 simulation and it is used for the geometrical calculation rather than the geometrical center of the crystals. The crystal's physical size, together with the uncertainty of the vertex position give an uncertainty in the detecting angle of 2.7° (sigma value). The cumulative effect of the vertex position uncertainty (via the emitting angle and fragment velocity) on the Doppler corrected γ-ray energy is 88.56 keV (sigma value), which comes on top of the resolution of 55-60 keV in energy for a 3.4 MeV γ-ray for the NaI(Tl) crystals. With this width of the peak for a γ-ray energy above 3 MeV, the Compton edge appears no longer separated from the full-energy peak, but rather as a shoulder in the left side of the peak.

The spectrum for the ^{52}Ca (p,pn) ^{51}Ca reaction channel corrected for the Doppler - shift is given in the Figure 2.19 (blue line). A main distribution around 3 MeV appears after this correction showing at first sight two peaks. The one in the right side is the full-energy peak at 3.4 MeV energy, corresponding to the $7/2^- \rightarrow 3/2^-$ transition of ^{51}Ca and the left one is the Compton edge of it.

Add - Back correction for the γ-ray spectrum

The interaction of the γ rays with matter, hence the detector material, takes place via three possible processes: the photoelectric effect, the Compton effect or the pair production. The Figure 2.21 shows the probability of each effect as a function of the γ-ray energy. The Compton effect is the dominating one for γ-rays with energies as high as 3.4 MeV as in the ^{51}Ca γ-ray spectrum. In order to improve the full-energy peak efficiency, one can correct at some degree for the Compton events by performing the add - back correction. The add - back correction is focused on the γ-rays resulting from a Compton event (or sequential Compton events) at the interactions of the incident γ-ray with the detector material that may escape the detector volume and be detected in neighbouring crystals. Such clusters of γ-rays can be identified and added back. This way a full-energy event can be build and the information is restored.

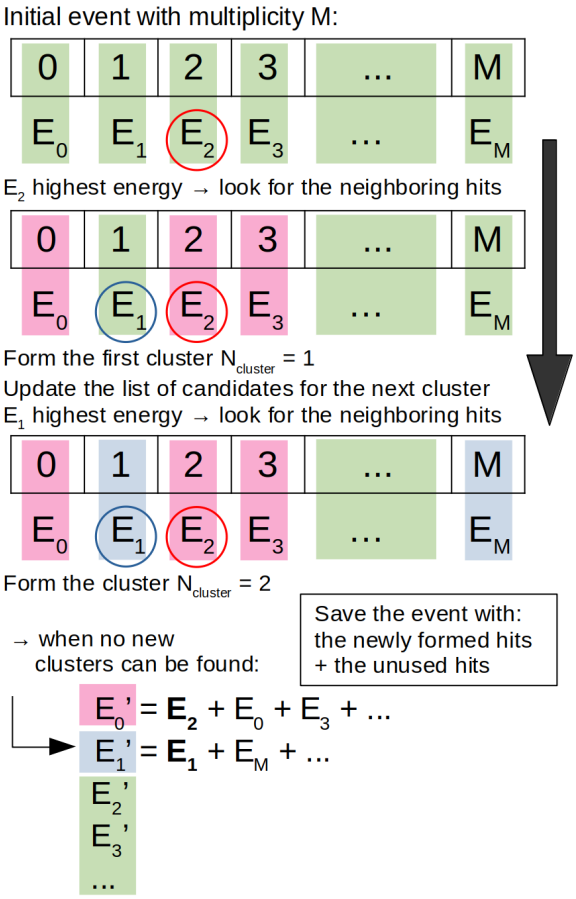

Figure 2.20: Scheme for the Add - Back algorithm implemented for the analysis of the γ-ray spectra.

The spatial range for which the add - back correction is applied can be chosen by keeping a balance between the following: adding too much and reconstructing false high-energy hits by taking a large range, or missing the reconstruction of part of the Compton events by taking a range that is too small. In this analysis an add - back range of 12 cm was considered. In the scheme shown in Figure 2.20 the add - back algorithm is illustrated. Starting with an event with M γ-ray hits registered, the list of candidates for the clustering is formed (marked with green). The highest-energy hit of this list of candidates is identified (circled on the scheme) and the cluster with hits registered within the add - back range is generated (magenta shown as the first cluster and blue shown as the second cluster). The range of add - back is not a sphere around the highest-energy hit, but rather the union of spheres around each of the clustered hits. After the first cluster is formed, the list of candidates for the next cluster is updated and the process continues until no more clusters can be formed. At the end for this event, a new list of γ-ray is saved with the new hits as well as with the unused hits. The Doppler - shift correction is applied on the fully reconstructed γ-ray considering the time and the spatial

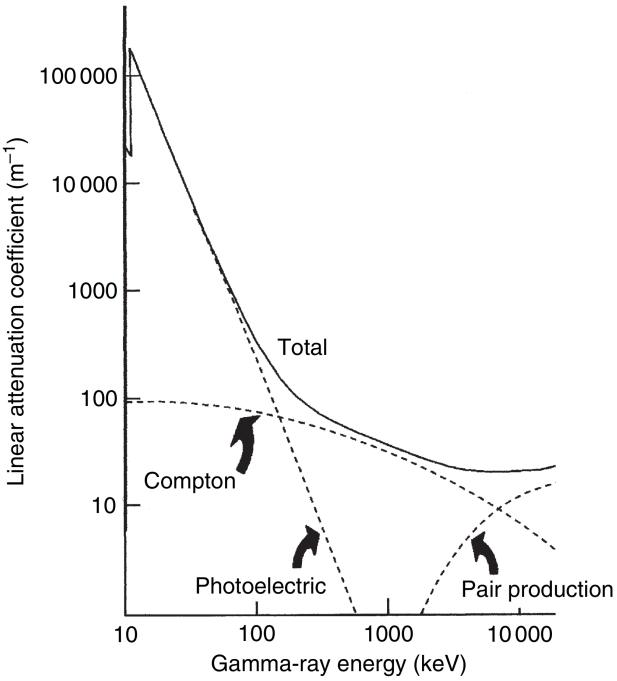

Figure 2.21: The γ rays interact with matter via the photo-electric effect, Compton effect or pair production. Each effect dominates different energy regions. For γ rays with the energy above 1 MeV, the Compton effect is the dominating one.

coordinates of the highest-energy hit. The resulting spectrum after the add - back correction is shown in Figure 2.19 (red line). A net increase of the photo-peak was achieved. The height of the full-energy peak was increased by a factor of 1.48 after the add-back correction.

Determination of MINOS efficiency

The MINOS efficiency for the ^{52}Ca (p,pn) ^{51}Ca reaction was obtained from the two γ-ray spectra with add - back correction with and without using the vertex position information from MINOS. The two spectra are shown in Figure 2.19 with the red and the black line. Each simulated response function (with and without vertex position information) for the main peak at 3.4 MeV was fitted together with a double exponential curve for the background shape to the two spectra. The ratio of the obtained amplitudes of the two response functions gives the MINOS efficiency. The response function and the determined γ-ray energy for the case without MINOS are obtained by considering that the reaction takes place in the middle of the liquid hydrogen target. For the specific phase space of the ^{52}Ca (p,pn) ^{51}Ca reaction the value of 64.7(18)% was determined for the MINOS efficiency.

2.3.5 Gamma spectrum for the ^{52}Ca (p,pn) ^{51}Ca reaction

The validity of the Doppler-shift correction of the gamma energy can be checked via its correlations with various quantities such as the emitting angle of the γ-ray, vertex position or the velocity of the fragment. These are quantities that enter into the calculation of the gamma energy, but in a correct analysis no correlations between them and the gamma energy should exist. In the Figure 2.22, the gamma energy is plotted on the Y-axis with a binning of 50 keV /

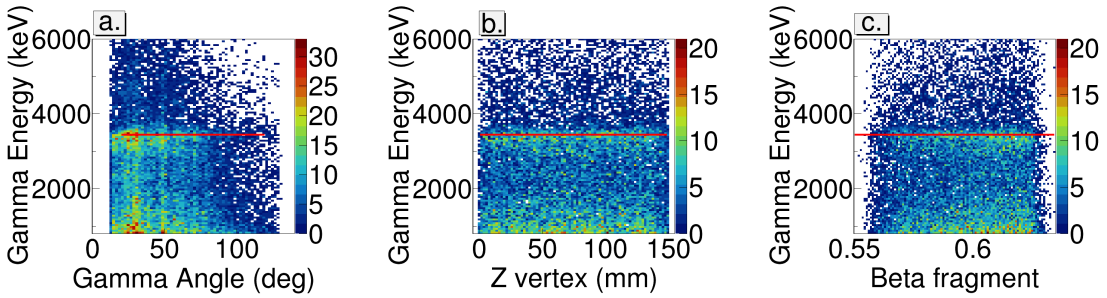

Figure 2.22: Plot with the gamma energy vs. the gamma angle (a.), the vertex position (b.) and the fragment velocity (c.) for the ^{52}Ca (p,pn) ^{51}Ca reaction. A red line is shown horizontally corresponding to 3453 keV energy for visual guidance. No correlations are observed.

bin and all plots show no shift in the gamma energy over the range of the gamma angle (10° to 130°), the vertex position (0 to 151 mm) or the velocity of the fragment at the reaction point (0.55 to 0.64 c). An additional γ-particle timestamp difference condition of 8 ns was applied in order improve the peak-to-total ratio. The distribution of the gamma-particle timestamp difference is shown in Figure 2.23.

Figure 2.23: Gamma-particle timestamp difference for the ^{52}Ca (p,pn) ^{51}Ca reaction. A timestamp window was selected based on this distribution.

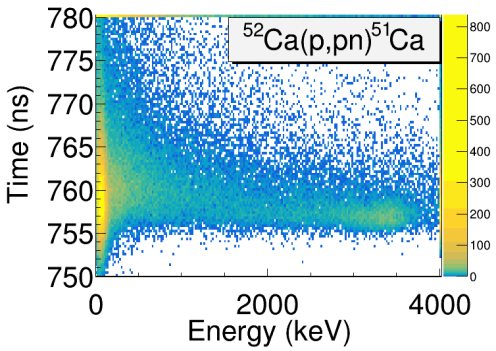

The main plot shown in Figure 2.24 (blue dots) is the final γ-ray spectrum after the corrections mentioned above. The peaks that can be identified in the spectrum are the following: 3453(20) keV, 2375(13) keV, 1720(25) keV, 1461(20) keV, and 691(4) keV (labeled on the plot from A to E). A small bump of unknown origins is also visible at 4.8 MeV. The experimental spectrum is fitted with the simulated response functions (dotted red) and a double-exponential background shape (dashed black). The error bars represent statistical uncertainties. The level scheme of ^{51}Ca was already deduced in past studies [101, 102] and the transition energies observed in this experiment are in agreement with the literature values (comparison in Table 2.1). The level scheme is shown in Figure 2.24 (top) and the transitions are labeled in the same way as in the γ-ray spectrum from A to E. Also in the Figure 2.24 (middle), one finds the single-particle configuration of the ground state, 1.7 MeV state and the 3.4 MeV state. They correspond to the knockout of a neutron from ^{52}Ca from the $p_{3/2}$, $p_{1/2}$, and $f_{7/2}$, respectively starting from the ground state of ^{52}Ca $0p - 0h$: $(f_{7/2})^8(p_{3/2})^4$ or

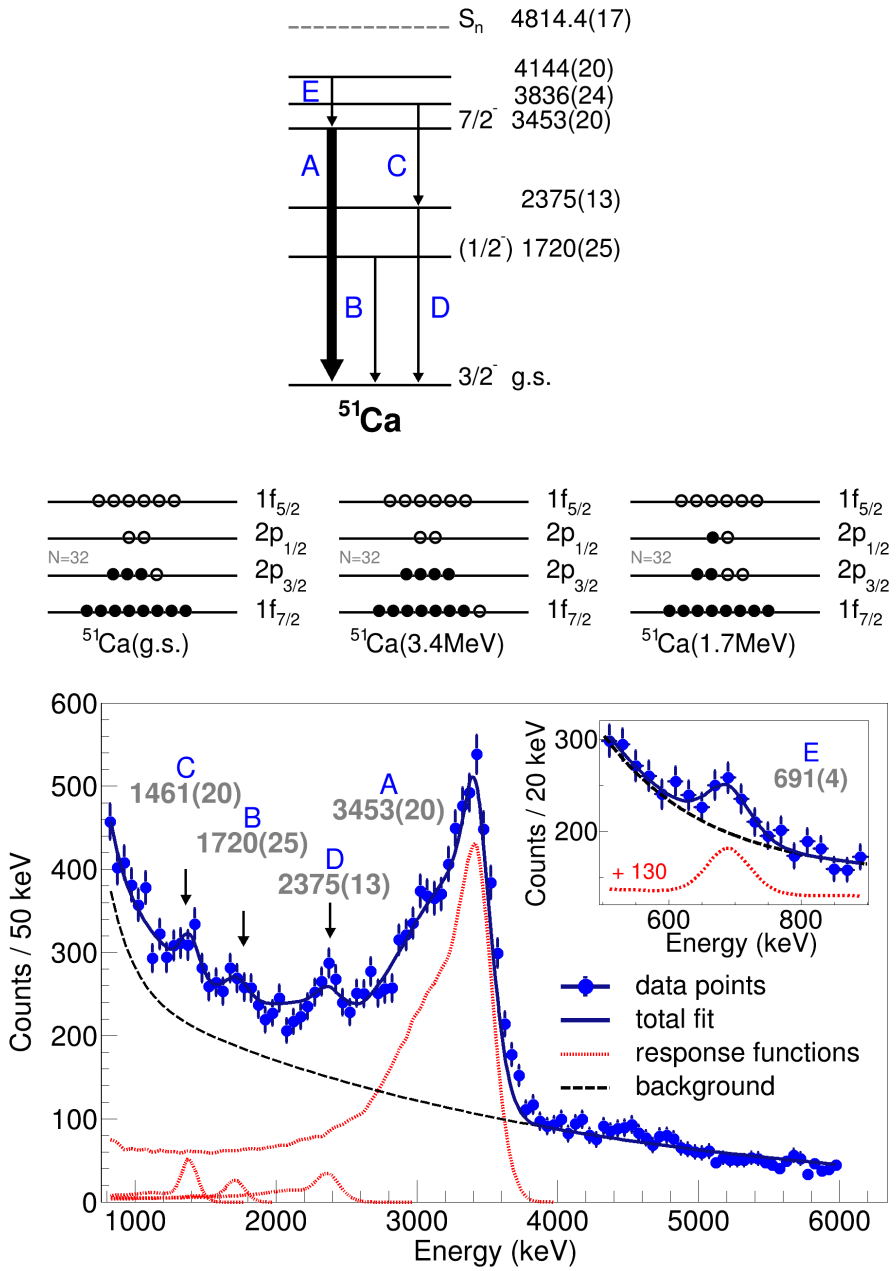

Figure 2.24: Top: The low-energy level scheme of ^{51}Ca with the observed transitions labeled from A to E. Middle: The single-particle configuration of the g.s., 3.4 MeV and 1.7 MeV states of ^{51}Ca. The filled circles represent occupied states and the open circles represent hole states. Bottom: The γ-ray decay spectrum of ^{51}Ca via the (p, pn) reaction after Doppler-shift and add-back correction. The neutron-evaporation contribution is not subtracted. The experimental γ spectrum (blue circles) is fitted with the simulated response functions (dotted red line) and a double-exponential background (dashed black line). The inset shows a low energy region of the spectrum containing the transition at 691(4) keV and the response function was shifted vertically (+130) for visualisation. Similar figure published in [9]© CC-BY-4.0.

E_γ [keV] (this work)	E_γ [keV] (literature, experiment)
691(4)	-
1461(20)	1466 [101] 1466 [102]
1720(25)	1718(1) [103] 1721 [101]
2375(13)	2377(1) [103] 2379 [101] 2378 [102]
3453(20)	3460(2) [103] 3437 [101] 3462 [102]

Table 2.1: Table with the γ-ray transitions of ^{51}Ca. The values obtained in this work are compared with the values found in literature.

the $2p-2h$ configuration: $(f_{7/2})^8(p_{3/2})^2(p_{1/2})^2$.

Significance analysis

For deciding upon the significance of the secondary peaks, namely the ones at 2375(13) keV, 1720(25) keV, 1461(20) keV, 691(4) keV, and 4.8 MeV energy, a significance analysis using the likelihood method [104] was used in which the two hypotheses, without (the null hypothesis) and with (alternative hypothesis) the peak existence assumptions are compared. In order to determine the log-likelihood ratio in the two cases for each of the peaks under question, the function `GetStats` of the `TVirtualFitter` class of `ROOT` was used. The log-likelihood ratio of two hypotheses asymptotically follows the chi-squared distribution χ^2_d with the number of degrees of freedom (dof) d, equal to the difference of the dof's in the null (H_0) and alternative hypothesis (H_1); in this case d = 1. With the log-likelihood ratios of the null hypothesis and the alternative hypothesis being a_0 and a_1, one gets:

$$-2 \cdot log\left(\frac{L_{H_1}}{L_{H_0}}\right) = 2 \cdot (a_0 - a_1) \approx \chi^2_d \tag{2.13}$$

In this case the p-value (P) will be the right-hand side cumulative distribution function of $\chi^2_{d=1}$ and the calculation of the significance level or n-σ confidence is done using the cumulative distribution function of the normal distribution, which in `ROOT` was calculated as `-1.0*TMath::NormQuantile(P)`. In determining the significance level of the above - mentioned peaks, the background shape was varied. Background shapes from other (p,pn) reactions on ^{53}Ca, ^{51}K and ^{53}K were used for cross checks. The other secondary peaks were also successively included and excluded in the calculation of the significance of each peak. In conclusion the determined significance for the secondary peaks at 2375(13) keV, 1720(25) keV,

1461(20) keV, 691(4) keV, and 4.8 MeV were the following: $3\,\sigma$, $2.5\,\sigma$, $3\,\sigma$, $3\,\sigma$, and $2\,\sigma$, respectively. Given its low significance and the absence of any peak at 4.8 MeV in the ^{51}Ca spectra from other reaction channels, the 4.8 MeV 'bump' will not be taken into consideration further in the analysis.

2.3.6 The ^{51}Ca spectrum and $\gamma - \gamma$ coincidences

Because the statistics for $\gamma - \gamma$ coincidences from the ^{52}Ca$(p, pn)^{51}$Ca channel is poor, the $\gamma - \gamma$ coincidences for the ^{51}Ca spectrum were evaluated considering all reaction channels populating bound states in ^{51}Ca. The distribution of the beam particles leading to ^{51}Ca is shown in Figure 2.25 plotted as Z vs. A/Q. In this plot, the condition for a valid reaction vertex is imposed, i.e. vertex within the physical location of the target and the minimum distance between the beam-proton or proton-proton to be smaller than 10 mm. The main population of ^{51}Ca occurs from scandium and calcium isotopes. In the case of Scandium isotopes, we have reactions of the type $(p, 2pXn)$ where we detect 2 protons and a number of X neutrons are also emitted, while in the case of calcium beam isotopes, the ^{51}Ca fragment is obtained through reactions of the type (p, pXn), where we only detect one proton in MINOS. The two types of reactions, the removal of a proton and several neutrons or the removal of neutrons exclusively, can lead to the population of different sets of bound states in ^{51}Ca. The associated spectra of the two types of reactions are shown in Figure 2.26 for an energy interval of 400-4400 keV, 40 keV binning and 200-1200 keV, 10 keV binning (inset). The peaks or the positions where we expect the peaks are labeled with the corresponding energy on the spectra. To the right of the γ-spectrum, a more complete level scheme of ^{51}Ca is shown. The level scheme was constructed using the literature values from Refs. [101–103] and the values found in the present studies. The level scheme includes transitions which could not be confirmed by this study.

The $\gamma - \gamma$ coincidences that we expect by gating on the 2375 keV transition are with 1461 keV, 310 keV, 485 keV and 1945 keV. For the 1461 keV transition, the 2375 keV, 310 keV and 485 keV should show in the coincidence spectrum. While the $\gamma - \gamma$ coincidence for the 3453 keV transition should be with 691 keV. Each of the expected coincidence was observed in our data. The spectra for one of the cases, the coincidence with the 3453 keV transition, are given in Figure 2.27. The gate region as well as the background region of choice is mentioned in the caption of the figure. With the above mentioned $\gamma - \gamma$ coincidences from several channels leading to ^{51}Ca, we can conclude that our data agrees to the level scheme constructed from Refs. [101–103].

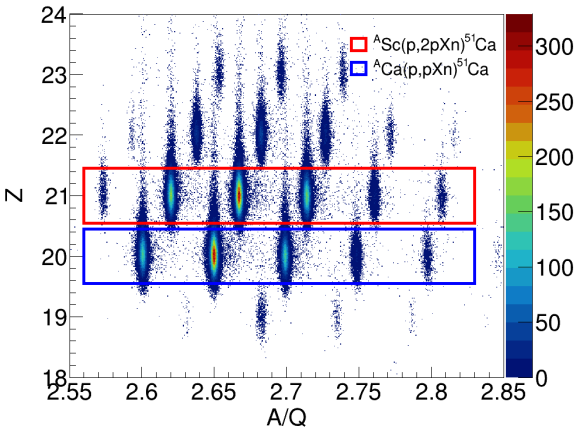

Figure 2.25: The beam particles leading to the population of ^{51}Ca with conditions for a valid vertex reconstruction. The two rectangular boxes mark the Scandium (red) and calcium (blue) isotopes leading to ^{51}Ca via $(p, 2pXn)$ and (p, pXn) reactions, respectively.

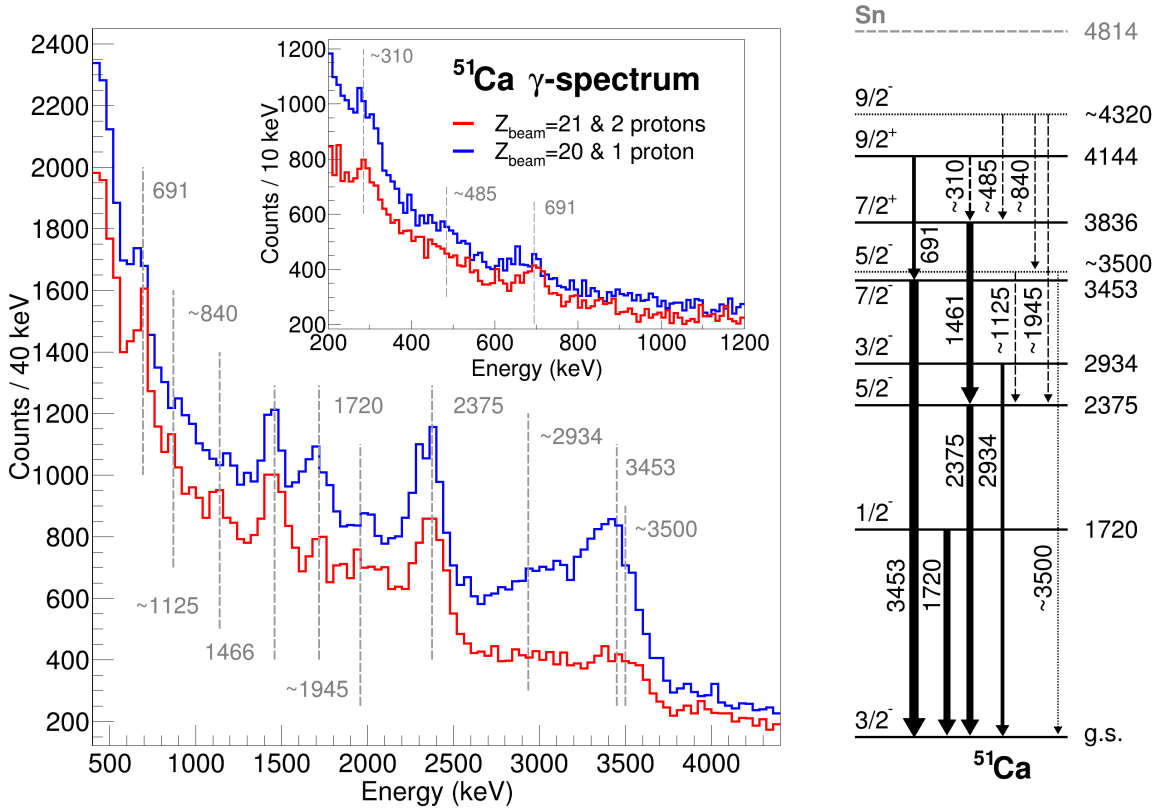

Figure 2.26: Total γ-ray spectra of ^{51}Ca fragments and the energy level scheme of ^{51}Ca.

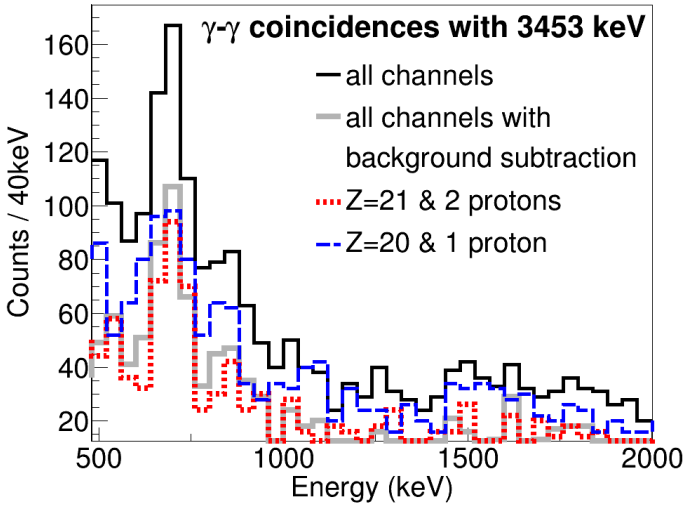

Figure 2.27: The $\gamma-\gamma$ coincidences with the 3453 keV transition. The energy gate that is used is 3200-3600 keV. The gated spectrum from all channels is plotted with solid black line. A background subtraction using the energy range of 3800-4000 keV was done and the spectrum is plotted with solid grey line. The spectra corresponding to $(p, 2pXn)$ and (p, pXn) reaction types are shown with dotted red and dashed blue lines respectively. The later two were re-scaled by a factor of 2 for visualization purpose. The γ-γ coincidence of the 3453 keV transition with the 691 keV transition is observed.

2.3.7 Neutron-evaporation channel

At the interaction of the ^{52}Ca within the liquid hydrogen target, a competing channel is the inelastic scattering followed by the neutron evaporation from the excited ^{52}Ca nucleus ($S_n = 6$ MeV for ^{52}Ca). This process results in detecting a ^{51}Ca fragment and a scattered proton in the MINOS TPC, being so far indistinguishable from the (p,pn) reaction channel. The difference between the neutron-evaporation events and (p,pn) events is that the neutron in the neutron-evaporation events is emitted isotropically in the ^{52}Ca rest frame, or forward in the lab frame (schematics in Figure 2.33), which was covered by existing neutron detectors, while the neutron from the (p,pn) events is emitted at larger angles due to the kinematics of the reaction, in a region which was not covered by any neutron detector.
The NeuLAND and NEBULA detectors were calibrated for the time and charge. The charge was calibrated using cosmic radiation measurements acquired prior to the experiment. Throughout the presented analysis the change is expressed in units of energy-equivalent. For the time calibration the photons coming from the target and reaching the neutron detectors were used because of their well-known velocity, c. The uncertainty comes from the emission point from the 151-mm long target, but the middle point of it was considered as the source. In the Figure 2.28 one can see the time vs. detector number. The sharp distributions (at timestamp values of $\sim$40 or $\sim$50-55 ns) in each detector module correspond to the photons and give the

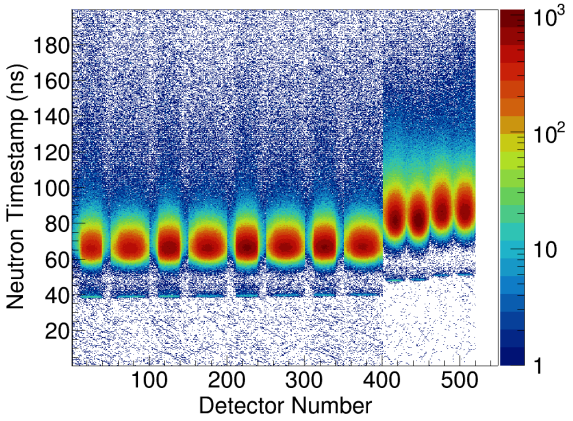

Figure 2.28: Detection time distribution for the 520 neutron detector modules of NeuLAND and NEBULA after the calibration.

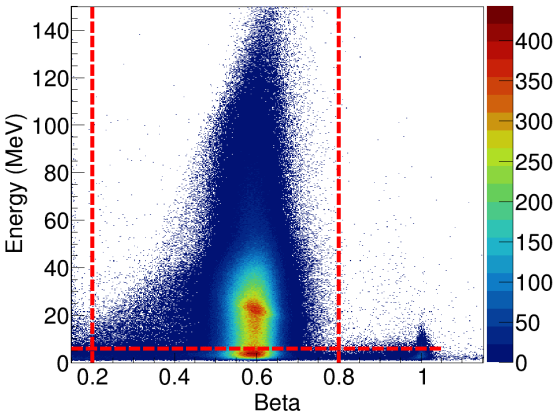

Figure 2.29: Energy (charge) vs. β plot. The cuts applied for neutron selection were: Energy (charge) > 6 MeV, $\beta > 0.2$ and $\beta < 0.8$ (red lines).

absolute time calibration and the broad distributions are the detected neutrons. A shift in the timestamp value is seen after detector number = 400 and this is related to the position of the NEBULA detectors further from the target.
At the interaction of the neutrons with the detector material, several processes can take place. The neutron can do quasi-free scattering on ^{12}C or on the protons in the scintillator material or γ-rays can be emitted. All these cases contribute to the cross-talk events. Out of the large number of hits registered for each event the *first* signal that has the charge > 6 MeV, $\beta > 0.2$ and $\beta < 0.8$ was kept (see Figure 2.29). This assured the rejection of the photons. No further cross-talk analysis is required since only one neutron is detected in this reaction channel. The phase space obtained after these cuts is also well reproduced by simulated neutron-evaporation events.

Simulation of relative energy spectrum

A simulation with GEANT4 is performed for the decay of the ^{52}Ca emitting isotropically the neutron and the ^{51}Ca fragment. The simulated neutron evaporation events are followed by the detection of the neutrons, the tracking of the fragment through the SAMURAI magnet and its detection in FDC1, FDC2 and hodoscope detectors. The relative energy of the fragment and the neutron could be reconstructed from the simulation for the events generated with input relative energy varying between 0 and 15 MeV.
Starting from a flat distribution of relative energies, after running the generated events through the simulation, a non-flat distribution of the *successful* input relative energies is obtained. For each input relative energy, a new reconstructed simulated relative energy value is calculated. The correlation of the successful input relative energy and the simulated relative energy is

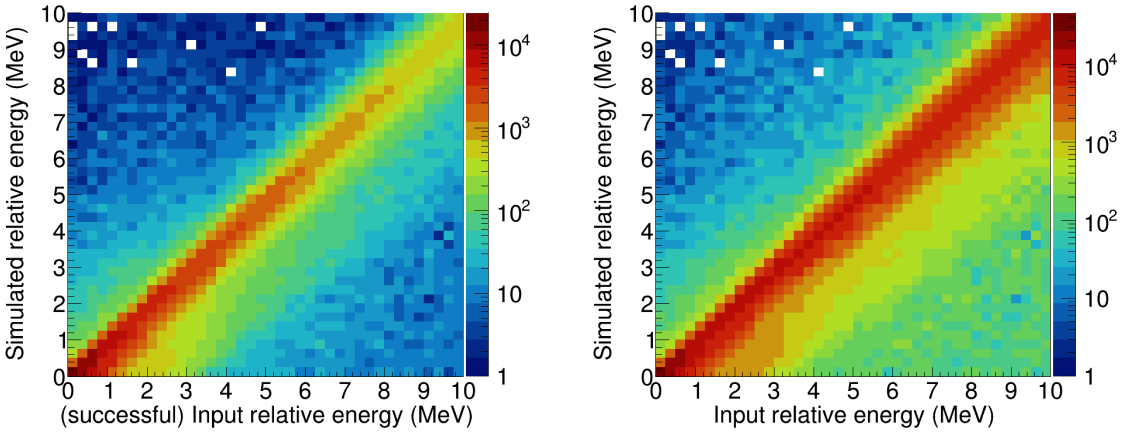

Figure 2.30: Correlation matrix (left) and normalized correlation matrix (right) for the relative energy simulation for the neutron-evaporation channel. A flat distribution of input relative energy was generated for the GEANT4 simulation.

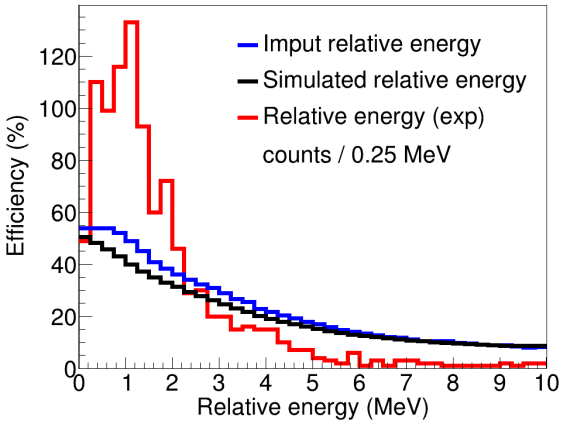

Figure 2.31: The experimental relative energy distribution (red) and the efficiency curves in the basis of the input relative energy (blue) and the simulated relative energy (black).

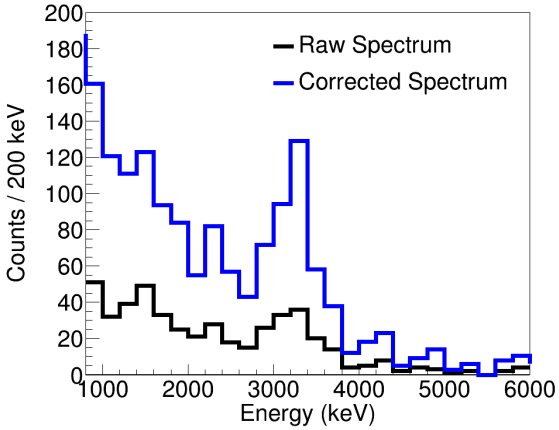

Figure 2.32: Gamma spectrum obtained by gating on the detection of one neutron before (black) and after the correction for the efficiency (blue).

shown in Figure 2.30 (left). A binning of 0.25 MeV was used for the relative energy throughout the analysis. The efficiency depending on the determined relative energy is calculated from this simulation. The initial number of events needs to be recovered for counting purposes for the efficiency, while keeping the same simulated relative energy response function. The correlation matrix from Figure 2.30 (left) will be renormalized and the new correlation matrix from Figure 2.30 (right) is obtained. The renormalization was done for each vertical column, for each bin of the input relative energy and the flat distribution of the input relative energy was recovered. The ratio between the projections of the two matrices will give the efficiency. It can be projected on the two axes, either in the basis of the input relative energy, or in the basis of the simulated relative energy, both efficiency curves are shown in Figure 2.31. The conversion of the efficiency between the two bases (successful input relative energy and simulated relative energy) can also be obtained using the correlation matrix from Figure 2.30 (left) with the following relation:

$$\frac{1}{\epsilon_y} = \frac{\sum N_{xy} \frac{1}{\epsilon_x}}{\sum N_{xy}} \tag{2.14}$$

ϵ being the efficiency in each bin (x) or (y) in either of the bases and N_{xy} represents the counts in the bin (x,y). The conversion is valid both ways.

Neutron-evaporation channel contribution

The efficiency obtained from the simulation and shown in Figure 2.31 (black line) accounts both for the geometrical coverage of the detectors and for the efficiency of the neutron detection and was used as a function of relative energy. Figure 2.33 (3.) shows a schematics of the ^{52}Ca ground state level relative to the ^{51}Ca + n system with the visualization of the relative energy, excitation energy of ^{52}Ca and the neutron separation energy. From experimental measurements one can obtain the four-momenta of ^{51}Ca and the emitted neutron. With this information one can obtain the invariant mass of the ^{52}Ca in the excited state before the neutron-evaporation process:

$$|\mathbf{P}_{^{52}Ca*}| = |\mathbf{P}_{^{51}Ca} + \mathbf{P}_n| \tag{2.15}$$

with bold **P** signifying four-momenta and $|\mathbf{P}|$ giving the invariant mass. The relative energy for the ^{51}Ca and the neutron is calculated as follows:

$$E_{rel} = |\mathbf{P}_{^{51}Ca} + \mathbf{P}_n| - |\mathbf{P}_{^{51}Ca}| - |\mathbf{P}_n| \tag{2.16}$$

The excitation energy is given by the following expression:

$$E_{exc} = |\mathbf{P}_{^{51}Ca} + \mathbf{P}_n| - |\mathbf{P}_{^{51}Ca}| - |\mathbf{P}_n| + S_{n(^{52}Ca)} \tag{2.17}$$

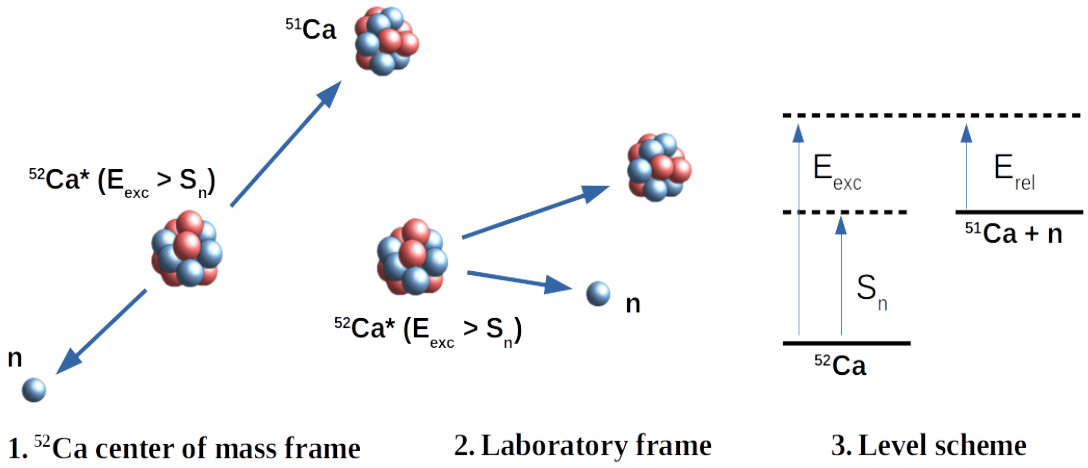

Figure 2.33: Schematics of the n-evaporation process.

or

$$E_{exc} = |\mathbf{P}_{^{51}Ca} + \mathbf{P}_n| - |\mathbf{P}_{^{52}Ca}| \tag{2.18}$$

Figure 2.31 (red line) shows the experimental relative energy distribution. The obtained average efficiency for this relative energy distribution is 32.3%. The γ-ray spectrum with a gate on the detection of a neutron and the condition for the relative energy to be ≤ 10 MeV is given in Figure 2.32 (black line). A number of 1004 events fall into the mentioned conditions corresponding to an inclusive cross section of 1.64(7) mb, which amounts to 3106 events or an inclusive cross section of 5.08(17) mb after the efficiency correction.
The gamma spectrum for neutron-evaporation receives contributions from each bin of the relative energy spectrum shown in Figure 2.31 (red line). If each γ-ray sub-spectrum corresponding to the 250 keV-bins of the relative energy distribution is firstly corrected by the efficiency for that relative energy and then summed back together, the new and corrected gamma spectrum shown in Figure 2.32 (blue line) is obtained. This γ-ray spectrum can now be fitted with the simulated γ-ray response functions and a background shape and the amplitude corresponding to each peak is finally generated leading to exclusive cross sections for the neutron-evaporation channel.

2.3.8 Cross section evaluation

The inclusive cross section for the total events of ^{52}Ca (beam) $\rightarrow$ ^{51}Ca (fragment) with the detection of a proton is 60.24(194) mb. The cross section for the n-evaporation channel is 1.64(7) mb and after the correction for the neutrons efficiency (average value 32.32%), the value of 5.08(17) mb is obtained. The contribution of neutron-evaporation events to the total cross section needs to be subtracted. It results that the inclusive cross section for the ^{52}Ca (p,pn) ^{51}Ca reaction channel is 55.16(211) mb.

E_γ (keV)	$J_i^\pi \rightarrow J_f^\pi$	σ_{total} (mb)	$\sigma_{n-evaporation}$ (mb)	$\sigma_{(p,pn)}$ (mb)
3453(20)	$7/2^- \rightarrow 3/2^-$	24.63(223)	1.33(15)	23.30(238)
1720(25)	$1/2^- \rightarrow 3/2^-$	0.64(32)	-	0.64(32)
1461(20)	$7/2^+ \rightarrow 5/2^-$	0.95(29)	0.07(7)	0.89(37)
2375(13)	$5/2^- \rightarrow 3/2^-$	1.27(44)	0.31(8)	0.96(52)
691(4)	$9/2^+ \rightarrow 7/2^-$	0.95(23)	-	0.95(23)
g.s.		-	-	30.30(418)
inclusive		60.23(194)	5.08(17)	55.15(211)

Table 2.2: Inclusive and exclusive cross sections for ^{52}Ca(p,pn)^{51}Ca and neutron-evaporation channels.

The exclusive cross sections are obtained using the amplitudes of the response functions after fitting the γ-ray spectrum, Figure 2.24. The amplitudes give the total number of events populating each final state which is then corrected for the MINOS efficiency, divided to the number of unreacted events and to the number of scattering centers per area in the target:

$$\sigma^i = \frac{N^i_{reacted} \cdot \epsilon_{MINOS}}{N_{transmitted} \cdot n_{target}} \tag{2.19}$$

The efficiency of the DALI2$^+$ array is already included in the response functions and other efficiencies entering into the number of events are canceled when taking the ratio to the unreacted or transmitted events. The exclusive cross sections for the ^{52}Ca (p,pn) ^{51}Ca reaction channel as well as for the neutron-evaporation channel and the total cross sections are summarized in the Table 2.2. Considering the cascade transitions, the 3836-keV state is populated with 0.92(63) mb cross section, the 4144-keV state is populated with 0.95(23) mb cross section, while the 3453-keV state with 22.35(239) mb. The cross section to the ground state is obtained by subtracting the exclusive cross sections from the inclusive cross section giving the final value of 30.30(418) mb.

2.3.9 Parallel and Perpendicular Momentum Distributions (PMDs)

In the (p,pn) knock-out reaction at ∼230 MeV/nucleon, the momentum distribution of the fragment relative to the beam reflects the momentum distribution of the knocked-out nucleon. The momentum distribution analysis is used for accessing the size of the neutron orbital from which the neutron is knocked-out via the (p,pn) reaction. The results of the study are going to be discussed in section 2.5.

Figure 2.34 shows a schematics of the experimental setup around the target. For the (p,pn) reaction, the vertex position within the 151-mm long liquid hydrogen target is determined using the tracked proton in the MINOS TPC and the beam trajectory before the reaction. The trajectory of the beam can be determined using the position measured in BDC1 and BDC2,

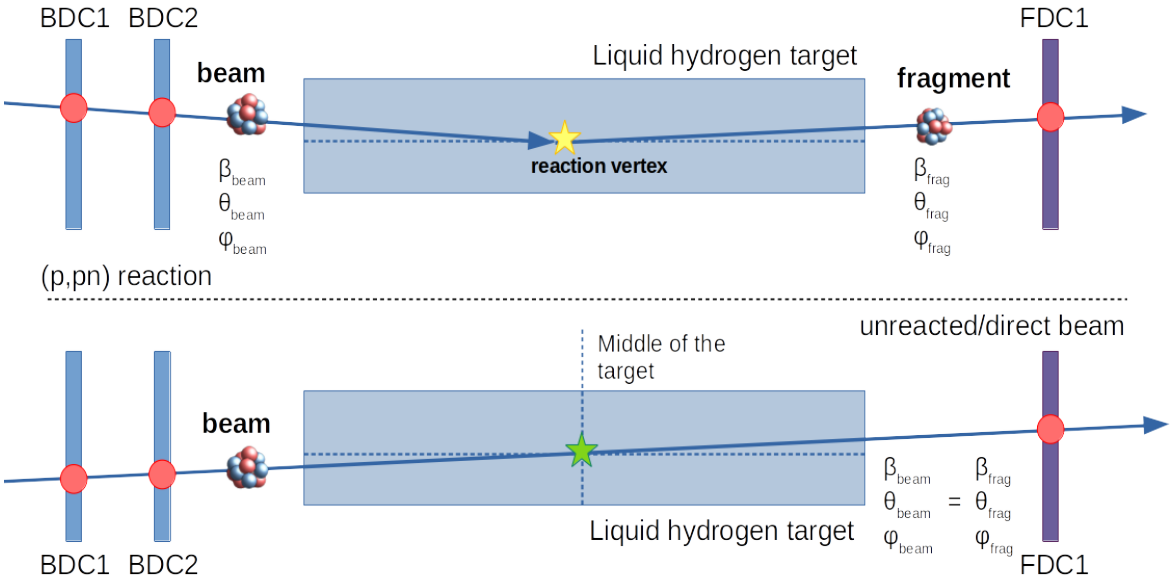

Figure 2.34: Scheme of complete kinematics of beam and fragment particles in the liquid hydrogen target for the (p,pn) reaction (top) and the direct (unreacted) beam case (bottom). The red circles represent the position measured in the beam and fragment drift chambers. The yellow star represents the reaction vertex reconstructed by the MINOS TPC. The green star represents the chosen virtual point to play the role of the reaction vertex in case of no reaction. The vertical dashed line shows the x-y plane through middle of the target. The horizontal dashed lines represent the z-axis relative to which θ_{beam} and θ_{frag} are calculated.

as well as using the vertex position information. After the reaction, the fragment particle is tracked using the FDC1 detector. From these measurements, one obtains the θ and φ angles of the beam and of the fragment particles. The velocities β_{beam} and $\beta_{fragment}$ were determined in BigRIPS and the SAMURAI magnet, respectively, using the magnetic rigidity method: $\gamma\beta = \frac{(B\rho)\cdot c}{(A/Q)\cdot m_u}$. From BigRIPS and SAMURAI, the beam and fragment velocities were corrected for the energy loss along the beam line and in the liquid hydrogen target up to the reaction vertex position. The momentum distribution of the fragment is calculated as the Lorentz boost transformation with $-\vec{v}_{beam}$ (beam velocity) of the fragment four-momentum, $\mathbf{P}_{frag}$.

For the unreacted beam, an arbitrary virtual point is chosen to play the role of the reaction vertex. In this analysis, the point of intersection between the trajectory of the beam and the x-y plane at the middle of the target was chosen (marked with a green star in Figure 2.34). The fact that the fragment (in SAMURAI) is identified as the beam (in BigRIPS), does not discard the possibility to have single or multiple scatterings in the target; but this cannot be measured, so the trajectory is considered a straight line inside the target spanned between the positions measured in the beam and fragment drift chambers. The rest of the calculations for the momentum distribution determination are the same as described for the (p,pn) reaction

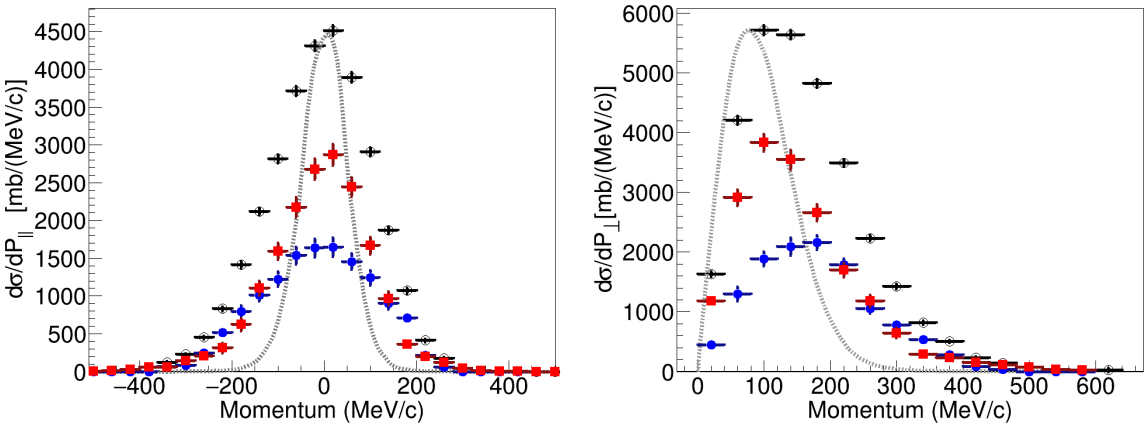

Figure 2.35: Parallel (left) and perpendicular (right) momentum distributions for the ^{52}Ca (p,pn) ^{51}Ca reaction channel. Inclusive PMDs are shown with open back circles, full blue circles for the population of 3453-keV state and red squares for the ground state. The error bars represent the statistical errors in each of the cases. The grey dashed lines show the PMDs of the unreacted beam. A bin size of 40 MeV/c is used for both plots.

events.

The absolute magnitude of the momenta of the beam and the fragment are in the range of 30 000-40 000 MeV/c. The two components of the momentum distribution of the fragment in the center of mass of the beam for the ^{52}Ca (p,pn) ^{51}Ca reaction channel are plotted in Figure 2.35. The total PMDs are shown with open black circles and the error bars represent the statistical errors, $\sqrt{N}$ of each bin (vertical) and the bin size (horizontal). The PMDs for the unreacted (direct) ^{52}Ca beam are plotted with gray dashed lines and are reflecting the resolution of the determined momentum distributions; the parallel ΔPMD contains Δp_z = 49.5 MeV/c, while the perpendicular ΔPMD contains Δp_x and Δp_y = 76.5 MeV/c added in quadrature. The unreacted beam includes the uncertainty coming from the measurements of β values of the beam and fragment from BigRIPS and SAMURAI and no uncertainty related to the reaction vertex. An additional degradation of the resolution of $\Delta p_{\parallel}$ = 1.5 MeV/c and $\Delta p_{\perp}$ = 7.5 MeV/c originating from the vertex position uncertainty within the liquid hydrogen target is considered. The resolution of the PMDs is needed in later steps for the convolution of the theoretical PMDs with the experimental resolution.

The decomposition of the total PMDs for individual populated states is done using the γ-ray spectrum. For each bin in the PMDs the corresponding partial γ-ray spectrum is obtained and it is fitted with the response functions of the existing γ-rays. The number of events found for each state and each bin is plotted obtaining the differential parallel and perpendicular momentum distributions $d\sigma/dp_{\parallel}$ and $d\sigma/dp_{\perp}$ to individual final states. A direct cut on the γ-ray spectrum is not suited for our case because of the broad shape that the peaks have and the background laying underneath each peak. Using the explained method for the deconvolution only allows the PMDs for the most populated 3453-keV state to be obtained. In the

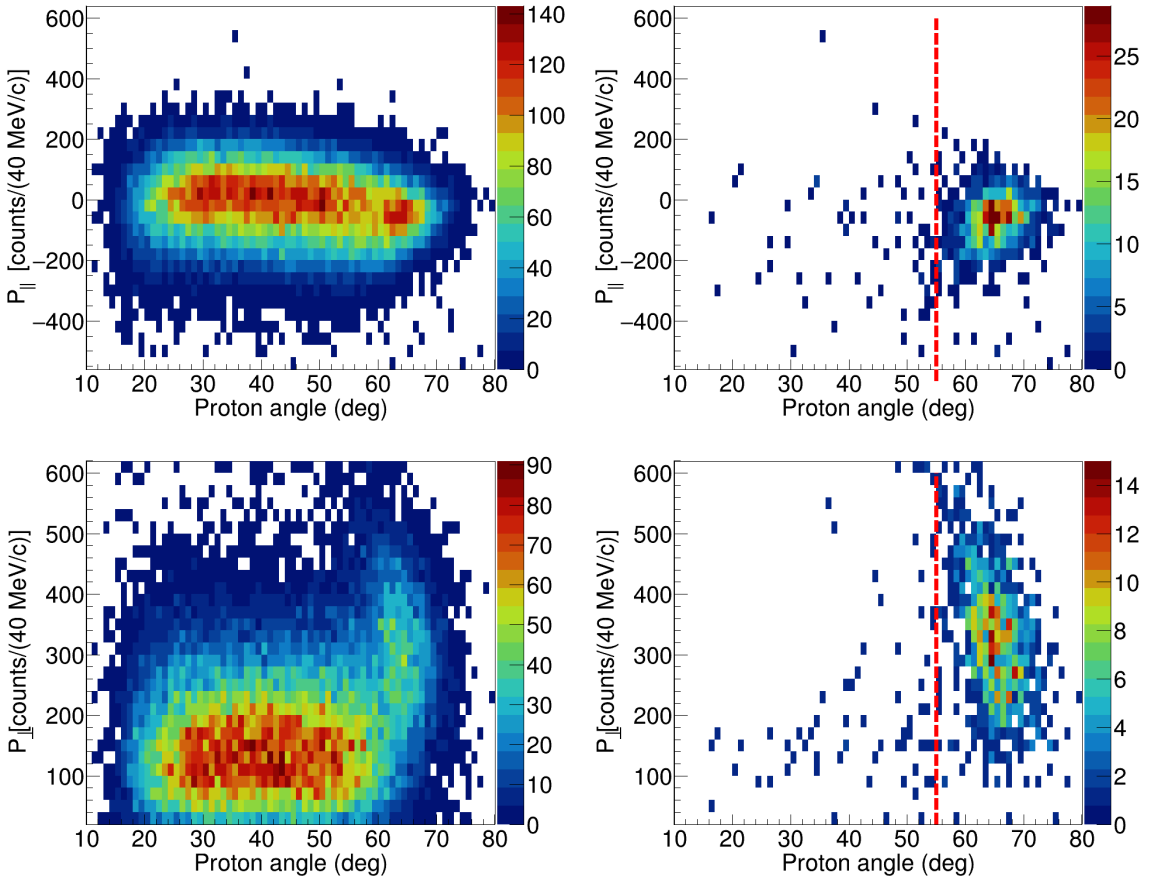

Figure 2.36: The parallel (top) and perpendicular (bottom) PMDs vs the angular distribution of the protons detected by the MINOS TPC for all ^{52}Ca $\rightarrow ^{51}$Ca events (left) and for the neutron-evaporation events (right).

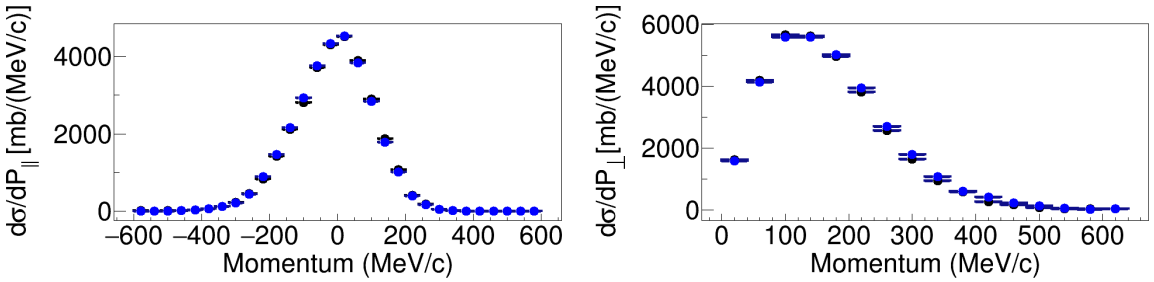

Figure 2.37: Comparison of total PMDs via the angle cut method (black) and difference method (blue). See the text for detail.

Figure 2.35, both parallel and perpendicular momentum distributions for the 3453-keV state are plotted with full blue circles. The difference between the total PMDs and the ones for the 3453-keV state gives the ground-state PMDs neglecting the small non-ground-state contributions and it is plotted with red squares. In these cases as well, the error bars represent the statistical errors.
One can already observe how the momentum distributions for the 3453-keV are wider than those corresponding to the ground state. This is expected as the population of the 3453-keV state is the result of the knock-out of a $f_{7/2}$ neutron while the ground state population is the result of the knock-out of a $p_{3/2}$ neutron via (p,pn).

Subtracting the neutron-evaporation channel contribution from PMDs

For assuring that the momentum distributions do not contain any neutron-evaporation events, a cut on the proton angle was applied. The Figure 2.36 shows the parallel (top) and perpendicular (bottom) PMDs plotted against the proton angle for all events (left) and only for the events registering a neutron (right). It is observed that the neutron-evaporation events have an angular distribution for the protons restricted to large values. A cut at 55° (*mean - rms* value of the proton angular distribution for neutron-evaporation events) was chosen, which is marked by a vertical dotted red line in the figure. Only 6.4% of the neutron-evaporation events are found at proton angles $<55^{\circ}$, which amounts to 0.53% of the total number of events. The alternative is to obtain the individual PMDs with the neutron detection gate, to correct the PMDs for the neutron detection efficiency and then to subtract the PMDs in order to remain with only (p,pn) events. The two methods are compared in Figure 2.37. Both methods are in very good agreement, but for its smaller uncertainties and simplicity, the angle cut is preferred (proton angle $< 55^{\circ}$).

2.4 Theoretical Calculations and Results

For the interpretation of the experimental data the Distorted-Wave Impulse Approximation (DWIA) reaction theory and Shell-Model (SM) calculations were conducted by our collaborators Y. Chazono, K. Ogata, F. Nowacki, A. Poves and K. Yoshida. Details about the calculations are given in this section.

2.4.1 DWIA calculations with HFB input

The Distorted-Wave Impulse Approximation (DWIA) [105–108] was used for this study for calculation the neutron knockout from ^{52}Ca. The method was benchmarked [109] on the neutron knockout reaction from ^{54}Ca, data from the same experiment as the present study [46]. The theoretical framework as in the Refs. [109, 110] for DWIA will be exposed shortly in the followings for a proton (p) induced nucleon (N) knockout reaction, $A(p,p'N)B$.
The DWIA is a theoretical method suitable for the study of (p,pN) reactions where the knocked-out nucleon (N) can be either a neutron or a proton. It assumes that the knockout occurs by a single interaction of the nucleon in the target with the incident proton. The DWIA transition amplitude is:

$$T^{jlm} = \sqrt{S} \left\langle \chi^{(-)}_{p'} \chi^{(-)}_{N} \right| \tau_{pN} \left| \chi^{(+)}_{p} \psi_{jlm} \right\rangle$$

where $\chi^{(-)}_{p'}$ and $\chi^{(-)}_{N}$ are the distorted wavefunctions of the outgoing proton and N interacting with the residual nucleus B, $\chi^{(+)}_{p}$ is the distorted wavefunction of the incoming proton interacting with the target nucleus A, ψ_{jlm} is the bound-state wavefunction of the knocked-out nucleon in the target nucleus A, $\sqrt{S}$ is the spectroscopic amplitude of the ejected nucleon and τ_{pN} is the two-body scattering matrix.
The two-body scattering matrix can be obtained using phenomenological nucleon-nucleon scattering amplitudes. In our case the effective nucleon-nucleon interaction parameterized by Franey and Love [111] was used. The incoming and outgoing waves were obtained using the folding potential (FP) [112] with the Melbourne G-matrix interaction [113]. Here, the proton and neutron densities in the target and fragment are needed. In our calculations these were obtained from HFB calculations with the SKM interaction.
The wavefunction of the knocked-out nucleon in the target nucleus, ψ_{jlm}, has a strong impact on the cross-sections results. More details on how we deal with this part in order to probe the size of the single-particle orbitals follow in the next subsection.
The triple differential cross section for the knockout process is:

$$\frac{d^3\sigma}{dE_{p'} d\Omega_{p'} d\Omega_N} = \frac{K}{(2s_p+1)(2J_A+1)} \sum_{jlm} |T^{jlm}|^2$$

with K being a kinematic term and the denominator being the degeneracy in the entrance channel.
Another quantity that can be measured experimentally is the momentum distribution of the fragment nucleus B:

$$\frac{d\sigma}{d\vec{P}_B} = \int d\vec{P}_p d\vec{P}_{p'} \delta(E_f - E_i)\delta(\vec{P}_f - \vec{P}_i)\frac{d^3\sigma}{dE_{p'}d\Omega_{p'}d\Omega_N}$$

with E_i ($\vec{P}_i$) and E_f ($\vec{P}_f$) being the initial and final energy (momentum). The total momentum can be divided into its parallel and perpendicular components:

$$\frac{d\sigma}{dP_{||}} = \int\int \left|\frac{d\sigma}{d\vec{P}_B}\right| P_\perp dP_\perp dP_{||} d\phi = 2\pi \int \left|\frac{d\sigma}{d\vec{P}_B}\right| P_\perp dP_\perp$$

and

$$\frac{d\sigma}{dP_\perp} = \int\int \left|\frac{d\sigma}{d\vec{P}_B}\right| P_\perp dP_\perp dP_{||} d\phi = 2\pi P_\perp \int \left|\frac{d\sigma}{d\vec{P}_B}\right| dP_{||}$$

with $|d\vec{P}_B| = P_\perp dP_\perp dP_{||} d\phi$ being the volume unit in the momentum phase space expressed in terms of the parallel momentum component (along z-axis) and the perpendicular momentum component (in the x-y plane). The ϕ angle is the orientation of the perpendicular component in the x-y plane taking values from 0 to 2π with the integral $\int d\phi = 2\pi$. The relation between the total momentum (P_B), parallel momentum ($P_{||}$) and the perpendicular momentum ($P_\perp$) is:

$$P_B^2 = P_{||}^2 + P_\perp^2$$

In a simple picture, the momentum of the fragment relative to the target nucleus gained after the reaction can be approximated with the momentum that the knocked-out nucleon had inside the target nucleus and this makes the parallel and perpendicular momentum distributions (PMDs) a good observable for the study of the single-particle state of the knocked-out nucleon inside the nucleus. The next subsections will expose the steps of our study for determining the size of the neutron single-particle $f_{7/2}$ and $p_{3/2}$ orbitals via the neutron knock-out reaction for ^{52}Ca.

2.4.2 Default calculations

The ^{52}Ca(p,pn)^{51}Ca is measured in the inverse kinematics, thus ^{52}Ca is the beam and ^{51}Ca is the target nucleus, and N, the knocked-out nucleon, is a neutron. In the default calculations, the neutron and proton density distributions of the beam and fragment nuclei as well as the single-particle wavefunction of the knocked-out neutron are calculated using the Woods-Saxon potential with the routinely chosen Bohr-Mottelson parametrisation:

$$V(r) = \frac{V_0}{1 + exp(\frac{r-r_0}{a_0})}$$

with a_0=0.67, r_0=1.26 fm and V_0 adjusted in order to reproduce the effective separation energy. The excitation energy of the final state of the fragment is included as well in the potential depth V_0.
In the ^{52}Ca(p,pn)^{51}Ca neutron knock-out reaction, we can remove the $f_{7/2}$, $p_{1/2}$ or the $p_{3/2}$ neutron from ^{52}Ca, for which the single-particle cross sections were calculated. With reasonable statistics for a momentum distribution analysis we could only use the events with the $f_{7/2}$ and $p_{3/2}$ neutron knock-out. The neutron knock-out from the $f_{7/2}$ orbital leaves the ^{51}Ca fragment in an excited state at an energy of 3.4 MeV, the neutron knock-out from the $p_{3/2}$ orbital will leave the fragment in the ground state, and $p_{1/2}$ neutron knock-out lead to 1.7 MeV excitation energy for the fragment. For this analysis we will deviate from the default DWIA calculations (using the Bohr-Mottelson parametrization) as described in the following subsections.
For the ^{54}Ca(p,pn)^{53}Ca and ^{48}Ca(p,pn)^{47}Ca we are only interested in the single-particle cross section values and no momentum distribution analysis. The calculations are needed for the knock-out of the $p_{3/2}$, $p_{1/2}$ and $f_{5/2}$ for ^{54}Ca and $d_{3/2}$ and $f_{7/2}$ for ^{48}Ca. For these cases we will stick to the default DWIA calculations and they will be discussed in subsection 2.4.8.

2.4.3 Neutron and proton density distributions with HFBRAD

Neutron and proton total densities and single-particle wavefunctions can be calculated with the Hartree-Fock-Bogoliubov (HFB) method using the HFBRAD code [114]. HFB allows to obtain the nuclear structure starting from an initial guess for the nucleon-nucleon interaction or for the single-particle wavefunctions. It is then constructing the wavefunctions and energies in an iterative way. The nuclear density $\rho(r)$ will be:

$$\rho(r) = \sum_i |\psi_i(E_i, r)|^2 n_i$$

a sum over all single-particle occupied states with ψ_i and E_i being the wavefunction and energy, and n_i the occupation number of the state i. The density can also be expressed using the radial wavefunctions, u_i as follows:

$$\rho(r) = \sum_i \frac{u_i^2(E_i, r)}{4\pi r} n_i$$

The sum goes over all occupied single-particle orbitals of neutrons in case of the neutron density ρ_n, for protons in case of the proton density ρ_p or both in case of the matter density ρ_m.
The rms radius of a single-particle orbital (i) expressed using the radial wavefunction is:

$$\langle r^2 \rangle_{sp,i}^{1/2} = \left(\frac{\int r^2 u_i^2(E_i, r) dr}{\int u_i^2(E_i, r) dr} \right)^{1/2}$$

And the rms radii of the neutron (n), proton (p) or matter (m) are calculated as:

$$\langle r^2 \rangle_n^{1/2} = \left(\frac{\int r^4 \rho_n(r) dr}{\int r^2 \rho_n(r) dr} \right)^{1/2}$$

$$\langle r^2 \rangle_p^{1/2} = \left(\frac{\int r^4 \rho_p(r) dr}{\int r^2 \rho_p(r) dr} \right)^{1/2}$$

$$\langle r^2 \rangle_m^{1/2} = \left(\frac{\int r^4 \rho_m(r) dr}{\int r^2 \rho_m(r) dr} \right)^{1/2} = \left(\frac{\int r^4 \rho_n(r) dr + \int r^4 \rho_p(r) dr}{\int r^2 \rho_n(r) dr + \int r^2 \rho_p(r) dr} \right)^{1/2}$$

In order to choose among the interactions to be used in the HFB calculations, the neutron, proton and total matter rms radii were calculated with the following interactions: SKM, SLY4 and SIII for ^{48,50,52,54}Ca and compared to experimental data. The results are shown in the Table 2.3. For each isotope the neutron (n), proton (p) and matter (m) rms radius values is given in fm and the interaction used in the calculation is shown in the first column of each block. Additionally, a comparison with the value obtained from the Woods-Saxon calculation with the Bohr-Mottelson parametrisation (BM) is given as well as the experimental value. The experimental values come from isotopic-shift measurements, inelastic scattering, and interaction cross section measurements. In the case of protons, the charge radius is given as well. Overall, the HFB calculations give better results than the BM calculations. Given that our main focus is ^{52}Ca, we chose the interaction that matched the best the experimental value for the proton rms radius because this is the only experimental information that it available. Even though the rms radius value is matched well, we know that the HFB calculations do not reproduce the slope, or the difference $\delta\langle r^2 \rangle^{48,52}$, but for our needs it is still the best behaving interaction. We will continue using the HFB (with SKM interaction) for the total neutron and proton densities for the beam and the fragment nuclei in the DWIA calculations.

Starting from the even-even beam nuclei, we end up with odd-A fragment nuclei in a (p,pn) neutron knock-out reaction. The HFBRAD code is restricted to the calculation of even-even isotopes. The odd-A fragments of the reactions ^{48}Ca(p,pn)^{47}Ca, ^{52}Ca(p,pn)^{51}Ca, and ^{54}Ca(p,pn)^{53}Ca were treated within the following approximations:

- the proton densities of the odd-A fragments were considered the same as for their corresponding even-A beams (shown in Figure 2.38).

- the neutron densities can be calculated in 4 ways summarized in Table 2.4. Cases a and b give similar results, as well as the cases c and d. The neutron densities for the odd-A nuclei for the cases a and d are plotted in Figure 2.38. Out of the 4 cases, case a was used for the DWIA calculations. The fragment densities as calculated starting from the

^{48}Ca: Z=20, N=28				^{50}Ca: Z=20, N=30			
	n	p	m		n	p	m
SKM	3.580	3.424	3.516	SKM	3.664	3.444	3.578
SLY4	3.606	3.453	3.543	SLY4	3.696	3.475	3.609
SIII	3.599	3.462	3.542	SIII	3.685	3.488	3.608
BM	3.662	3.362	3.537	BM	3.763	3.369	3.605
Exp	-	3.38$^{(IS)}$ 3.47$^{(IS*)}$	3.48$^{(pp)}$ 3.49$^{(pp)}$ 3.47$^{(xs)}$	Exp	-	3.43$^{(IS)}$ 3.51$^{(IS*)}$	3.64$^{(xs)}$
^{52}Ca: Z=20, N=32				^{54}Ca: Z=20, N=34			
	n	p	m		n	p	m
SKM	3.746	**3.462**	3.639	SKM	3.856	3.487	3.724
SLY4	3.777	3.494	3.671	SLY4	3.698	3.521	3.744
SIII	3.772	3.513	3.674	SIII	3.842	3.542	3.733
BM	3.743	3.373	3.601	BM	3.889	3.388	3.704
Exp	-	**3.46**$^{(IS)}$ 3.55$^{(IS*)}$	-	Exp	-	-	-

Table 2.3: The neutron (n), proton (p), $^{(*)}$or charge, and matter (m) rms radii for ^{48,50,52,54}Ca nuclei calculated with the interaction indicated in the first column corresponding, or with the Woods-Saxon potential with the Bohr-Mottelson parametrization (BM) and the available experimental data (Exp). All values are given in fm. The experimental data come from isotopic shift measurements $^{(IS)}$, (p,p) elastic scattering $^{(pp)}$ and interaction cross section measurements $^{(xs)}$, from Refs. [4, 6].

case	^{47}**Ca**	^{51}**Ca**	^{53}**Ca**
a	^{48}**Ca - $f_{7/2}$ of ^{48}Ca**	^{52}**Ca - $p_{3/2}$ of ^{52}Ca**	^{54}**Ca - $p_{1/2}$ of ^{54}Ca**
b	^{48}Ca - $f_{7/2}$ of ^{46}Ca	^{52}Ca - $p_{3/2}$ of ^{50}Ca	^{54}Ca - $p_{1/2}$ of ^{53}Ca
c	^{46}Ca + $f_{7/2}$ of ^{46}Ca	^{50}Ca + $p_{3/2}$ of ^{50}Ca	^{52}Ca + $p_{1/2}$ of ^{52}Ca
d	^{46}Ca + $f_{7/2}$ of ^{48}Ca	^{50}Ca + $p_{3/2}$ of ^{52}Ca	^{52}Ca + $p_{1/2}$ of ^{54}Ca

Table 2.4: The 4 cases for calculating the odd-A neutron density distributions (for ^{47,51,53}Ca) using the even-even density distributions (^{46,48,50,52,54}Ca) and the single-particle wavefunctions of the valence neutrons ($f_{7/2}$, $f_{5/2}$, $p_{3/2}$ and $p_{1/2}$). Case **a** was finally chosen for the density calculations for odd-A nuclei.

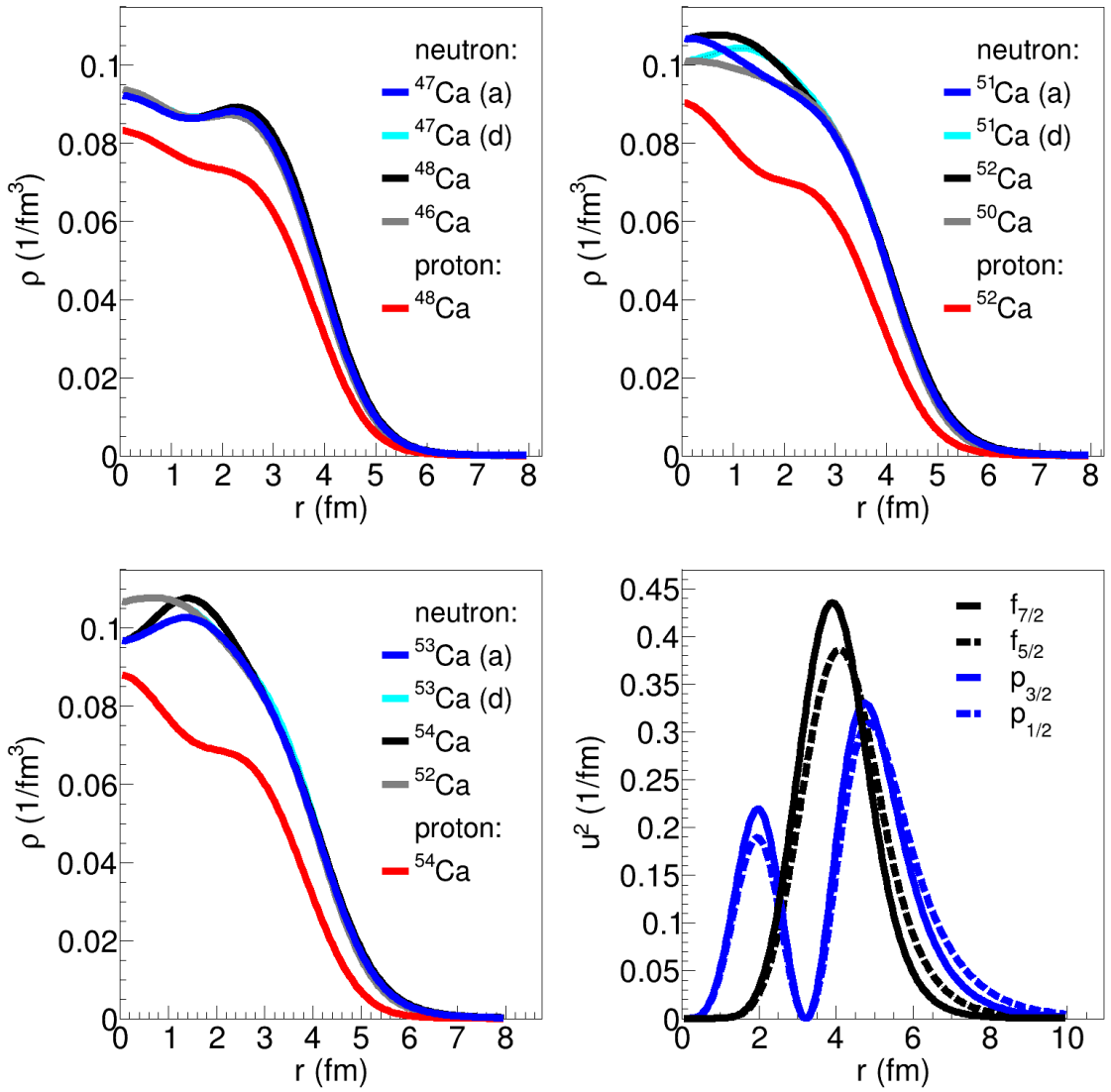

Figure 2.38: Top-left, top-right and bottom-left: The density distribution of protons and neutrons for odd-A (cases a and d) and even-A nuclei. Bottom-right: The radial wavefunctions of $f_{7/2}$, $f_{5/2}$, $p_{3/2}$ and $p_{1/2}$ neutron orbitals in neutron-rich Ca-isotopes. HFB calculations performed using the SKM interaction.

	relative change in cross section		relative change in $P_{||}$ width	
case	$p_{3/2}$ (g.s.)	$f_{7/2}$ (3.4 MeV)	$p_{3/2}$ (g.s.)	$f_{7/2}$ (3.4 MeV)
+both	-16%	-13%	-1.14%	-0.59%
-both	27%	24%	1.29%	1.02%
+p	-7%	-5%	-0.41%	-0.25%
-p	10%	9%	0.53%	0.46%
+n	-11%	-9%	-0.92%	-0.16%
-n	15%	14%	0.54%	0.59%

Table 2.5: The relative change in cross section and parallel momentum distribution ($P_{||}$) width for the variation of the beam and fragment radial extension of the proton (p), neutron (n), or both distributions by +10% (+) or -10% (-) for the g.s. and 3.4 MeV states of the fragment in the exit channel. The DWIA calculations are using HFB (with the SKM interaction) calculated density distributions which are then artificially expanded or shrunk in the radial coordinate.

beam nuclei (with mass number A) as below:

$$\rho_{A-1}(r) = \rho_A(r) - \frac{u^2_{sp,A}(r)}{4\pi r}$$

For reference, the rms radii of the neutron density distribution in each of the nuclei are the following: for ^{47}Ca, one obtains 3.559 fm in case a and 3.528 fm in case d, starting from ^{48}Ca with 3.579 fm and ^{46}Ca with 3.505 fm, respectively. For ^{51}Ca, one obtains an rms radius of 3.709 fm in case a and 3.641 fm in case d starting from ^{52}Ca with 3.746 fm and ^{50}Ca with 3.614 fm. Lastly, ^{53}Ca will have an rms radius of 3.816 fm in case a and 3.783 fm in case d, with ^{54}Ca bein 3.855 fm in size.
Also, the binding energy of the removed neutron from the HFB calculations (with SKM) are: -10.43 MeV for ^{48}Ca (literature value: -9.95 MeV), -5.82 MeV for ^{52}Ca (literature value: -6.00 MeV), and -2.73 MeV for ^{54}Ca (literature value: -3.84 MeV). The agreement between the calculations and literature values is good, with deviations of the order of 1 MeV or lower in the neutron rich Ca-isotopes.

2.4.4 Variation study of the beam and fragment nuclear size

A first attempt to probe the impact of the nuclear size on the PMDs was to artificially increase or decrease the nuclear radial extension for the DWIA. The following cases were treated: change in size by -10% only on protons (-p), +10% only on protons (+p), -10% only on neutrons (-n), +10% only on neutrons (+n), -10% on both neutrons and protons (-both) and +10% on both neutrons and protons (+both). In all these cases, the single particle wavefunction of the knocked-out neutron was kept the same as obtained from the HFB

calculations. The change in the cross section values is summarized in Table 2.5. We observe an impact larger than $\pm$10% on the cross sections for the $\pm$10% variation of the radial component in the densities. This is because if we keep the same single particle wavefunction and vary the fragment density, we directly vary the overlap between the two, and thus, the cross sections. One can look for reference at Figure 2.38, top-right and bottom-right plots. Most of the probability distribution of the single particle wavefunctions for both $1f$ and $2p$ lies at the decreasing part or the tail of the total neutron or proton distribution in the fragment. On the other hand, the width of the parallel momentum distribution changes very little because it reflects mostly the single-particle wavefunction of the removed nucleon (in the momentum space) rather than the fragment or the target density distribution.

Calculations with HFB vs. BM single-particle wavefunction of the knocked-out neutron

Calculations using the single-particle wavefunction for the knocked-out nucleon from HFB or using the Woods-Saxon potential (Bohr-Mottelson parametrization, BM) were performed for comparison. In both cases the target and fragment proton and neutron density distributions from the HFB calculations were used as they better reproduce the experimental data. The resulting cross sections do show a difference. The cross sections obtained with the HFB single-particle wavefunctions are on average 20% lower than with BM. The difference arises from the tails of the wavefunctions obtained in the two cases. In Figure 2.39 one can see with the blue dots the HFB wavefunctions for the $p_{3/2}$ (left) and $f_{7/2}$ (right) neutrons in ^{52}Ca. On the other side, the BM wavefunctions are plotted with black solid line. For both orbitals, the tails of the wavefunctions are longer for the BM case compared to the HFB case, increasing the overlap with the density probability of the fragment and thus increasing the cross section for neutron knock-out. In the next steps of the study we will continue using the BM single-particle wavefunctions and check the sensitivity of the various parameter entering into the calculations such as the radial parameter of the Woods-Saxon potential or the diffuseness parameter.

2.4.5 Sensitivity of PMDs to the r_0 radial parameter

As all examples of shell evolution taught us, the nuclear structure changes in many aspects when one moves away from the valley of stability. As we see, the momentum distributions and the cross sections calculated via the DWIA method are very sensitive to the single-particle wave-function of the knocked-out neutron. On one hand, using the experimental momentum distribution, we could select the wavefunction with a proper radial extension and pin down the size of the orbitals from which we remove the neutron, and on the other hand, using the wavefunction that fits the best, we can finally calculate the neutron knock-out cross sections. Starting from the default radial parameter value, $r_0 = 1.27\,fm$, a variation of $\pm$5%, $\pm$10%, $\pm$20%, $\pm$30% and $\pm$40% was used for additional momentum distribution and cross-section calculations. As the radial parameter of the Woods-Saxon potential, directly relates to the radial extension of the single-particle wavefunctio, we obtained a set of single-particle

wavefunctions of different rms radii values. For the $p_{3/2}$ neutron orbital, the set of wavefunctions obtained with the radial parameter varied between -40% and 40% have the following rms radii: 3.749 fm, 3.955 fm, 4.167 fm, 4.382 fm, 4.491 fm, 4.601 fm (default), 4.711 fm, 4.822 fm, 5.048 fm, 5.276 fm, and 5.507 fm. Also the set of rms radius values for the $f_{7/2}$ neutron orbital are: 3.051 fm, 3.343 fm, 3.646 fm, 3.955 fm, 4.112 fm, 4.269 fm (default), 4.428 fm, 4.587 fm, 4.906 fm, 5.228 fm, and 5.549 fm. The rms radii of the neutron orbital calculated with HFB, SKM interaction are 4.492 fm and 4.118 fm, for the $p_{3/2}$ and $f_{7/2}$ orbitals respectively. The set of wavefunctions with the different r_0 values and the wavefunction from HFB are shown in Figure 2.39 for both neutron orbitals $p_{3/2}$ and $f_{7/2}$ and the plots with the rms radius value as a function of r_0 are shown in Figure 2.44 of section 2.5. The set of momentum distribution curves (parallel and perpendicular projections) with the different r_0 parameter values and with the wavefunction from HFB are also plotted in Figures 2.41 and 2.40. The change in cross section and the width of the parallel momentum distribution as one varies the radial parameter is listed in Table 2.6. For all these calculations with the variation of r_0, other parameters remained the default ones, including the diffuseness parameter a_0 set at the value 0.67.
From the Table 2.6, one can see how sensitive the cross section and the momentum distribution are to the radial parameter. For a change by 40% in the radial parameter, the cross section can jump to up to 144% of the default value, or the parallel momentum distribution widens as much as 19% more compared to the initial width.

Relation between the single-particle orbitals rms radius and PMDs

The calculated PMDs can be fitted to the experimental PMDs and the quality of the fit, or the χ^2 can be extracted for each of the PMD curves. One can construct χ^2 as a function of the r_0 parameter with which the PMD curve was calculated and from the minimum of the χ^2 function, one can find the optimum r_0 value. Additionally, the two points with $\chi^2_{min} + 1$ on either side of the minimum point on the y-axis correspond to a $\pm 1 - \sigma$ interval for r_0 on the x-axis. In the next section of this chapter, the fitting procedure and the results for the optimum r_0 and the rms radii are presented. After the r_0 optimum value with the σ value are found, one can extract the rms radius, and the corresponding 1-σ value, of the orbital from the relation between rms radius and r_0 parameter. This will be presented in section 2.5.

2.4.6 Sensitivity of PMDs to the a_0 diffuseness parameter

As it was done for the r_0 radial parameter of the Woods-Saxon potential, the a_0 diffuseness parameter was also varied and the sensitivity of the cross sections and momentum distributions to a_0 was studied. The Table 2.7 shows the relative change in the cross section and in the parallel momentum distribution width as the a_0 parameter varies from -40% to +40%. The diffuseness parameter is not influencing the results of the DWIA calculations too much, the variations are very small, especially for the PMDs, such that the same analysis as for r_0

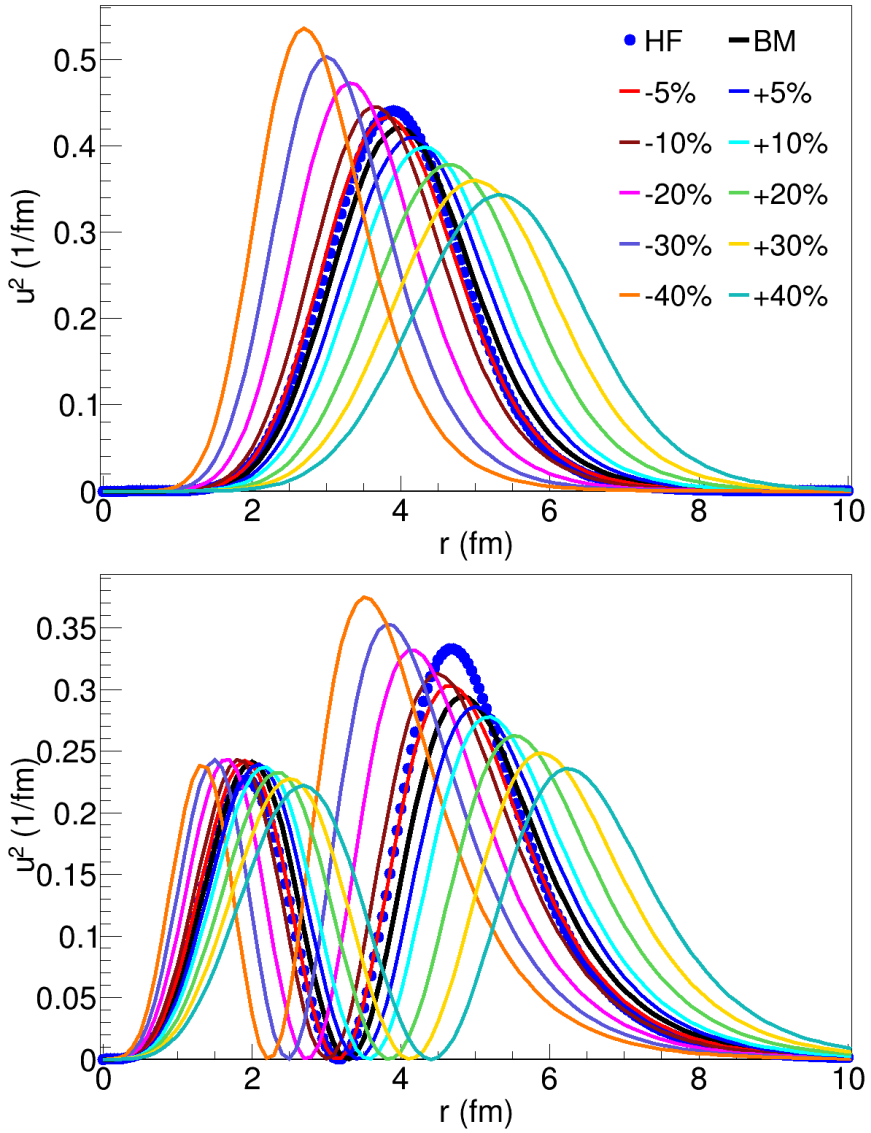

Figure 2.39: The single-particle wavefunctions for the neutron $p_{3/2}$ (left) and $f_{7/2}$ (right) orbitals. They are calculated with the HFBRAD code with the SKM interaction (HF) and with the Woods-Saxon potential, with the Bohr-Mottelson parametrisation (BM). The additional coloured solid lines represent the wavefunctions calculated using a different r_0 radial parameter of the Woods-Saxon potential, having values from -40% to +40% relative to the default r_0=1.27 fm (BM). The X-axis represents the radial coordinate in fm and the Y-axis represents the probability density of the radial wavefunction, $u(r)$.

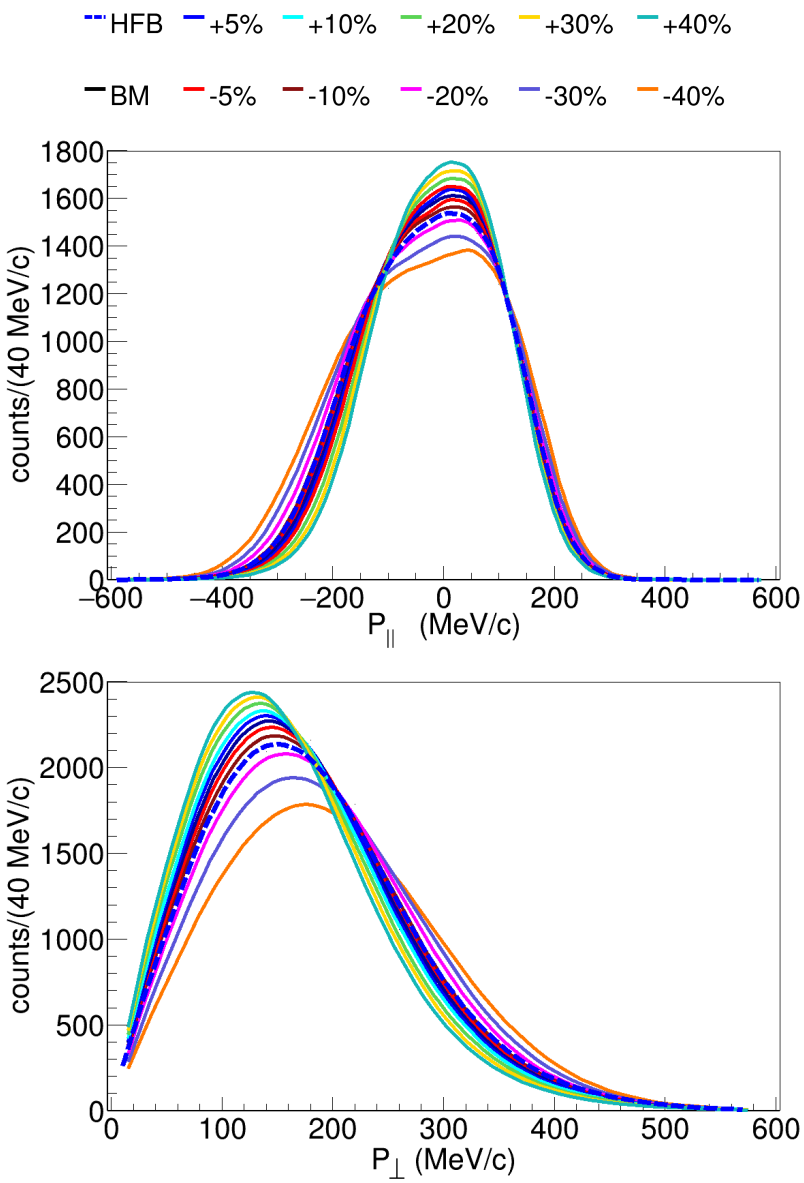

Figure 2.40: The parallel (top) and perpendicular (bottom) momentum distributions for the knock-out of a neutron from the $f_{7/2}$ orbital from the ^{52}Ca beam, leaving the fragment in the 3.4 MeV excitation energy calculated with the HFB single-particle wavefunction (HFB, dashed blue curve) and the Woods-Saxon potential with Bohr-Mottelson default parametrisation (BM, solid black) or variations of the r_0 radial parameter by -40% up to +40% compared to the default value of r_0=1.27 fm (colored solid curves, percentage shown).

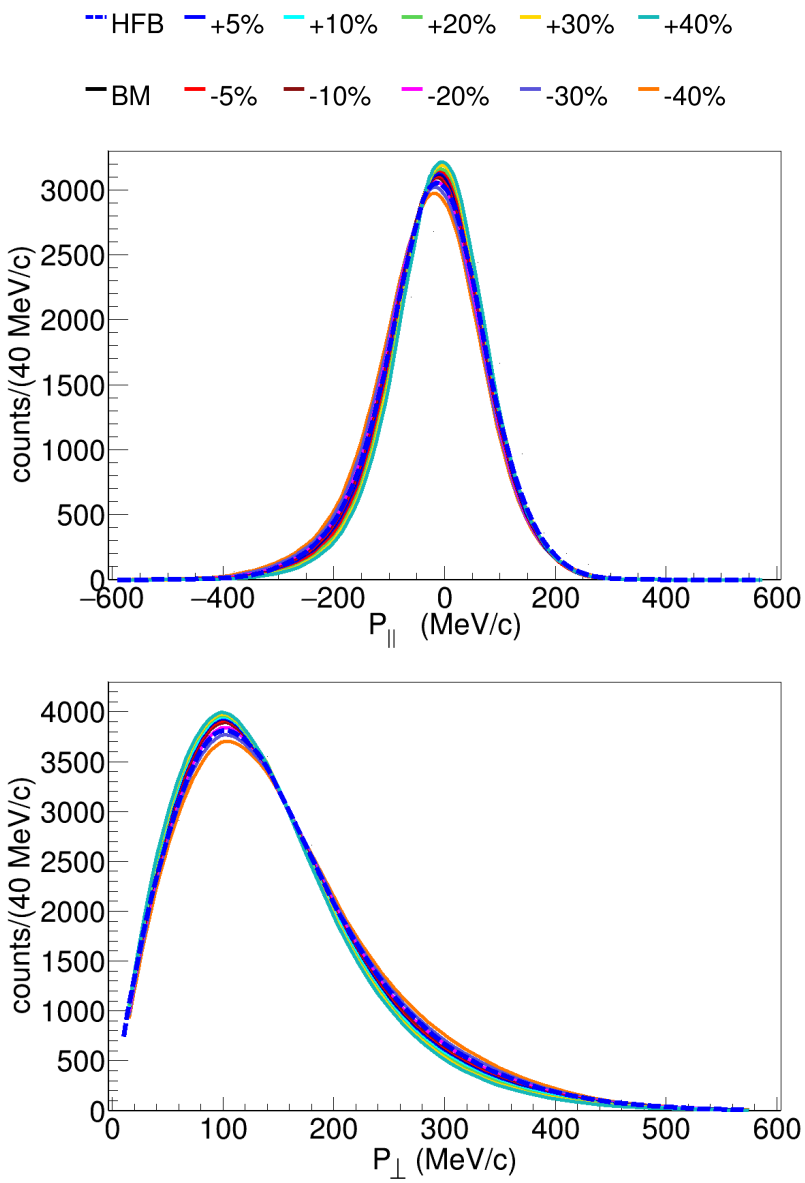

Figure 2.41: The parallel (top) and perpendicular (bottom) momentum distributions for the knock-out of a neutron from the $p_{3/2}$ orbital from the ^{52}Ca beam, leaving the fragment in the ground state calculated with the HFB single-particle wavefunction (HFB, dashed blue curve) and the Woods-Saxon potential with Bohr-Mottelson default parametrisation (BM, solid black) or variations of the r_0 radial parameter by -40% up to +40% compared to the default value of r_0=1.27 fm (colored solid curves, percentage shown).

parameter r_0		**relative change in cross section**		**relative change in $P_{||}$ width**	
$\%_{rel}$	value	$p_{3/2}$ (g.s.)	$f_{7/2}$ (3.4 MeV)	$p_{3/2}$ (g.s.)	$f_{7/2}$ (3.4 MeV)
-40%	0.762	-50.3%	-56.6%	19.6%	8.9%
-30%	0.889	-40.9%	-47.9%	13.6%	6.3%
-20%	1.016	-29.6%	-36.4%	8.3%	3.7%
-10%	1.143	-16.0%	-20.7%	3.7%	1.5%
-5%	1.2065	-8.3%	-11.1%	1.7%	0.8%
0%	**1.27**	**0%** **5.79 mb**	**0%** **3.75 mb**	**0%** **92 MeV/c**	**0%** **120 MeV/c**
5%	1.3335	8.89%	12.6%	-1.6%	-0.6%
10%	1.397	18.2%	26.7%	-3.0%	-1.2%
20%	1.524	38.2%	60.0%	-5.5%	-2.3%
30%	1.651	58.9%	99.6%	-7.8%	-3.5%
40%	1.778	79.4%	144.7%	-9.9%	-4.7%

Table 2.6: The relative change in the cross section and the width of the parallel momentum distribution for a variation of the radial parameter r_0 by -40% up to +40%. The calculations are performed for the neutron knock-out off the $f_{7/2}$ or the $p_{3/2}$ orbital.

parameter a_0		**relative change in cross section**		**relative change in $P_{||}$ width**	
$\%_{rel}$	value	$p_{3/2}$ (g.s.)	$f_{7/2}$ (3.4 MeV)	$p_{3/2}$ (g.s.)	$f_{7/2}$ (3.4 MeV)
-40%	0.402	-20.4%	-9.5%	4.5%	2.0%
-30%	0.469	-15.6%	-7.7%	3.16%	1.6%
-20%	0.536	-10.6%	-5.6%	2.1%	1.1%
-10%	0.603	-5.4%	-3.0%	0.9%	0.5%
-5%	0.6365	-2.7%	-1.6%	0.6%	0.2%
0%	**0.67**	**0%** **6.45 mb**	**0%** **3.38 mb**	0% **92 MeV/c**	0% **120 MeV/c**
5%	0.7035	2.8%	1.7%	-0.3%	-0.3%
10%	0.737	5.6%	3.5%	-0.9%	-0.6%
20%	0.804	11.2%	7.3%	-1.7%	-1.2%
30%	0.871	17.0%	11.6%	1.7%	1.9%
40%	0.938	22.9%	16.2%	-3.3%	-2.5%

Table 2.7: Same as above, but the variation is done for the a_0 diffuseness parameter, keeping the r_0 radial parameter at its optimum value: 1.21 fm for $f_{7/2}$ and 1.35 fm for $p_{3/2}$.

cannot be done here. We would further keep the a_0 parameter at the default value of 0.67.

2.4.7 Sensitivity of PMDs to the chosen potential

In order to address the sensitivity of our calculations to the chosen potential, the Dirac phenomenology was selected as an alternative potential in the DWIA calculations. All calculations were done with the folding potential (FP) and Dirac phenomenology (Dirac) for the optimum r_0 value and $a_0 = 0.67$ (default). The PMDs obtained in these two ways were compared and the relative differences are the following:
$p_{3/2}$: 3.2% in $P_{||}$ and 4.5% in $P_{\perp}$
$f_{7/2}$: 2.2% in $P_{||}$ and 1.3% in $P_{\perp}$
The two PMD sets of curves are shown in the final PMDs plot, Figure 2.43 in section 2.5. The solid line in both the parallel and perpendicular momenta of the two states represent the calculations with the folding potential, while the dashed line represents the Dirac phenomenology calculations. Also, in terms of cross section values, they differ by less than 5% in the given energy range. As the conclusion of this additional check, we validate that the choice of potential does not have a strong impact on the final results.

2.4.8 Calculations for ^{48}Ca and ^{54}Ca

For ^{48}Ca we found experimental data for triple-differential cross section (TDX) for the (p,pn) reaction on ^{48}Ca, at $\sim$150 MeV/nucleon energy, published in Ref. [115]. Theoretical DWIA calculations for the TDX were performed by our collaborators and they were fitted to the experimental data. The calculations were done with both FP and Dirac potential. Figure 2.42 shows the fit to the experimental data. The result of the fitting procedures is the proportionality factor between the single-particle TDX curves and the experimental data, which is an "experimental spectroscopic factor". The plots (a) and (d) are corresponding to the $1f_{7/2}$ neutron orbital of ^{48}Ca. The plots (b) and (e) correspond to the sd orbitals, $2s_{1/2}$ (blue curve) and $1d_{3/2}$ (green curve). The experimental data gives the TDX as a sum of the two orbitals, thus the sum of the two theoretical TDX with a scaling factor each was fitted to the data in this case (red curve). Finally, the plots (c) and (f) correspond to the $1p$ orbitals ($1p_{1/2}$ and $1p_{3/2}$). The resulting experimental spectroscopic factors, or the ration between experimental and the single-particle TDX, are given in Table 2.8. The maximum occupation numbers, $(2J+1)$, for the $f_{7/2}$, $s_{1/2}$, $d_{3/2}$ and the two p orbitals are 8, 2, 4, and 6, respectively. Only for the p orbitals the resulting value is too large with both of the potentials that were used. We speculate that it has to do with removing deeply bound nucleons, in which case the theory might not successfully describe the data. The experimental spectroscopic factors are used in the current study as a reference for a standard doubly-magic nucleus and are compared to the experimental spectroscopic factors of ^{52}Ca and ^{54}Ca. There are differences

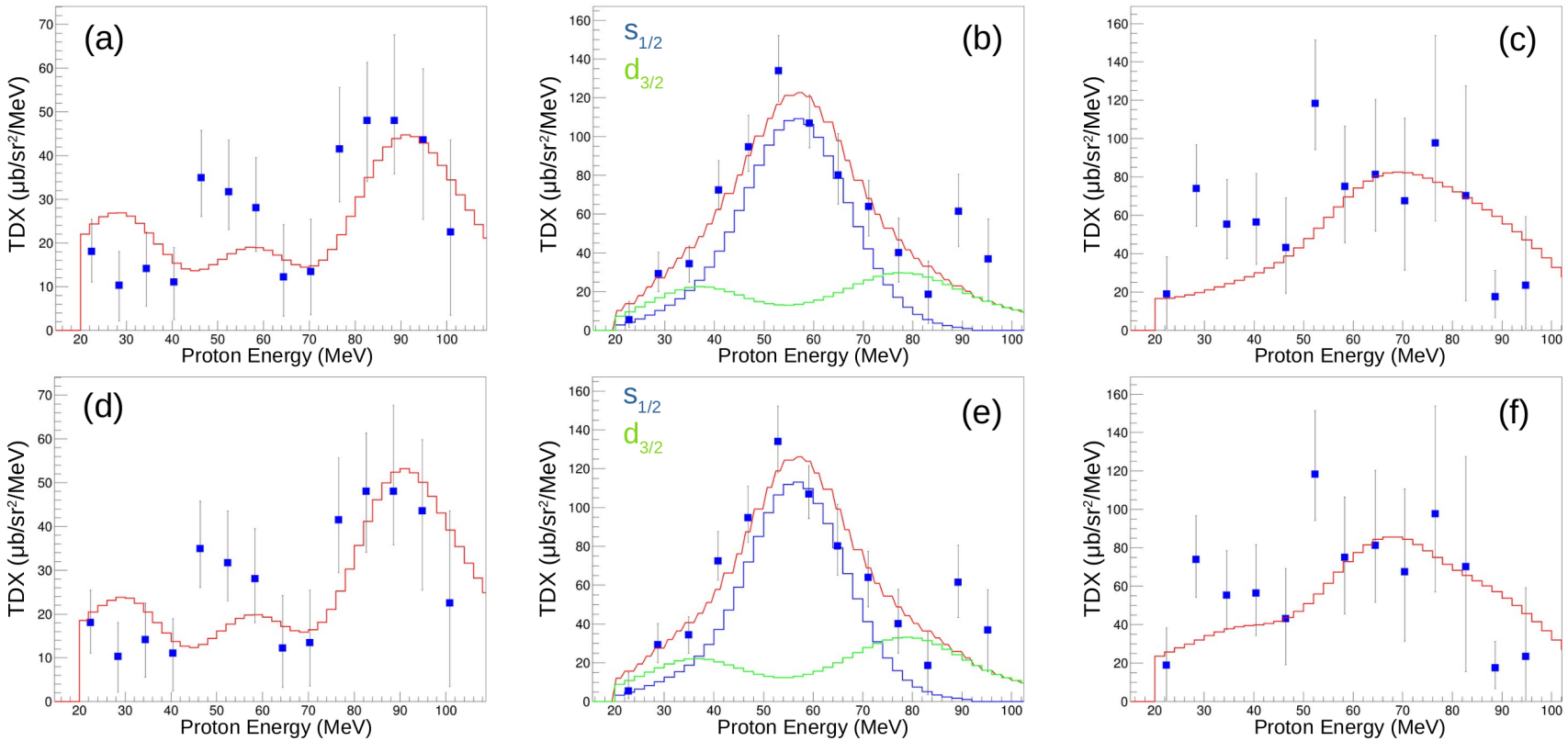

Figure 2.42: The experimental TDX (blue dots) and the theoretical TDX curves for the ^{48}Ca(p,pn) reaction. The neutron knock-out cross sections are shown for the $1f_{7/2}$ orbital (a) and (d), the sd orbitals (b) and (e), and for the $1p$ orbitals (c) and (f). For the sd orbitals, the blue curve shows the $1s_{1/2}$ calculation and the green curve shows the $1d_{3/2}$ calculation, while the red curve is the sum of the two. The calculations were done with the FP (lower panels) and the Dirac (top panels) potentials. The experimental data is extracted from [115].

orbital	TDX_{exp}/TDX_{sp} (FP)	TDX_{exp}/TDX_{sp} (Dirac)
$1f_{7/2}$	11.94(139)	9.48(107)
$2s_{1/2}$	1.09(10)	0.96(9)
$1d_{3/2}$	4.07(92)	3.13(76)
$1p$	22.24(289)	13.36(179)

Table 2.8: The resulting experimental spectroscopic factors, or the ratio between the experimental TDX and the single-particle TDX, for ^{48}Ca with both FP and Dirac potentials.

	Occupation number (n)				n/(2J+1)			
Nucleus	$f_{7/2}$	$p_{3/2}$	$p_{1/2}$	$f_{5/2}$	$f_{7/2}$	$p_{3/2}$	$p_{1/2}$	$f_{5/2}$
^{48}Ca	7.704	0.171	0.023	0.103	0.963	0.043	0.012	0.017
^{52}Ca	7.803	3.857	0.142	0.198	0.975	0.964	0.071	0.033
^{54}Ca	7.809	3.944	1.861	0.385	0.976	0.986	0.931	0.064

Table 2.9: The occupation numbers (n) are given in the columns 2-5 for the neutron orbitals $f_{7/2}$, $p_{3/2}$, $p_{1/2}$, and $f_{5/2}$. The next 4 columns show the occupation numbers normalized to (2J+1). The values are given for the three calcium isotopes, ^{48}Ca, ^{52}Ca, and ^{54}Ca, calculated with the shell-model.

Nucleus	2J+1	E_{ex}	Amp	SF	SF/(2J+1)
^{47}Ca	**8**	**0**	**-2.739**	**7.503**	**0.938**
^{51}Ca	**4**	**0**	**-1.926**	**3.708**	**0.927**
	2	**1.620**	**0.269**	**0.073**	**0.036**
	4	2.956	-0.292	0.085	0.021
	6	3.810	0.156	0.024	0.004
	7	**3.927**	**-2.720**	**7.399**	**0.925**
	8	6.716	-0.378	0.143	0.018
	2	9.030	-0.115	0.013	0.007
	6	12.992	-0.132	0.017	0.003
^{53}Ca	**2**	**0**	**1.365**	**1.862**	**0.931**
	7	**2.124**	**0.385**	**0.148**	**0.025**
	4	**2.394**	**-1.822**	**3.359**	**0.840**

Table 2.10: The spectroscopic factors (SF) calculated with the shell-model. The first column shows the fragments, ^{47}Ca, ^{51}Ca, and ^{53}Ca for the (p,pn) reactions on ^{48}Ca, ^{52}Ca, and ^{54}Ca, respectively. The second column gives the 2*J number of each of the final state of the fragments and the third column gives the excitation energy for each of these final states. The fourth column gives the amplitude, and the square of it gives the spectroscopic factor from the fifth column. In the last column, one sees the spectroscopic factors normalized to (2J+1). The bold rows show the final states that we observe and use in the analysis.

between the results obtained with the two potentials. This is because of the low beam energy used for this experiment. In this study we will keep both values for the comparison, but Dirac describes the data in the case of ^{48}Ca better. The ^{54}Ca experimental cross section and single-particle cross section values are published in Ref. [46] and are used as such.

2.4.9 Spectroscopic factors from Shell Model

Calculations with the shell-model (SM) were carried out by our collaborators, A. Poves and F. Nowacki. The pf-shell part of the PFSDG-U [116] interaction assuming a ^{40}Ca core and a neutron effective charge of 0.46 *e* were used. The occupation numbers predicted by the SM calculations are listed in Table 2.9. They correspond to a neutron shell closure at $N = 32$ in ^{52}Ca.

Calculations were also done for the excitation energies and the spectroscopic factors for the fragments of the (p,pn) reactions on ^{48}Ca, ^{52}Ca, and ^{54}Ca, which are shown in Table 2.10.

From this work, we can obtain *experimental* spectroscopic factors from the ratio between the inclusive cross section and the single-particle cross sections obtained from the DWIA calculations, $\sigma_{-1n}^{exp}/\sigma_{sp}^{DWIA}$. The spectroscopic factors normalized to (2J+1) were compared between the three calcium isotopes and the results are discussed in section 2.6.

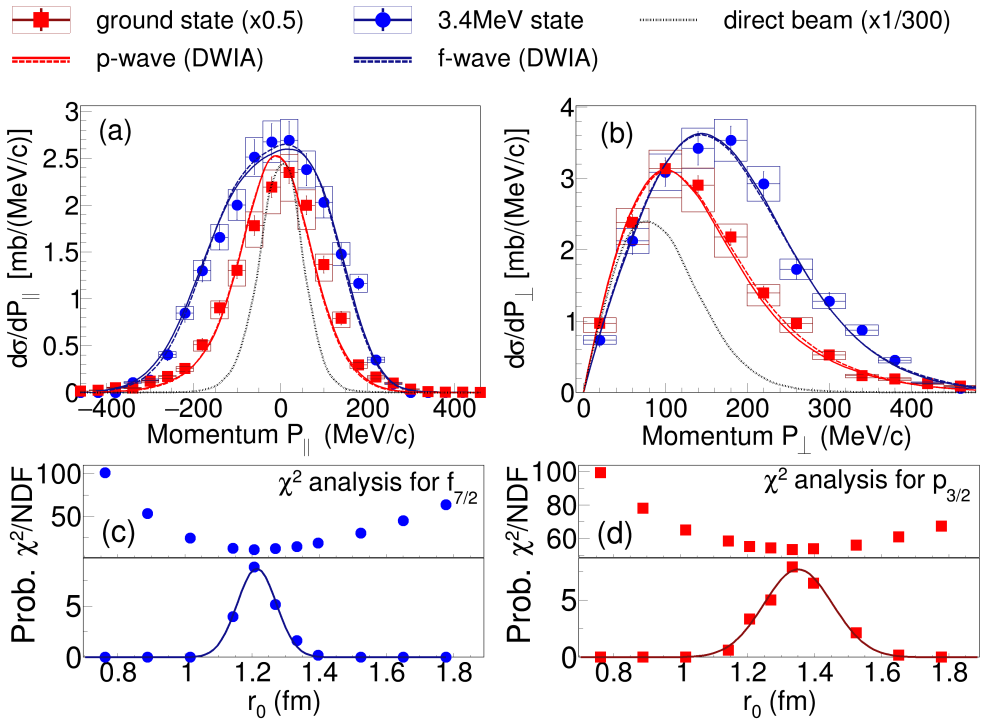

Figure 2.43: Experimental parallel (a) and perpendicular (b) momentum distributions of the ^{51}Ca corresponding to the direct beam (dotted black) and the population of the ground state (red squares) and of the 3453-keV state (blue circles) together with the theoretical curves for p-wave (dashed red) and f-wave (solid blue) with a binning of 40 MeV/c. The statistical errors are marked with crosses and the systematic errors with boxes. The solid lines correspond to the theoretical distributions calculated with the FP potential and the dashed lines with the Dirac potential (see section 2.4.7 for details). The (c) and (d) panels show the reduced χ^2 (upper panels) and the probability distribution (lower panels) for the $f_{7/2}$ and $p_{1/2}$ orbitals as function of the parameter r_0.

2.5 Results for the rms radii of neutron orbitals

The quasi-free scattering reaction at large energies are among the cleanest reactions to study and to calculate theoretically under the sudden approximation and in with the assumption that final state interactions are negligible. The proton in the target knocks out a neutron from the ^{52}Ca beam particle without interacting with the other nuclei, leaving the ^{51}Ca fragment in an excited state, depending on the neutron that was initially knocked-out. Moreover, the momentum of the fragment relative to the beam particle will reflect the very momentum distribution that the knocked-out neutron in ^{52}Ca and as a result, the single-particle wave function of the neutron. The momentum distribution is thus a very powerful experimental tool which can help in studying the neutron orbitals via the (p,pn) reaction. The experimental parallel and perpendicular momentum distributions for the 3453-keV excited state and ground state were extracted and could be compared to the theoretical momentum distribu-

tions. The theoretical shapes were convoluted with the incident energy profile and with the experimental resolution. The theoretical PMDs were fitted to the experimental PMDs with an amplitude as free parameter. The plots in Figure 2.43a and b show the experimental and theoretical PMDs and their agreement confirms the spin-parity assignment of the 3453-keV state and the ground state.
As discussed in section 2.4.1, several theoretical PMDs were calculated for a set of radial parameter values ranging from -40% to +40% relative to the Bohr-Mottelson default value of 1.27 fm. Each theoretical shape was fitted to the experimental PMD and the χ^2/NDF distributions ($\chi^2 = \chi^2_{P_\parallel} + \chi^2_{P_\perp}$) for both $f_{7/2}$ and $p_{3/2}$ neutron orbitals are shown in Figure 2.43c and d, upper panels. In order to transform the χ^2 distribution into a probability distribution the following formula was used:

$$P = C_0 \cdot exp(-\frac{\chi^2}{2})$$

A normalization constant C_0 can be chosen freely. This transformation links the $\chi^2_{min} + 1$ values to $r_0 \pm \sigma$. The obtained probability distribution was fitted with a Gauss function where the amplitude parameter is related to the chosen C_0 normalization constant and is not relevant, but the mean r_0 value will give us the optimum radial parameter for each neutron orbital, together with its 1-σ uncertainty.

The optimal r_0 and associated 1-σ uncertainty for neutron-removal from the $p_{3/2}$ and $f_{7/2}$ orbitals are 1.35(10) fm and 1.21(5) fm, respectively. The correlation of the sp wavefunction rms and the r_0 parameter for both orbitals is plotted in Figure 2.44 with full black circles. The red line is the polynomial interpolation function. The mean r_0 obtained from the χ^2 distribution and probability analysis are marked with vertical solid black lines in both plots, while the vertical dotted grey lines mark the $\pm$1-σ uncertainties. Using the interpolation function, the mean value and $\pm$1-σ values for the rms are found and marked with corresponding horizontal lines. The deduced r_0 values correspond to the rms radii of the single-particle wave-functions of the removed neutron of 4.74(18) fm for $p_{3/2}$ and 4.13(14) fm for $f_{7/2}$.

The single-particle wave-functions were also obtained from Hartree-Fock-Bogolyubov (HFB) using the HFBRAD [114] code and the SKM interaction [117]. The SKM interaction was chosen for its best agreement to experimental data for the proton and matter radii. The rms radii of the single-particle wave-function in this case were found at 4.49 fm for the $p_{3/2}$ orbital and 4.12 fm for the $f_{7/2}$ orbital, the rms radius of $f_{7/2}$ being in perfect agreement with the rms radius obtained with the optimal r_0, while the $p_{3/2}$ radius is underestimated. The HFB rms values are marked with horizontal solid blue lines in Figure 2.44.
The proton, neutron, and matter total density rms radii obtained with HFB calculations with the SKM interaction for ^{52}Ca are 3.46 fm, 3.74 fm, and 3.63 fm, while the values obtained with the Bohr-Mottelson potential, with the original parameters are 3.37 fm, 3.74 fm and 3.60 fm, respectively. Experimental data from isotopic shift measurements situate the charge distribution radius at 3.55 fm [4] and thus the proton rms radius at 3.46 fm [6].
The charge radius for ^{52}Ca is found by Ref. [4] to be "unexpectedly" large which is explained

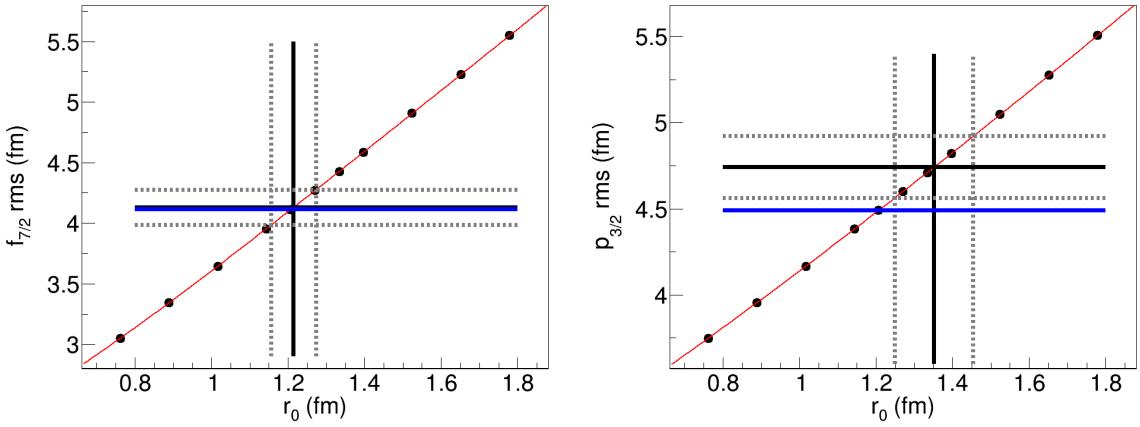

Figure 2.44: The rms-r_0 relation for the $f_{7/2}$ (left) and $p_{1/2}$ (right) orbitals. The red line is a polynomial fit through the calculated points. The vertical black line represents the mean r_0 value found by fitting of the PMDs and the two vertical dotted lines show the $\pm$1-σ interval for r_0. The horizontal solid and dotted lines give the mean and the $\pm$1-σ values for the rms. The blue horizontal line marks the rms value from the HFB calculation.

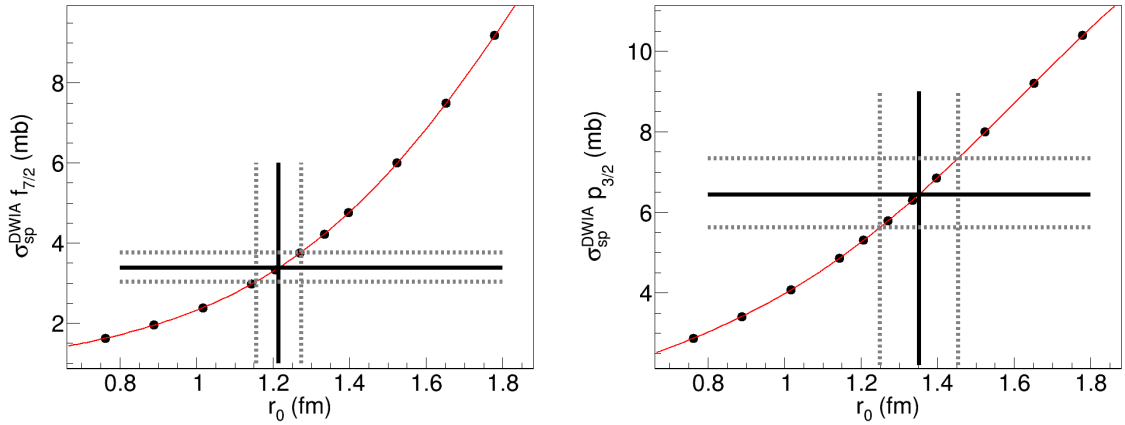

Figure 2.45: The σ_{sp}^{DWIA}-r_0 relation for the $f_{7/2}$ (left) and $p_{1/2}$ (right) orbitals. The red line is a polynomial fit through the calculated points. The vertical black line represents the mean r_0 value found by fitting of the PMDs and the two vertical dotted lines show the $\pm$1-σ interval for r_0. The horizontal solid and dotted lines give the mean and the $\pm$1-σ values for the cross section values obtained for the optimal r_0 parameter vaule.

Table 2.11: Experimental excitation energies (E_{ex}^{exp}) with associated spin-parity assignment (J^{π}) and the experimental cross sections (σ_{-1n}^{th}) using r_0 = 1.21(5) fm, 1.35(10) fm and 1.27 fm (default) for the neutron removal from $f_{7/2}$, $p_{3/2}$ and $p_{1/2}$ orbitals, respectively, are listed in the table below together with the SM prediction for the excitation energies of ^{51}Ca (E_{ex}^{SM}) and spectroscopic factors (C^2S). The theoretical cross sections σ_{-1n}^{th} are calculated using the shell model spectroscopic factors and the DWIA single-particle cross section values, σ_{sp}^{DWIA}.

E_{ex}^{exp} (keV)	J^{π}	-1n	σ_{-1n}^{exp} (mb)	E_{ex}^{SM} (keV)	C^2S	σ_{sp}^{DWIA} (mb)	σ_{-1n}^{th} (mb)
g.s.	$3/2^-$	$p_{3/2}$	30.3(42)	0	3.7	6.5(9)	23.9(32)
1720(25)	$(1/2^-)$	$p_{1/2}$	0.6(3)	1.620	0.1	4.8	0.5
3453(20)	$7/2^-$	$f_{7/2}$	22.3(24)	3.927	7.4	3.4(4)	25.0(27)

by the "pronounced halo nature" of the $p_{3/2}$ and $p_{1/2}$ orbitals, 0.7 fm larger than the rms radii of the $f_{5/2}$ and $f_{7/2}$ orbitals proposed by Ref. [7]. The rms radii difference between the $p_{3/2}$ orbital and the $f_{7/2}$ orbital obtained by the present analysis is 0.61(23) fm, in agreement with this prediction.

The calculated single-particle neutron knock-out cross sections with the Bohr-Mottelson original parametrization, $r_0 = 1.27$ fm, are 5.78 mb ($p_{3/2}$), 3.75 mb ($f_{7/2}$), and 4.82 mb ($p_{1/2}$). Using the same r_0 sensitivity study the values and associated uncertainties of 6.45(86) mb and 3.38(36) mb were found for $p_{3/2}$ and $f_{7/2}$ orbitals, respectively. The single-particle cross sections are listed in Table 2.11.

2.6 Results on the N=32 shell closure

The neutron knock-out cross sections obtained from this experiment are shown in the Table 2.11 for the $f_{7/2}$, $p_{3/2}$, and $p_{1/2}$ neutron orbitals. In the same table one finds the spectroscopic factors and the excitation energies in ^{51}Ca populated via (p,pn) from shell-model calculations. The theoretical single-particle neutron knock-out cross sections from DWIA are listed in the table as well and the theoretical cross sections are calculated as $\sigma_{-1n}^{th} = C^2S \cdot \sigma_{sp}^{DWIA}$.

The experimental neutron-knockout cross sections agree within 2-σ uncertainty with the total theoretical cross sections. The experimental results for the cross section corresponding to the $f_{7/2}$ and $p_{3/2}$ orbitals are much larger than the value obtained for $p_{1/2}$. This is in agreement with the neutron shell closure at $N = 32$. Moreover, the shell-model predictions for the spectroscopic factors show the same pattern, values close to the maximum admitted $(2J + 1)$ value for the knock-out of a $f_{7/2}$ or $p_{3/2}$ neutron and very small spectroscopic factor for $p_{1/2}$.

For a systematic comparison among the three calcium isotopes, ^{48}Ca, ^{52}Ca, and ^{54}Ca, we choose to use the ratio between the experimental neutron knock-out cross section and the the-

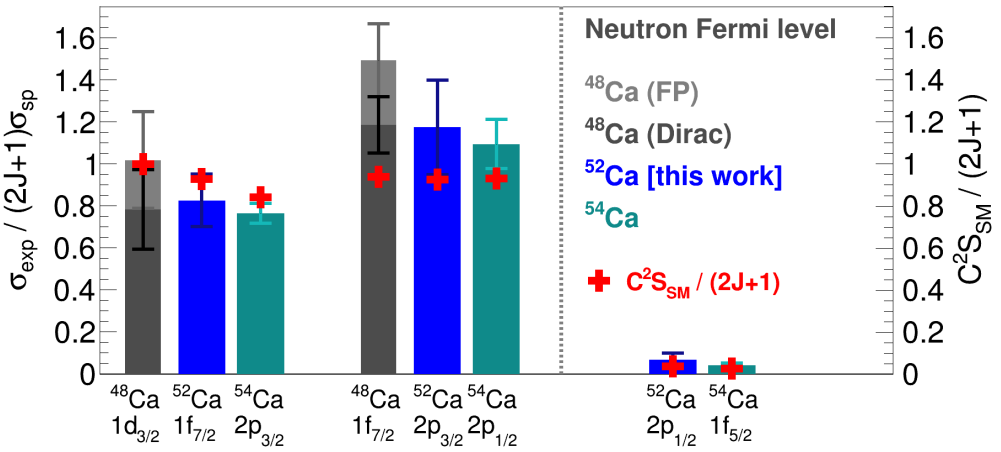

Figure 2.46: The ratio of experimental neutron knock-out cross sections and theoretical single-particle cross sections normalized to $(2J+1)$ for ^{48,52,54}Ca (grey, blue and turquoise bars, respectively) below and above the corresponding shell closure. The error bars contain experimental cross section uncertainties and, for ^{52}Ca, theoretical uncertainties from the r_0 sensitivity study. The C^2S from SM calculations are plotted with red crosses. Figure published in [9]© CC-BY-4.0.

oretical single-particle cross section, normalized to $(2J+1)$: $R_S = \sigma^{exp}_{-1n}/[(2J+1)\sigma^{DWIA}_{sp}]$. For this comparison the experimental data for ^{48}Ca comes from Ref. [115], while for ^{54}Ca from Ref. [46]. The theoretical single-particle cross sections for ^{52}Ca are calculated with the following radial parameters: 1.21(5) fm, 1.35(10) fm (optimum r_0 radial parameter from the PMDs analysis) and 1.27 fm (default) for the neutron removal from $f_{7/2}$, $p_{3/2}$ and $p_{1/2}$ orbitals, respectively. For $^{48 \text{ and } 54}$Ca the default Bohr-Mottelson parametrization was used for the Woods-Saxon potential in the calculation of the single-particle cross sections. For ^{48}Ca the calculations were done with both a folding potential and Dirac phenomenology. The calculations with the Dirac phenomenology is more appropriate for the energy range of the experimental data set for the well-established doubly-magic nucleus, ^{48}Ca. For $^{52 \text{ and } 54}$Ca only the results with the folding potential are shown. Details about the calculation of the single-particle neutron-knockout cross sections are given in Section 2.4. The R_S values, equivalent to "experimental spectroscopic factors", are plotted in Figure 2.46 together with the theoretical spectroscopic factors from the shell-model. On the x-axis, the values corresponding to each neutron orbital were shifted such that the neutron shell closures at $N = 28$, $N = 32$, and $N = 34$ are aligned.

In this plot one immediately observes a similar pattern for all three calcium isotopes: large R_S values before the neutron Fermi level and very little cross section above the neutron Fermi level. This is a direct result of the energy gap after each shell closure. The theoretical spectroscopic factors give values of about 90% of $(2J+1)$ below the shell closure and very small values after the shell closure, in agreement to the experimental results. These results place ^{52}Ca among the doubly-magic calcium isotopes and confirm the shell closure at $N = 32$.

2.7 Conclusions and further prospects

Experimental data for ^{52}Ca(p,pn)^{51}Ca from the SEASTAR3 campaign taking place at the RIBF, RIKEN facility in Japan were analyzed. The experimental setup consisted of MINOS, a liquid hydrogen target of 15 cm in length with a TPC (Time projections chamber), MINOS, placed around the target for the proton tracking. The identification of the beam particles was done using BigRIPS and the fragments were separated and identified in the SAMURAI experimental area. The final states of the fragments were tagged via γ-ray spectroscopy using DALI2^{+}. Additional neutron detectors NeuLAND and NEBULA were used for removing non-(p,pn) events and ensuring a clean data selection.
Exclusive cross section values are obtained corresponding to the knock-out of a $f_{7/2}$, $p_{3/2}$ or $p_{1/2}$ neutron from ^{52}Ca, as well as exclusive momentum distribution. DWIA calculations for single-particle neutron knock-out cross section and momentum distributions were performed, as well as Shell model calculations for the spectroscopic factors. The results of this study show that the $N = 32$ shell closure in ^{52}Ca is as strong as the $N = 28$ and $N = 34$ in neutron-rich Calcium isotopes. Moreover, using the momentum distribution analysis, the rms radius values of 4.13(14) fm and 4.74(18) fm were obtained for the $f_{7/2}$ and $p_{3/2}$ neutron single-particle orbitals. These results lead to a 0.61(23) fm difference in size between the p and f neutron orbitals, result which is in agreement with the prediction from Ref.[7]. This difference between the p and f orbitals explains the large matter and charge radii observed in the neutron-rich K and Ca isotopes as one starts filling the $p_{3/2}$ neutron orbital [4–6]. The results presented in this chapter were recently published: [9].

This study was the first one giving an insight on the size of the neutron single-particle orbitals in this region of the nuclear chart and proved the capability of doing this using the momentum distribution analysis. Still, this first study requires further work to validate the method. As a first step in that direction, we propose to systematically apply this method to other nuclei. A dedicated experiment on C and O isotopes has been proposed and approved at the RIBF facility. In the following chapter, we present the data analysis of ^{53}Ca and ^{54}Ca (p,pn) reactions, focused on the momentum distribution analysis and the determination of the rms radii of neutron single-particle orbitals in a similar manner as presented in this chapter for the ^{52}Ca(p,pn) case.

3 Momentum width analysis for neutron single-particle rms radii in the pf-shell

3.1 Neutron knock-out reaction from ^{53}Ca and ^{54}Ca

As a continuation of the analysis performed for the determination of rms radii of ^{52}Ca via the (p,pn) reaction, the rms radii determination of of neutron single-particle orbitals in ^{53}Ca and ^{54}Ca is presented in this chapter. The data set is part of the same experiment as the ^{52}Ca(p,pn) reaction presented in the previous chapter. The analysis method is using the experimental momentum distributions from the quasi-free neutron knockout reaction coupled with DWIA calculations for the theoretical momentum distribution curves. The rms radii for the $p_{3/2}$, $p_{1/2}$, $f_{7/2}$ and $f_{5/2}$ neutron single-particle orbitals can be determined and the results can prove if the rms radii determination using the momentum distribution analysis method can give consistent results. Additionally, the level scheme of ^{52}Ca was studied using γ-ray spectroscopy, including γ-γ coincidence measurements, and momentum distribution measurements for spin assignments. Shell model calculations were also used for the construction of the level scheme of ^{52}Ca. The DWIA and shell-model calculations were performed by our collaborators K. Ogata, F. Nowacki, A. Poves and K. Yoshida as presented in the previous chapter.

3.2 Channels selection and kinematics

The same data analysis methods are used for the ^{53}Ca(p,pn)^{52}Ca and ^{54}Ca(p,pn)^{53}Ca reactions as described in the previous chapter for ^{52}Ca(p,pn)^{51}Ca. The presented particle identification procedures of the beam and the fragment are valid for all involved nuclei with some small adjustments. One of the modifications includes the magnetic rigidity and flight length functions for the fragment particles as they travel through the SAMURAI magnet obtained from the GEANT4 simulations which were previously calculated for ^{51}Ca fragments and needed to be adjusted for the ^{52}Ca and ^{53}Ca fragments. The separation power achieved for the calcium isotopes in the BigRIPS and SAMURAI separators are listed in Table 3.1.

The (p,pn) channel selection was done imposing a 2-dimensional 4-σ cut on Z and A/Q for the beam and fragment particles and imposing the detection of one proton in the MINOS TPC. A clean selection was achieved with no contamination from other channels. Additionally, a condition for the reconstructed vertex position to have values within the physical target area,

	^{53}Ca(p,pn)^{52}Ca	^{54}Ca(p,pn)^{53}Ca
Reacted events	84149	37252
Unreacted events	4008009	2307635

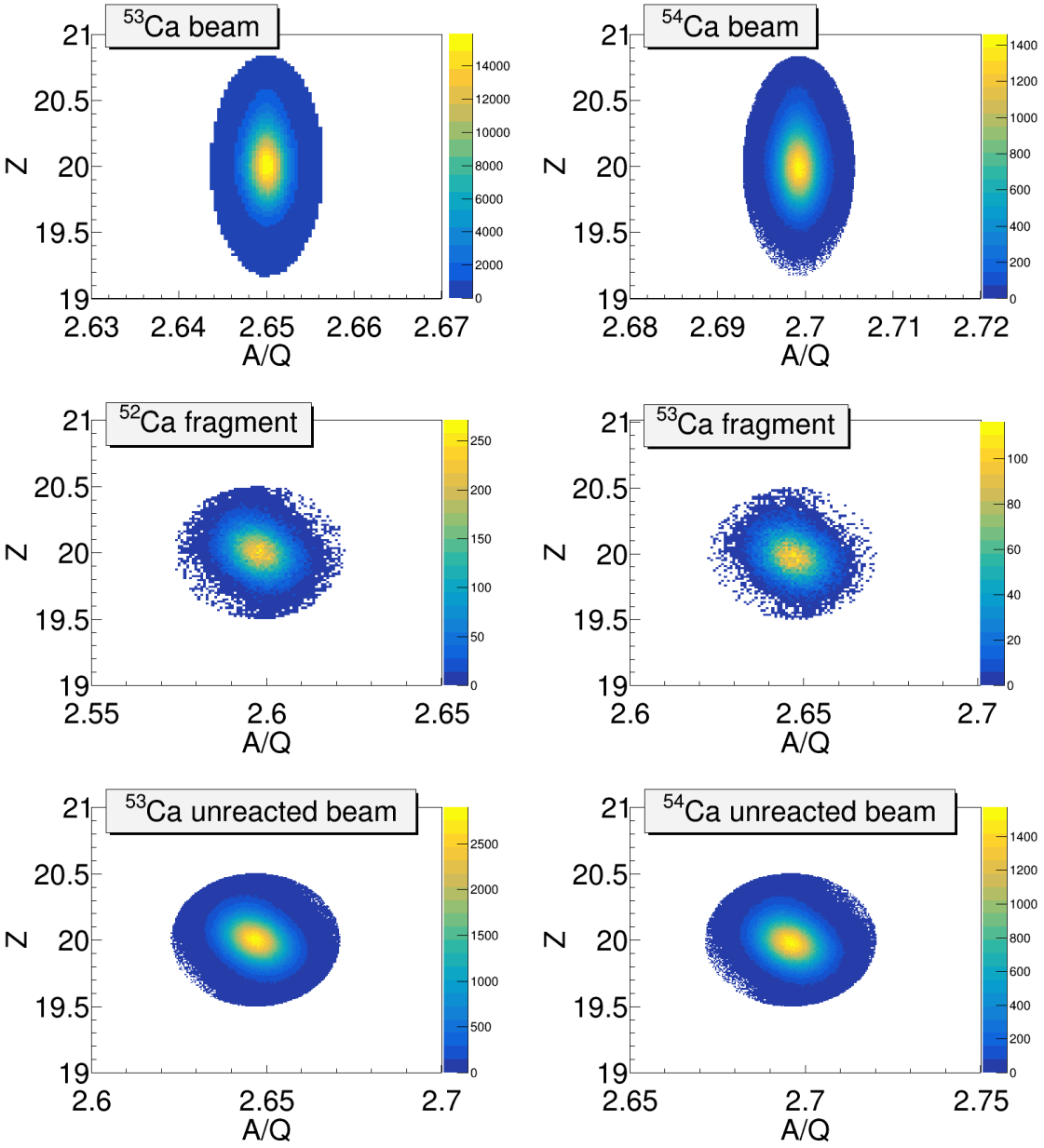

Figure 3.1: Particle identification for the beam and fragments of the ^{53}Ca(p,pn) (left) and ^{54}Ca(p,pn) (right) reactions. The top row shows the beam particles identified in BigRIPS. The middle row shows the fragments of the (p,pn) reactions identified in SAMURAI. The bottom row shows the unreacted beam identified in SAMURAI. The table shown at the top of this figure gives the number of events found in the two reaction channels.

Beam PID in BigRIPS	separation for Z	separation for A/Q
^{52}Ca	4.8 σ	31.4 σ
^{53}Ca	4.8 σ	31.9 σ
^{54}Ca	4.8 σ	31.6 σ

Fragment PID in SAMURAI	separation for Z	separation for A/Q
^{51}Ca	7.2 σ	8.1 σ
^{52}Ca	7.1 σ	8.2 σ
^{53}Ca	7.1 σ	8.2 σ

Table 3.1: The separation power for the beam and fragment particles in BigRIPS (left table) and SAMURAI (right table) for calcium isotopes obtained by this analysis.

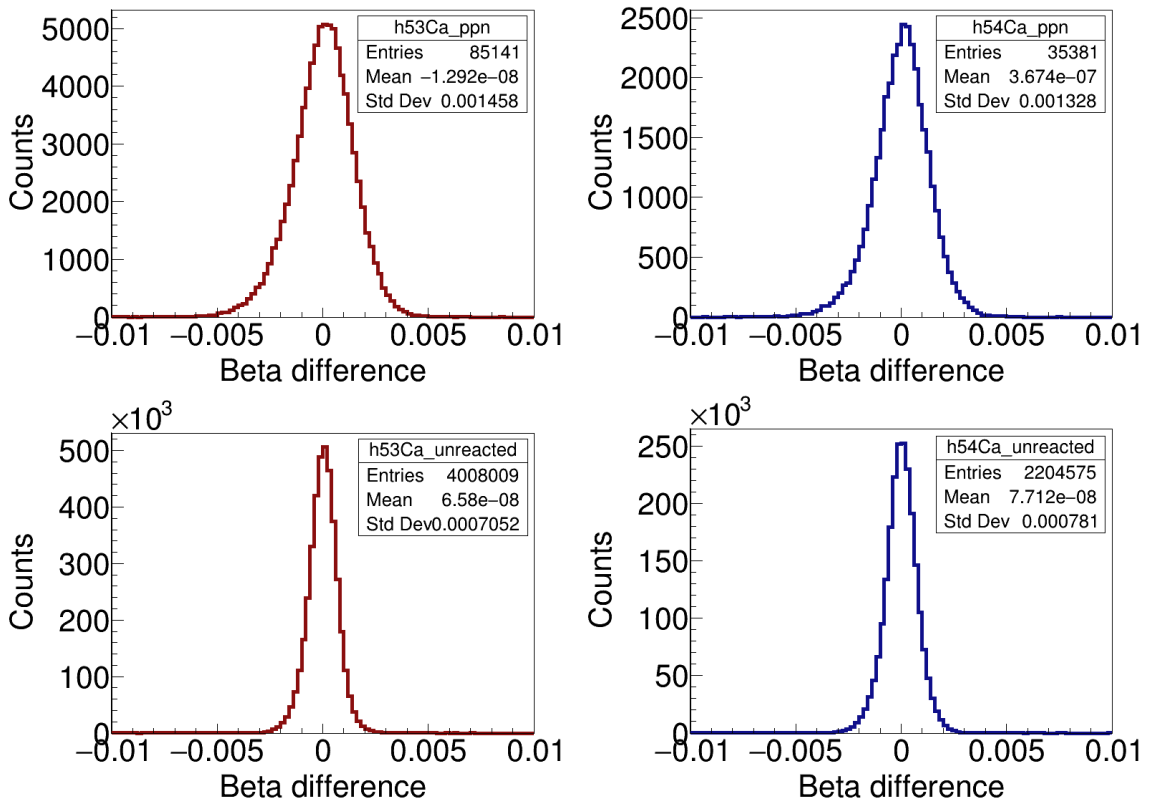

Figure 3.2: Kinematic checks for the beam and fragment velocities for the ^{53}Ca(p,pn) (left) and ^{54}Ca(p,pn) (right) reactions. The top row shows the beta difference distribution for the (p,pn) events and the bottom row shows the beta difference distribution for the unreacted beam events. All plots show a good kinematic matching, the distributions are centered close to zero beta difference values.

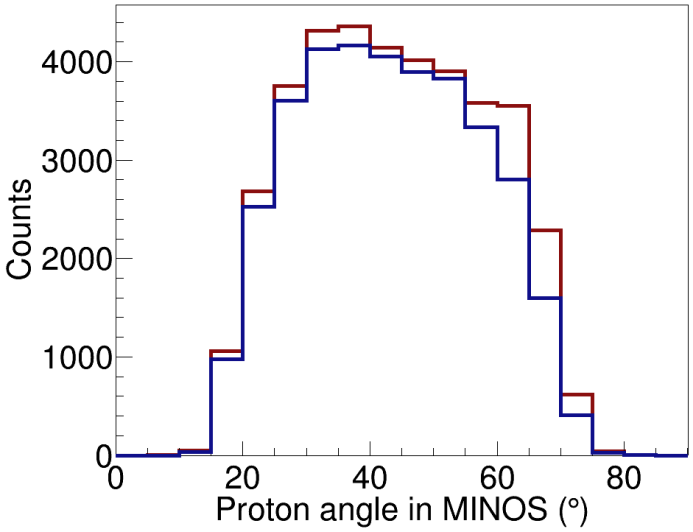

Figure 3.3: The distribution of the proton angle detected by the MINOS TPC plotted for the ^{53}Ca(p,pn) (dark red, rescaled x0.45) and the ^{54}Ca(p,pn) (dark blue) reaction channels.

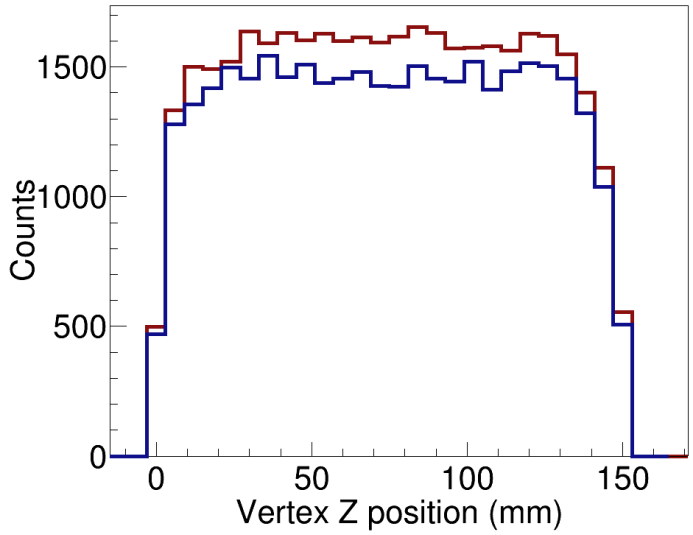

Figure 3.4: The distribution of the vertex position along the Z-axis plotted for the ^{53}Ca(p,pn) (dark red, rescaled x0.45) and the ^{54}Ca(p,pn) (dark blue) reaction channels. The events with the reaction vertex between 0 and 151 mm are selected.

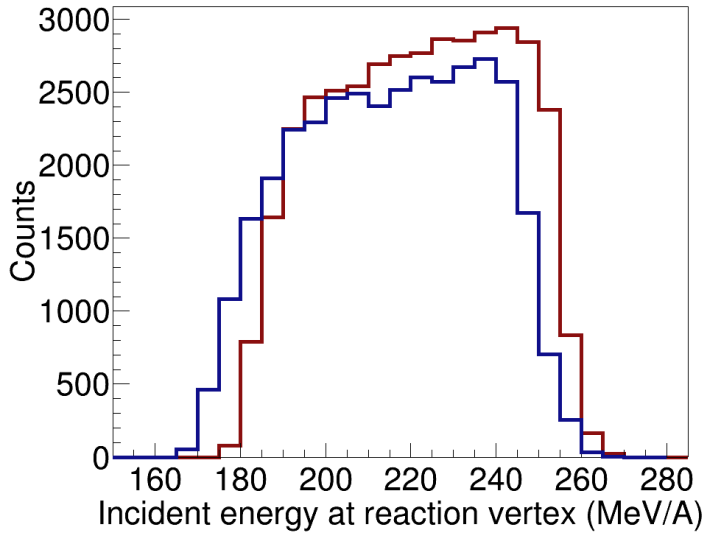

Figure 3.5: The incident energy distribution at the reaction vertex position within the liquid hydrogen target for the (p,pn) reactions from ^{53}Ca (dark red, rescaled x0.45) and ^{54}Ca (dark blue).

from Z=0 to Z=151 mm was imposed, the beam to be within a 15-mm radius spot on the target window, and that the beam and proton tracks have a distance of maximum 10 mm for the vertex reconstruction. For the ^{53}Ca(p,pn)^{52}Ca reaction 8.4 10^4 events were found obeying the conditions mentioned above while for ^{54}Ca(p,pn)^{53}Ca a total of 3.7 10^4 events were found. Plots with the identified beam, the unreacted fragment and the reacted fragment particles for both ^{53}Ca(p,pn) and ^{54}Ca(p,pn) channels are shown in Figure 3.1.

After the PID of beam and fragment, additional kinematic checks were performed. The matching between velocities of the beam and the fragment at the reaction vertex was checked and plots are shown in Figure 3.2 for the (p,pn) events and for the unreacted beam. The proton angle, as well as the vertex position within the liquid hydrogen target are plotted for both reactions in Figures 3.4 and 3.3. The incident energy at the reaction vertex ranges between ∼170-270 MeV/nucleon for ^{53}Ca(p,pn)^{52}Ca and ^{54}Ca(p,pn)^{53}Ca reactions as shown in Figure 3.5.

3.3 Inclusive momentum distributions

The experimental setup presented in section 2.1 allows for the determination of complete kinematics of the beam and fragment particles. Section 2.3.9 describes the data analysis for extracting the momentum distributions. The parallel and the perpendicular components of the fragment momentum relative to the beam (with Lorenz boost correction) are extracted knowing the full kinematics at the reaction vertex of both the beam and the fragment. They are plotted in Figure 3.6.

For the events with unreacted beam, the momentum distributions reflect the resolution containing all contributions except for the uncertainty coming from the vertex position. The momentum resolution values extracted from the unreacted beam events are listed in Table 3.2. In this table, one finds the momentum resolution obtained for the ^{52}Ca(p,pn)^{51}Ca reaction channel for comparison. One observes similar values for the momentum resolution for all three reaction channels. Nevertheless, the resolution for the ^{54}Ca(p,pn)^{53}Ca reaction channel turns out to be slightly worse. The momentum distributions for the unreacted beam are shown as well in Figure 3.6 with dotted lines. A simulation is performed for evaluating the contribution to the resolution of the vertex position uncertainty. The vertex position uncertainty is propagated to the distances in which the beam and fragment particles loose energy inside the target. This uncertainty is further translated into an uncertainty for the velocities and implicitly for the momentum distributions. This contribution to the resolution was evaluated as: 1.8 MeV/c (1.7MeV/c) for the parallel momentum distribution and 9.6 MeV/c (9.7MeV/c) for the perpendicular momentum distribution, for the ^{53}Ca(p,pn) (^{54}Ca(p,pn)) reaction.

The momentum distributions corresponding to the neutron evaporation channel are plotted in Figure 3.6 with dashed lines in order to show how they contribute to the total inclusive momentum distributions. These are plotted without a correction for the neutron-detection efficiency. For the parallel momentum distributions, the neutron evaporation channel contributes

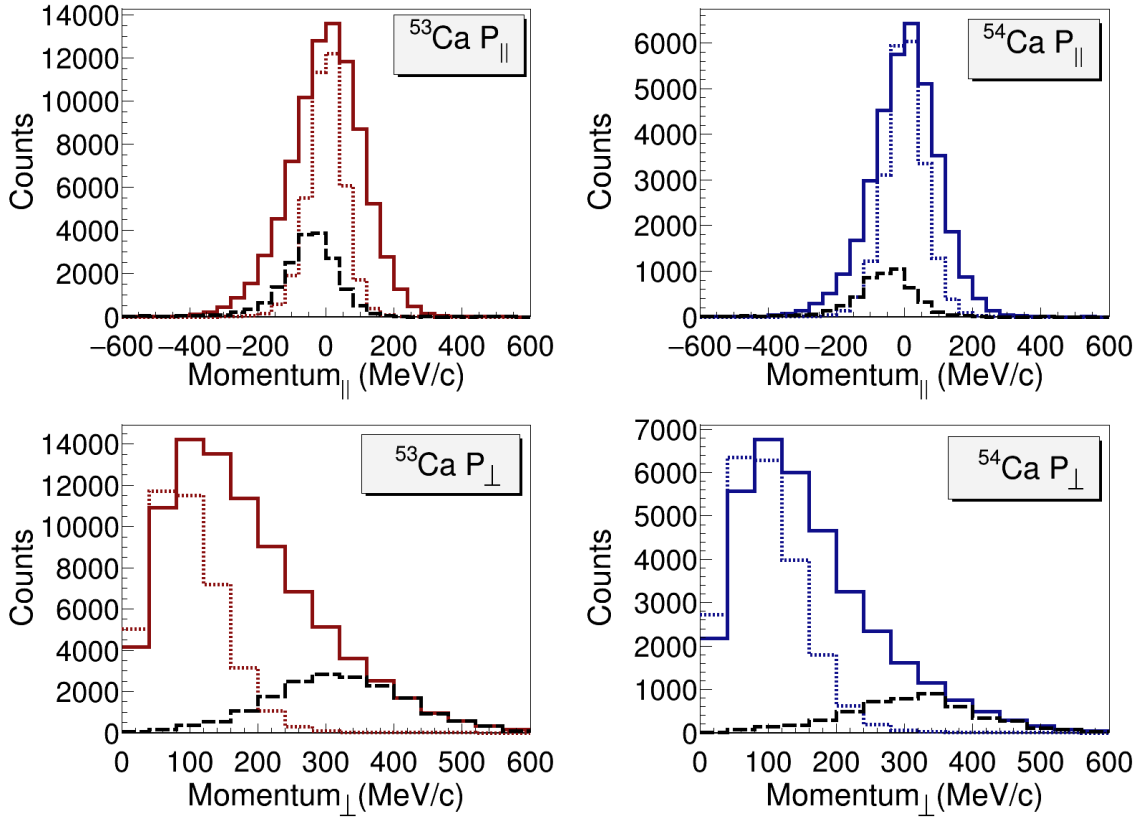

Figure 3.6: Inclusive momentum distributions for the ^{53}Ca(p,pn) (left) and ^{54}Ca(p,pn) (right) reactions (solid lines). The parallel component of the momentum distribution is plotted in the top row, while the perpendicular component of the momentum distribution is plotted on the bottom row. The dotted curves show the momentum distribution of the unreacted beam (rescaled x0.01). The black dashed lines show the neutron evaporation contribution to the total momentum distribution (rescaled x5), not corrected for the neutron-detection efficiency. A binning of 40 MeV/c is used for all plots.

Momentum resolution	^{52}Ca(p,pn)^{51}Ca	^{53}Ca(p,pn)^{52}Ca	^{54}Ca(p,pn)^{53}Ca
Parallel (z)	non-Gauss σ = 49.5 MeV/c RMS = 52.0 MeV/c	non-Gauss σ = 47.8 MeV/c RMS = 53.2 MeV/c	non-Gauss σ = 52.5 MeV/c RMS = 59.5 MeV/c
Perpendicular (x)	σ = 76.9 MeV/c	σ = 77.6 MeV/c	σ = 78.5 MeV/c
Perpendicular (y)	σ = 75.7 MeV/c	σ = 77.0 MeV/c	σ = 77.7 MeV/c

Table 3.2: Table with the experimental momentum resolution values for the parallel (z) and perpendicular (x and y) components. The resolution is obtained from the unreacted ^{53}Ca and ^{54}Ca beam. An additional small contribution to the momentum resolution comes from the reaction vertex uncertainty which is not included in the unreacted beam momentum, see text for details. For comparison, the momentum resolution from the ^{52}Ca unreacted beam was included in the table, more details about the ^{52}Ca(p,pn)^{51}Ca momentum distribution analysis are found in section 2.3.9.

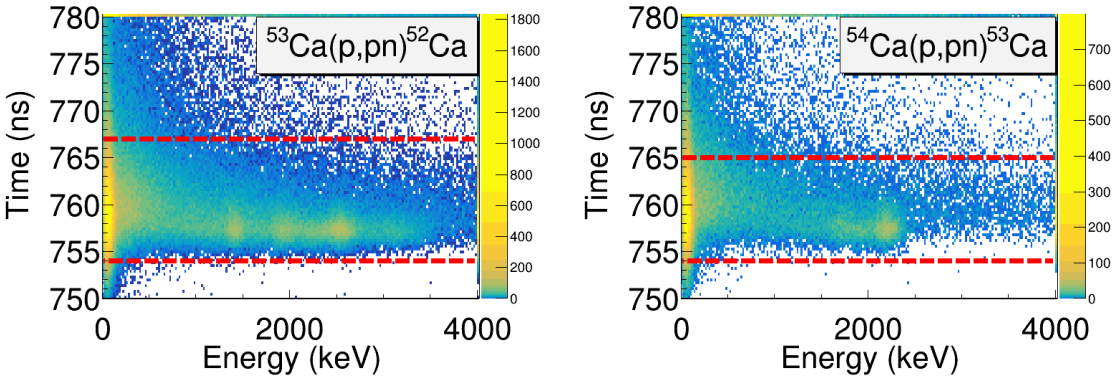

Figure 3.7: The timestamp distribution of the γ-ray spectra for the ^{53}Ca(p,pn) and ^{54}Ca(p,pn) reaction channels. The dashed red lines show the cuts in the γ-particle timestamp difference imposed for the analysis of the γ-ray spectra.

in the left side of the distribution with a small offset from the center, while for the perpendicular momentum component, it contributes to high values. Similar to the momentum distribution analysis for the ^{52}Ca(p,pn) reaction, one needs to discard the neutron-evaporation contribution to the momentum distributions from the (p,pn) channel. A separation of these events can be done by imposing a cut for the proton angle as seen in Figure 2.36. The cut was done at $\theta_{proton} = 57°$ for both for ^{53}Ca(p,pn) and ^{54}Ca(p,pn) reactions. With this cut, only 0.31% and 0.25% for the ^{53}Ca(p,pn) and ^{54}Ca(p,pn) reactions, respectively, of the events contributing to the momentum distribution plots belong to the neutron-evaporation channel.

3.4 Gamma spectroscopy

3.4.1 Shell Model calculations for ^{52}Ca

For helping to identify the energy levels of ^{52}Ca and assign the spin-parity, shell model calculations were performed for the energy spectrum of ^{52}Ca and spectroscopic factors for neutron knockout from ^{53}Ca ($1/2^-$, g.s.). The calculations were performed by our collaborator A. Poves, using the pf-shell part of the PFSDG-U [116] interaction and assuming a ^{40}Ca core. The energy spectrum for ^{52}Ca and the occupation numbers for each state predicted by the shell model calculations are listed in Table 3.3. The resulting spectroscopic factors are also shown in Table 3.3.

3.4.2 Analysis of the γ-ray spectra

Gamma spectroscopy was used for identifying the final states of the fragment particles after the (p,pn) reaction. The data from the DALI2$^+$ γ-ray detection array, presented in section 2.1, was analysed as described in section 2.3.4. The raw γ-ray energy spectra were calibrated in

		Occupation Numbers for ^{52}Ca				Spectroscopic Factors from ^{53}Ca(1/2$^-$, g.s.)			
J^π	E_{exc} (keV)	$f_{7/2}$	$p_{3/2}$	$f_{5/2}$	$p_{1/2}$	$f_{7/2}$	$p_{3/2}$	$f_{5/2}$	$p_{1/2}$
0_1^+	0	7.891	3.899	0.109	0.102				0.946
2_1^+	2381	7.907	2.955	0.134	1.004		2.298		
1_1^+	2978	7.866	3.012	0.192	0.930		1.331		
0_2^+	4115	7.793	2.171	0.429	1.606				0.034
3_1^+	4492	7.901	2.931	1.075	0.093	0.023		0.007	
1_2^+	4630	7.894	2.948	1.051	0.106		0.042		0.001
4_1^+	4751	7.899	2.950	1.065	0.086	0.042			
2_2^+	4918	7.850	2.418	0.819	0.914				
2_3^+	5355	7.868	2.544	0.807	0.780		0.112	0.001	
4_2^+	6400	7.000	4.000	0	1.000	4.120			
3_3^+	6730	7.400	3.000	0.600	1.000	1.634			
3_4^+	6860	7.400	3.000	0.600	1.000	1.708			

Table 3.3: Shell model calculations for the energy spectrum and the occupation numbers of ^{52}Ca as well as the spectroscopic factors for neutron knockout from ^{53}Ca (1/2$^-$, g.s.). The first two columns indicate the spin-parity (J^π) and the energy (E_{exc}) of each state. The next four columns show the occupation numbers for the p and f neutron orbitals. The last four columns show the spectroscopic factor for the neutron knockout from the p and f neutron orbitals.

energy and timestamp, an add-back correction was applied (12 cm range), and then they were corrected for the Doppler shift. No correlation of the γ-ray energy was observed with respect to the velocity of the fragment, the vertex position, or the angle of the emitter γ ray. The timestamp distribution of the γ-ray spectrum is plotted in Figure 3.7 for both ^{53}Ca(p,pn) and ^{54}Ca(p,pn) reaction channels. Based on these plots, a particle-γ time window was imposed for all spectra. The selected time window is marked with dashed red lines in Figure 3.7: [754,767] ns for ^{53}Ca(p,pn) and [754,765] ns for ^{54}Ca(p,pn).

Figure 3.8 shows the γ-ray spectra for both reaction channels only with the Doppler-shift correction (blue curves) as well as with add-back correction (red curves). At a first glimpse, the ^{53}Ca(p,pn)^{52}Ca spectrum has three main peaks, at 1.4 MeV, 1,9 MeV and 2.5 MeV. After the add-back correction, a wide peak is observed at the energy of 3-3.3 MeV as well. For the

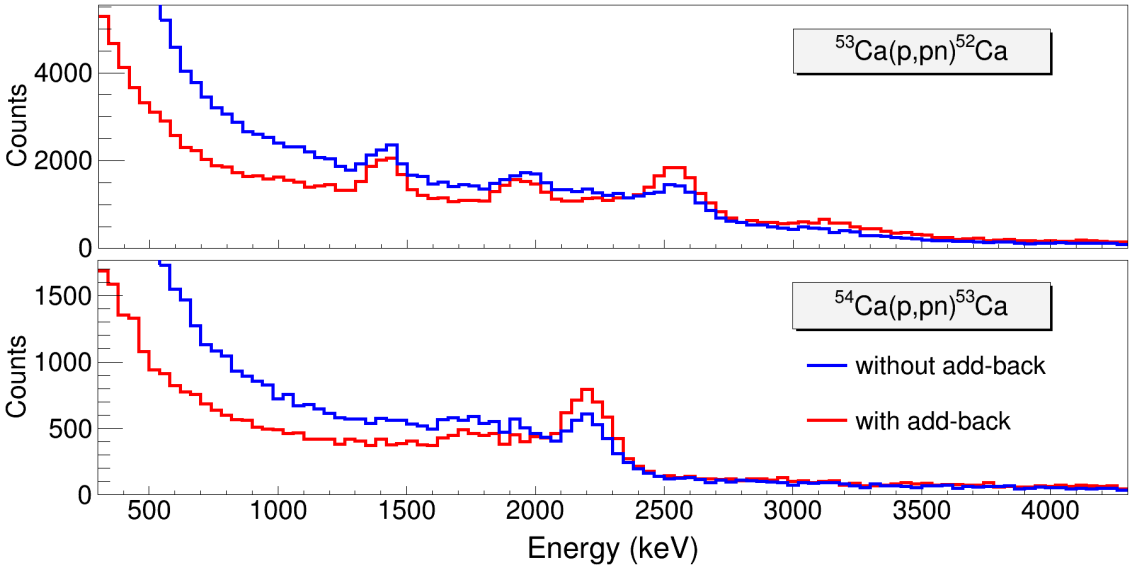

Figure 3.8: The analysed γ-ray spectra for the ^{53}Ca(p,pn) and ^{54}Ca(p,pn) reaction channels. The γ-ray spectra were corrected for the Doppler-shift (blue curves) and also add-back correction was applied (red curves). A binning of 40 keV was used for all plots.

^{54}Ca(p,pn)^{53}Ca reaction a strong peak at 2.2 MeV is visible as well as a very weak peak at 1.7 MeV γ-ray energy. The add-back correction successfully increases the full-energy peaks and lowers the Compton components in both spectra.

3.4.3 Energy level scheme of ^{52}Ca

The energy of the γ-ray transitions was determined by fitting the ^{53}Ca(p,pn)^{52}Ca γ-ray spectrum with the response functions of the DALI2+ detector array as shown in section 3.4.4. For each transition, the response function was shifted in a range of $\pm$100 keV and the position corresponding to the minimum χ^2 value was determined. Using the distribution of the χ^2 values as a function of the peak position, one could also obtain, aside form the peak position, the uncertainty (1-σ value $\leftrightarrow\chi^2+1$) for each transition. The obtained peak positions and the corresponding uncertainties are: 552(10) keV, 1426(12) keV, 1951(19) keV, 2563(10) keV, 3150(41) keV, and 3388(53) keV. The peak positions determined from this work and literature experimental values from Refs. [2, 45, 101, 103] are listed in listed in Table 3.4. The literature values are more precise than what can be achieved with the high-efficiency DALI2+ array. A transition which is not found in literature, but observed in this study is the one at 552(10) keV.

In order to construct the level scheme of ^{52}Ca, one can look at the γ-ray transitions in coincidence with all reaction channels leading to ^{52}Ca. With the increased statistics from all the contributing reaction channels, one can obtain information about γ-γ coincidences which

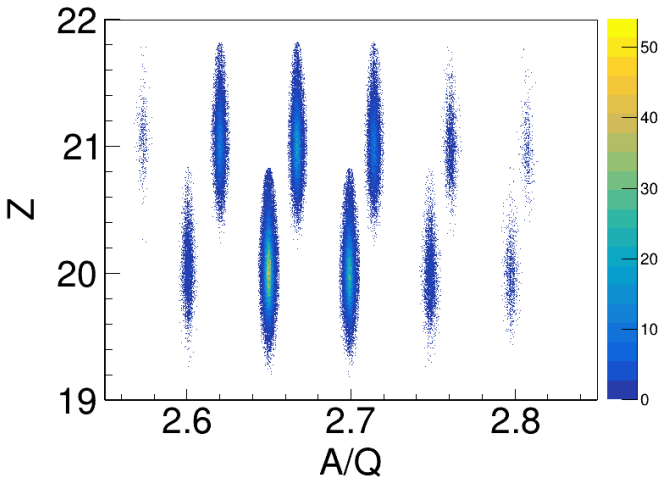

Figure 3.9: The beam PID for (p,pXn)^{52}Ca and (p,2pXn)^{52}Ca reactions. One identifies the calcium isotopes (Z=20, A=52-56) and the scandium isotopes (Z=21, A=54-59) for the two types of reactions.

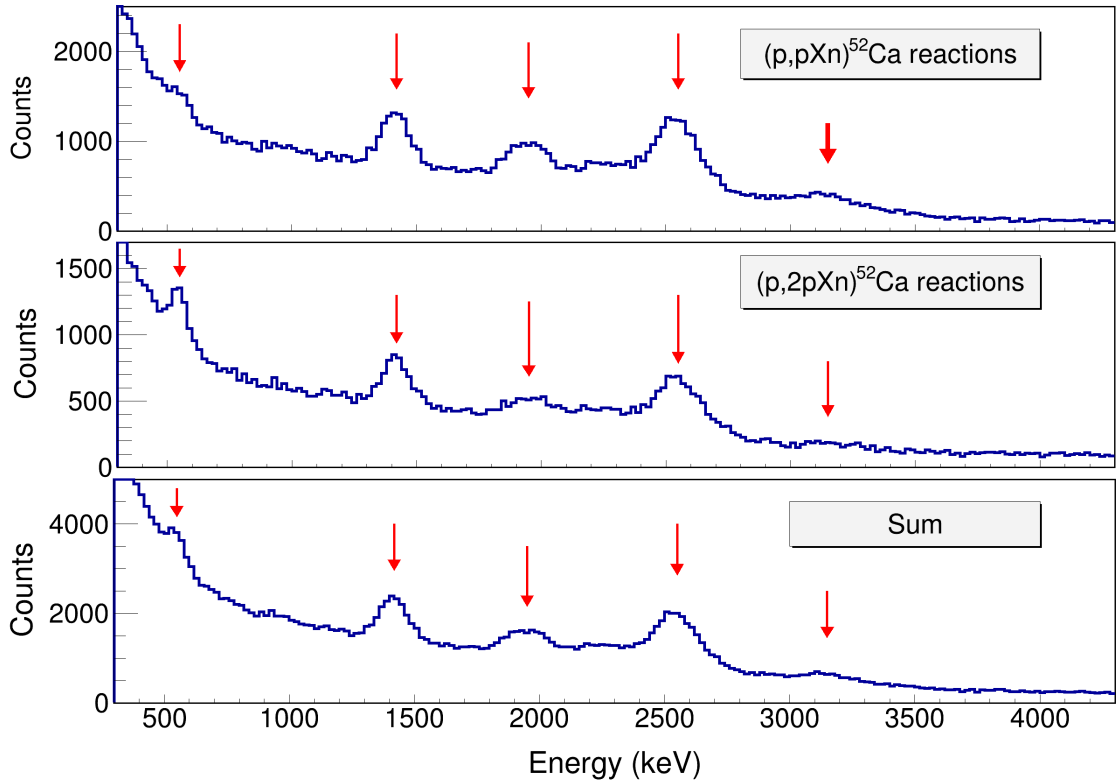

Figure 3.10: The γ-ray spectra for ^{52}Ca corresponding to all possible reaction channels. Top plot: from reactions of the type (p,pXn). Middle plot: from reactions of the type (p,2pXn). Bottom plot: from both types of reactions. All spectra have a binning of 20 keV. The peaks of interest are marked with red arrows.

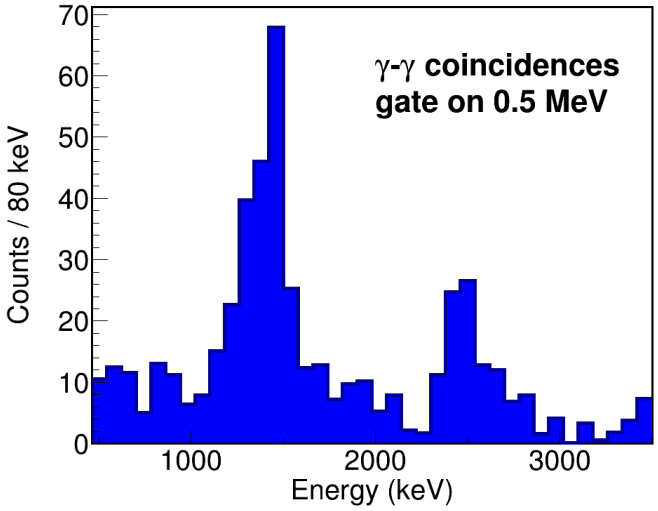

Figure 3.11: Gamma-gamma coincidence spectrum gated on the 0.5 MeV transition. The events from (p,2pXn)-type of reactions were used for this plot. The 0.5 MeV transition appears in coincidence with the transitions at 1.4 MeV and 2.5 MeV. The gated plot has already the background coming from random coincidences subtracted. A gate between 500 keV and 580 keV was used and the background was subtracted using the energy ranges of [300,400] keV and [600,800] keV. The bin size in this plot is 80 keV as indicated on the vertical axis.

is needed for constructing the energy level scheme. The reaction channels with ^{52}Ca as a fragment can be divided into two categories, (p,pXn) reactions and (p,2pXn) reactions. In the first type, the beam identified in BigRIPS is a calcium isotope (Z=20) and only one proton is detected in MINOS. In the second type of reaction the beam is a scandium isotope (Z=21) and two protons are identified in MINOS. Figure 3.9 shows the beam PID for the two types of reactions producing ^{52}Ca. In this plot one can see the scandium isotopes (Z=21) with a mass number A=54 up to A=59 and the calcium isotopes (Z=20) with a mass number from A=52 and A=56. This means that in the observed (p,pXn)^{52}Ca and (p,2pXn)^{52}Ca reactions many neutrons can be knocked-out or evaporated.

Gamma-gamma coincidences of ^{52}Ca

In Figure 3.10 one sees the gamma spectra corresponding to (p,pXn)^{52}Ca and (p,2pXn)^{52}Ca types of reactions as well as from both types. The two kinds of reactions can populate different states of ^{52}Ca. The peak around 552 keV appears stronger for (p,2pXn)^{52}Ca than for (p,pXn)^{52}Ca reactions, but the 1951 keV peak appears stronger in the (p,pXn)^{52}Ca reactions. For obtaining the γ-γ coincidence spectra, a first (gated) spectrum was obtained, with the events in coincidence with the events found in the peak of interest; a second (background) spectrum was obtained with the events in coincidence with the events found in the left and the right sides of the peak of interest; finally, the γ-γ coincidence spectrum is obtained by subtracting the background spectrum from the gated spectrum using a normalization based

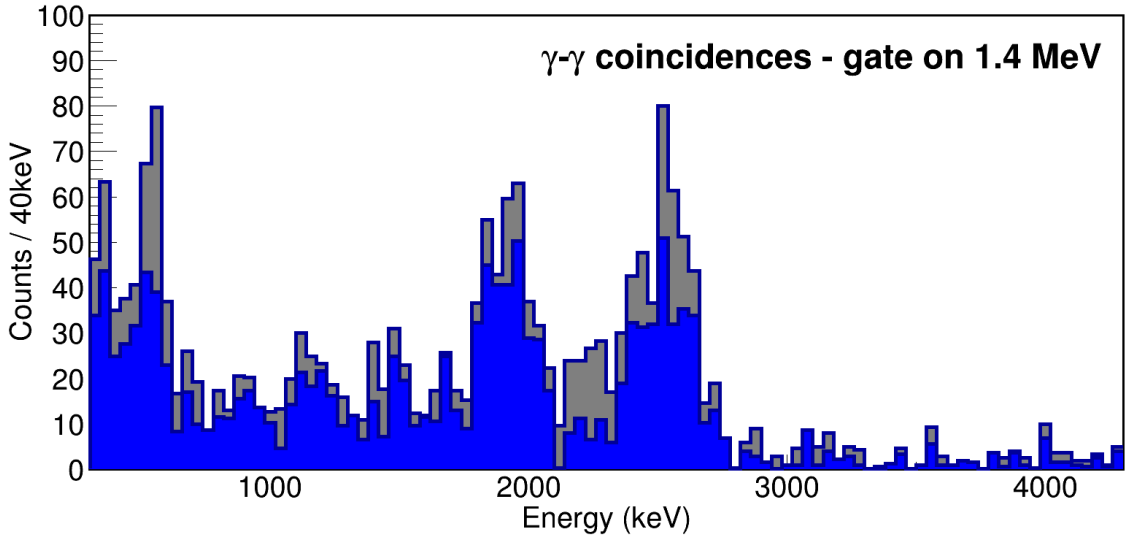

Figure 3.12: Gamma-gamma coincidence spectrum gated on the 1.4 MeV transition. The events from (p,pXn)-type of reactions are shown with blue and from both types of reaction with grey. The transitions at 0.5 MeV, 1.9 MeV, and 2.5 MeV appear in the coincidence spectrum. A gate between 1350 keV and 1450 keV was imposed and the random coincidences background was subtracted using the energy ranges of [1100,1300] keV and [1500,1600] keV.

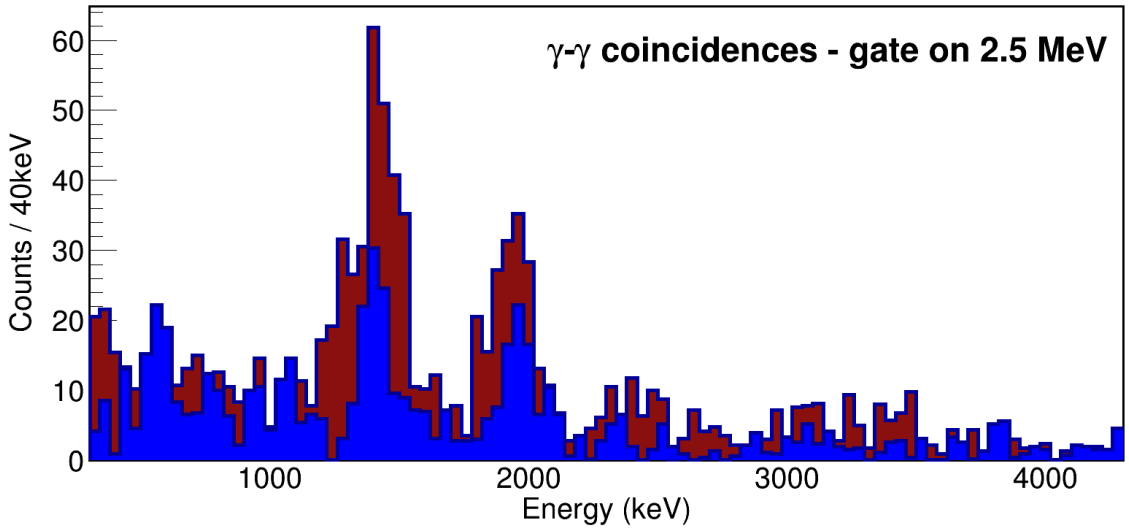

Figure 3.13: Gamma-gamma coincidence spectrum gated on the 2.5 MeV transition. The events from (p,pXn)-type of reactions are shown with dark red and events from (p,2pXn)-type of reactions are shown with blue. The transitions at 0.5 MeV, 1.9 MeV, and 2.5 MeV appear in the coincidence spectrum. A gate between 2480 keV and 2600 keV was imposed and the random coincidences background was subtracted using the energy ranges of [2300,2400] keV and [2700,2800] keV.

on the energy intervals for the gate and background. In the energy interval found in the left side of the peak of interest there will always be Compton events on top of the background events, but the background is dominating, such that the lost of coincidence events is smaller than the gain by subtracting the background events. With this method the γ-γ coincidences could be evidenced for obtaining the energy level scheme of ^{52}Ca. The γ-γ coincidence spectrum gated on the peak at 552 keV shows two transitions. One is at 1426 keV and one is at 2563 keV. The coincidence spectrum is plotted in Figure 3.11. The γ-γ coincidence spectrum gated on the 1426 keV γ-ray transition is shown in 3.12, where three peaks at 552 keV, 1951 keV, and 2563 keV are visible. In the γ-γ coincidence spectrum with the 2563 keV transition, the 552 keV, 1426 keV, and 1951 keV transitions appear. The transition at 1951 keV does not appear in coincidence with the transition of 552 MeV, but they are both in coincidence with the 1426 keV and the 2563 MeV transitions. One can deduce that they both feed an excited state which is then decaying by emitting the 1426 keV and the 2563 keV γ rays. This results in having an excited state at 2563(10) keV, which is known as the first 2^+ state [2], one at 3989(15) keV (decaying by the cascade 1426(12) + 2563(10)), one at 4541(18) keV (decaying by the cascade 552(10) + 1426(12) + 2563(10)), and another excited state at 5940(24) keV (decaying by the cascade 1426(12) + 1951(19) + 2563(10)). The transition at 3388(53) keV is the sum 1426(12) + 1951(19) keV, so it must be the second decaying branch of the 5.9 MeV excited state. The γ-γ coincidence spectrum by gating on a region between 3 and 3.5 MeV is very poor because of the small statistics of the peaks in this region, but one can see a small increased distribution in the 2.5 MeV region, explaining the second decay branch of the 5.9 MeV state. Using the transitions of the second decay branch a value of 5951(54) was obtained for the excited state, which has a higher uncertainty than the one obtained from the first decay branch, but it is closer to the literature values. This excited state is very close to the neutron separation energy of ^{52}Ca, found at 6.0053(8) MeV [118]. The 3150(41) keV transition comes from the decay of an excited state directly to the ground state, as it does not appear in coincidence with any other transition.

E_γ [keV] (this work)	E_γ [keV] (literature, experiment)
552(10)	-
1426(12)	1427(1) [103], 1426 [101], 1430(7) [45]
1951(19)	1961(1) [103]
2563(10)	2563(1) [103], 2564 [101], 2562(12) [45], 2563 [2]
3150(41)	3150(2) [103]
3388(53)	3388(2) [103]

Table 3.4: The γ-ray transitions of ^{52}Ca obtained from this work (first column) and published values (second column) from Refs. [2, 45, 101, 103]. The uncertainties are given in the parentheses.

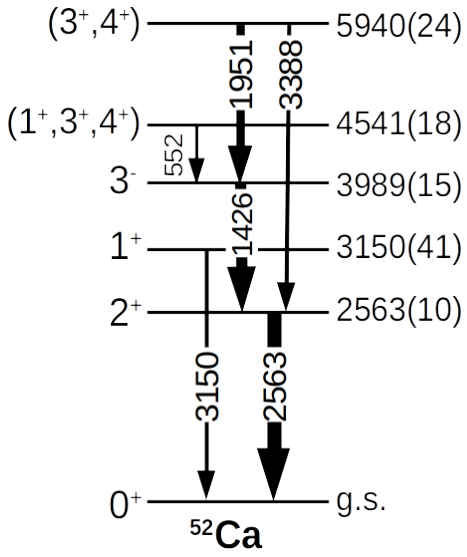

Figure 3.14: The level scheme of ^{52}Ca.

The constructed level scheme as a result of this work and guided by the published data from Refs. [2, 45, 101, 103] is shown in Figure 3.14. The spin-parity assignment for the ground state is 0^+ corresponding to a single particle configuration of $(f_{7/2})^8(p_{3/2})^4$. The shell model calculations confirm the spin-parity assignment and the single-particle configuration. The shell model calculations give a spectroscopic factor of 0.946 for the neutron knockout of a $p_{1/2}$ neutron from ^{53}Ca ($1/2^-$, g.s.) for populating the ^{52}Ca ground state .

The energy level at 2563 keV is assigned to have $J^\pi=2^+$ with a single particle configuration of $(f_{7/2})^8(p_{3/2})^3(p_{1/2})^1$. Out of the coupling of 3 neutrons found on the $p_{3/2}$ orbital (two of them paired to 0^+) with a neutron from the $p_{1/2}$ orbital, one has two non-degenerate energy levels, one with $J^\pi=2^+$ and one with $J^\pi=1^+$. The 1^+ state is found at the energy of 3150 keV. The 2^+ and the 1^+ states have a spetroscopic factor of 2.298 and 1.331, respectively, for the neutron knockout of a $p_{3/2}$ neutron from ^{53}Ca according to the shell model calculations.

The next excited state appears at 3989 keV and this is identified as a core excitation with a non-natural parity with $J^\pi=3^-$. The J^π assignments are based on the work of Ref. [2, 45, 101, 103] and the single particle configurations are according to Ref. [101]. This state is not included in the shell model calculations because it involved core excitations, while the calculations are done for a rigid ^{40}Ca core.

According to theoretical calculations from Ref. [101], there should be a 4^+ state with the single-particle configuration of $(f_{7/2})^8(p_{3/2})^3(f_{5/2})^1$ at an energy of $\sim$4.5 MeV. In this experiment we observe an excited state at 4541 keV. Additionally, the shell model calculations predict three states with the single-particle configuration of $(f_{7/2})^8(p_{3/2})^3(f_{5/2})^1$ with the excitation energy between 4.49 MeV and 4.75 MeV and spin-parity $J^\pi=3^+,1^+$, and 4^+. The three states, based on the shell model calculations, show small spectroscopic factors for the knockout of p and f neutrons, which is in agreement with the very low yield obtained experi-

mentally for the population of the 4541 keV state presented in Table 3.6 in section 3.4.4. The statistics for the 4541 keV state is too low for identifying the spin-parity of it using the momentum distribution analysis, so we will tentatively assign the spin-parity of $J^{\pi}=(3^{+},1^{+},4^{+})$.

Based on the work of Ref. [103], the 5940 keV state needs to have a spin at least greater than 4 and a positive parity. From the present work using the momentum distribution analysis, it can be proved that the 5940 keV state is populated by the removal of an f neutron orbital. The momentum distribution analysis confirming the assignment of the 5940 keV state is presented in section 3.5. This is in agreement with the single particle configuration of $(f_{7/2})^{7}(p_{3/2})^{3}(f_{5/2})^{1}(p_{1/2})^{1}$ also predicted by the shell model calculations for the states with excitation energy of 6.4-6.8 MeV and spin-parity of $J^{\pi}=4^{+}$ and 3^{+}, listed in Table 3.3. For these three states from the shell model calculations, we obtain large spectroscopic factors for the knockout of an $f_{7/2}$ neutron. The large spectroscopic factors are in agreement with the large yield measured experimentally for the 5940 keV state presented in Table 3.6. The 5940 keV state is found just below the neutron separation energy. A total spectroscopic factor of 7.527, close to the maximum allowed value for the $f_{7/2}$ neutron orbital is distributed among several 4^{+} and 3^{+} states according to the shell model calculation, part of these states are found above the neutron separation energy. For the 5940 keV state we can assign the tentative spin-parity of $J^{\pi}=(3^{+},4^{+})$ based on the present work.

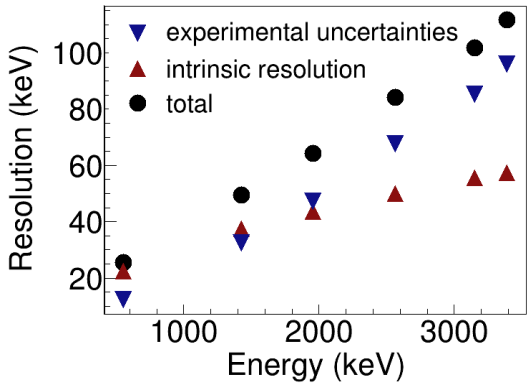

Figure 3.15: The total resolution of the γ-ray energy as a function of the energy divided into the intrinsic resolution and the contribution coming from experimental uncertainties.

3.4.4 Gamma-ray spectrum fitting for ^{53}Ca(p,pn)^{52}Ca

Gamma energy resolution

The energy resolution can be divided into several contributions. The main ones are the intrinsic resolution of the detector crystals and the resolution dependent on the experimental conditions. In the second group one can have the contribution of the velocity uncertainty of the fragments emitting the γ rays, the uncertainty in the interaction point within the detectors crystals impacting the photon angle, and also the uncertainty of the reaction vertex which impacts both the fragment velocity and the photon angle. The experimental uncertainties and the intrinsic resolution of the detectors are both a function on the γ-ray energy as plotted in Figure 3.15. The measured sigma values of the γ-rays present in the spectrum of the ^{53}Ca(p,pn) channel, the spectrum from all channels leading to ^{52}Ca and the simulated response functions for the ^{53}Ca(p,pn) reaction are listed in Table 3.5.

Energy	sigma(keV) exp, all channels	sigma(keV) exp, 52Ca(p,pn)	sigma(keV) sim
555	27.88		25.49
1425	55.84	55.73	49.41
1951	85.62	66.57	64.27
2562	86.16	81.69	84.13
3150			101.81
3388			111.75

Table 3.5: The experimental and simulated sigma values for the transitions of ^{52}Ca.

Response functions and fitting methods

The response functions can be simulated either for each single transition (singles) or for each decaying excited state (cascades). As a result, one has two possible methods to fit the experimental γ-ray spectrum, but the obtained yields should be the same. Figures 3.16 and 3.17 show the fitted experimental spectrum using the two methods.
The decays via the cascade transitions are shown in Figure 3.18. The ground state yield is

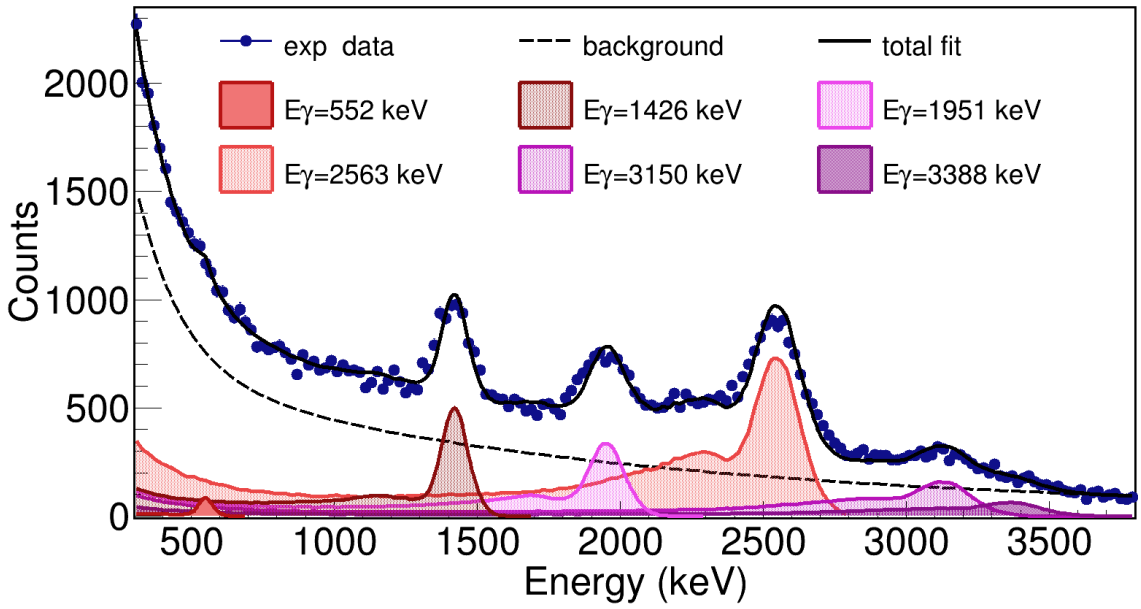

Figure 3.16: The fitted γ-ray spectrum for ^{53}Ca(p,pn)^{52}Ca. The experimental data (dark blue circles) are fitted with a double exponential background shape (dashed line) and with the response functions of the single γ-ray transitions (colored) filled curves). The binning of the histograms is 20 keV.

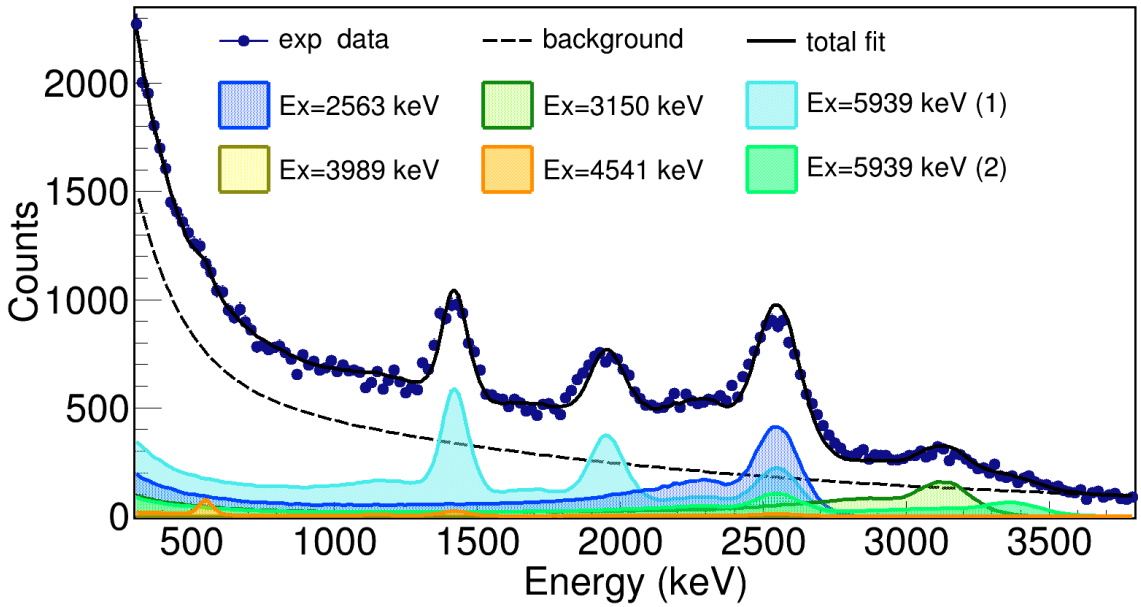

Figure 3.17: The fitted γ-ray spectrum for ^{53}Ca(p,pn)^{52}Ca. The fitting is done as in Figure 3.16, but using the response functions of the γ-ray cascade transitions of the excited states of ^{53}Ca. The 3989 keV and 4541 keV energy levels have zero or very low population and cannot be well seen in the plot. The binning of the histograms is 20 keV.

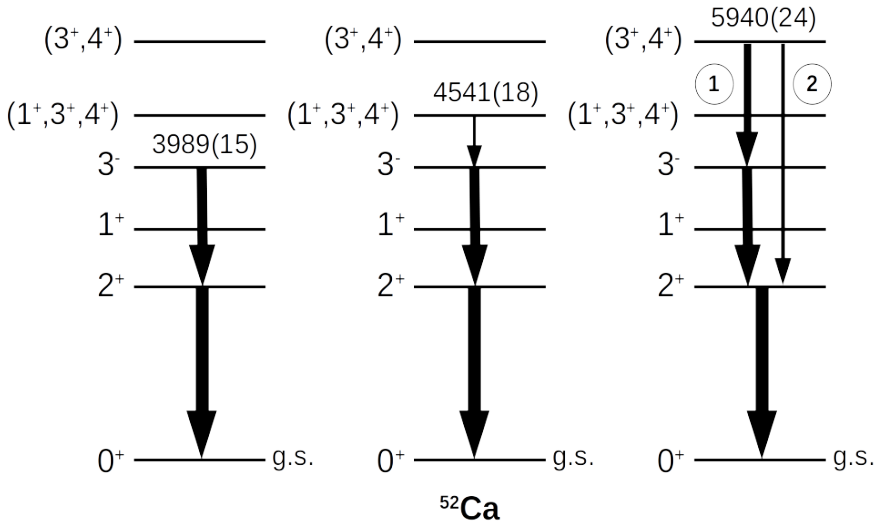

Figure 3.18: Sketch of the decay of the 3.9 MeV, 4.5 MeV, and 5.9 MeV excited states of ^{52}Ca via cascade transitions.

^{53}Ca(p,pn)^{52}Ca single transitions		^{52}Ca levels population cascade transitions		Level population fraction (%)	
Energy transition (keV)	Counts	Energy level (keV)	Counts	singles	cascades
552	639 (214)	2563	22142(687)	26.63(92)	26.31(82)
1426	11946(407)	3150	11158(439)	13.22(52)	13.26(52)
1951	12516(457)	3989	0(152)	0.00(77)	0.00(18)
2563	39245(526)	4541	513(202)	0.76(25)	0.61(24)
3150	11127(440)	5940	16787(528)	20.69(72)	19.95(63)
3388	4892(395)	g.s.	33549(1045)	40.14(89)	39.87(124)
g.s.	33777(745)				
Total	84149(290)				

Table 3.6: The yields for ^{53}Ca(p,pn)^{52}Ca obtained via the singles and the cascades methods. The first 2 columns show the results of fitting the γ-ray spectrum with the single transitions. The γ-ray transition energies are given in the first column. The counts obtained with this method and the fitting errors are shown in the second column. The total number of events and the ground state yield calculated using the γ-ray transition yields are also listed. The columns 3-4 show the yields obtained fitting the γ-ray spectrum with the cascade transitions. In column 3 the energy levels are listed and in column 4, the counts and the errors for populating each energy level as a result of the γ-ray fitting are given. Columns 5 and 6 show the fraction of the level population obtained by using the singles and the cascades method, respectively. In the case of the singles method, the yields for each energy level of ^{52}Ca were calculated using the yields of the γ-ray transitions. The fractions are the ration between the yield of one energy level and the total number of events. The errors are given in the parentheses.

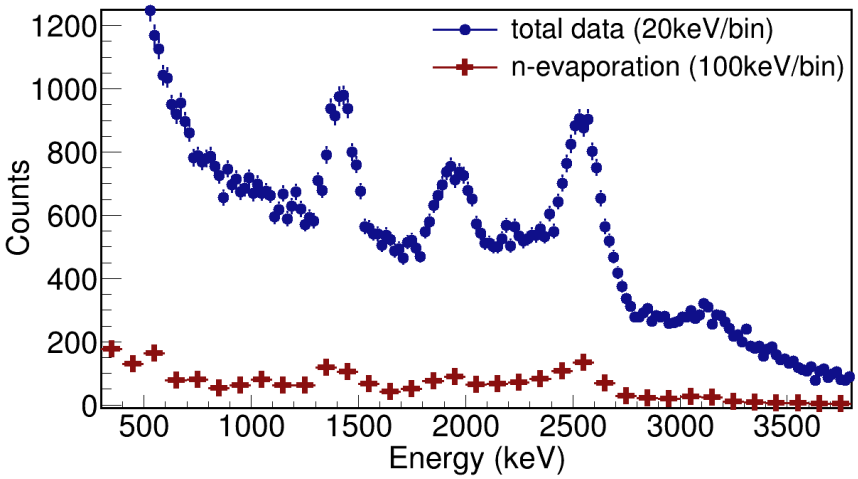

Figure 3.19: The γ-ray spectrum for the neutron-evaporation events (red crosses) in comparison to the total events (dark blue circles) found for ^{53}Ca$\rightarrow^{52}$Ca. The binning of the total histogram is 20 keV and the binning for the neutron-evaporation histogram is 100 keV.

calculated as the total minus the yields for the 2.5 MeV and the 3.1 MeV states (the states feeding the ground state) yields in the first method (singles), while in the second method (cascades) it is calculated as the total minus the yield of populating each excited state. The population yield of the excited energy levels using the information from the single transitions are calculated as the sum of decaying transitions minus the sum of feeding transition of each level. A comparison of the two methods, fitting with single transitions versus cascade transitions is given in Table 3.6. The counts found for each single transition are given in the second column. The counts for each populated level using cascades fitting method is given in the fourth column. In the last two columns one can see the comparison of the level population fraction (out of total) using the two methods. The errors are given in the parentheses. The population yield of each state obtained by the two fitting methods are in agreement with a relative difference of 1.19%, which will be considered in the systematic errors. It can be observed that the errors for the excited energy levels population is lower using the cascades method, while for the ground state the errors are lower by using the singles method. This information will be used for the exclusive momentum distribution analysis in section 3.5.

The binning of the γ-ray spectrum used for obtaining the yields listed in Table 3.6 and Figures 3.16 and 3.17 is 20 keV. For obtaining the exclusive momentum distributions one will need to apply the same fitting procedure on partial γ-ray spectra corresponding to each step/interval of momentum which will have lower statistics compared to the total spectrum. In that case one will have to increase the binning. The effect of the binning size was investigated and the average relative differences between the yields obtained with a binning of 50 keV and a binning with 10 keV is 1.73%. Also the same relative difference between the binning of 50 keV and a binning of 20 keV is 1.61%. The fitting errors obtained with the

two method are comparable. The relative difference as an effect of the binning size will be included in the systematic errors.

In the procedure of fitting the γ-ray spectra shown in Figures 3.16 and 3.17, the amplitudes of the response functions are free parameters. The position on the energy axis of each response function was fixed after determining the exact peak positions. The background was fitted with a double exponential function. The shown spectra are obtained by imposing the identification of the beam as an ^{53}Ca particle, the identification of the fragment as an ^{52}Ca particle, the detection of one proton in MINOS and the vertex reconstruction within the physical location of the liquid hydrogen target. As a result, it includes (p,pn) events as well as neutron-evaporation events. The spectrum gated on the detection of a neutron in the NeuLAND and NEBULA detectors is shown in Figure 3.19 (red crosses) in comparison to the total events (dark blue circles). For the analysis of the exclusive momentum distributions, the neutron-evaporation events will be discarded by imposing kinematic conditions for the detected proton rather than γ-ray spectra subtraction, for minimizing the errors of the results. The difference between these two methods are discussed in section 2.3.9 and it amounts to 3.5%, which is included in the systematic errors.

Significance analysis

A significance analysis for the γ-ray transitions appearing for the ^{53}Ca(p,pn) reaction channel was performed in the same manner as described in section 2.3.5 for the ^{52}Ca(p,pn) reaction channel. A significance level of 1.5σ was found for the 552 keV transition and the yield of this transition amounts to less than 1% of the total yield for this reaction. The significance levels of the 3150 keV and 3388 keV transitions are 19.8 and 13.2σ, respectively. The significance levels of the rest of the transitions is much greater than 20σ.

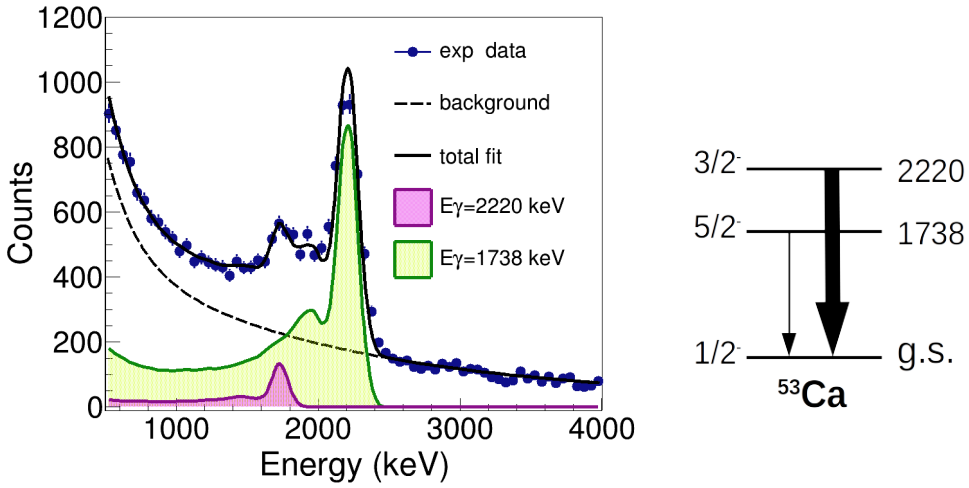

Figure 3.20: Left: Gamma spectrum of ^{54}Ca(p,pn)^{53}Ca. The experimental data (dark blue circles) are fitted with a double exponential background shape (dashed line) and the response functions of the γ-ray transitions of ^{53}Ca. The binning of the histograms is 50 keV. Right: Energy level scheme of ^{53}Ca.

3.4.5 Gamma-ray spectrum fitting for ^{54}Ca(p,pn)^{53}Ca

The ^{54}Ca(p,pn)^{53}Ca reaction measured in this experimental campaign was analysed and published (see Ref. [46]). In this paper the transitions found in the γ-ray spectrum of ^{53}Ca were identified and their spin-parity was confirmed by the corresponding exclusive momentum distributions. The exclusive neutron knock-out cross sections were also evaluated and used as an evidence for the N=34 neutron shell closure in ^{54}Ca. In this analysis, the published values for the γ-ray transitions are going to be used. In the γ-ray spectrum of ^{53}Ca populated by the (p,pn) reaction one finds two transitions, one at 1738 keV and one at 2220 keV. The γ-ray spectrum and the energy level scheme of ^{53}Ca are shown in Figure 3.20. The two transitions correspond to the neutron knock-out off the $f_{5/2}$ and the $p_{3/2}$ orbitals. The population of the ground state by the (p,pn) reaction corresponds to knocking out a neutron off the $p_{1/2}$ orbital. The fitting procedure of the ^{53}Ca γ-ray spectrum is the same as described for ^{52}Ca and ^{51}Ca. The statistics for the $3/2^- \rightarrow 1/2^-$ transition is very low which causes the corresponding momentum distribution analysis to have large uncertainties.

3.5 Exclusive momentum distributions

The exclusive momentum distributions ($dY/dP_{//}$ and $dY/dP_{\perp}$, Y being the yield) are obtained by fitting the gamma spectrum corresponding to momentum intervals (in steps of 40 MeV/c) in the same manner as done for ^{52}Ca(p,pn)^{51}Ca described in section 2.3.9. The parallel and perpendicular momentum distributions (PMDs) for populating the ground state (-n $p_{1/2}$), the 2563 keV (-n $p_{3/2}$), the 3150 keV (-n $p_{3/2}$) and the 5940 keV (-n $f_{7/2}$) excited states were obtained for the ^{53}Ca(p,pn)^{52}Ca reaction channel. The PMDs for the 4541 keV state population could not be obtained because of the low statistics of the 552 keV transition with low significance in the γ-ray spectrum of this study. For the 5940 keV excited state, the PMDs were obtained separately for the two decay branches, 1 and 2, sketched in Figure 3.18. The second decay branch presents statistical fluctuations in the PMDs because of the low statistics. For the ^{54}Ca(p,pn)^{53}Ca reaction channel the PMDs corresponding to the population of the ground state (-n $p_{1/2}$), the 1738 keV (-n $f_{5/2}$) and the 2220 keV (-n $p_{3/2}$) excited states were obtained from the experimental data.

The momentum distribution of the fragment in the center of mass frame is directly related to the momentum distribution of the neutron before the knockout, bound inside the nucleus due to the sudden approximation of the quasi-free nucleon scattering reactions. Also, the momentum distribution of the bound neutron is dependent on the spatial configuration of the neutron orbital. The parallel momentum width is a function of the orbital number, l, and on the neutron separation energy, S_n. If the orbital number is larger, the momentum width is larger as well. Also, if the separation energy is larger, as for a deeper bound nucleon, the momentum width is larger. The momentum distribution can be used for assigning the spin-

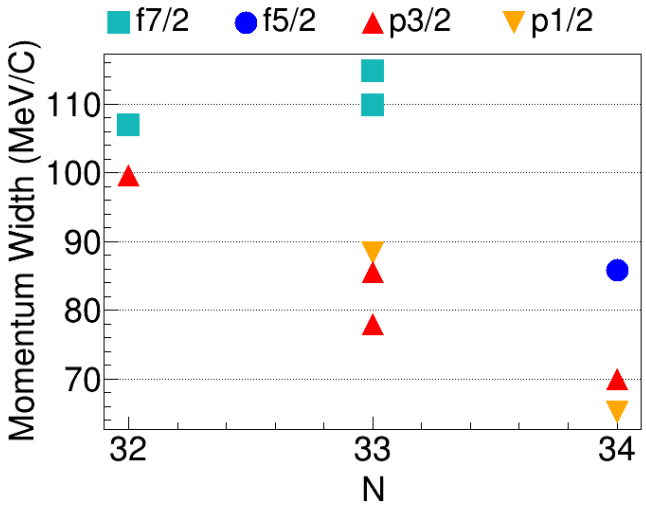

Figure 3.21: Width (RMS value) of the parallel momentum of the ^{51}Ca, ^{52}Ca, and ^{53}Ca fragment from (p,pn) reactions corresponding to the neutron knockout from the p and f orbitals. The data is given as a function of the neutron number N for each neutron orbital after the experimental resolution was deconvoluted.

parity of certain states or it can be used to obtain information on the orbital from which the nucleon was knocked out. For the neutron orbitals in the ^{52,53,54}Ca isotopes one can compare the parallel momentum width for each neutron orbital that could be accessed during the studies presented in this thesis via proton induced neutron knock-out reactions. Figure 3.21 shows the width values after the deconvolution of the experimental resolution. From this plot we expect small differences or a smooth evolution of the size of the p and f orbitals as a function of the neutron number. Also, one observes a larger difference between the f and p orbitals for N=33 compared to N=32, so one could expect the same for the rms radii of the corresponding single-particle orbitals.

Figures 3.22 to 3.28 show the PMDs corresponding to each populated state of the fragments via (p,pn) reactions from ^{53}Ca and ^{54}Ca beams in inverse kinematics. The binning used for the momentum is 40 MeV/c and the binning used for the γ-ray partial spectra is 50 keV. The binning of the γ-ray partial spectra with small statistics, mainly to the tails of the momentum distributions, was changed to 100 keV. The experimental data points are shown with circles, the statistical errors are marked with bars and the systematic errors are marked with boxes. The horizontal dimension of the errors represents the bin size. The statistical errors include $\sqrt{N}$-type of uncertainties and fitting uncertainties. The systematic errors include the followings: (1) γ-ray spectrum fitting systematic uncertainty, 5%; (2) MINOS efficiency uncertainty, 3%; (3) The systematic uncertainty due to the binning effect, 1.7%; (4) the systematic uncertainty due to the method (singles vs. cascades), 1.19%; (5) the systematic uncertainty due to the subtraction method of the neutron-evaporation events (angle cut vs. subtraction), 3.5%. For each reaction channel, ^{53}Ca(p,pn)^{52}Ca and ^{54}Ca(p,pn)^{53}Ca, one finds the PMDs of the direct beam (Figures 3.22 and 3.26) plotted with dotted blue lines as reference of the resolution of the experiment.

In the same figures one finds the momentum distribution calculated with the DWIA. The theoretical models that were used are described in section 2.4. The shown calculations are using the wavefunction of the knocked-out neutron obtained with the Woods-Saxon potential with the Bohr-Mottelson parametrisation, which is labeled as (BM) and plotted with solid line, and alternatively with the HFB calculation using the SKM interaction, which labeled as (HFB) and plotted with dotted lines. The difference between the two calculations was discussed in section 2.4 and in most of the cases as one sees in the current plots, the differences are negligible. What is important to notice is that the values in the low-statistics tails for the exclusive PMDs could not be obtained. In these regions, the experimental data points are shown with 0 values and the fitting of the theoretical curved to the experimental PMDs was only done in the regions with available data points.
In Figures 3.22 and 3.23, one sees how the theoretical calculations for the neutron knock-out from the $p_{3/2}$ orbitals describes well the data. For comparison, f-wave PMDs were also plotted with dashed grey lines.
The ground state PMDs for the ^{53}Ca(p,pn)^{52}Ca reaction channel correspond to removing a neutron from the $p_{1/2}$ orbital. The experimental data (Figure 3.24) for ground state PMDs obtained using the singles or using the cascades γ-ray spectrum fitting methods are both plotted

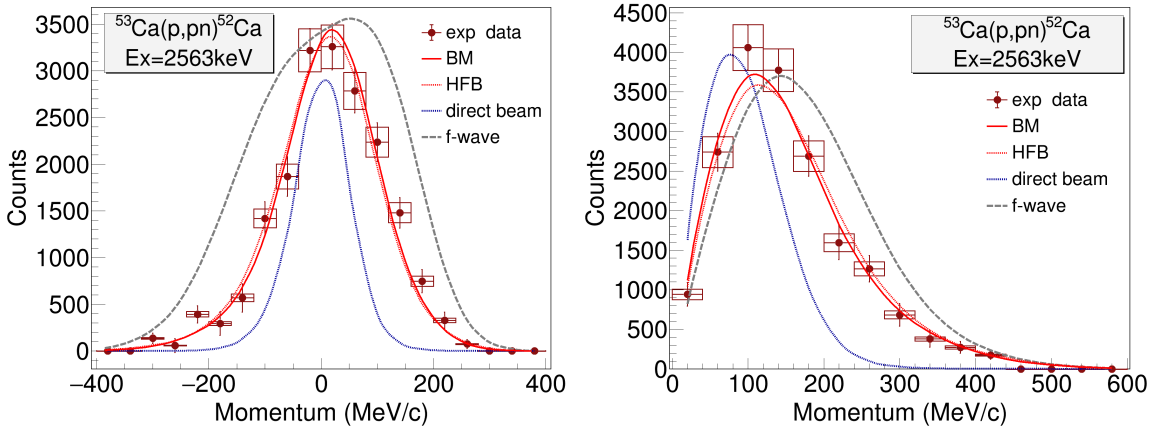

Figure 3.22: The momentum distribution, parallel (left) and perpendicular (right) components, of the ^{52}Ca fragment left in the 2563 keV excited state after the knockout of a $\mathbf{p_{3/2}}$ neutron via the (p,pn) reaction. The solid and dotted colored curves are the theoretical calculations in the BM and HFB cases, respectively. The dotted blue lines represent the PMDs of the direct beam. The grey dashed line is an f-wave PMD for comparison. The experimental data (circles) are shown together with statistical (bars) and systematic (boxes) errors.

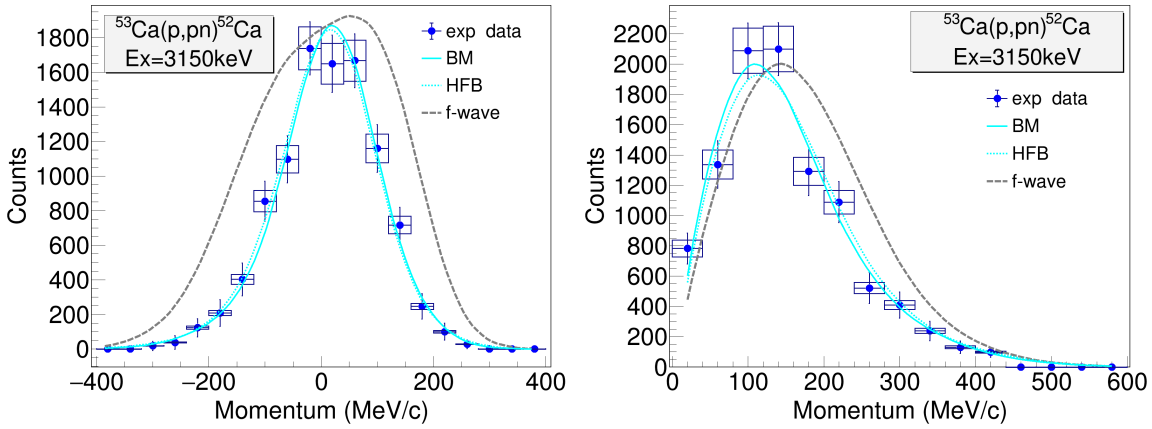

Figure 3.23: The momentum distribution, parallel (left) and perpendicular (right) components, of the ^{52}Ca fragment left in the 3150 keV excited state after the knockout of a $\mathbf{p_{3/2}}$ neutron via the (p,pn) reaction. The labeling is the same as for Figure 3.22.

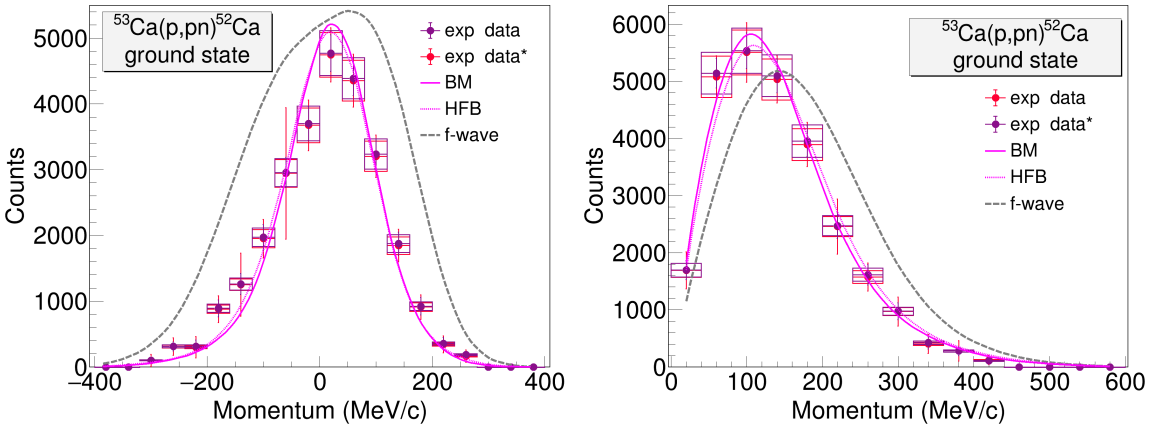

Figure 3.24: The momentum distribution, parallel (left) and perpendicular (right) components, of the ^{52}Ca fragment left in the ground state after the knockout of a $\mathbf{p_{1/2}}$ neutron via the (p,pn) reaction. The experimental data (circles) come from two mothods of fitting, using singles (purple) and using cascades (pink). The solid and dotted colored curves are the theoretical calculations in the BM and HFB cases, respectively. The grey dashed line is an f-wave PMD for comparison. The experimental data (circles) are shown together with statistical (bars) and systematic (boxes) errors.

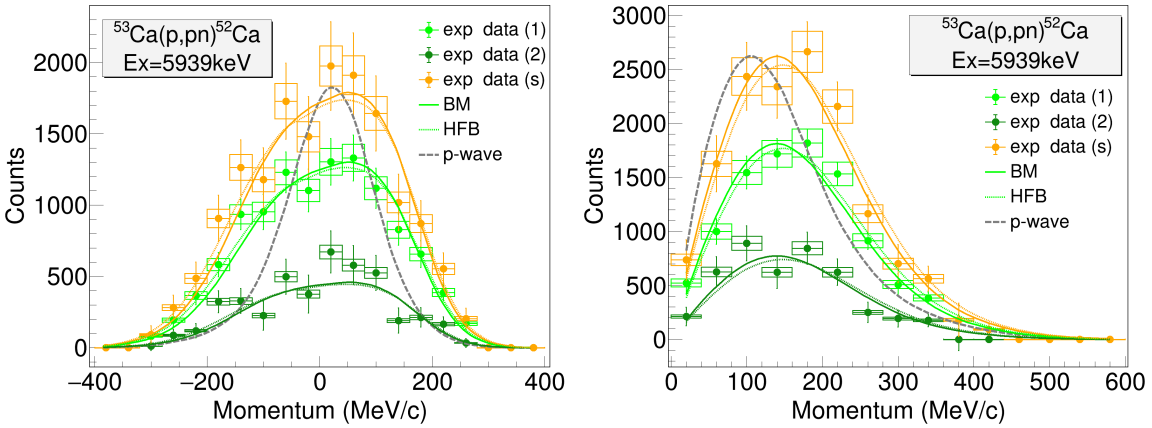

Figure 3.25: The momentum distribution, parallel (left) and perpendicular (right) components, of the ^{52}Ca fragment left in the 5940 keV excited state after the knockout of a $\mathbf{f_{7/2}}$ neutron via the (p,pn) reaction. The light green data is for the first decay branch (1951 keV+1426 keV+2563 keV) and the dark green data is for the second decay branch (3388 keV+2563 keV). The orange data is the total momentum distribution for populating the 5940 keV state (sum of the two decay branches). The grey dashed line is an p-wave PMD for comparison. The experimental data (circles) are shown together with statistical (bars) and systematic (boxes) errors.

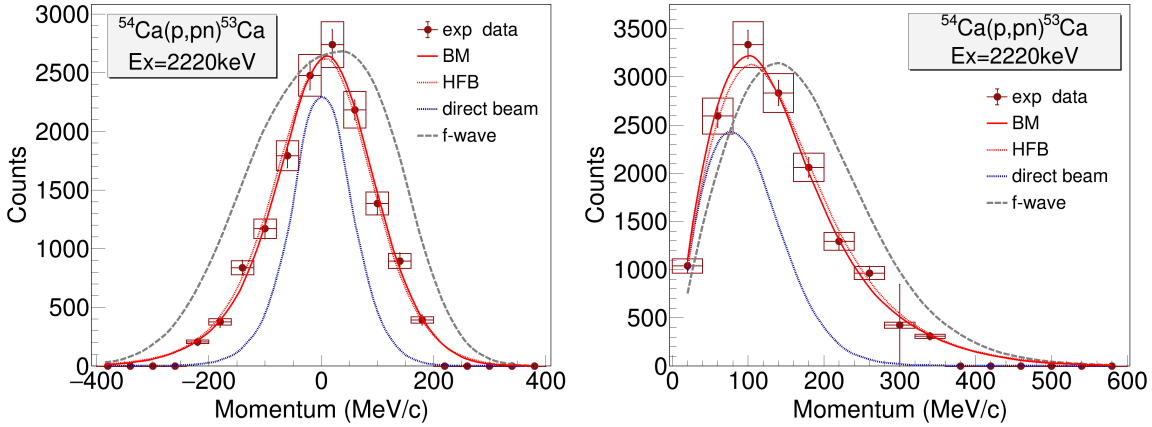

Figure 3.26: The momentum distribution, parallel (left) and perpendicular (right) components, of the ^{53}Ca fragment left in the 2220 keV excited state after the knockout of a $\mathbf{p}_{3/2}$ neutron via the (p,pn) reaction. The solid and dotted colored curves are the theoretical calculations in the BM and HFB cases, respectively. The dotted blue lines represent the PMDs of the direct beam. The grey dashed line is an f-wave PMD for comparison. The experimental data (circles) are shown together with statistical (bars) and systematic (boxes) errors.

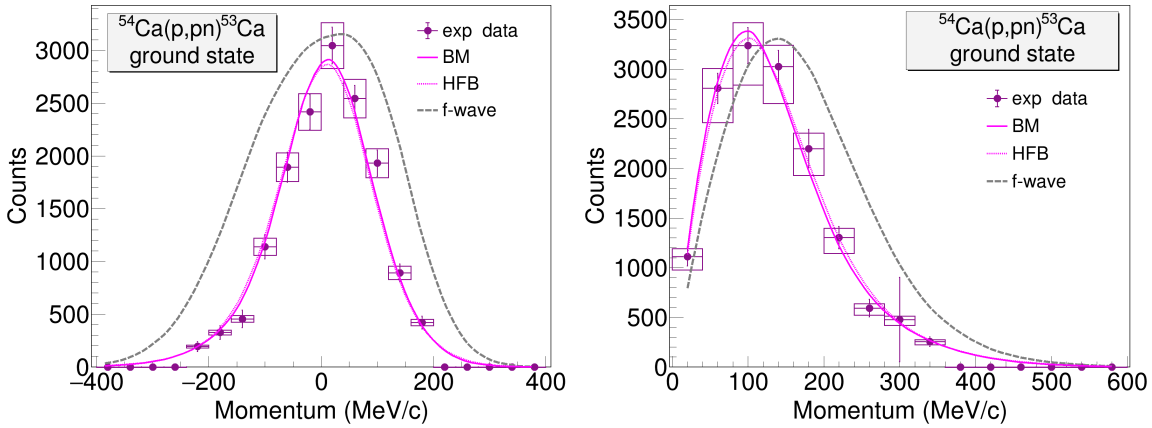

Figure 3.27: The momentum distribution, parallel (left) and perpendicular (right) components, of the ^{53}Ca fragment left in the ground state after the knockout of a $\mathbf{p}_{1/2}$ neutron via the (p,pn) reaction. The labeling is the same as for Figure 3.26.

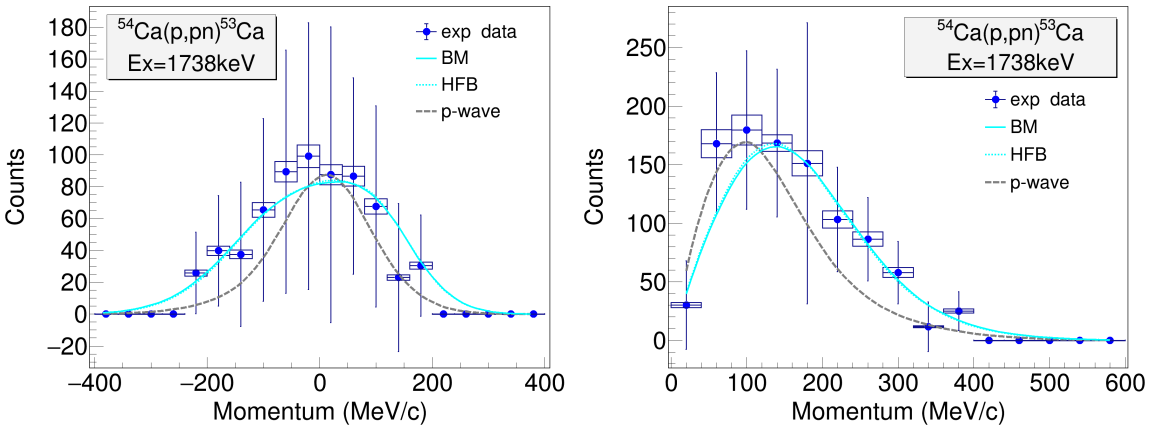

Figure 3.28: The momentum distribution, parallel (left) and perpendicular (right) components, of the ^{53}Ca fragment left in the 1738 keV excited after the knockout of a $\mathbf{f_{5/2}}$ neutron via the (p,pn) reaction. The experimental data (circles) are shown together with statistical (bars) and systematic (boxes) errors. The solid and dotted colored curves are the theoretical calculations in the BM and HFB cases, respectively. The grey dashed line is an p-wave PMD for comparison.

with purple and pink, respectively. The differences between the two methods are minimal, and they are already considered in the systematic errors, but one can observe that the errors with the singles method are smaller. The data is well reproduced using the theoretical curves for -n $p_{1/2}$ in this case as well and for comparison, an f-wave momentum distribution is also shown.

It can be now confirmed using the momentum distribution analysis that the 5940 keV excited state of ^{52}Ca is populated by the knockout of an f neutron. Figure 3.25 shows how the theoretical PMDs for the neutron knock-out of an $f_{7/2}$ neutron is describing very well the experimental data coming from both decay branches as well as the total (sum) distributions. In this plot, as well, a p-wave curve is shown for comparison plotted with dashed line. The momentum distributions calculated for the $f_{5/2}$ neutron orbital were also compared to the experimental PMDs and they fit the data as well as the calculations with the $f_{7/2}$ neutron. Hence, from the momentum distribution analysis, we cannot differentiate between the two f neutron orbitals.

Moving on to the ^{54}Ca(p,pn)^{53}Ca reaction channel, one can see in Figure 3.26 the momentum distribution from populating the 2220 keV excited state of ^{53}Ca. It corresponds to the neutron knock-out from the $p_{3/2}$ neutron orbital. The ground state population of ^{53}Ca takes place by knocking out a neutron from the $p_{1/2}$ orbital of ^{53}Ca and the corresponding PMDs are plotted in Figure 3.27. The theoretical calculations for the knock-out reaction are in agreement with the experimental data in both cases and f-wave distributions are shown for comparison plotted with dashed lines. The PMDs of these two states and their successful description by the theoretical calculations was obtained by Ref.[46] as well.

The knock-out of a neutron from the $f_{5/2}$ orbital from ^{54}Ca leads to the population of the

1738 keV state in ^{53}Ca. The present theoretical calculations can confirm this assignment despite the high statistical fluctuation. A p-wave curve is shown for comparison. The width of parallel momentum distribution is much better described by the f-wave compared to the p-wave. Also, for the perpendicular momentum component the f-wave fits most of the experimental points while the p-wave only fits better the first three low-momentum points. On the other hand, a g-wave is also excluded because the $g_{9/2}$ neutron orbital is too high in energy to be occupied.

3.6 The determination of rms radii of the *pf*-shell neutron orbitals

The determined momentum distributions are related to the single-particle wavefunctions of the orbitals from which the neutron was knocked out during the (p,pn) reaction. By using several single-particle wavefunctions of different sizes as an input for the DWIA calculations, one can see which hypothesis fits the best the experimental data based on a χ^2 minimization method. In the analysis of ^{53}Ca(p,pn) and ^{54}Ca(p,pn) channels the same approach described in sections 2.4 and 2.5 is used. The variation of the bound state single-particle wavefunctions size was done by varying the radial parameter around the default value of r_0=1.27 fm with ±30%. The rest of the calculations were conducted in the same manner for the full

		theoretical uncertainty for r_0 (fm)			theoretical uncertainty for rms radii (fm)		
nucleus	orbital	parallel	perpendicular	both	parallel	perpendicular	both
^{53}Ca	$p_{3/2}$	0.1329	0.1896	0.1063	0.2307	0.3291	0.1845
	10^6 ev.	0.0008	0.0073	$<10^{-4}$	0.0014	0.0127	$<10^{-4}$
	10^5 ev.	0.0395	0.0569	0.0323	0.0686	0.0988	0.0561
	10^3 ev.	0.4204	0.5220	0.3314	0.7298	0.9062	0.5753
	$p_{1/2}$	0.1781	0.2422	0.1413	0.3015	0.4101	0.2392
	$f_{5/2}$	0.1156	0.0718	0.0611	0.2582	0.1604	0.1365
	$f_{7/2}$	0.1075	0.0704	0.0589	0.2670	0.1749	0.1463
^{54}Ca	$p_{3/2}$	0.1331	0.1596	0.0976	0.2340	0.2806	0.1716
	$p_{1/2}$	0.1697	0.1890	0.1246	0.2897	0.3227	0.2128
	$f_{5/2}$	0.1313	0.0708	0.0620	0.3056	0.1648	0.1444

Table 3.7: The uncertainties for the radial parameter and for the rms radii calculated for each orbital of the pf-shell for ^{53}Ca and ^{54}Ca. The listed uncertainties come from the sensitivity of the shape of the PMDs to the radial parameter for 10 000 events. For one of the orbitals, the values for different number of events are also shown (grey). The values are given for three cases: using only the parallel component, only the perpendicular component or both components of the measured PMDs in the optimum radial parameter determination.

set of input radial parameters. The resulting theoretical curves for the parallel and perpendicular momentum distributions were convoluted with the reaction energy profile and the experimental momentum resolution. They were then fitted to the experimental momentum distributions and from each fit the χ^2 value was obtained. The χ^2/NDF (NDF=number of degrees of freedom) was obtained as a function of the input radial parameter and from this distribution an optimal radial parameter mean value and a sigma value could be obtained for each neutron orbital. The relation between the rms radius of each orbital and the radial parameter was used for transforming the results into the rms radius values with the associated uncertainties.

Sensitivity of PMDs to the rms radii

The optimum radial parameter can be obtained using the parallel momentum distribution, the perpendicular momentum distribution or their combination. In the third case, the χ^2 distributions are summed up for the minimization method. The sensitivity of the theoretical PMDs to the radial parameter varies from case to case. For obtaining the uncertainty for the r_0 parameter and the resulting rms radius value due to the method, the theoretical curves for each radial parameter value were rescaled to minimize the differences between each other and the χ^2 values relative to the curve for the central value of r_0=1.27 fm (the test could be done relative to any of the values) were obtained. Prior to this procedure, the r_0=1.27 fm curves were normalized to 10 000 events. This procedure was applied for the parallel, perpendicular and the combination of the parallel and the perpendicular curves for both ^{53}Ca and ^{54}Ca nuclei and for each single-particle neutron orbital studied in the present work. With this test one would see how different the theoretical PMDs are as a function of the radial

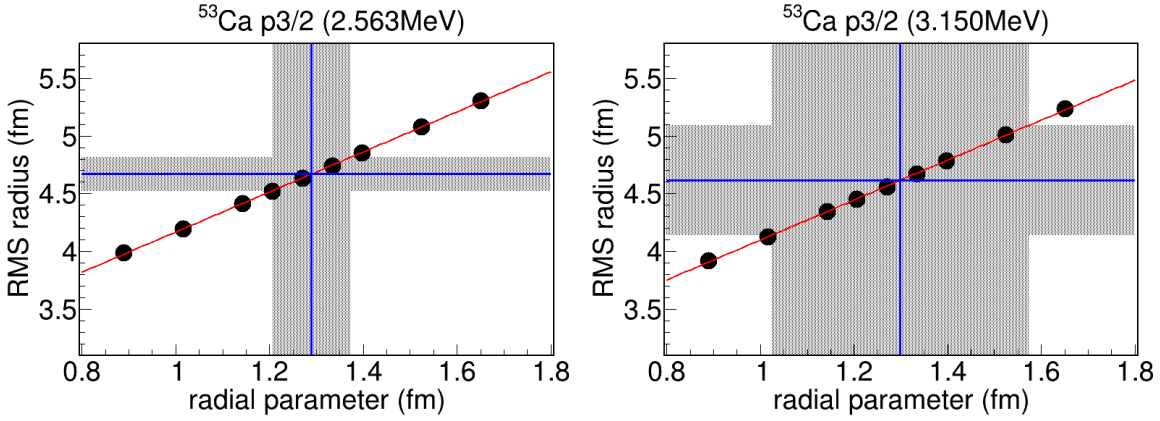

Figure 3.29: The rms radius as a function of the radial parameter for the $p_{3/2}$ neutron orbital of ^{53}Ca. The blue lines show the optimum radial parameter value obtained from the momentum distribution analysis of the ^{53}Ca(p,pn)^{52}Ca reactions and the resulting rms radius, respectively, obtained using the interpolation linear function (red line). The grey areas show the 1-σ uncertainty intervals for both the radial parameter and the rms radius. The plots are given for the 2.563 MeV excited state (left) and the 3.150 MeV excited state (right) of ^{52}Ca.

parameter. If the sensitivity is high, the curves would be very different as a function of the radial parameter and the χ^2 distribution would have a sharp minimum at the r_0=1.27 fm. On the contrary, if the sensitivity is low and the shape of the PMDs does not vary a lot, the χ^2 distribution would be flat. The transformation from χ^2 to a probability distribution of the form: $P = C \cdot exp(-\chi^2/2)$ gives us the sigma value of the distribution by fitting with a Gaussian function. The obtained sigma values, listed in Table 3.7 are considered as a measure of sensitivity (low sigma value for a high sensitivity). The equivalent uncertainties for the rms radii were also derived from the relation between the rms radii and the radial parameter. For one of the orbitals, the normalization to 10^6, 10^5, and 10^3 events was also tested. One can observe that the uncertainties of the rms radii obtained with the presented method are dominated by statistical uncertainties of the experiment. The p and f orbitals show small differences: the uncertainties using the parallel (perpendicular) component only are smaller for p (f) orbitals compared to using the perpendicular (parallel) component only. If one looks at the results using both parallel and perpendicular components, the uncertainties are slightly lower for the f orbitals compared to the p orbitals; and generally, the uncertainties are lowered if one uses both the parallel and perpendicular components of the momentum distribution as opposed to using only one of the components.
In some cases during the data analysis, both parallel and perpendicular experimental PMDs could be used, but in other cases one of them would lead to nonphysical results such us no minimum for the χ^2 distribution within the 1.27$\pm$30% fm range of the radial parameter. In those situations only the parallel or only the perpendicular momentum distributions were used. An additional check for each case was done by comparing the width of the parallel momentum distribution of the experimental data to the width of the theoretical curve obtained with the best fitting radial parameter value. The results for each single-particle neutron orbital are presented in this section.

$p_{3/2}$ neutron orbital of ^{53}Ca

During the $p_{3/2}$ neutron knockout off ^{53}Ca we populate two different final states of ^{52}Ca, at 2563 keV and 3150 keV excitation energy. One can use the information from the corresponding momentum distributions and obtain the rms radius of the $p_{3/2}$ independently from the two final state channels. For the 2563 keV final state, both momentum distributions showed good sensitivity and the optimum radial parameter of 1.29(8) fm was obtained. With this value, the rms radius of the $p_{3/2}$ neutron orbital is found at 4.67(15) fm. For the 3150 keV final state, the resulting optimum radial parameter is 1.30(28) fm (using both PMDs), which results in a value for the rms radius of 4.62(48) fm. The plots with the rms radius vs. radial parameter for both final states are shown in Figure 3.29. The black circles show the rms radius for each radial parameter value that was given as an input of the calculations. The red lines show an interpolating linear function. The vertical blue line show the position of the optimum radial parameter value obtained by the χ^2 minimization analysis and the grey vertical region shows the $\pm$ 1-σ interval. The horizontal blue line and grey region show the rms radius value and its $\pm$ 1-σ interval obtained using the interpolating linear function. The

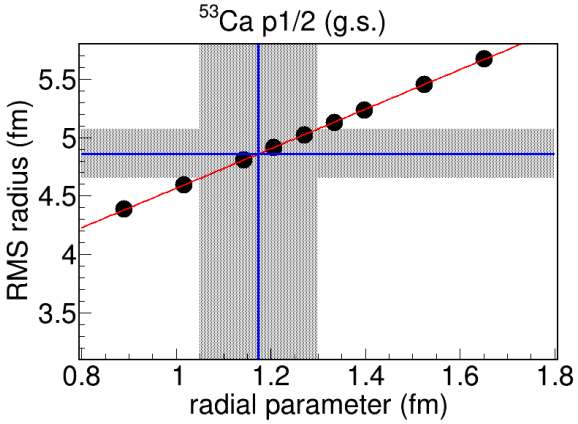

Figure 3.30: The rms radius as a function of the radial parameter for the $p_{1/2}$ neutron orbital of ^{53}Ca. The red line is an interpolation linear function. The blue lines show the optimum radial parameter value obtained from the momentum distribution analysis and the resulting rms radius, respectively. The grey areas show the 1-σ uncertainty intervals for both the radial parameter and the rms radius.

errors using the 3150 keV final state are larger than for 2563 keV. Nevertheless, the two values obtained independently for the $p_{3/2}$ orbital agree with each other and also they agree within 1-σ uncertainty with the 4.74(18) fm value obtained for $p_{3/2}$ neutron orbital of ^{52}Ca. Although the probed neutron orbital is the same, the final state of ^{52}Ca is different in the two cases. Thus the data from the two final states is not combined for obtaining a common rms radius value, but rather the obtained rms radius values will be kept separately.

$p_{1/2}$ neutron orbital of ^{53}Ca

For the knockout of the $p_{1/2}$ neutron orbital of ^{53}Ca, which is the last neutron orbital below the Fermi level, the ^{52}Ca fragment in left the ground state. For this case the optimum radial parameter was found to be 1.17(13) fm, and the rms radius for the $p_{1/2}$ neutron orbital was found to be 4.86(21) fm. The value was obtained using only the perpendicular momentum distribution for its better sensitivity to the radial parameter variation. The rms radius vs. radial parameter plot used for the determination of the $p_{1/2}$ neutron orbital size is shown in Figure 3.30.

$f_{7/2}$ neutron orbital of ^{53}Ca

For the $f_{7/2}$ neutron orbital we have again two independent data sets for obtaining the rms radius. Via the neutron knockout from the $f_{7/2}$ orbital, we populate the 5940 keV excited state of ^{52}Ca. This state has two decay branches (Figure 3.18) from which one could obtain the momentum distributions. The both decay branches have relatively low statistics, but the second decay branch presents high statistical fluctuations. Despite the low statistics, due to the increased sensitivity of the f-wave PMDs to the radial parameter, one could obtain a value of 1.20(6) fm for the optimum radial parameter for the first decay branch using both the parallel and perpendicular components successfully. With this value, one obtains the rms radius

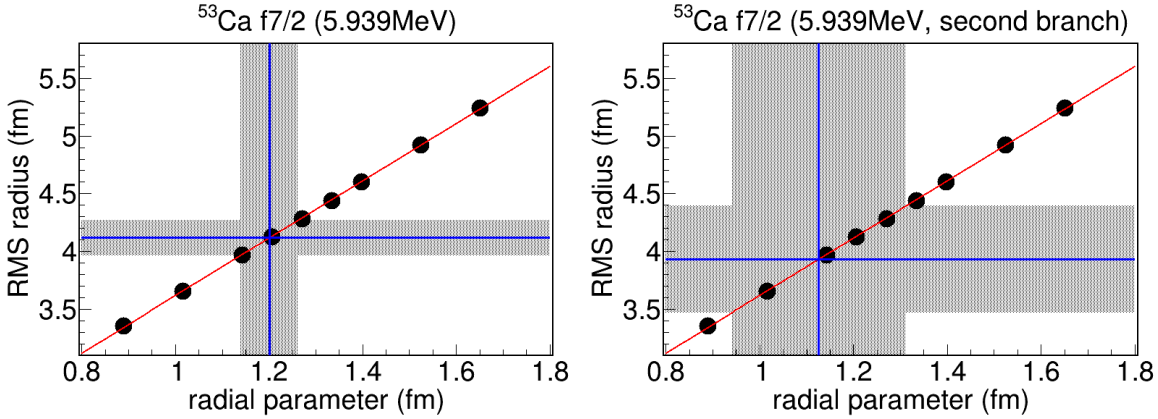

Figure 3.31: The rms radius as a function of the radial parameter for the $f_{7/2}$ neutron orbital of ^{53}Ca. The red line is an interpolation linear function. The blue lines show the mean values and the grey areas show the 1-σ uncertainty intervals for both the optimum radial parameter the resulting rms radius. The two plots show the results for the two decay branches of the 5.939 MeV excited state of ^{52}Ca.

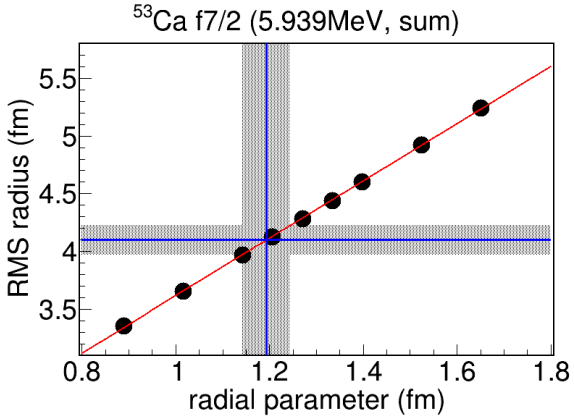

Figure 3.32: The rms radius as a function of the radial parameter for the $f_{7/2}$ neutron orbital of ^{53}Ca (sum of the two decay branches). The labeling is the same as for Figure 3.31.

value of 4.12(15) fm for the $f_{7/2}$ neutron orbital of ^{53}Ca. For the second decay branch, only the parallel momentum could give a good χ^2 minimization analysis, the statistical fluctuations being too high for the parallel momentum component. In this case a value of 1.13(19) fm was obtained for the optimum radial parameter and 3.93(46) fm for the rms radius. The rms radius vs. radial parameter plots for the two decay branches are shown in Figure 3.31. The two independently obtained values agree with each other, but the uncertainties are much higher for the second decay branch. The results using the sum of the two decay branches are the following: 1.19(5) fm for the optimum radial parameter and 4.10(13) fm for the rms radius. The rms radius vs. radial parameter plot for the sum of the two decay branches is shown in Figure 3.31. The results using the sum of the two decay branches give a smaller uncertainty. The same analysis was also carried for the potential neutron knockout of an $f_{5/2}$ neutron

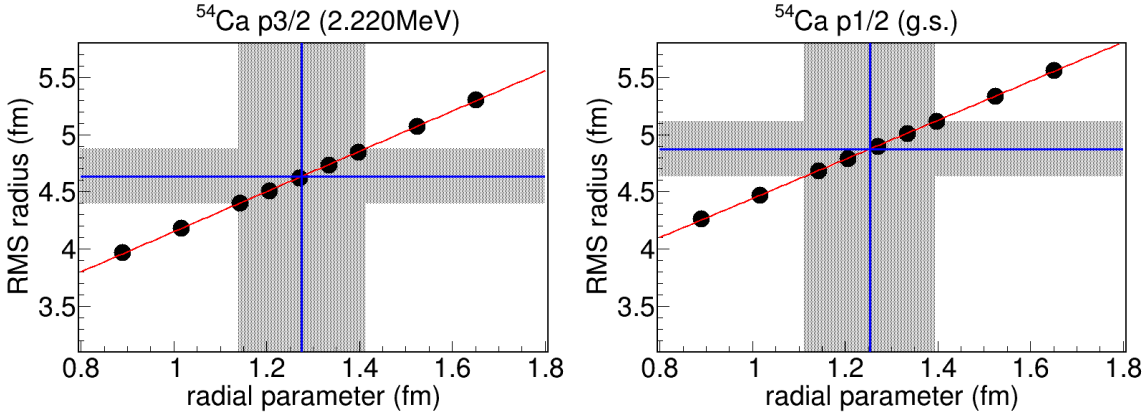

Figure 3.33: The rms radius as a function of the radial parameter for the $p_{3/2}$ (left) and $p_{1/2}$ (right) neutron orbitals of ^{54}Ca. The red line is an interpolation linear function. The blue lines show the optimum radial parameter value obtained from the momentum distribution analysis and the resulting rms radius, respectively. The grey areas show the 1-σ uncertainty intervals for both the radial parameter and the rms radius.

populating the 5940 keV state, which gave the following results: optimum $r_0 = 1.24(7)$ fm with rms radius of 3.97(15) fm from the first decay branch and optimum $r_0 = 1.24(17)$ fm with rms radius of 3.97(39) fm from the second decay branch. This check shows that even if the single-particle configuration of this state would be different than the assigned one, the difference between the determined rms radii of the p and f neutron orbitals in ^{53}Ca is similar.

$p_{3/2}$ neutron orbital of ^{54}Ca

Moving on to ^{54}Ca and its $p_{3/2}$ neutron orbital, we face again the negative effect of the low sensitivity of the p-wave momentum distributions to the radial parameter. For this case, a value of 1.28(14) fm was obtained for the optimum radial parameter. The rms radius vs. radial parameter plot is shown in Figure 3.33. Only the perpendicular momentum component could lead to a physical resulting value of the χ^2 minimization analysis. With this value, the rms radius of the $p_{3/2}$ neutron orbital of ^{54}Ca was found to be 4.64(24) fm. The determined rms radius value is showing consistency with the results found for ^{52}Ca and ^{53}Ca.

$p_{1/2}$ neutron orbital of ^{54}Ca

The $p_{1/2}$ neutron orbital of ^{54}Ca is studies using the ground state population momentum distributions of the ^{54}Ca(p,pn)^{54}Ca reaction. As in the case of the $p_{3/2}$ neutron orbital, one could only use the χ^2 distribution from the perpendicular momentum component for obtaining a physical value for the optimum radial parameter. The obtained value is 1.25(14) fm. The rms radius vs. radial parameter plot is shown for this case in Figure 3.33. The rms radius value for the $p_{1/2}$ neutron orbital of ^{54}Ca is 4.88(24) fm, in very good agreement with the value for the $p_{1/2}$ neutron orbital of ^{53}Ca.

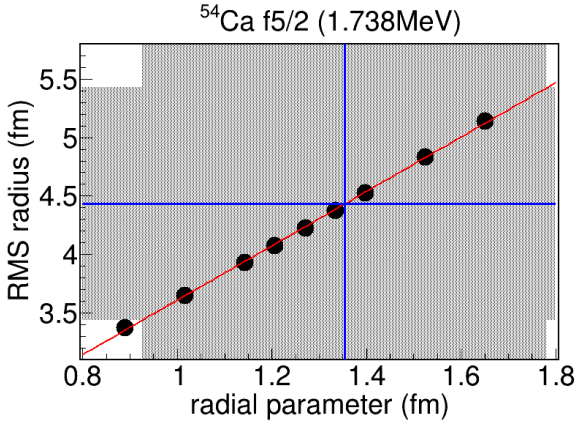

Figure 3.34: The rms radius as a function of the radial parameter for the $f_{5/2}$ neutron orbital of ^{54}Ca. The red line is an interpolation linear function. The blue lines show the optimum radial parameter value obtained from the momentum distribution analysis and the resulting rms radius, respectively. The grey areas show the 1-σ uncertainty intervals for both the radial parameter and the rms radius.

$f_{5/2}$ neutron orbital of ^{54}Ca

The momentum distribution for the $f_{5/2}$ neutron orbital has the least statistics in this analysis. A value for the optimum radial parameter could still be found, using only the parallel momentum component, as it was the case for the second decay branch of the 5940 keV state of ^{52}Ca for $f_{7/2}$ neutron orbital of ^{53}Ca. The optimum radial parameter is 1.35(43) fm and the rms radius was found to be 4.43(100) fm. The rms radius vs. radial parameter plot for this case is shown in Figure 3.34. The rms value was obtained with very large uncertainties due to the small statistics, but the χ^2 minimization analysis could converge in a good physical region because of the high sensitivity of the momentum distributions on the radial parameter for the

N \ orbital	RMS radius (fm)			
	$f_{7/2}$	$p_{3/2}$	$p_{1/2}$	$f_{5/2}$
32	4.13(14)	4.74(18)		
33	4.10(13)	4.67(15) 4.62(48)	4.86(21)	
34		4.64(24)	4.88(24)	4.43(100)
32 (SKM)	4.12	4.49	4.59	4.31
34 (SKM)	4.13	4.58	4.91	4.44

Table 3.8: Table with the rms radii of the neutron single-particle orbitals in the pf-shell of calcium isotopes. The first column shows the neutron number. Columns 2-5 show the rms radius values for the $f_{7/2}$, $p_{3/2}$, $p_{1/2}$, and $f_{5/2}$ orbitals in units of fm. The 1-σ uncertainty is given in the round parentheses. The last two rows show the values calculated using HFB with the SKM interaction for comparison.

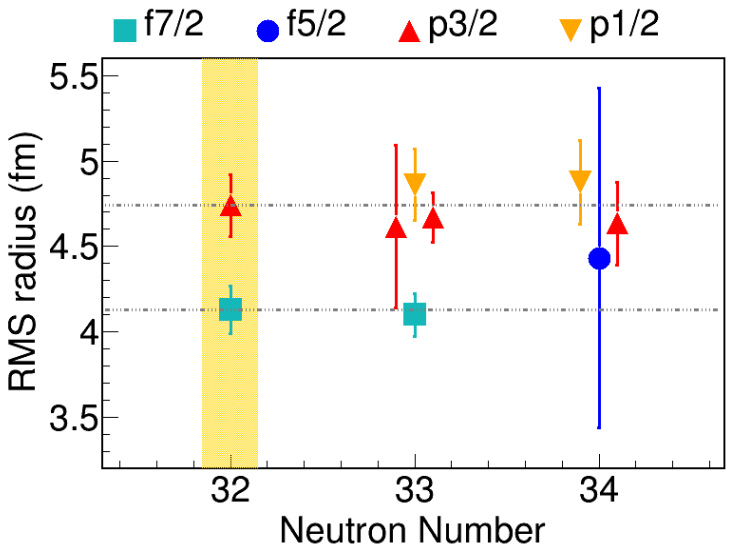

Figure 3.35: The systematics of rms radii of neutron single-particle orbitals determined using the momentum distribution analysis. The values for the $f_{7/2}$, $p_{3/2}$, $p_{1/2}$, and $f_{5/2}$ neutron single-particle orbitals are given as a function of the neutron number for the calcium isotopes. The orange area marks the data for ^{52}Ca. The the horizontal dot-dashed grey lines are shown to guide the eye for comparing the results of the present analysis for ^{53}Ca and ^{54}Ca with the results of ^{52}Ca. The vertical lines give the 1-σ uncertainties for each data point.

f-wave. Because the 1738 keV state is so weakly populated, and the momentum distribution analysis has large errors, we cannot clearly state if it is a single-particle state.

The summary of the results for the rms radii is given in Table 3.8. Also, the resulting rms radii are plotted in Figure 3.35 for each neutron single-particle orbital as a function of the neutron number for the studied calcium isotopes.

From the systematics of the rms radii of the pf-shell orbitals (Figure 3.35), one can observe consistent results for ^{53}Ca and ^{54}Ca with the values obtained for ^{52}Ca. The p orbitals present rms radii larger than the f orbitals. Except for the large-uncertainty $f_{5/2}$ data point of ^{54}Ca, the data show a difference larger than 0.5 fm between the p and f orbitals. In Table 3.8, in the last two rows, one can see listed the values obtained from HFB calculations using the SKM interaction for comparison.

3.7 Conclusions

Using the momentum distribution analysis for proton-induced quasi-free neutron scattering reactions on ^{53}Ca and ^{54}Ca, one could obtain the rms radii of the $p_{3/2}$, $p_{1/2}$, $f_{7/2}$ and $f_{5/2}$ neutron single-particle orbitals in the framework of DWIA. This is an extension of the data analysis presented in the second chapter of this thesis. The (p,pn) reactions were measured at the RIKEN facility using a liquid hydrogen target and the MINOS TPC. Additionally, the final states of the fragments were tagged via γ-ray spectroscopy using the DALI2^{+} detector array. The beam and the fragment particles were selected and identified using BigRIPS and the SAMURAI spectrometers.

The following values were determined for the single-particle neutron orbital rms radii: for $p_{3/2}$, 4.67(15) fm (N=33), 4.62(48) fm (N=33), and 4.64(24) fm (N=34); for $p_{1/2}$, 4.86(21) fm (N=33) and 4.88(24) fm (N=34); for $f_{7/2}$, 4.10(13) fm (N=33); and for $f_{5/2}$, 4.43(100) fm (N=34). The resulting differences between the rms radii of the p and f orbitals in the A = 52, 53, 54 calcium isotopes of 0.5-0.95 fm are consistent with the prediction made by Bonnard *et al.* [7]. Within the uncertainties of the experiment and analysis, the $f_{7/2}$, $p_{3/2}$ and $p_{1/2}$ rms radii of the pf-shell single-particle neutron orbitals of ^{52}Ca, ^{53}Ca, and ^{54}Ca are consistent with each other.

4 Development of the STRASSE Silicon tracker and the cryogenic target

4.1 General overview

4.1.1 STRASSE

STRASSE is composed of a silicon tracker and a liquid hydrogen target and it is designed for studying proton induced quasi-free knock-out reactions, (p,2p) and (p,3p), in inverse kinematics. **STRASSE** stands for **S**ilicon **T**racker for **RA**dioactive nuclei **S**tudies at **S**AMURAI **E**xperiments. As the name suggests, the experimental setup is foreseen to be used at SAMURAI experiments at the RIBF facility, Japan. Moreover, STRASSE is designed to be compatible with CATANA [11], a CsI detector array. A drawing of the STRASSE silicon tracker and the liquid hydrogen target, placed inside the CATANA detector array is shown in Figure 4.1. The grey-colored cylinder is the liquid hydrogen target and two layers of silicon sensors are shown with dark blue and magenta. The vacuum chamber is shown with grey-purple and layers L2-L7 of CATANA are also shown around the vacuum chamber. The figure is from the overview paper of STRASSE [10]. The STRASSE silicon tracker has two layers of double-sided silicon strip sensors arranged in a hexagonal geometry. A side of a hexagonal layer is composed of 2 sensors in order to cover a length of almost 300 mm. The active width of each side of the hexagonal outer layer is 62.6 mm, while for the inner layer the active width is 30 mm. The active length of each sensor of the outer (inner) layer is 122 (121) mm. The distance from

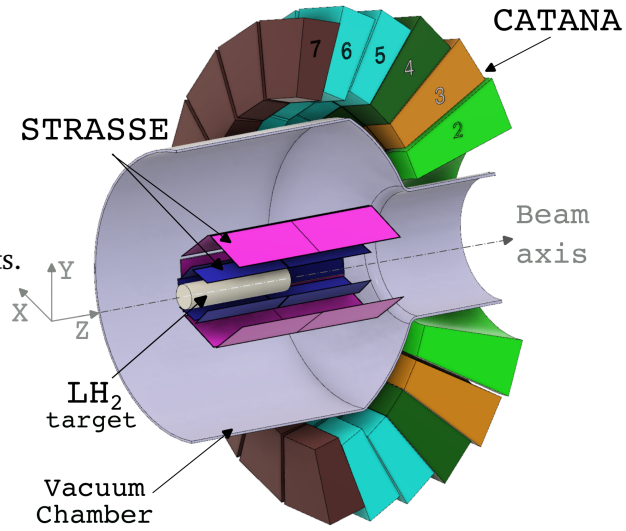

Figure 4.1: Drawing of STRASSE with the silicon tracker and the liquid hydrogen target. The CATANA detector array is found around the reaction chamber. Figure reprinted with the permission from [10]© CC-BY-4.0.

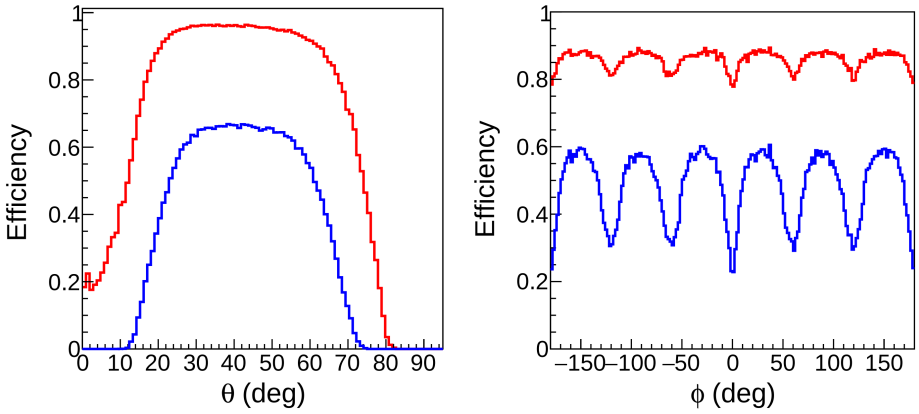

Figure 4.2: The detection efficiency of the STRASSE silicon tracker. The efficiency is plotted as a function of the azimuthal angle θ (left) and of the polar angle ϕ (right). The red curves represent the efficiency for one proton detection and the blue curves represent the efficiency for two protons detection. Figure reprinted with the permission from [10]© CC-BY-4.0.

the center to the outer layer is 60.5 mm and to the inner layer is 28.5 . The thickness of the silicon sensors is 300μm (200μm) for the outer (inner) layer with a pitch size of 200μm. The silicon tracker will reconstruct the trajectories of the protons and the reaction vertex for proton-induced knock-out reactions. The geometry of the silicon layers and the placement of the readout electronics have been optimized in order to reduce the inactive material along the protons' trajectories. The resulting angular coverage is shown in Figure 4.2. The detection efficiency integrated over the angles for two protons detection in a (p,2p) reaction is 49% and for the detection of at least one proton detection, the efficiency goes up to 86% [10]. The vertex reconstruction resolution obtained from simulations with the STRASSE silicon tracker coupled with the 15-cm-long liquid hydrogen target is σ_{vertex}=0.17 mm [10].

For the measurement of the total energy of the protons and also for the detection of γ rays, CATANA [11] will be used and placed around the STRASSE reaction chamber, as shown in Figure 4.1. The coupling of STRASSE with CATANA allows for missing mass measurements, complementary to invariant mass measurements at the SAMURAI experimental area. The missing mass for a (p,2p) reaction can be calculated as:

$$E_x = \sqrt{(E_{beam} + E_{target} - E_{p1} - E_{p2})^2 - (\vec{P}_{beam} - \vec{P}_{p1} - \vec{P}_{p2})^2} - M_{fragment} \tag{4.1}$$

The STRASSE setup together with CATANA is able to measure all the quantities entering into the missing mass expression. The expression includes E_{beam}, E_{target}, E_{p1}, E_{p2}, the total energies of the beam, the target and the two detected protons, as well as $\vec{P}_{beam}$, $\vec{P}_{p1}$, $\vec{P}_{p2}$, which are the momenta of the beam and the two protons, and $M_{fragment}$ being the mass of the fragment resulting from the (p,2p) reaction. The missing mass measurement will give information on the excitation energy of the fragments in the final state. The simulated missing mass resolution is σ_{Ex}= 1.7 MeV [10].

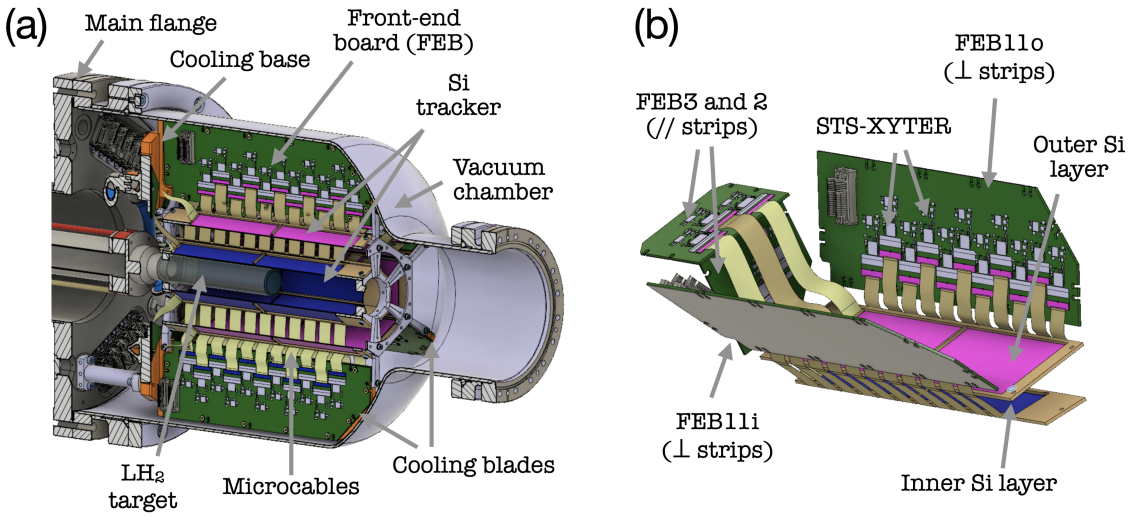

Figure 4.3: Geometry of the silicon tracker and the electronics of STRASSE. (a) A section view of STRASSE. One finds the liquid hydrogen target, the two layers of silicon sensors (blue and magenta) and the front-end boards electronics (green). (b) One sixth of the STRASSE system. One sees the geometry of the silicon sensors and the electronics. The ASICs (STS-XYTER) for readout receive the signals from the sensors via microcables shown with yellow. Figure reprinted with the permission from [10]© CC-BY-4.0.

The readout electronics, based on the XYTER2.2 (**X**-**Y** coordinate, **T**ime and **E**nergy **R**esolution) chip [119], will be mounted on supports going radially outwards in the cylindrical symmetry of the silicon tracker, filling in the dead areas between the sensors. The strips perpendicular to the beam of the sensors on the outer layer will be read out by 11 XYTER chips for the outer layer and another 11 chips for the inner layer for each side of the hexagon. The strips parallel to the beam are read out only from one end and the strips are daisy-chained. These strips are readout by 3 XYTER chips for the outer layer, and 2 XYTER chips for the inner layer. The signals from the Si sensors are carried to the FEBs (front-end boards) via custom-made Microcables. These cables have a low capacitance, are flexible and light, complying with the constrained geometry of STRASSE. The arrangement of the read-out electronics with the XYTER chips and the Microcables is shown in Figure 4.3, sourced from [10].

The choice of ASIC (application-specific integrated circuit) was based on the low dead time ($0.8\mu s$), good time resolution (3.125ns), low power consumption (<8 mW per channel), low noise and the dynamic range (0-15 fC in STS mode and 0-100 fC in MuCH mode) of the XYTER chips. The energy deposited in the silicon sensors ranges from ∼100 keV to ∼1 MeV. This energy range fits the MuCH mode dynamic range of the XYTER chips. A total of 162 ASICs will be used for STRASSE. For this amount of ASICs, active cooling is necessary. The cooling will be done by circulating water through the main flange and dissipate the heat from the electronics via the copper cooling blades supporting the FEBs (orange in the drawings of Figures 4.3 and 4.4).

A 150 mm-long liquid hydrogen target with a diameter of ∼30 mm is placed inside the silicon tracker. Using a high density proton target, as the liquid hydrogen target of this length, gives a high interaction yield for the studied reactions. The liquid hydrogen target, together with the cryostat used for cooling down the hydrogen, is a compact system (∼1 m in height), able to cool down in 12 hours and to perform empty target measurements with a fast refill afterwards. A full drawing of STRASSE and the cryostat is shown in Figure 4.4.

The STRASSE project (*Strasse* means *street* in the German language) starts with a prototype, **PFAD** (*path*), which is a smaller silicon tracker, equivalent to one third of the silicon tracker of STRASSE, with similar readout electronics. The back-end electronics and the timestamp integration with the RIBF system is being tested using the PFAD prototype before the final construction of STRASSE.

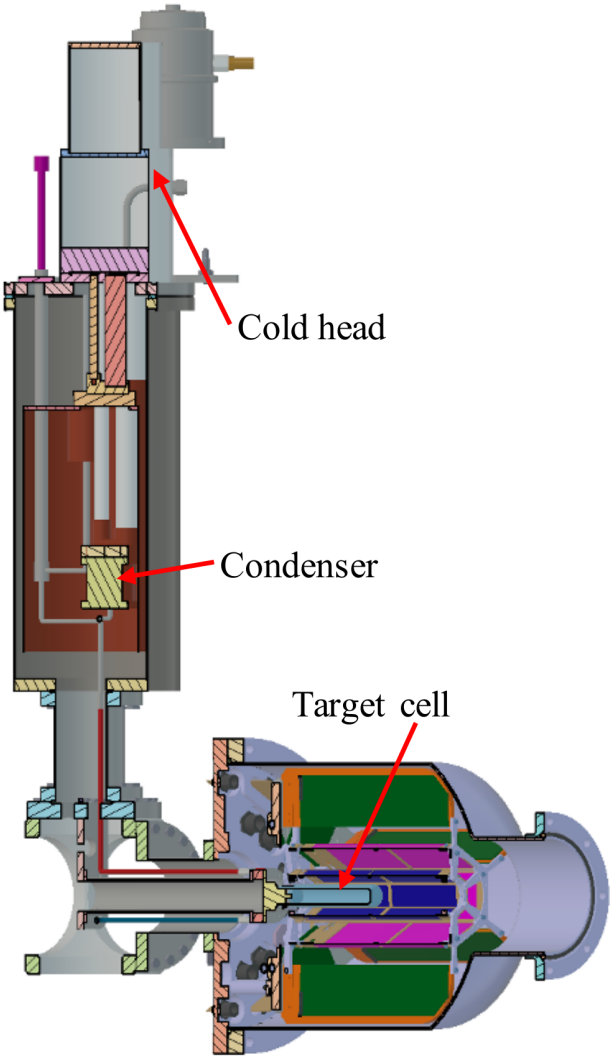

Figure 4.4: A full view of the STRASSE silicon tracker and the liquid hydrogen target together with the cryostat. Figure reprinted with the permission from [10]© CC-BY-4.0.

4.1.2 PFAD

PFAD, **P**rototype **f**or **A**dvanced **D**etectors, is a silicon tracker composed of four 2D planes, two of them on each side of the beam axis. A picture of the PFAD silicon tracker is shown in Figure 4.5 mounted on the reaction chamber flange. Each 2D plane is composed of two layers of one-sided silicon strip sensors, one layer with longitudinal strips and one layer with perpendicular strips to the beam direction. The sensors are 100μm in thickness with a pitch size of 100μm. As in the case of the STRASSE silicon tracker, each layer has two Si sensors covering an active area of $\sim$16 x $\sim$5 cm. The ones with longitudinal strips are daisy-chained and read out only at one end. All strips are read out in pairs of two, so the effective pitch size becomes 200μm. There are two XYTER chips mounted on the front-end boards for reading out the longitudinal strips (FEB2) and six XYTER chips mounted on the front-end boards for reading out the perpendicular strips (FEB6). A photo with one layer, composed out of one FEB6 with sensors with perpendicular strips and one FEB2 with sensors with parallel strips is shown in Figure 4.6 together with other close-up photos of the FEBs, sensors and the ceramic PCBs (green). The ceramic PCBs are used for distributing the bias voltage from the FEB to the silicon sensors. Moreover, the silicon sensors are supported by the ceramic PCBs by gluing. The ceramic PCBs are glued onto the aluminum frame of the detector module. The layer of glue ensures adhesion as well as a small degree of flexibility and shock absorption. The strips are bounded to the ASIC via a pitch adapter (white strip before each XYTER chip in the photos of Figure 4.6). Between the FEBs and the aluminum frames a thermal sheet is used for thermal conductivity needed for dissipating the heat from the ASICs. PFAD is a modular system, each detector module composed of FEB2/6 with the corresponding sensor mounted on the aluminum frame can be stored and transported separately, also allowing for easy replacements with spare parts in

Figure 4.5: Picture of the PFAD silicon tracker assembled at TU Darmstadt.

Figure 4.6: Photos of the front-end boards for PFAD. Top-left: One layer of the PFAD silicon tracker. Top-right: Close-up photo of FEB2, FEB6, the ceramic PCBs and the silicon sensor. Bottom-left: The daisy-chained area between the two sensors for the parallel strips of one layer. Bottom-right: Close-up photo of FEB6.

case it is needed. There are two thick aluminum cooling blocks for each arm of the silicon tracker, on each side of the beam axis. These blocks ensure the support of the silicon tracker as well as the cooling of the electronics. The detector modules are secured on the cooling blocks using 3 screws and there is a thermal sheet added between the aluminum frames and the cooling block as well.

The front-end boards were adapted after the *FEB8* used for STS from the CBM collaboration. The readout of PFAD is done via the GBTxEMU board [121], based on Artix7 FPGA. The FEBs communicate with the GBTxEMU board via LVDS signals. One downlink with the clock (80 MHz) and data LVDS signals is shared by a FEB2 and a FEB6 of each layer of the silicon tracker. The downlink signals are going from the GBTxEMU board via the feed-through PCB, found on the reaction chamber flange, to FEB6 and then to FEB2. Each XYTER chip sends data via one uplink to the GBTxEMU board. For the uplink and downlink LVDS signals 1.75-mm pitch flat ribbon cables are used inside the reaction chamber with pin-header connectors and flat flexible ribbon for outside the reaction chamber with ZIF connectors. On the GBTxEMU

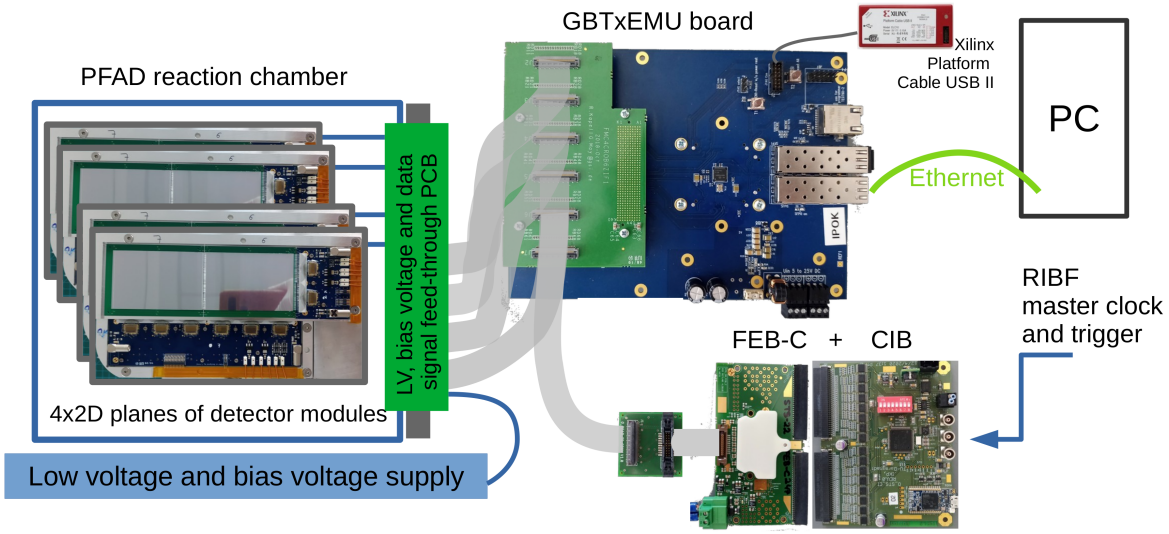

Figure 4.7: Schematics of the PFAD electronics for the full silicon tracker consisting of four 2D planes. The data signals are routed via a feed-through PCB between the GBTx-EMU board and the FEBs. The green card on the GBTxEMU board is the FMC-to-ZIF adapter. Through the feed-through PCB the low voltage and bias voltages are also supplied. FEB-C and the CIB are used for integrating the RIBF timestamp from the LUPO module into the PFAD DAQ.

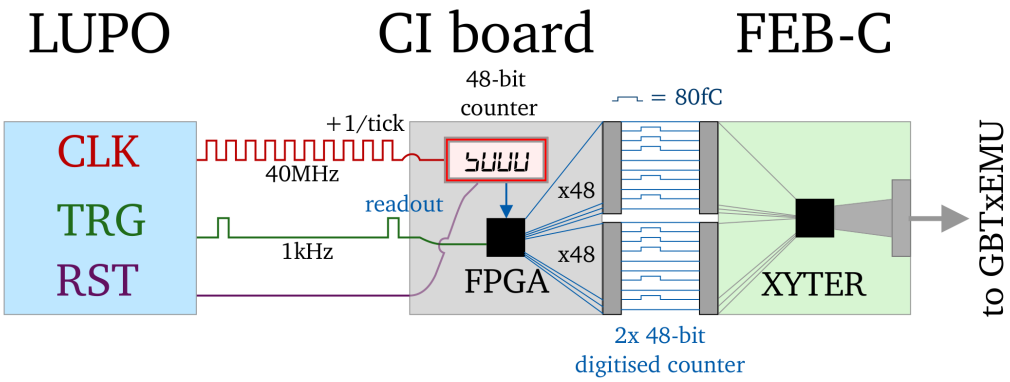

Figure 4.8: Schematics of the RIBF timestamp integration into the PFAD DAQ via the FEB-C. Source of the figure: PhD Thesis of A. Frotscher [120]© CC-BY-SA-4.0.

board a FMC-to-ZIF adapter board is used. A schematics of the PFAD configuration is shown in Figure 4.5. The GBTxEMU board is programmed with a custom pre-compiled firmware via JTAG using Xilinx Platform Cable USB II and Vivado SDK software. The GBTxEMU board is connected via Ethernet to the PC. For the control and DAQ the IPbus [122] protocol, as well as STS-HTCP [123] protocol are used. The control and DAQ scripts are written in Python3.

The readout electronics of PFAD is a trigger-less system. In order to synchronize with the RIBF DAQ system at RIKEN, an additional ASIC is used for registering the trigger timestamp coming from the RIBF DAQ system, via LUPO module. The ASIC is an XYTER2.2 chip as the ones used on FEB2 and FEB6, but mounted alone on a board that can receive signals for each channel of the XYTER chip via two ERNI connectors. A charge injection board (CIB) will inject pulses in the 128 channels of this ASIC encoding the timestamp. The timestamp is 48-bit long and it is injected two times, in the first 64 channels and in the last 64 channels of the ASIC, using a duplicated pattern allowing to reconstruct the correct timestamp in case of a channel failure. The timestamp is injected binary: 0 if channel not fired and 1 if channel fired. The amplitude of the injected signals of 80 fC is close to the upper end of the energy range of the ASIC in the MuCH mode for ensuring that all channels are fired regardless of the chosen energy range during the experiment. A schematics of the integration of the RIBF timestamp into PFAD/STRASSE is shown in Figure 4.8, image from Ref. [120].

The purpose of the prototype detector, PFAD, is to perform test measurements and to help design an improved version of the electronics for STRASSE. Part of the work and tests done with PFAD are presented in the PhD thesis of A. Frotscher [120].

In the next section of this chapter, the PFAD detector modules characterisation and commissioning will be presented. The detectors modules are calibrated in energy and the linearity of the calibration is tested. The electronic noise level of the detectors is also measured and an offline measurement with an ^{241}Am γ-ray source is performed. The PFAD silicon tracker is commissioned in an in-beam experiment at the HIMAC facility in Japan. The results of the vertex reconstruction performance of PFAD from the online analysis are presented. Section 4.3 presents the production method of the liquid hydrogen target used for STRASSE. After production, the target cells are stress-tested at high pressure and at cryogenic temperatures. Additionally, in the same section, the results of the vacuum simulations performed for the reactions chamber of STRASSE will be shown. Both the above-mentioned sections present original work done during this PhD study.

4.2 PFAD - the prototype of STRASSE

4.2.1 Detector module characterisation

XYTER2.2 chips (or SMX2.2)

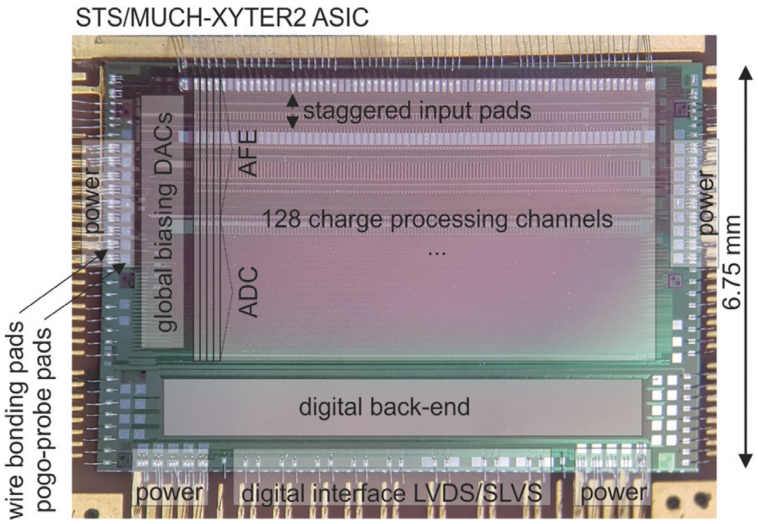

Figure 4.9: The XYTER2.2 chip with a simplified diagram. Figure reprinted with the permission from [119] ©2023 by Elsevier.

The XYTER2.2 chip is an ASIC designed for the STS and MuCH detector systems of the CBM collaboration. The chip has a compact size of 10 mm × 6.75 mm and it is designed to be radiation-hard. The XYTER2.2 chip is able to read out 128 channels, has two additional test channels and it has an internal pulse generator used for calibrations. The ASIC has two dynamic ranges, 1-15 fC for the STS mode and 0-90 fC for the MuCH mode. It features a 5-bit ADC and 14-bit timestamp reaching a nanosecond-range accuracy for the time measurement and it is designed for high-rate (>500 kHz) measurements. A picture of the XYTER chip with a simplified diagram is shown in Figure 4.9. Additionally in Figure 4.10, one finds the diagram of one out of the 128 analog front-end channels of the XYTER chip.

The accepted input signal can have both negative (electrons) or positive (holes) polarity. The input signal (as well as the ones generated by the internal pulser) goes first through the charge sensitive amplifier (CSA). For the two dynamic ranges, the amplifier uses two gain modes: 9.2 mV/fC (STS) and 1.6 mV/fC (MuCH). After this, the polarity selection circuit (PSC) will simply pass further the positive signals or invert the negative signals, as one can see on the diagram in Figure 4.10. The signal is then processed using two parallel paths, one with a fast shaper followed by a discriminator with a comparator (global threshold) used for the timestamp determination (signal with positive amplitude). The second path has a slow shaper followed by 31 ADC comparators obtained by a resistors ladder stretched between two reference voltages (VrefP and VrefN) with an effective threshold set by VrefT (signal with negative amplitude). The VrefP, VrefN, VrefT and the global threshold values can be

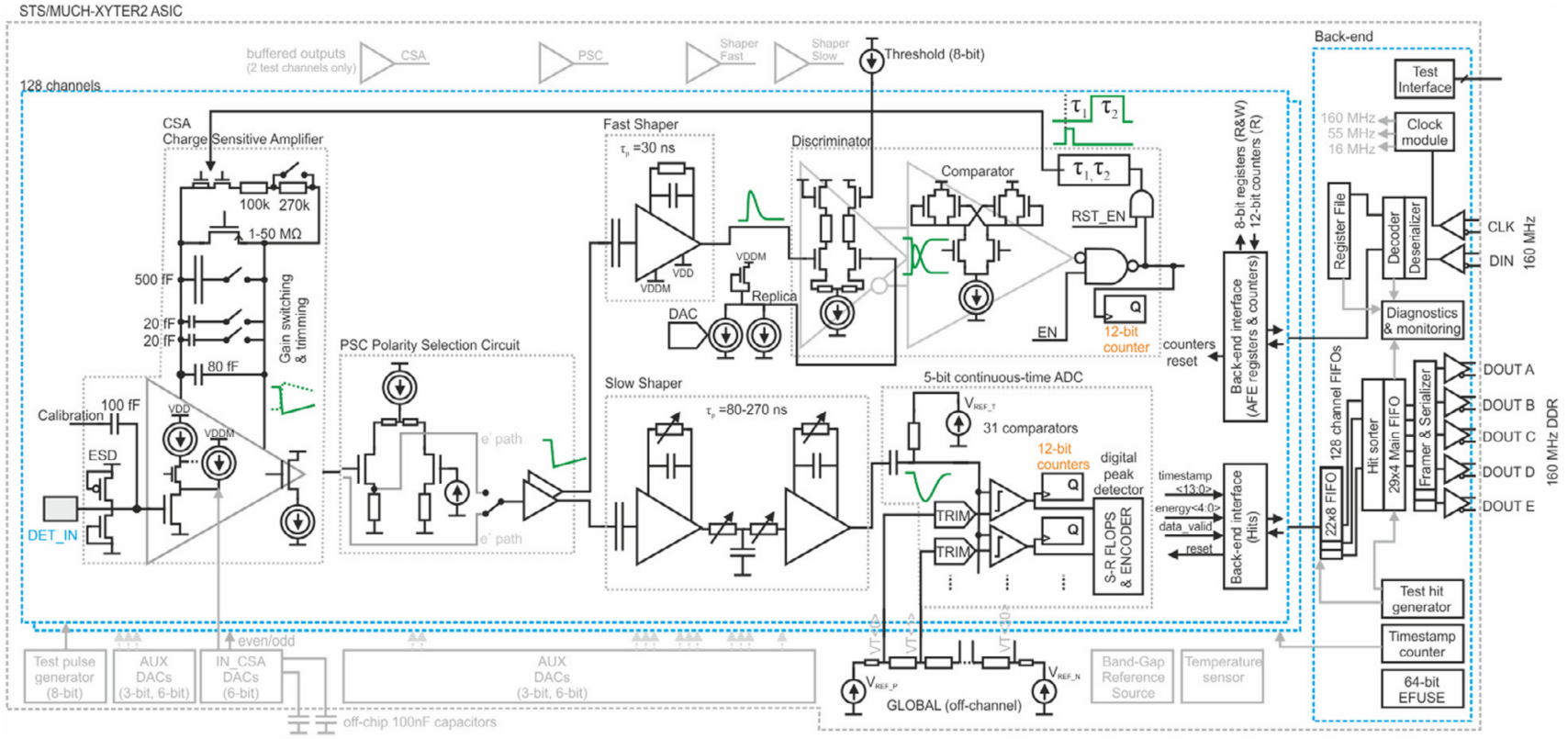

Figure 4.10: Diagram of one analog front-end channel in the XYTER2.2 chip. Figure reprinted with the permission from [119] ©2023 by Elsevier.

set for the entire chip, and not for individual channels (marked outside the blue dashed line representing one channel in Figure 4.10). After the signal is registered by the fast comparator, there is a waiting time until the signal passed through the slow comparators. If the signal is also registered by the slow comparators, we get a signal with complete information, time and energy. If the signal is not registered in the slow comparators, the signal has only time information. But typically the ASICs are configured such that the fast comparator and the first slow comparator match in the detected signal amplitude. By doing so, the detected signals it will have complete information. More details about the STS-XYTER chip are found in Ref. [119].

Energy range and the trim calibration

For the experiments with PFAD we are interested in an energy range up to 1.2 MeV, which corresponds to $\sim$53 fC. This means that we need to use the MuCH dynamic range of the XYTER chips. In order to obtain the same ADC characteristics for all channels, each of the 31 ADC discriminators can be corrected by a trim value (marked as "TRIM" on the diagram in Figure 4.10). The energy and trim calibration is performed using the internal pulse generator. The amplitude of the pulses can take values from 0 to 255 units, covering the range of the selected dynamic range of 0 to 90 fC. In our case, we aim to calibrate the first and last ADC discriminators such that they trigger at pulses of amplitudes between $\sim$100 keV and 1200 keV (13 to 150 in terms of the internal pulser units) and the rest of the ADC discriminators to be linearly distributed between these values. Once the VrefP and VrefN registers are set to take appropriate values for the aimed energy range, a scan is performed for all channels and ADC discriminators of each ASIC in which the trim value for each ADC discriminator is varied. The ADC trim values range from 0 to 255 corresponding to a shift of -150 mV to +150 mV (a value of 128 means no shift, 0 mV). For each discriminator, the selected trim value is the one for which the discriminator triggers at the desired pulse amplitude. If no suitable trim value is found during this scan, it is a sign that the VrefP and VrefN registers were not set correspondingly for the aimed energy range. A similar procedure is done for the fast discriminator as well. Typically the fast discriminator is set to trigger at similar pulse amplitudes as the first ADC discriminator. The trim calibration, the linearity of the ADC discriminators and the electronic noise can be checked and characterized using the S-curve analysis described below.

S-curve analysis

The S-curve analysis involves performing a scan in which pulses of varying amplitudes are sent using the internal pulse generator and then the counts accumulated in each discriminator and channel of each ASIC are read from registers. One should observe that as the amplitude of the pulses increases, the ADC discriminators (and the fast discriminator as well) trigger gradually. In an ideal system, a discriminator should not trigger at all (zero counts) if the pulse amplitude is lower than the value for which that discriminator was calibrated and trigger each time for pulses above the calibrated one, forming a step function with respect to the pulse amplitude. In practice, because of the fluctuations of the base line due to electronic noise,

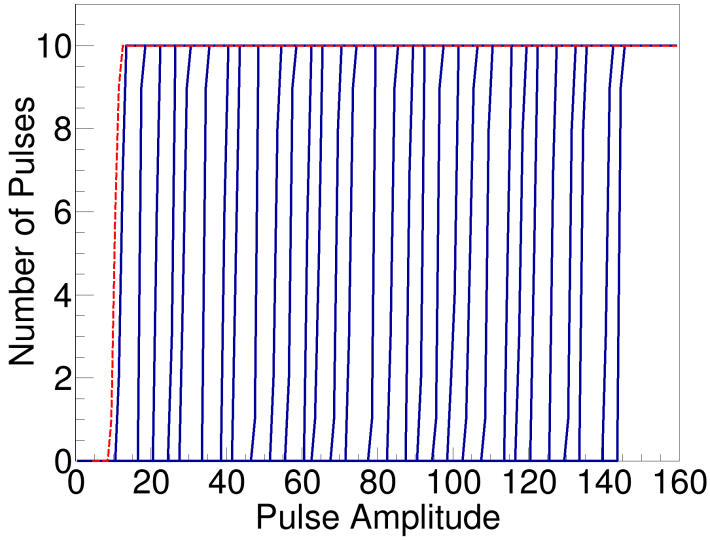

Figure 4.11: Example of S-curves for one channel of one XYTER chip obtained by performing an amplitude scan with the internal pulse generator, injecting 10 pulses for each amplitude value. The amplitude scan had an increment of one unit and a range from 0 to the maximum value of 255 (the plot shows the amplitude pulse only up to 160). The XYTER chip was calibrated for the amplitude range between 13 and 150 units in the MuCH mode. The solid blue lines correspond to the 31 ADC discriminators and the dashed red line corresponds to the fast discriminator.

one will observe S-curves instead of step functions. An example of S-curves for all ADC and fast discriminators of one channel as a result of an amplitude scan is shown in Figure 4.11.

As a result of the S-curve analysis one can get information such as ADC gain, ADC/fast discriminator deviation and electronic noise. The ADC gain is the distance in terms of the pulse amplitude between the ADC discriminators, or the slope:

$$ADC^{id}_{gain} = (A^{id}_{ADC} - A^{id=0}_{ADC})/id$$

with A being the pulse amplitude at which the discriminator triggers and id being the index of the discriminator going from 1 to 30. The amplitude is found using the S-curve as the position at 50% of the maximum number of injected pulses, or the mean value of the gauss-shape derivative of the S-curve. One expects here a constant value for the gain for all discriminators if the channel was linearly calibrated. In Figure 4.12, on the top row, one finds examples of ADC gain plots from three of the ASICs. The ADC gain is given in pulser amplitude units (0-255 corresponds to 0-$\sim$90 fC in MuCH mode). The values of the ADC gain are given for each of the discriminator of each channel, with the error bars coming from the determination of each A^{id}_{ADC}. The mean values of the ADC gain and the corresponding standard deviation value are given on each plot, showing consistency in the ADC gain from one channel to the

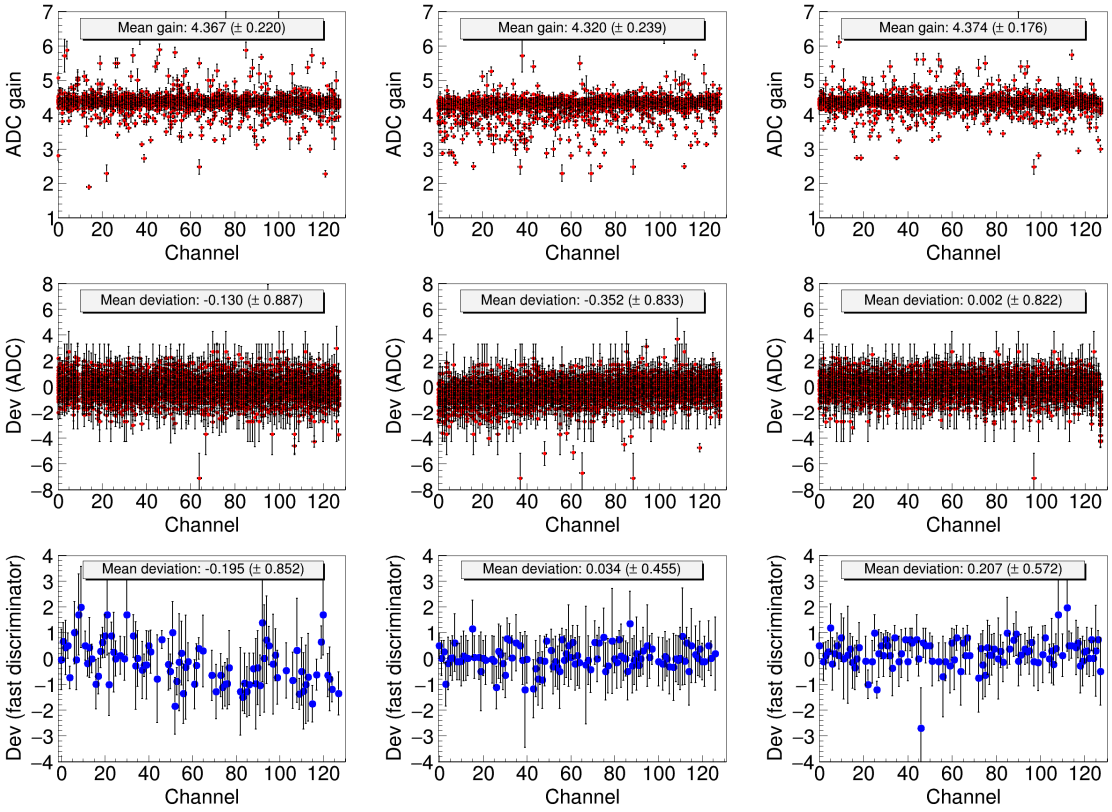

Figure 4.12: Example of ADC gain, ADC deviation and fast deviation plots from the S-curve analysis from three of the ASICs of the PFAD system.

other and from one ASIC to the other.

The ADC and fast discriminators deviation (Dev) shows the difference between the amplitude at which the discriminator triggers during the S-curve analysis and the amplitude at which it was calibrated to trigger:

$$Dev^{id} = A^{id} - A^{id}_{Calibrated}$$

for both ADC and fast discriminators. Example plots with the ADC and fast discriminator deviation are also shown in Figure 4.12 on the middle and bottom rows. The mean deviation (and the corresponding standard deviation of this value) is given on each of the plots. The deviations show little difference between the channels and the ASICs, evidencing the capability for performing a reliable trim calibration using the internal pulser.

The electronic noise, or the ENC level is an important quantity for the system. Based on the measured ENC values we can have a first idea on where to place the lower edge of the energy range. The ENC level is determined for each channel and discriminator as the σ-value of the gauss-shape derivative of the S-curve. The value is obtained in pulser amplitude

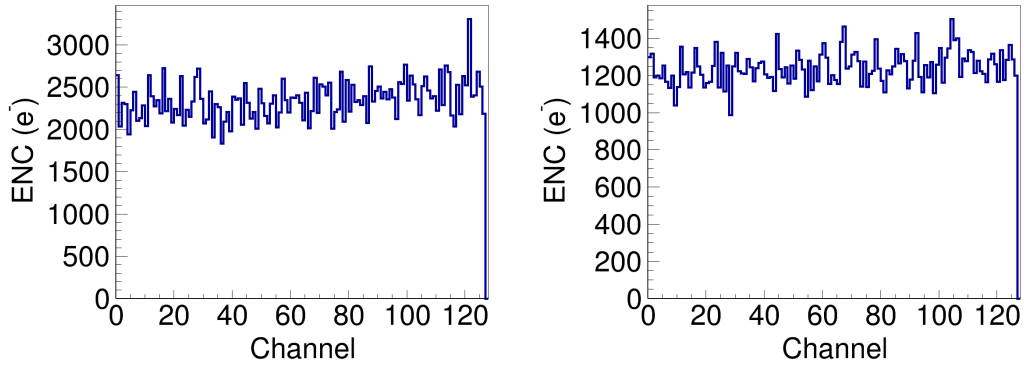

Figure 4.13: ENC level for ASICs mounted on a FEB2 (left) and a FEB6 (right) with the silicon sensors connected.

units and then it can be converted to the equivalent number of electrons. The ENC levels of each ASIC of the PFAD system are listed in Table 4.1. A difference is observed in the ENC level between the ASICs used on FEB2 and FEB6. The Figure 4.13 shows as an example the ENC level distributes over the channel number/strip for one ASIC on a FEB2 (left) and for one ASIC on a FEB6 (right). The difference between the two type of FEBs come from the length of the strips that are read out on each FEB type. The intrinsic ENC level of the ASIC before mounting the pitch adapters and the silicon sensors takes values of $\sim$375 e^-. From this value on, the ENC rises as a function of the input capacitance. On FEB2 the capacitance corresponding to each channel becomes larger than for FEB6. Also small variation appear between the ASICs also because of the variations in the sensor characteristics. The ENC level as a function of the input capacitance (on top of the intrinsic ENC level of the ASIC and pitch adapter) was found to take values of 27 e^-/pF (44 e^-/pF) for ADC (fast) by Ref. [119] and 24(1) e^-/pF for ADC, by Ref. [120]. The total ENC level (sigma value) as seen in Table 4.1 is of $\sim$1.2 ke^- (equivalent to 5 keV) for FEB6-type and double for FEB2-type. This sets the threshold at $\sim$30 keV for FEB6 and $\sim$60 keV for FEB2 if we require 6-σ threshold.

The S-curve analysis presented above was performed with the full PFAD system and 40 V bias voltage applied on each of the silicon sensors. The ENC level for no bias voltage applied takes very large values and then it gradually decreases as bias voltage is applied on the silicon sensors until it reaches a plateau. Figure 4.14 (right) shows this dependence for some of the ASICs used for PFAD. The red curves correspond to ASICs on FEB2-type boards and the blue ones for FEB6-type. Among the sensors for each FEB-type we observe how some of them show low ENC already from 10 V bias voltage, while others need more than 20 V to reach the low ENC level plateau.

Offline source measurement

As an offline measurement with PFAD we chose to look at the energy spectrum of an ^{241}Am source. It emits γ-rays at the energy of $\sim$59.6 keV. For these measurements we used the STS dynamic range and calibrated the ASICs for a narrow energy range around 60 keV. Figure 4.14

FEB type	FEB#	ASIC#	ENC (e^-)
FEB2	2	0	2410
FEB2	2	1	2402
FEB2	3	0	2197
FEB2	3	1	2296
FEB2	4	0	2663
FEB2	4	1	2566
FEB2	9	0	2177
FEB2	9	1	2343
FEB6	2	0	1306
FEB6	2	1	1302
FEB6	2	2	1279
FEB6	2	3	1264
FEB6	2	4	1356
FEB6	2	5	1307
FEB6	4	0	1288
FEB6	4	1	1241
FEB6	4	2	1233
FEB6	4	3	1281
FEB6	4	4	1288
FEB6	4	5	1310
FEB6	7	0	1255
FEB6	7	1	1281
FEB6	7	2	1222
FEB6	7	3	1307
FEB6	7	4	1288
FEB6	7	5	1253
FEB6	9	0	1298
FEB6	9	1	1264
FEB6	9	2	1315
FEB6	9	3	1267
FEB6	9	4	1253
FEB6	9	5	1250
FEB-C			987

Table 4.1: The ENC level for the full PFAD system. The first column shows the type of FEB 2/6 and the second column shows the index of the FEB. The third column shows the index of the ASIC, there are two ASICs on each FEB2 and 6 ASICs on each FEB6. Finally on the last column the ENC level is given in units of electrons, e^-.

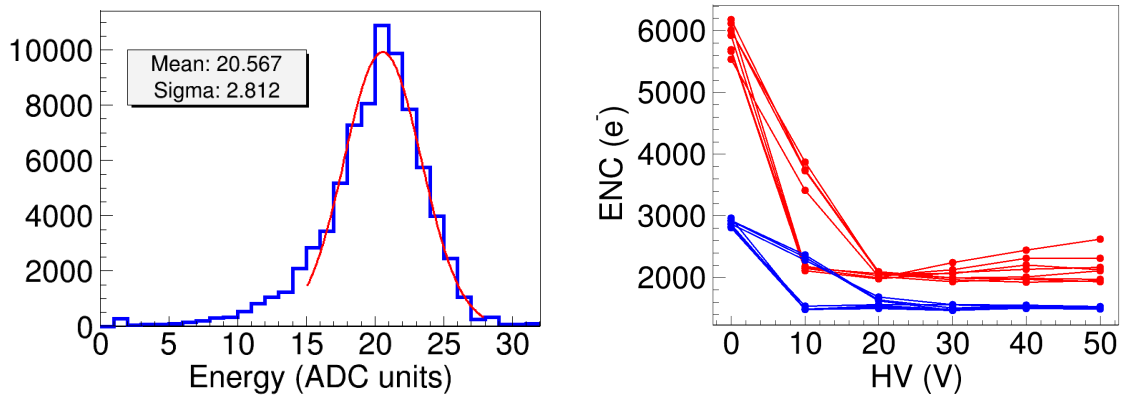

Figure 4.14: Left: offline source measurement with PFAD; the red curve is a fit with a Gauss function and the obtained mean and sigma values from this fit are shown on the figure. Right: ENC level dependence on the bias voltage for ASICs on FEB2 (red) or FEB6 (blue).

shows the measured peak in the FEB6 detector modules only. FEB2 modules have double ENC and so the 59.6 keV peak was covered with noise and could not be measured. Also, a tail towards low energy is visible in the spectrum which was observed by Ref [119]. Based on the present measurements, this tail is caused by a shift in the baseline for some channels of the ASIC. The shift pattern is the same for all chips and cannot be observed by using the S-curve analysis with the internal pule generator, which seems to suffer the same shift. Understanding the cause of this shift would require further investigations, but the shift is small relative to the energy range needed for the experiments with PFAD (range of more than 1 MeV). The sigma value obtained for the shown peak is equivalent to $\sim$8 keV. The ADC capabilities of the XYTER chip are not enough for performing spectroscopic measurements, but the energy information from the XYTER chips can help in the tracking algorithm for cutting the low energy background events.

4.2.2 In-beam commissioning experiment with PFAD

Experimental Setup

The in-beam test experiment with PFAD took place in May 2023 at the HIMAC facility. HIMAC (Heavy Ion Medical Accelerator In Chiba) is a medical facility located in Chiba, Japan. It offers particle therapy for cancer patients with carbon beams obtained with a heavy ion synchrotron. Aside from the medical treatments it gives beam time for physics and biology experiments during nights and over the weekends with various other ion species accelerated at hundreds of MeV/u with high beam intensity (up to 10^8-10^{10} pps, depending on the beam species).

For our experiment with PFAD, a 0.5-1$\times 10^6$ pps beam of protons was requested with the energy of 120 MeV and 230 MeV. The experiment duration was of two nights, one night for each beam energy. The full PFAD array was used for the experiment surrounded by a layer of

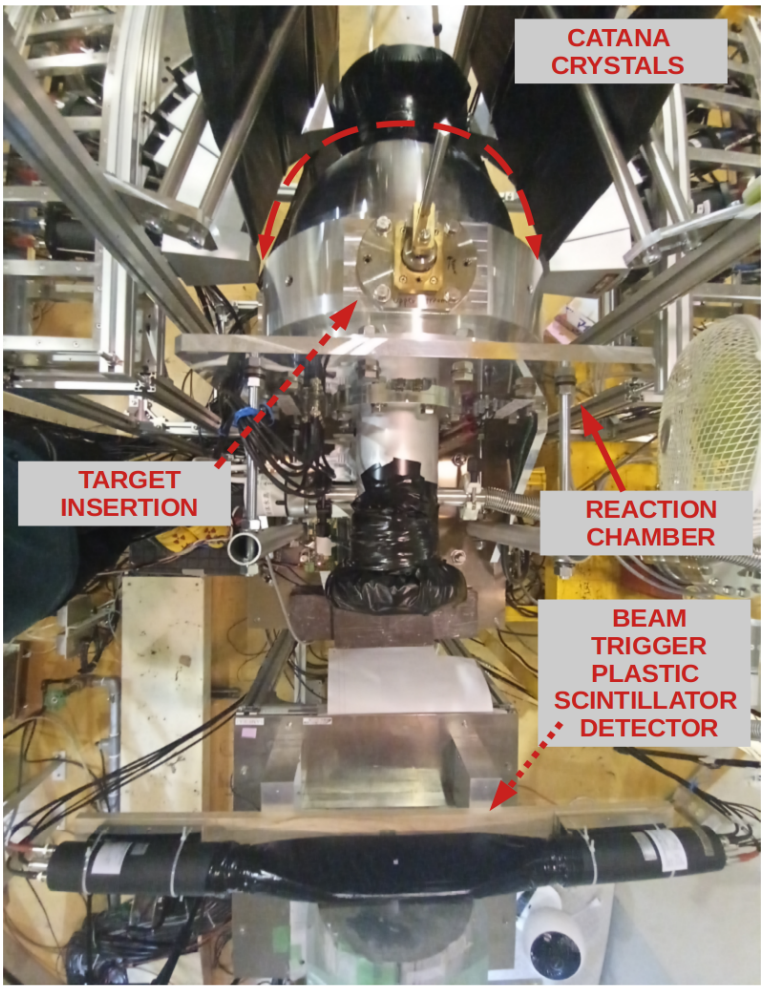

Figure 4.15: The experimental setup for the in-beam experiment with PFAD.

CATANA detectors. The second objective during this commissioning experiment was the integration of PFAD and the RIBF DAQ system. The CATANA CsI(Na) crystals [11] coupled with photomultiplier tubes are capable to detect γ-ray and total proton energies simultaneously using two gain modes.

PFAD and the target system were placed inside the reaction chamber under vacuum. A plastic scintillator detector was placed before the reaction chamber as a trigger for the incoming beam. Two targets composed of several layers were used during this experiment. The first one was composed of a 1 mm CH2 thick target, a 0.1 mm CH2 thin foil and a system of CH2 wires positioned along the X and Y directions. The second target consisted of a 1 mm Carbon (^{nat}C) thick target, a 0.1 mm CH2 thin foil and the same system of X and Y wires. The system of wires was composed of two layer, one with wires along X axis and on along the Y axis. On each layer 5 wires were placed of 0.25 mm diameter and placed at 2.125 mm distance

(center-to-center) from each other. A sketch of the target assembly is shown in Figure 4.18 a. This multi-layer target was used for proving the vertex tracking capabilities of the PFAD silicon tracker. Several reactions could take place using this complex target: proton elastic scattering on H, proton elastic and inelastic scattering on C, and quasi-free proton knockout, ^{12}C(p,2p). In each case one detects two tracks, one in the left arm and one in the right arm.

Logistics and assembly of PFAD

After building and testing PFAD at TU Darmstadt, the full PFAD system had to be transported to Japan and reasembled there. If the rest of the equipment could be shipped using conventional methods, special equipment needed to be prepared for the transportation of the fragile parts. Transportation cases were designed for the FEB2 and FEB6-type detector modules of PFAD using PLA 3D-printed frames with plexiglas walls and high density electrostatic-discharge-safe foam inside. The modules are designed for being transported in the personal hand luggage during a plane flight from Germany to Japan. We chose this way for making sure that we handle them with care. This method also requires the transportation cases to be transparent to the usual airport X-ray scans. This is why only plastic and no metal was used for the frames of the protection cases and the plexiglas wall allowed visual inspection without opening the cases. The detector modules were kept in suspension between the high-density foam in the points of enforcement of the Aluminium frames, such that the sensors and the wire bond are never touched. Additionally the individual protection cases were transported inside PELI cases [124], which is a professional and shock-resistant equipment. Photos of the transportation equipment are shown in Figure 4.16.

Vertex tracking performance results

Each of the 2D planes is composed of two layers, one with strips parallel to the beam, along the Z direction and one layer containing strips perpendicular to the beam direction, along the Y direction. There is an offset between each pair of perpendicular and parallel layers of $\sim$6 mm. For the particle tracking in each of the four 2D planes one must have one event in the parallel strips and one event in the perpendicular strips. For the tracking algorithm, even if there can be more events triggering in each layer, only the event with the highest energy is considered. This ensures that the low-energy noise is discarded and also for the interstrip events, the position of the strip where most of the energy was deposited is considered. The strips of the two layers will give the Z and Y position and the X position will be given by the middle between the two layers. As a result, one obtains the position in each of the 2D planes, two position points for one particle tracked in one arm and two position points for the second particle tracked in the second arm. The two tracks can be used to reconstruct the vertex position as the middle point at the minimum distance between the two tracks.

The Z coordinate of the reconstructed vertex is shown in Figure 4.17(top). The first observed peak corresponds to the thick target and the second peak corresponds to the thin foil. Two smaller peaks corresponding to the XY wires are seen in the right side of the plot. One of the wire layers is not visible as a separate peak because the thin foil was bent towards the wires during the experiment. This was caused by a pocket of air trapped between the thick

Figure 4.16: Photos with the PFAD detector modules transported to Japan for the commissioning experiment.

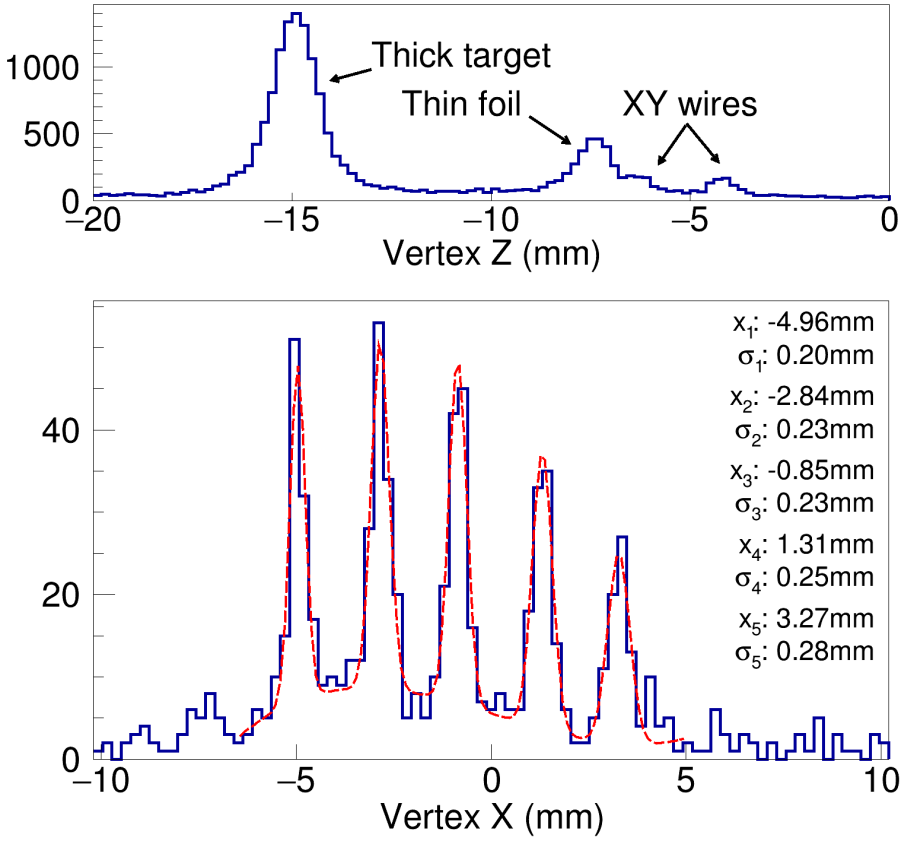

Figure 4.17: The vertex position on the Z (top) and the X (bottom) axes. The layers of the target are visible and labeled in the top plot and the 5 wires of one of the wire planes is shown in the bottom plot. The red line is a fitting function with 5 Gauss peaks and a polynomial background. The mean and σ values obtained for the 5 wires are displayed on the figure.

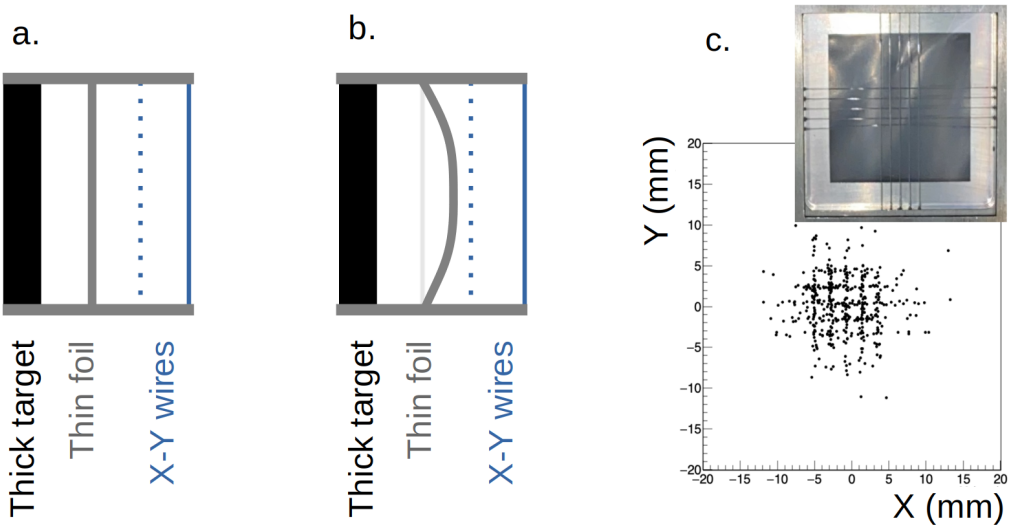

Figure 4.18: Sketch of the multilayer target used during the HIMAC experiment (a.) with highlight on the deformation that occurred inside the chamber (b.). The reconstruction of the X-Y wires with a real photo for comparison (c.).

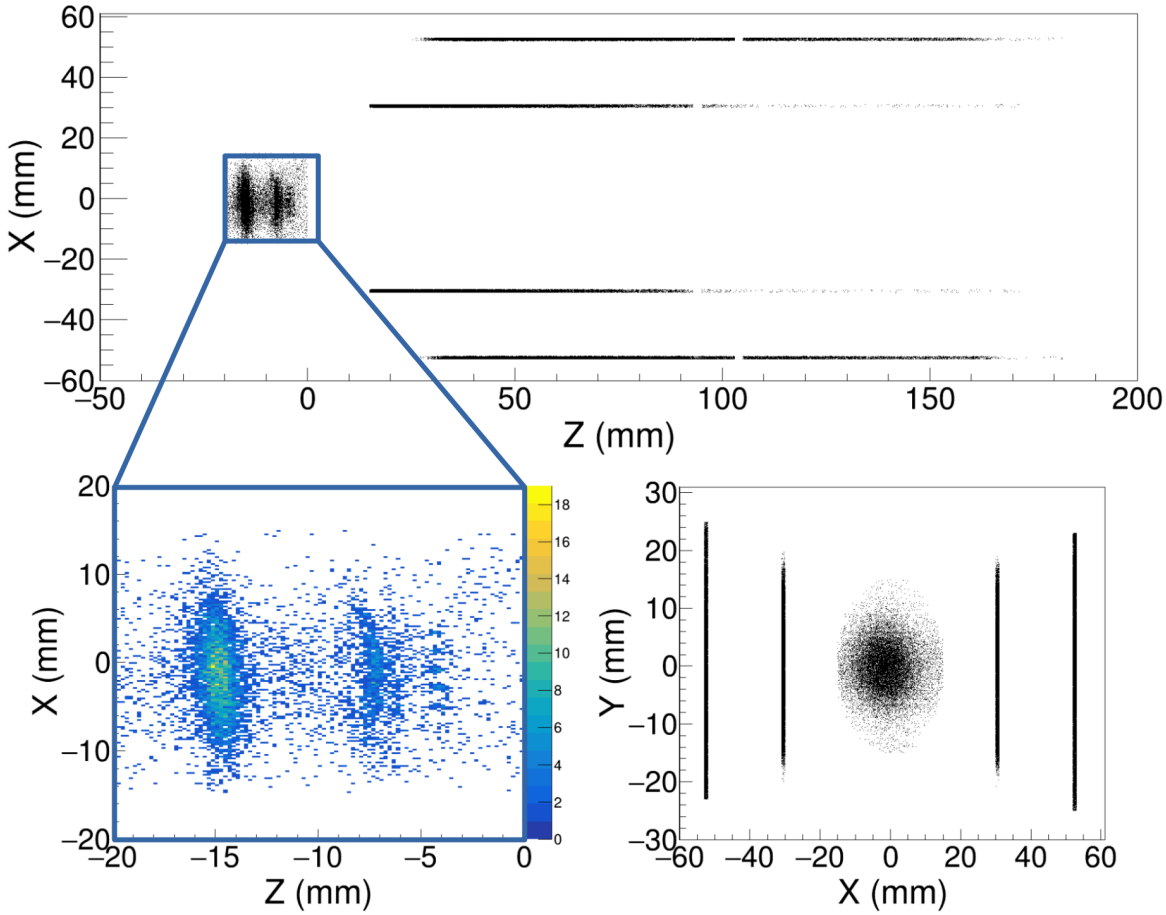

Figure 4.19: Position points in the 4 planes of the PFAD silicon tracker and the reconstructed vertex position. The top figure shows the X-Z plane, the bottom-right figure shows the Y-X plane and the bottom-left figure is a zoom in the target region with the reconstructed vertex seen in the X-Z plane.

target and the thin foil and a pressure difference accumulated on the two sides of the thin foil as the pressure was decreased inside the vacuum chamber. A sketch of the bent foil is shown in Figure 4.18b.

If one gates around the last peak on the Z axis, the X coordinate shows the five wires well separated in Figure 4.17(bottom). The mean and sigma values obtained as a result of fitting with 5 Gauss functions and a polynomial background are listed on the figure. The sigma values vary between 0.20 mm and 0.28 mm and the center-to-center distance between the wires varies between 1.96 mm and 2.12 mm (the measured diameter of the wires is 0.25 mm and the measured center-to-center distance is 2.125 mm). Gating around both XY wire peaks on the Z axis, one obtains the X-Y plot from Figure 4.18c. In this figure, the two perpendicular sets of 5 wires each are recognized and a real photo of the target is shown for comparison. The position points reconstructed in each of the 2D planes are plotted in Figure 4.19 as well as the vertex position. In the zoom-in XZ plot on the target region one can also see and con-

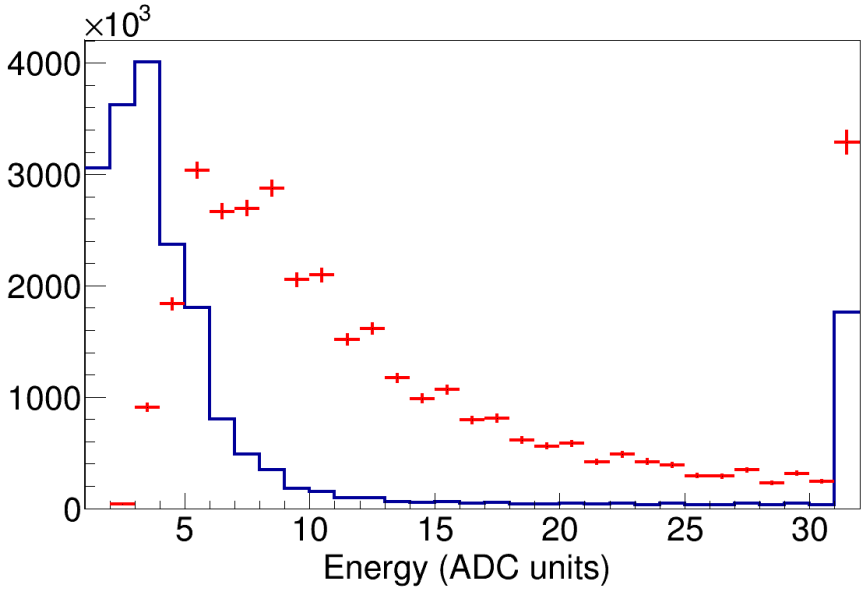

Figure 4.20: PFAD energy distribution of all events (blue) and of the events with vertex reconstruction (red). The red histogram was rescaled by x2000 and its last channel was rescaled by a factor of x1000 for display. The last channel shows the overflow, events with energy larger than the ADC range.

firm the bent foil using the vertex reconstruction. The energy spectrum in Figure 4.20 shows the distribution for all events (blue) and for the events used for vertex reconstruction (red, rescaled). Many of the events come from low-energy electronic noise/background but they lay below the energy deposited in the Si tracker by the tracked particles. This shows that the physical events from quasi-free scattering reactions are found above the threshold and there are no event losses.

The in-beam experiment with PFAD at HIMAC turned out to be a success in terms of vertex reconstruction. The presented plots are very preliminary results, part of the online analysis performed during the commissioning experiment. Optimisation and corrections for the position and tilt of the silicon sensors compared to the ideal positioning is needed in order to improve the vertex reconstruction. The data merging with the full energy measurements with CATANA is also going to be performed for obtaining the missing mass information. The data analysis was initiated by V. Girard-Alcindor (formerly at TU Darmstadt) and it was continued by our collaborators from TiTech. The results of the HIMAC commissioning experiment are in preparation for being published.

4.2.3 Summary and perspectives

PFAD, the prototype of the STRASSE silicon tracking system, was tested in lab as well as in-beam. The XYTER2.2 chips used for PFAD were characterised in terms of electronic noise, linearity of the ADC discriminators, and detection capabilities. The PFAD detectors modules

with silicon sensors attached were prepared for the commissioning experiment at HIMAC: they were calibrated and configured for the requirements of the experiment and the electronics noise level was benchmarked before and after the experiment. The specific software needed for the diagnostics, characterisation, calibration and configuration (line command and GUI) of the PFAD electronics was developed during this PhD study. Also, the assembly and safe transportation was ensured for the PFAD setup.

After the commissioning experiment of PFAD at the HIMAC facility, the back-end electronics was upgraded. The DAQ via the IPbus had a limitation in the hit rate that it could handle (up to 0.5 Gbit/s [122]). The upgraded system includes the *GERI* board. The GERI board hardware is commercially available, PCIe FMC Carrier mit Xilinx Kintex-7 410T board, which is plugged into the PCIe card of the PC. The GBTxEMU board is connected to the GERI board via optic fibers instead of being connected to the PC via Ethernet. Moreover, up to 8 GBTxEMU boards can be connected to one GERI board, increasing the number of ASICs that can be readout. The DAQ via the GERI board accesses directly the DMA of the PC, supporting a larger hit rate than before (up to 7.8 GByte/s using PCIe x8). The firmware and software development for the DAQ via the GERI board is still an ongoing effort.

Another improvement is to separate the FEB2 and the FEB6 downlink (clock and data) LVDS signals. It was observed that by routing the downlink LVDS signals to FEB6 and then to FEB2, large signal distortions were accumulating for FEB2 and often times the communication with the FEB2 boards was failing. The flat flexible ribbon cables used on the outside of the chamber between the GBTxEMU board and the feed-through PCB were change to twisted pair ribbon cables for improving the signal quality. The connectors used with these cables were changed from ZIF connectors to pin-header connectors for robustness. These modifications have been brought recently to the PFAD setup. The back-end electronics of STRASSE is the same as for the upgraded PFAD version, via the GBTxEMU board together with the GERI board.

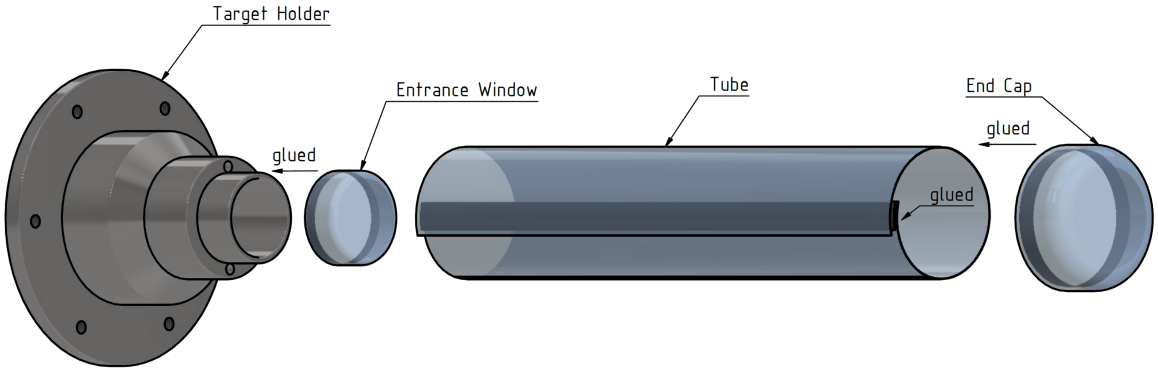

Figure 4.21: Drawing of the liquid hydrogen target cell composed of the target holder, the entrance window, the tube part and the end cap. The entrance window has a diameter of 20 mm, the end cap has a diameter of 31 mm and the length of the target cell is 150 mm.

4.3 STRASSE liquid hydrogen target

4.3.1 General overview

A liquid hydrogen target of 150 mm length and 31 mm diameter made out of 150 μm-thick Mylar (Bo-PET) is intended for the experiments with the STRASSE silicon tracker. For cooling down the hydrogen, a custom-made cryostat is being used, made by the Cryo.TransMIT company [125]. The production method of the target cell and the design of the target holder are the presented in this thesis. Several iterations were needed for the design of the production method and the production tools in order to find the right dimensions of the molds and the right procedure. Tests with water and high pressure and with liquid nitrogen are also done in order to validate the quality of the target cells.

4.3.2 Production of the target cell

The target cell is composed of three parts: the tube part, the end cap and the entrance window as shown in Figure 4.21. The concept is based on the target cell made for Minos [8], by CEA Saclay. The tube part is obtained by thermo-molding a rectangular sheet of Mylar and then gluing the two sides in order to form a tubular shape. The end cap is thermo-pressed and the molded piece is glued at the end of the tube part. The entrance window is obtained in a similar manner as the end cap. The necessary tools for the production of the target cell as well as the methods are described in the following mini-sections. The method is planned to be automatized as much as possible in order to have a high grade of replicability.

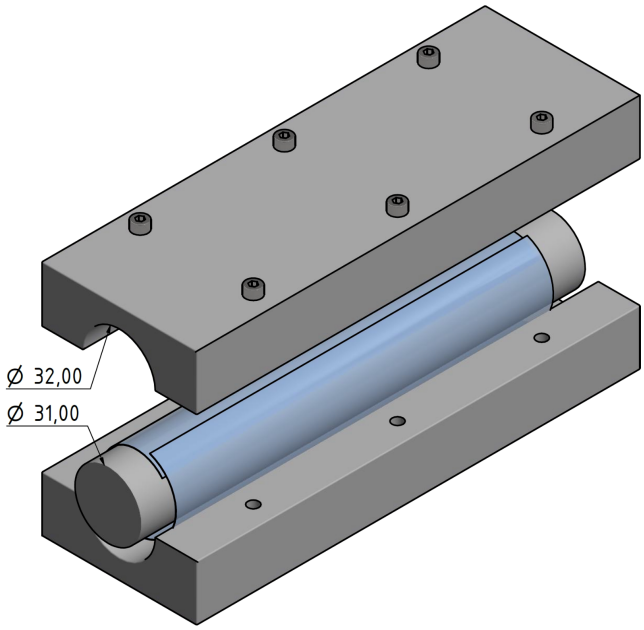

Figure 4.22: The mold for the tube part.

Molding the tube part

The mold for the tube part is shown in Figure 4.22. It consists of a full tube of 31 mm in diameter and 2 identical pieces coming around the tube with the diameter of 32 mm. The molds are made out of stainless steel. A rectangular piece of Mylar was cut to the size of 200 mm x 110 mm. The foil is rolled around the full tube of the tube mold (with the side of 110 mm folding around the tube). The tube mold is put in the oven at the constant temperature of 200°C for 20-30 min and then it is taken out of the oven and left to cool. After it is cooled, the Mylar foil is taken out of the mold. It takes about 1-2 h for the mold to cool down, to a temperature at which one can touch the mold with the bare hand. The cooling time depends on the ambient temperature. If the mold stays too much time in the oven, the Mylar will start of turn blurry. If the mold stays too little in the oven, or if it is removed from the mold before it cools down, the Mylar foil will not retain the shape. The oven used for the production of the target cell is Borel Laboratory Line Oven 300°C BLF300-245. At this step, the Mylar foil is molded only to retain a circular shape. The exact dimension of the tube diameter will be fixed when it is glued.

Gluing the tube part

For gluing the tube part, some preparation steps are required. The Mylar tubular foil is sanded on the gluing sides in order to increase the adhesion of the glue. The sanding region has a width of ∼5 mm. Sanding paper (ISO standard P150) is used and ∼8-10 scratches are made longitudinally. After this step, the Mylar foil is cleaned of any dust or grease.
The tools for gluing the tube cylinder are: an inner clamp, an empty aluminium tube, an outer clamp and a block with a semicircular dip for support purpose. These tools are shown

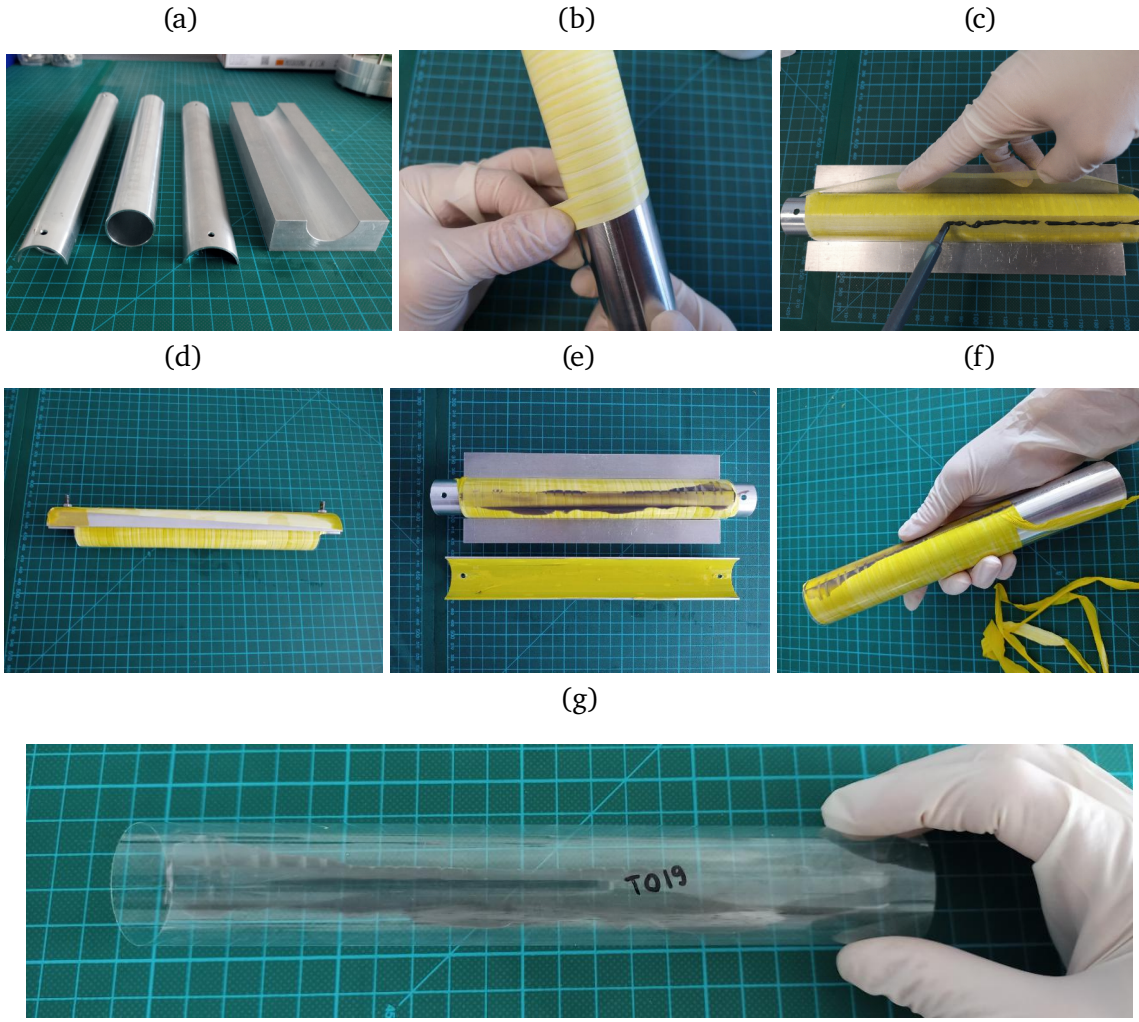

Figure 4.23: Photos with the tools (a), the preparation of the tools (b) and the gluing procedure (c) of the tube part of the target cell. After curing (d) and unmolding (e-f), the glued tube is shown in photo (g).

in Figure 4.23 (a) from left to right. The empty tube is rolled with 100 μm tape in two layers without tensing/stretching it. It has an outer diameter of 30.6 mm. This dimension accounts for the usage of 2 layers of 100 μm Teflon tape around the tube as shown in Figure 4.23 (b). The ends of the tape are left longer so that they can be pulled for unmolding. The taped rod is sprayed with WD-40 for lowering the adhesion of the glue to the tape. The inner clamp is placed inside the empty rod. The outer clamp is also taped with Teflon, as in Figure 4.23 (e), and sprayed with WD-40 for the same reason.

After these preparations, using the block support, the Mylar foil is put around the prepared empty tube. Special care is taken so that the regions which are going to be glued do not get greasy from the WD-40 spray. The inner clamp should be oriented with the screw holes on top, to match the gluing region. The glue is applied on one side, see Figure 4.23 (c), and the second side is pressed so that the glue is evenly distributed. The outer clamp is placed on top

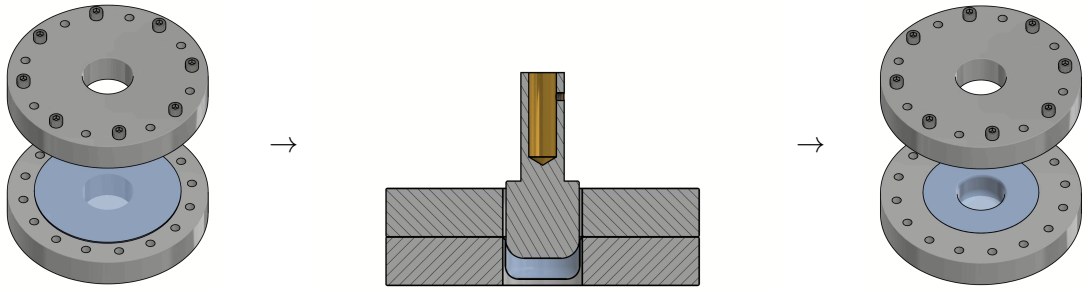

Figure 4.24: Schematics of the end cap molding process. The Mylar foil is placed in the mold and brought to the oven (left). The hot mold with the Mylar foil is pressed, molded and left to cool (center). After the mold cooled down, the final end cap is taken out of the mold (right).

and it is secured with the two screws at the ends (see Figure 4.23 (d)). It is left to dry in this mold for 1-2 days at ambient temperature.

The glue that is used is an epoxy structural adhesive DP190 from 3M in the grey color. After the glue is cured, the two screws holding the inner and outer clamps are removed. The greasy Teflon tape should make is easy to remove the outer clamp. The tape around the empty tube can be removed by pulling the end of the tape, as in Figure 4.23 (e-f). After unfolding the tape, the Mylar tube should be released from the mold. In Figure 4.23 (g) one can see the resulting glued tube part. In the case in which the outer clamp gets glued on the Mylar foil, one should first remove the empty tube by unfolding the tape. Once the empty tube is removed, the tube can be bent for softly peeling the glue off the outer clamp. If the glued outer clamp is removed forcefully, it can damage the Mylar foil completely or partly, in which case it will not be further used for making a target cell.

Molding the end cap and the entrance window

For molding the end cap and the entrance window, the Mylar foil is sandwiched between two aluminium disks as in Figure 4.24. The optimum diameters for the bottom disks, through which the foil is pressed in each case, are the following: 32 mm for the end cap and 23.5 mm for the entrance window. The following press was used: Fog AUTOMOTIVE, type 254 9610. In order to be able to mold 3 end cap pieces at the same time, a system of triple-head press was designed (Figure 4.25). The diameter of the cylindrical part of the head for molding the end cap is 30.4 mm with a curvature of 7.5 mm on the edge. The entrance window head press has the diameter of 22 mm and a smaller curvature of 1 mm on the edge.

A circular piece of Mylar with the diameter of 95 mm is cut and placed in the mold as in Figure 4.24(left) and 8x M6 screws are used applying precisely a 0.3 Nm torque. The end cap mold is placed in the oven at 200°C for 60-90 min. The hot mold is then placed on the press. Caution needs to be taken that the disk support was already centered on the press head. It is then slowly pressed until the desired depth is reached. The optimum depth is ∼20-25 mm.

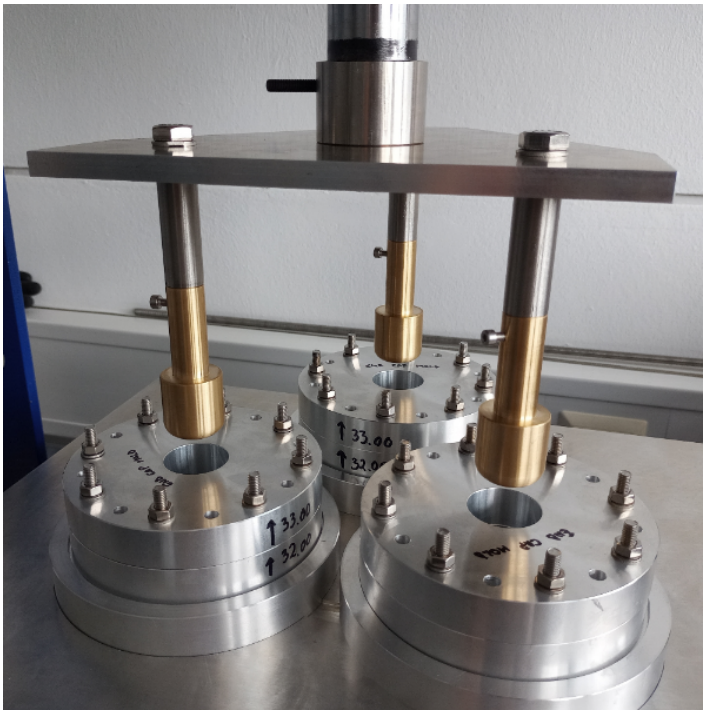

Figure 4.25: Photo of the triple-head press used for molding a batch of 3 end caps.

After pressing, the mold is left to cool in the same “pressed” position (Figure 4.24(middle)). After it is completely cooled down to ambient temperature, the Mylar piece is removed from the mold (Figure 4.24(right)). The extra material around the end cap is trimmed.

The bottom disk for end cap molding was designed such that the final end cap diameter can fit around the tube part, while the inner diameter of the target cell is 31 mm. The top disk has a diameter larger than the bottom one in order to allow material to fall inside while pressing. The torque applied on the screws was adjusted such that sufficient material is allowed to sink, without breaking the foil. One will observe that the diameter of the piece is closer to the disk diameter and not to the press head diameter. The right dimensions for both of them needs to be found depending on the working procedure and thermal conditions.

Gluing the tube and the end cap together

The glued tube part is placed around a 31 mm-diameter aluminum rod. The upper last 2 cm of the tube are left above the aluminium rod. The contact regions are being sanded as in the case of tube gluing. The glue is applied on the inside of the end cap. The tube is slightly bent and the end cap is placed around the tube, then the bent tube is released. The aluminum rod slides into the gluing region to ensure full contact and coverage of the glue. An additional ring clamp can be put around the glued region. All surfaces in potential contact with the glue are taped with Teflon to avoid the target cell getting stuck in the rod or with the ring clamp. The glue of the target cell is left to dry for 1-2 days before it is removed from the mold.

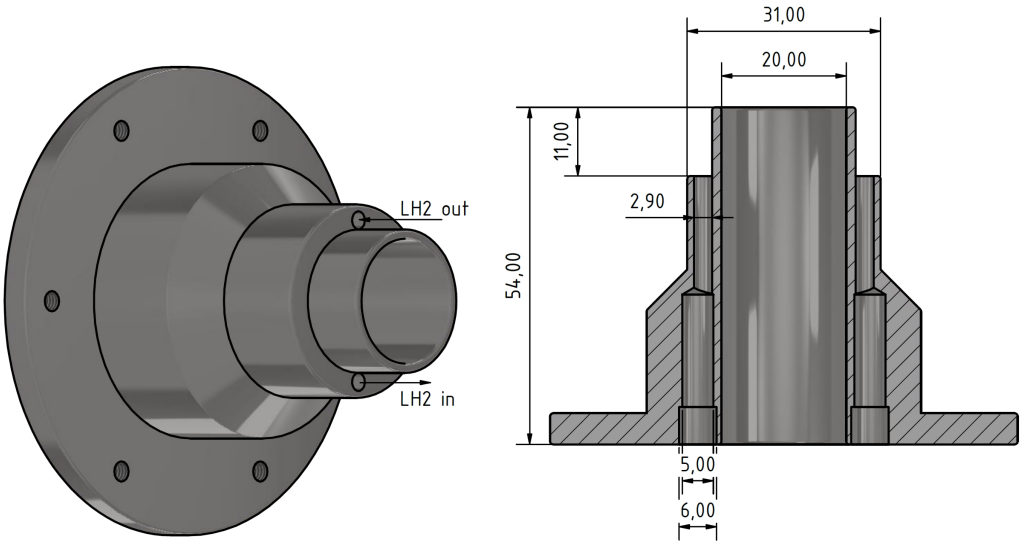

Figure 4.26: Drawing of the target holder. Left: Full view. Right: Section view. The dimensions are shown in mm. The two channels through the target holder will let the liquid hydrogen in and out of the target cell. The target holder is made out of stainless steel.

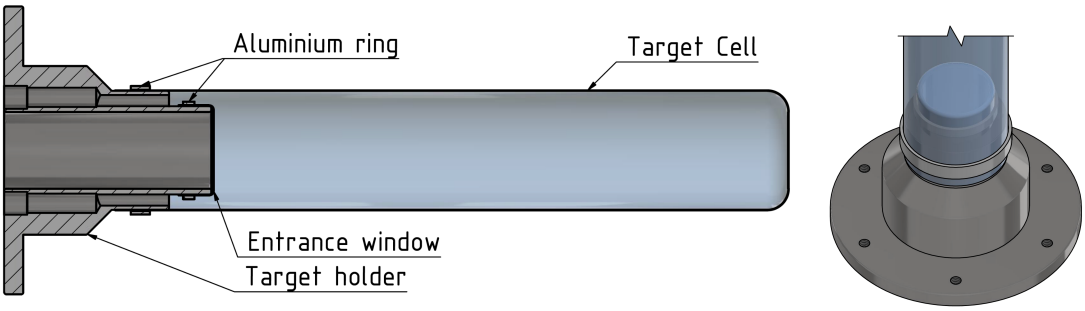

Figure 4.27: The target cell and entrance window attached to the target holder and secured with the aluminium rings. Left: Section view. Right: 3D view.

4.3.3 Target holder design

The design and dimensions of the target holder are shown in Figure 4.26. The target holder shape is constrained in many aspects. The effective entrance window needs to be as close in size as possible to the total diameter of the target in order to reduce the liquid hydrogen volume which is not reached by the beam. In this case the entrance window is 20 mm in diameter and the target cell diameter is 31 mm. A minimum size is left for the liquid hydrogen supply and exhaust pipes. In terms of the total diameter of the target holder, it needed to be very narrow close to the entrance to the target in order to fit inside the silicon tracker support and in the upstream side wide enough for the liquid hydrogen piping connections and mechanical support. The 11 mm distance between the starting of the liquid hydrogen volume and the entrance window plane arose from the technical difficulty to maintain the narrow pipes of

Figure 4.28: Pictures of the hydrogen target cell.

2.9 mm diameter over longer distance. The supply and exhaust of liquid hydrogen is done via the 6 mm-wide connections at the entrance of the target holder. The mechanical support of the target is done using a standard DN100 flange.
Images of the target holder are shown in Figure 4.28(d-f). In photo (e), the inlet and outlet pipes are soldered into the target holder. The pipes have 6 mm outer diameter and 4 mm inner diameter made out of stainless steel. The pipes were inserted using thermal dilatation and contraction (process known as *shrink-fitting*) and then welded. The target holder was heated in the oven at 200°, while the pipes were sunk in liquid nitrogen. This difference of temperature ensured a contraction of the pipes and a dilatation of the holes of the target holder enough to be able to insert the 6 mm pipes into the 6 mm holes. At room temperature the pipes are tightly inserted and create an inmovable bond and a metal-to-metal sealing. Additionally the pipes were welded by the TIG method, Tungsten Insert Gas, which is ideal for quality and precision welding. The inlet and outlet holes get narrower further into the

	“175” target cells	“125” target cells
end cap [μm]	170.5(118)	128.1(27)
tube [μm]	185.8(52)	128.8(25)
1-layer average [μm]	172.2(130)	128.3(27)
glue layer [μm]	89.6(419)	116.8(279)
inner diameter [mm]	31.04(9)	-

Table 4.2: Thickness characterisation of the target cells. The mean values for the thickness are given in units of μm and the standard deviation values are shown in parentheses.

target holder, being 2.9 mm in diameter at the beginning of the target volume.

Gluing the Target Cell on the Target holder

The main body of the target cell and the entrance window then glued on the target holder and secured with two aluminium rings. The material chosen for the target holder is stainless steel. In Figure 4.27 one can see how the aluminium rings are mounted around the glued target cell and entrance window on the target holder. At low temperature, aluminium (linear temperature expansion coefficient 21-24·10^{-6}m/m/K) will contract more than the stainless steel (16·10^{-6}m/m/K), ensuring additional grip on top of the glue.

Target cell wall thickness characterisation

Before gluing the target cells, measurements for the wall thickness were conducted using a micrometer with a range of measurement of 0-25 mm and an error of measurements of 0.01 mm. The thickness of the Mylar foil that we used is stated by the producer (Goodfellow) as 175 μm with $\pm$20% tolerance. An additional batch of target cells with smaller thickness was produced with a Mylar foil of 125 μm thickness with $\pm$20% tolerance. The end caps were measured in the top, center point as well as in about 10 side points (see Figure 4.28 (b)). The tubes were measured in several points along their length and on the region of glue. The region of glue contains two layers of Mylar foil and a layer of glue. The Mylar foil in this region was sanded before being glues, so a slight decrease in the thickness of a single layer is expected here. The inner diameter of each tube was also determined by circumference measurement. After the targets were broken during stress tests described in the following subsection, the glue layer between the end cap and the tube was also accessible for measurements. The results of the thickness measurements are summarized in Table 4.2. The thickness of the foil is modified during the molding process where some parts of the foil get stretched and in other parts we get a high density of material. An observation to be made is that the 125μm-thick target cells were made with the same producing tools and molds, with no adaptation to the smaller thickness; as a result the production of these target cells was not optimal, but it was done in order to compare the robustness of the 175μm with a smaller thickness version during

over-pressure tests with water (described in the following subsection).
The measured thicknesses for the different parts of the target cell show a high replicability for a large batch of target cells and a high grade of uniformity along a single target cell surface and the variations from the mean values are not larger than the initial tolerance of the material. The inner diameter which is of big importance for the analysis of the nuclear reactions performed withing the liquid hydrogen target volume shows good results as well, with a mean value of 31.04 mm and a tolerance of only 0.09 mm. On the bad side, large variations and lack of replicability appears for the glue layer. Given the presented manual production method, the thickness characterisation shows reasonable results. The mean and variations of the dimension of the target cells can be improved by automatising the method and the limitation of the human input.

4.3.4 Target cell stress testing

Over-pressure tests with water

A first test for the target cells was the over-pressure test with water. We pumped water at high pressure and we were interested in the breaking pressure for the target cells and in the consistency of this maximum pressure among all the tested target cells. The target cells (tube + end cap) were glued for these tests on 3D-printed mock-up target holders made of PLA. Some of the target cells mounted on the 3D-printed target holders are shown in Frigure 4.28 (a). A manual water pump (Rothenberger Prüfpumpe TP25, manuell 60250) with a brass custom-made adapter for the target holders were used. Between the pump and the adapter we introduced a T-shape fitting for connecting a digital manometer (Gravity - Water pressure sensor SEN0257). The digital manometer was calibrated with 2 analog manometers. The readout of the digital manometer was done using an Arduino UNO board and a custom-made Labview program (with the interface shown in Figure 4.29). A photo of the small testing setup is found in Figure 4.28(c). The length of the tested target cells vary between 15 and 17 cm.

The water pressure was pumped in steps, as in the example in Figure 4.29. At the push of the handle of the manual pump, more pressure was introduced and the target cell was held at that pressure for a few seconds before the next push of the handle. Between each push of the handle, the pump was releasing some pressure, and this explains the small negative slope at each step. The pressure would drop completely when the target cell breaks as it happens at the end of the example plot. The target cells were placed and let to explode in a box with a plexiglas cover for visibility. All “175” target cells exploded slightly above the pressure measuring range of the manometer which is 11.7 bar. The exceptions were the target cells which were ripped off the target holder during the tests, but the aim was to test the target cell robustness and not the adhesion of the epoxy glue to the PLA target holders. In many cases to avoid this inconvenience, ring clamps were user around the base of the target cells to secure them to the target holders. In the case of the “125” target cells, the breaking pressure was 5.5-5.7 bars. The exceptional cases in which the thin target cells got ripped off the target

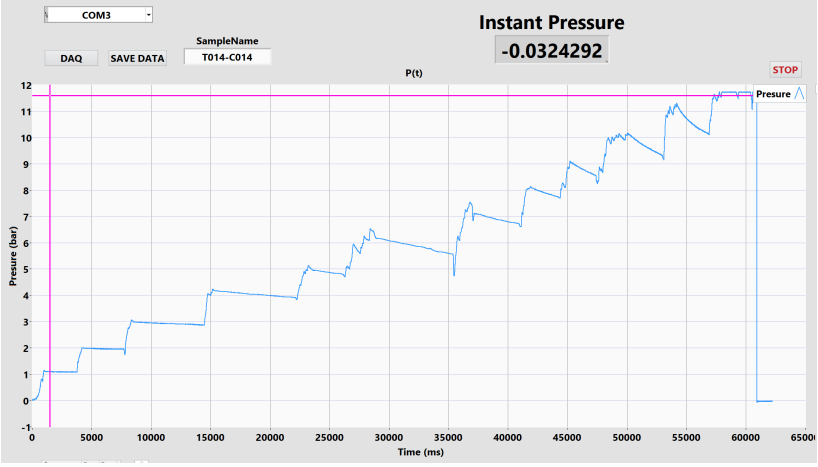

Figure 4.29: Example of a high pressure measurement during the tests with water.

holders, the breaking pressure was between 4.6 and 5 bars. Using a toy model calculation, where the target cells are considered to be made out of one piece, without the gluing regions, the breaking pressure was found to be at 10.6 bars for the “175” target cells and 7.6 bar for the “125” target cells.

Our conclusion is that the target cells stood a pressure larger than expected from toy model calculations, and also larger than needed during the experiment with liquid hydrogen. The target cells showed little variations in terms of the breaking pressure values and behaviour, reflecting a good replicability with our production method. The thickness of the material is a crucial factor in the maximum pressure that the target cells withstand. Despite the fact that the “125” thin targets stood at about half the pressure of the “175” ones, their breaking pressure, above 5.5 bars, fulfill and over-exceed the robustness requirements as well.

4.3.5 Going to cryogenic temperatures

The second test done with the target cells is to get them through several cryogenic temperature $\longleftrightarrow$ ambient temperature cycles using liquid nitrogen. The integrity of the tested target cells was checked by pumping water at 8 bars before and after the cryogenic cycles. The cryogenic cycles did not affect their ability to withstand 8 bars. The pressure of 8 bars was chosen because it is much higher than our requirements, but also not too close to the breaking pressure of the targets observed in the previous test.

Further tests with the targets will preformed, such as liquid nitrogen circulation and breaking point of the target cells at cryogenic temperatures, using a custom made test setup. The test setup consists of a 4-ways cross with two see-through plexiglas flanges, one flange adapted to connect the target holders with the target cells and one arm of the cross connected to a vacuum pump. Liquid nitrogen will be circulated through the target under vacuum while being monitored visually before being used further with liquid hydrogen.

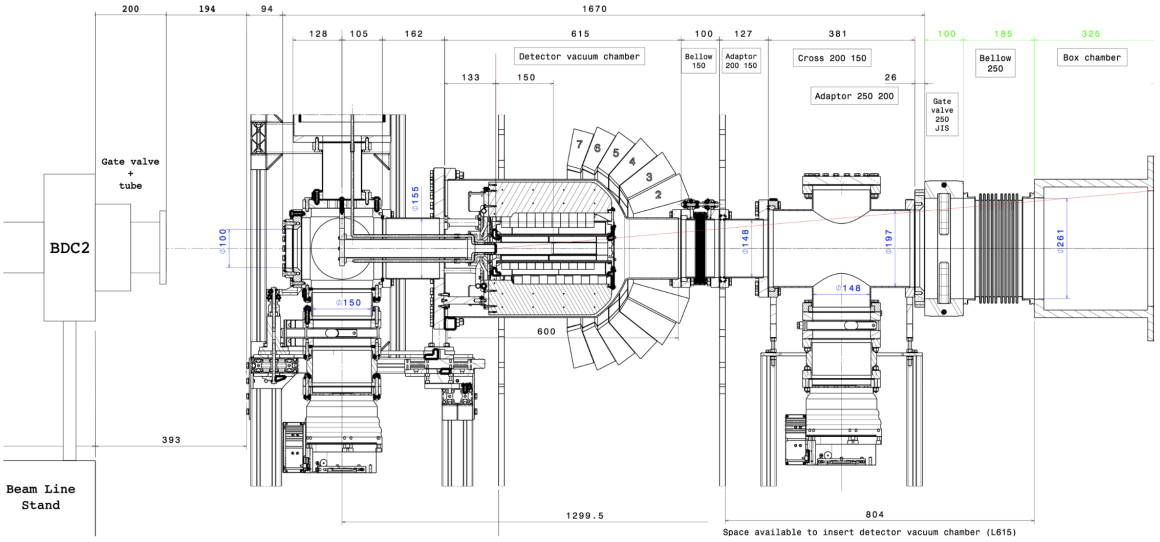

Figure 4.30: Drawing of the STRASSE experimental setup including cryostat and the CATANA system. Figure reprinted with the permission from [10]© CC-BY-4.0.

4.3.6 Vacuum in the STRASSE reaction chamber

The experimental setup STRASSE + CATANA is designed to fit at the focal point F13, the secondary target, in SAMURAI area of the RIBF facility. The experimental area comes right after the BDC1 and BDC2 detectors, used for beam position measurement, and before the FDC1 detector, used for the fragment position measurement. The space along the beam line between these two detector setups is limited. The Figure 4.30 shows a schematics of the STRASSE + CATANA system in the SAMURAI experimental area. The STRASSE system will be completely detached from the beam line, meaning that the beam will travel through air before and after the STRASSE reaction chamber. This is done in order not to interfere with the vacuum level existing in the beam line. The vacuum in the STRASSE system needs to be maintained during the cooling phase of the liquid hydrogen target, as well as during the full operation of the system. The cooling phase is particularly critical because during this stage, the hydrogen in the target cell is in a gaseous state before reaching cryogenic temperatures. In the gaseous state, hydrogen can permeate through the thin walls of the target cell and interfere with the vacuum in the system. On the other hand, the vacuum level is important for the operation of the silicon tracker (much less than 10^{-3} mbar needed).

As one sees in Figure 4.30, two spots for the vacuum pumps are foreseen, below the cryostat and after the reaction chamber. Simulations modeling the worst case scenario during the cooling phase of the liquid hydrogen target were done using COMSOL Multiphysics as well as the Molflow+ software package [126]. Both programs are able to simulate the free flow at low pressures, so we do not expect large differences between the simulations. Several combinations of the upstream and downstream pumping speeds were simulated, including the case in which only one pump is used, the one below the cryostat. Such simulations were done in order to check the possibility to limit the space needed by the system by using only

one vacuum pump. The requirement for the maximum pressure around the hydrogen cell and in between the sensor layers is 10^{-5} mbar or lower at any time during the operation of the system.

Permeation and outgassing

The outgassing is the *spontaneous* evolution of gas out of a solid or liquid. It is dependent on temperature, the pressure difference and the thickness of the material. It appears because of the contamination of the surfaces by being exposed to air or other conditions. The unit of outgassing is [mbar·l/s]. If we are talking about the outgassing due to permeation, as in the case of the hydrogen gas permeating through the Mylar material of the target cell, one can relate the two with the following expression:

$$Q = P \cdot \frac{ART\Delta p}{l} \tag{4.2}$$

where Q is the outgassing, P is the permeation, A is the area trough which the gas permeates, R is the gas constant (8.31 mbar·cm^3/K/mol), T is the gas temperature, Δp is the pressure difference and l is the layer thickness of the material. The permeation will have the unit of [mol/mbar/cm/s]. Additionally the area specific outgassing will be q = Q/A, measured in [mbar·l/s/cm^2]. The permeation of hydrogen through Mylar with a value of P=1.79·10^{-16} mol/cm/s/mbar [127] was considered in the simulation. This value for permeation will give an area specific outgassing rate of $\sim$1.85·10^{-8} mbar·l/s/cm^2 for a temperature of 30 K (before the hydrogen is liquefied), the target thickness wall of 175 μm and a pressure difference of about 600 mbar.

For the outgassing, the contribution of several gases can be taken into consideration such as hydrogen, CO or water. Any molecule dissolved in the bulk of materials is a source of gas and diffuses towards the surface for being released. In this simulation only the hydrogen outgassing was considered, this contributing the most. As an example, in stainless steel hydrogen travels 4μm/1 day, while oxygen travels 4μm/1000 years at room temperature. Hydrogen is dissolved in metals as single H atoms and after diffusing, it recombined at surface and it is released in the form of molecular hydrogen, H_2. The outgassing of water depends on the pumping time of the system and it is not an intrinsic value. The outgassing rate has a $1/time$ dependence on pumping time for metals and $1/\sqrt{time}$ dependence for polymers. The source of water is recharged each time the system is vented to air. Each time the metals are exposed to air water molecules are reabsorbed onto the surface while Hydrogen is not recharged in the bulk material. The outgassing rates from different materials depend on the environment and the preparation of those materials. For metals the preparations can involve baking the metal parts for several hours, cleaning with alcohol or acetone, polishing (chemical, electrical or mechanical), dipping in sodium hydroxide, rinsing in de-mineralized water, or other such methods in order to reduce the amount of gas trapped onto the surface or in the bulk material [128]. The plastic materials come in a large variety and as well the outgassing rates

are very specific to the components, how they were produced, treated and stored. Generally the outgassing of hydrogen for plastic materials is of the order of 10^{-7} mbar l/s or worse. On the other side for metals the outgassing is generally at least two orders of magnitude lower. Examples of area specific outgassing values of hydrogen from different metal and polymer materials are given in Table 4.3. A literature survey for outgassing rates can be found in Ref. [127]. What one observes from these various outgassing rates is that the values scatter a lot even for the same material and with the same preparations. For these reasons, giving an absolute value for the outgassing rates of the materials we plan to use in the STRASSE chamber is not realistic. The simulations will aim to be as close to reality as possible and to cover the worst case scenario in order to make safe decisions based on the results.

Geometry

In the simulation, the empty spaces, or the gaps, are modeled and so several modifications were done in order to simplify the geometry. The details of the reaction chamber, the supporting arm of the target cell and along the tubing and fittings were removed, but their surface area which is important for the outgassing process is kept the same. Inside the reaction chamber we have the Si sensors mounted on PCB frames which were modeled as two concentric hexagonal tubes. The geometry is close to reality, creating the separation between the layers (Target - Inner Si layer - Outer Si layer - Chamber walls). Because of these layers, we expect the pressure to show a step behavior, with the maximum pressure around the target, a median pressure value between the Si layers and lower pressure close to the chamber walls. The effective area specific outgassing value used in the simulation for the sensors and frames is reflecting the real arrangement. Additionally there is the supporting frame for the Si tracker, made out of stainless steel (SS), the cooling base (with SS on one side and Cu on the other side) and the cooling blades (Cu) which were modeled as one disk with 6 simplified blades. The readout electronics (FEBs) is found on the cooling blades, with the Microcables going from the sensors to the FEBs. The outgassing of the exposed Copper parts, the Stainless Steel parts, the outer layer of the FEBs and the outer layer of the Microcables (both sides) are all contributors to outgassing which was carefully considered in the simulation.
A complete list of components considered in the simulation including their area, the material and the value for the area specific outgassing is given in Table 4.4. Additionally the central source of outgassing is the target cell out of which Hydrogen is outgassing due to the permeation mechanism.

The vacuum pumps planned to be used for STRASSE are Edwards STP603 turbomolecular pumps delivering a maximum pumping speed of 550 l/s for H2. The simulations were done for pumping speeds up to 500 l/s for both the upstream (U) and the downstream (D) pumps. The simulations with no downstream pump were done by setting the pumping speed to zero and keeping the full geometry described in this section, but also by reducing the geometry and removing the T-shape fitting and the downstream part completely.

Metals

Material	Preparation	Outgassing
SS	1h at RT	7.1E-9
SS	1h at RT	2.8E-9
SS	1h at RT	9.0E-8
SS	10h at RT	1.0E-9
SS	20h baked at 200°C	1.3E-14
SS	100h baked at 430-480°C	3.0E-16
SS	electropolished	3.0E-12
SS	mechanically polished	1.7E-9
Al	1h at RT	6.3E-9
Al	100h at RT	1.3E-14
Cu	1h at RT	1.9E-8
Cu	mechanically polished and 1h at RT	1.9E-9
Cu	10h at RT	2.0E-10
Cu	24h baked at 250°C	4.9E-12

Polymers

Material	Preparation	Outgassing
Mylar	10h at RT	2.0E-7
Mylar	10h at RT	5.3E-7
PTFE	10h at RT	2.6E-7
PVC	24h baked at 95°C	2.7E-8
Si	5h at RT	2.6E-6
Si		1.8E-5
Teflon	10h at RT	3.3E-4
PI	12h at 300°C	5.3E-8
PEEK	12h at 300°C	5.0E-7
PE	10h at RT	1.1E-2
FR4		6.0E-10

Table 4.3: Literature survey of outgassing rates. Source: [127].
The area specific outgassing values are measured at room temperature and are given in units of [mbar·l/s/cm^2].
Achronyms: RT = room temperature; SS = Stainless Steel; PI = Polyimide; PEEK = Polyether ether ketone; PE = Polyethylene; FR4 = flame retardant epoxy resin; PTFE = Polytetrafluoroethylene.

Component	Material	Area (cm^2)	Outgassing (mbar·l/s/cm^2)
Target cell	Mylar	165.4	due to permeation
Target holder	SS	73.9	1.0E-9
Supporting arm	SS	660.7	1.0E-9
- interior		493.4	1.0E-9
Insulation Target	PEEK	42	5.0E-7
Reaction Chamber:			
- Flange	SS	995.3	1.0E-9
- Chamber	Al	5419.8	6.3E-9
Tubing and Fittings:	SS	8459.5	1.0E-9
- spherical cross		247.8	
- blank flanges		804	
- tube to pump U		1357.1	
- cryostat-to-chamber		804.2	
- Chamber exit		1627.3	
- T -fitting		2362.5	
- tube to pump D		1256.6	
Cooling base	SS	385.3	1.0E-9
Tracker support	SS	2882.4	1.0E-9
Copper blades (exposed)	Cu	714.6	1.9E-9
FEBs	FR4		6.0E-10
- FEB11(i&o)		6 X 517.2	
- FEB3		6 X 66.3	
- FEB2		6 X 53.5	
Microcables	PI		5.3E-8
- FEB11(i)		6 X 174.5	
- FEB11(o)		6 X 144.9	
- FEB3		6 X 121.4	
- FEB2		6 X 29.6	
Sensors	Si		2.6E-6
- inner		6 X 146.4	
- outer		6 X 305.6	
PCB frames	Rogers		2.6E-7
- inner	laminate	6 X 68	
- outer	(PTFE)	6 X 106.6	

Table 4.4: Table of outgassing values considered in the simulation.

Results

For the simulation using COMSOL Multiphysics, the *Free Molecular Flow* physics package was used with the *Number Density Reconstruction* enabled. The number density reconstruction is a computationally expensive tool that tracks the particles in the volume and not only at their interaction with the walls. The resulting number density can be plotted in the volume and is proportional to the pressure. The Figure 4.31 shows the plots for the XY, XZ, and YZ planes for the case with both pumping speeds (for U and D) set to 500 l/s. From these plots we observe that the maximum pressure is found around the target cell and we observe the expected three regions of pressure as we go radially out.

The region of interest for us is around the target, corresponding to the maximum pressure and number density values. In Table 4.5, these quantities are listed for all the combinations of pumping speed for the two pumps. Additionally, as reference, the average and minimum values for the pressure are also given in this table. The columns under 'COMSOL' are done with the full geometry as described in this section, while the column under 'COMSOL†' corresponds to the case where the geometry is reduced and there is no downstream pump in the system. In the case with the reduced geometry, there is only the upstream pumping speed as an input for the simulation. The results with the full geometry but zero downstream pumping speed are in perfect agreement with the case where we cut the part after the reaction chamber entirely.

The same simulation was performed with Molflow+, using the full geometry, where the maximum pressure value was evaluated by inserting a XZ plane going through the target cell, which has 100% transparency, but acts as a counter for the molecules passing through it. The resulting maximum pressure values are listed in the table in the last column and are corresponding as well to a region around the target cell. In the Molflow+ simulation, only the values of 300 l/s and 500 l/s as pumping speeds were considered, for the case with both pumps, and with the same pumping speed, and for the case with only the upstream pump, and zero pumping speed for the downstream one.

For the full geometry with the COMSOL Multiphysics simulation program, the best pressure (P_{MAX} value near the target cell) was obtained by using both pumps at 500 l/s pumping speed, $2.32{\cdot}10^{-5}$ mbar, and the worst pressure was obtained for the case when only one pump is used with the pumping speed of 100 l/s, $1.78{\cdot}10^{-4}$ mbar. There is an order of magnitude difference between these two cases. Very small differences in the results were obtained between the full geometry and the reduced geometry when using only one pump. This means that even though in reality one would not use the T-fitting if one does not use the downstream pump, only turning off the downstream pump in the simulation was a good approximation. When comparing the results obtained with the MolFlow+ simulation package relative to the results obtained with the COMSOL Multiphysics simulation package, we observe a consistent decrease (increase) with $\sim$25% of the P_{MAX} value when using both pumps (only one pump).

The supporting arm of the target cell is a simple tube in the current configuration. It was also checked in terms of the vacuum quality if it would help to create holes in the tubular supporting arm in order to facilitate the gas flow. It was found using the Molflow+ simulations that it has little impact on the vacuum in the reaction chamber. By creating holes on 25%

XY plane

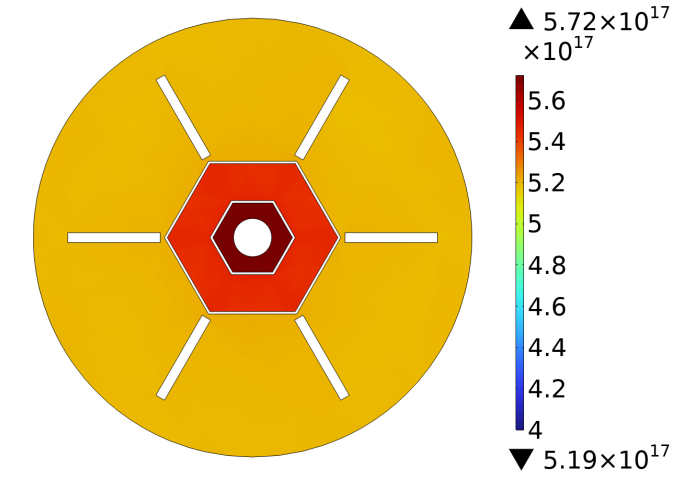

XZ plane

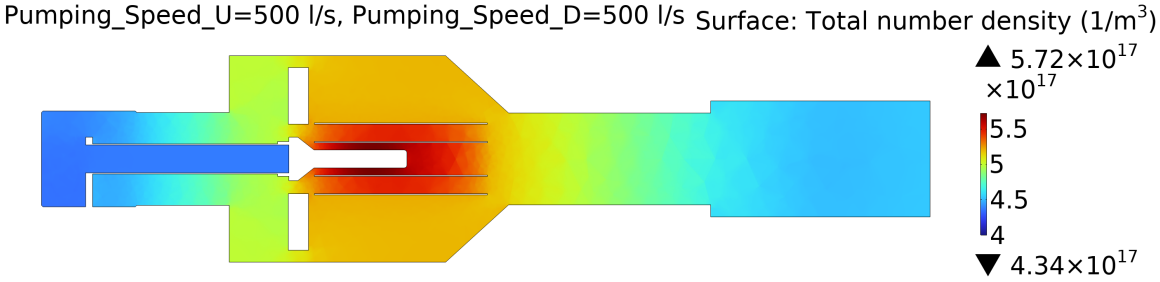

YZ plane

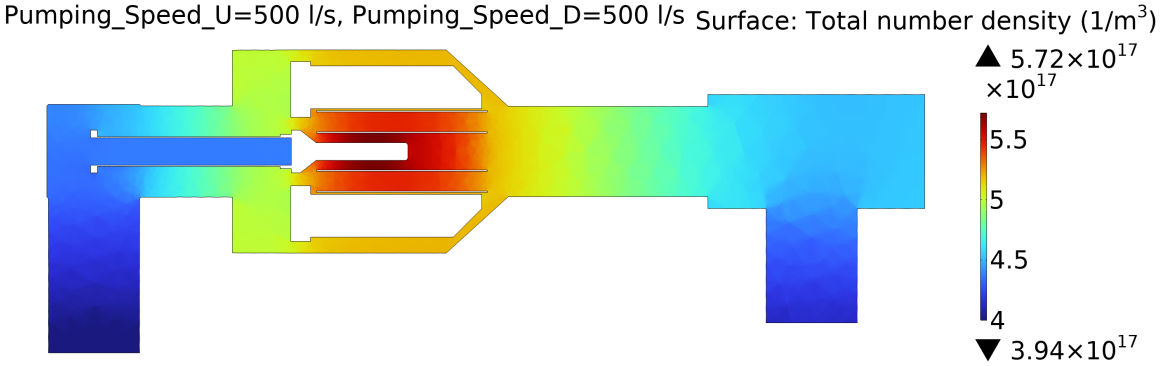

Figure 4.31: Simulated number density in the volume of the STRASSE reaction chamber. The plots are shown for the XY, XZ, and YZ planes for both pumps at 500 l/s speed obtained using COMSOL Multiphysics with the *Free Molecular Flow* physics package.

S		COMSOL				COMSOL†	Molflow+
U	D	N_{MAX}	P_{MAX}	P_{AVE}	P_{MIN}	P_{MAX}	P_{MAX}
100	0	4.40E+18	1.78E-04	1.74E-04	1.65E-04	1.79E-04	
100	100	2.23E+18	9.05E-05	8.72E-05	8.31E-05		
100	200	1.55E+18	6.29E-05	5.97E-05	5.49E-05		
100	300	1.22E+18	4.93E-05	4.62E-05	4.07E-05		
100	400	1.02E+18	4.13E-05	3.82E-05	3.22E-05		
100	500	8.87E+17	3.60E-05	3.29E-05	2.66E-05		
200	0	2.35E+18	9.51E-05	9.12E-05	8.19E-05	9.55E-05	
200	100	1.56E+18	6.31E-05	5.96E-05	5.39E-05		
200	200	1.20E+18	4.85E-05	4.51E-05	4.11E-05		
200	300	9.90E+17	4.01E-05	3.69E-05	3.28E-05		
200	400	8.56E+17	3.47E-05	3.15E-05	2.68E-05		
200	500	7.62E+17	3.09E-05	2.78E-05	2.27E-05		
300	0	1.67E+18	6.75E-05	6.36E-05	5.42E-05	6.77E-05	8.94E-05
300	100	1.23E+18	4.98E-05	4.62E-05	3.97E-05		
300	200	9.95E+17	4.03E-05	3.69E-05	3.20E-05		
300	300	8.50E+17	3.44E-05	3.11E-05	2.71E-05		2.62E-05
300	400	7.50E+17	3.04E-05	2.72E-05	2.33E-05		
300	500	6.78E+17	2.75E-05	2.43E-05	2.00E-05		
400	0	1.33E+18	5.37E-05	4.98E-05	4.04E-05	5.39E-05	
400	100	1.04E+18	4.20E-05	3.83E-05	3.14E-05		
400	200	8.66E+17	3.51E-05	3.16E-05	2.61E-05		
400	300	7.55E+17	3.06E-05	2.72E-05	2.26E-05		
400	400	6.76E+17	2.74E-05	2.41E-05	2.01E-05		
400	500	6.18E+17	2.51E-05	2.18E-05	1.81E-05		
500	0	1.12E+18	4.54E-05	4.15E-05	3.21E-05	4.56E-05	5.76E-05
500	100	9.08E+17	3.68E-05	3.31E-05	2.59E-05		
500	200	7.76E+17	3.15E-05	2.80E-05	2.20E-05		
500	300	6.87E+17	2.78E-05	2.44E-05	1.93E-05		
500	400	6.22E+17	2.52E-05	2.19E-05	1.74E-05		
500	500	5.72E+17	2.32E-05	1.99E-05	1.60E-05		1.65E-05

Table 4.5: The resulting number density (N) and pressure (P) from the vacuum simulations in units of [1/m^3] and [mbar], respectively. The simulations were done for several pumping speeds (S) [l/s] of the upstream (U) and downstream (D) pumps with the full geometry described in text and also with a reduced geometry, without pump D (†). The minimum (MIN), average (AVE), and maximum (MAX) values in the system are shown.

of the surface of the tubular supporting arm, the vacuum level was improved by less than 1%. Nevertheless, creating holes in the supporting arm would help reduce the weight of the mechanical structure.
Another check was if a structure aimed to guide the target cell as it is inserted in the reaction chamber, in the center of the Si tracker would impact the vacuum. This structure would block a considerable fraction of the area around the target holder. In this case it was found that the pressure in the region between the target and the inner Si layer increases linearly with the fraction this structure would occupy out of the area around the target holder. The maximum pressure is found to be almost 30% larger if a guiding structure obstructing 75% of the space around the target holder were to be used. The pressure in the other regions would stay unchanged.

After the presented simulation results and additional checks, one can agree that in order to reach down to the targeted maximum pressure of 10^{-5} mbar around the target cell, it is absolutely necessary to use both turbo-molecular pumps, one upstream the reaction chamber, below the cryostat and one downstream the reaction chamber.

4.3.7 Summary

The STRASSE silicon tracker is going to be used together with a 15-cm long liquid hydrogen target. In this section, the production method of the target cell was described in detail. After the production, the target cells were characterized in thickness and tested at high pressure and at cryogenic temperatures. The produced target cells seem to be very robust, withstanding pressures of $\sim$11.7 mbar. The thickness of the average layer of Mylar of the target cells was measured to be 172.2 μm with a relatively small standard deviation of 13 μm. Furthermore, the target cells did not suffer damage or degradation due to thermal stress induced by multiple cycles of going to cryogenic temperatures and then back to ambient temperatures. The consistent breaking pressure for the several target cells that were tested and the small standard deviation of the thickness of the target cells, show a good level of replicability by using the presented production method. The inconsistency appears in the glue layer thickness, which could be solved by automatising of the production process and minimising the human input. Additionally, vacuum simulations for the STRASSE reaction chamber were performed and presented. The interest was in the critical moment of filling the target cell with hydrogen, when the hydrogen is still in gaseous state and not fully liquefied and can permeate through the target cell. It was tested if two vacuum pumps are necessary in order to keep a pressure close to 10^{-5} mbar in the reaction chamber at any moment. As a result of the simulations, it is indeed needed to have both vacuum pumps in the system, one upstream and one downstream from the reaction chamber, set to at least 500 l/s pumping speed.

5 Conclusions

The first part of this thesis consists of the study of the $N = 32$ shell closure of ^{52}Ca and the size of the p and f neutron orbitals of ^{52}Ca, ^{53}Ca, and ^{54}Ca.

The one-neutron knockout from ^{52}Ca was measured at ∼230 MeV/u in inverse kinematics at the SAMURAI setup of RIBF, Japan. For this experiment, a 15-cm long liquid hydrogen target and the MINOS TPC [8] for tracking the vertex position were used. The excited bound final states of the fragment were tagged via γ-ray spectroscopy. The exclusive cross sections were determined corresponding to each bound final state. Additionally, the exclusive momentum distributions were determined corresponding to the neutron knock-out of an $f_{7/2}$ and a $p_{3/2}$ neutron. The experimental exclusive cross sections and momentum distributions were interpreted within the distorted-wave impulse approximation (DWIA) reaction framework. Based on experimental cross sections and shell model calculations, it is shown that the shell closure at $N = 32$ is as strong as the shell closures at $N = 28$ and $N = 34$ (see Figure 5.1). This result is in agreement with the shell closure observed for $N = 32$ via measurements of the energy of the 2^+ state of ^{52}Ca [2], mass measurements [50–53] and transition probabil-

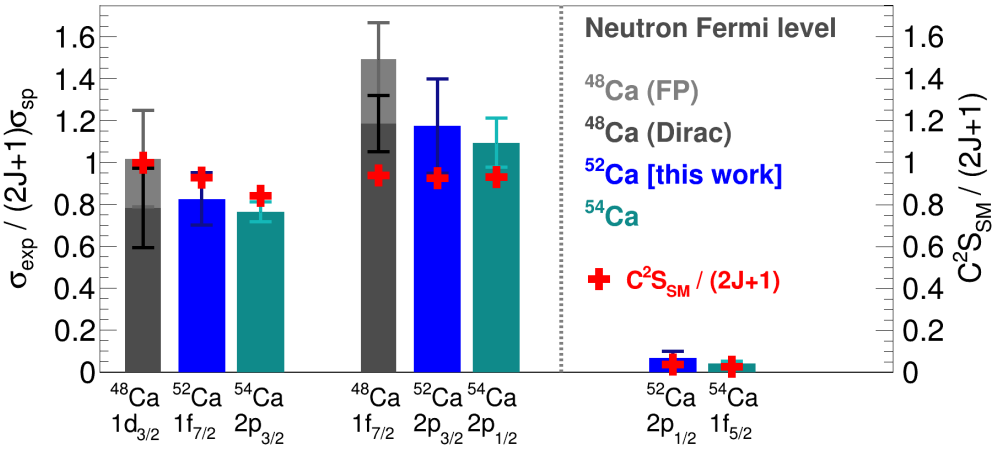

Figure 5.1: The spectroscopic factors obtained for ^{48,52,54}Ca nuclei from the quasi-free neutron knockout reaction. The experimental cross sections were divided by the DWIA single-particle cross sections and normalized to (2J+1). The shell model calculations for the spectroscopic factors are shown with red crosses. The plot show the same patter for the three calcium isotopes below and above the Fermi level, showing that the strength of the $N = 32$ shell closure is similar to that of the $N = 28$ and $N = 34$. Figure published in [9]© CC-BY-4.0.

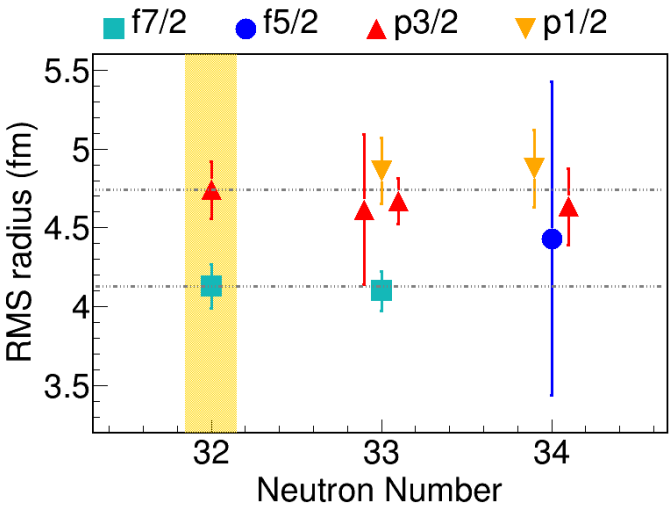

Figure 5.2: The rms radii for the neutron single-particle orbitals of the pf-shell in calcium isotopes.

ity measurements [55, 56]. Moreover, from the momentum distribution analysis one could access the rms radii of the $f_{7/2}$ and $p_{3/2}$ neutron single-particle orbitals. The experimentally determined momentum distributions of the fragment in the center of mass of the beam are directly related to the momentum distribution of the knocked out neutron. This in turn is linked to the size of the neutron orbitals due to the Heisenberg uncertainty principle. As a result of the momentum distribution analysis, the rms radii of the $f_{7/2}$ and a $p_{3/2}$ neutron single-particle orbitals were determined to be 4.13(14) fm and 4.74(18) fm, respectively. The results give a difference between the p and f orbitals of 0.61(23) fm, in agreement with the prediction of Ref. [7]. This work is published in Ref [9].

To verify the robustness of these conclusions, the ^{53}Ca(p,pn) and ^{54}Ca(p,pn) reaction channels were analysed in the same way. The data set is from the same experimental campaign as the ^{52}Ca(p,pn) data. The energy level scheme of ^{52}Ca, which is the fragment of the ^{53}Ca(p,pn) reaction, was established as well. The single-particle configuration of the exited states of ^{52}Ca were obtained from shell model calculations and could be confirmed from the width of the experimental momentum distributions. The $f_{7/2}$, $p_{3/2}$, $f_{5/2}$ and $p_{1/2}$ neutron single-particle orbitals could be accessed experimentally and the following rms radii values were obtained: for $p_{3/2}$, 4.67(15) fm (N=33), 4.62(48) fm (N=33), and 4.64(24) fm (N=34); for $p_{1/2}$, 4.86(21) fm (N=33) and 4.88(24) fm (N=34); for $f_{7/2}$, 4.10(13) fm (N=33); and for $f_{5/2}$, 4.43(100) fm (N=34), see Figure 5.2. Aside from $f_{5/2}$ of ^{54}Ca, for which the statistics was very poor, the rms radii could be determined successfully via the momentum distribution analysis method. The main result of this analysis is that the $p_{1/2}$ and $p_{3/2}$ neutron orbitals for the three calcium isotopes, ^{52}Ca, ^{53}Ca and ^{54}Ca, are consistent with each other within the uncertainties of the experiment and analysis method. The implications of these findings to the charge and matter radii in neutron-rich calcium isotopes still need to be investigated. The determination of rms radii of the neutron single-particle orbitals via the momentum dis-

tribution from quasi-free neutron knockout reactions is a method that needs to be further benchmarked.

The second part of this thesis presents the development of the STRASSE experimental setup, together with its prototype PFAD, and a liquid hydrogen target dedicated to quasi-free scattering experiments in inverse kinematics. Going further from stability on the nuclear chart requires new and more powerful facilities. The most exotic radioactive beams are obtained at low intensity. This implies that one needs to use thicker targets in order to increase the measured yields, but this comes with an uncertainty in the reaction vertex position. As a natural response to this, one would need to develop trackers for the reaction products, able to reconstruct the reaction vertex. STRASSE consists of a Silicon tracker for charged particles delivering a high-precision vertex reconstruction (σ_{vertex} =0.17 mm [10]) coupled with a 15-cm-long liquid hydrogen target. PFAD, which is the prototype of STRASSE and has the same back-end readout electronics as STRASSE, was constructed and tested offline as well as in-beam. The results of the tests and the in-beam commissioning experiment are described in this thesis. The target cell for the liquid hydrogen target of STRASSE was made out of Mylar using thermo-forming methods, mounted on a stainless steel target holder. The detailed production method and the testing of the target cell were presented as well in this thesis. The experiments with STRASSE are designed for the SAMURAI experimental area of RIKEN, Japan. The STRASSE reaction chamber is foreseen to be combined with the CATANA CsI(Na) crystals array for the detection of the total energy of the protons. The full setup can perform missing mass measurements, complementary to the measurements possible in the SAMURAI experimental area such as γ-ray spectroscopy, invariant mass measurements and the determination of complete kinematics of the beam and fragment nuclei. The STRASSE system is going to be used for quasi-free scattering reactions such as (p,2p) or (p,3p) for exploring the nuclear structure of nuclei far from stability using intermediate-energy radioactive beams and the high-density proton target in the liquid phase.

Acknowledgements

I would like to thank first of all my supervisor Prof. Dr. Alexandre Obertelli for giving me the opportunity to work on several interesting and challenging topics ranging from data analysis, simulations and results interpretation as well as hands-on activities involving electronics and cryogenic target cells production from which I acquired new skills and experience; and I would like to acknowledge his support and guidance throughout my doctoral studies. Along my three-years journey I benefited from the help of several people, the closest and most supporting being my family, Marilia and Alex. I would also like to thank for the help received from my colleagues and friends, Dr. Hongna Liu, Christina Xanthopoulou, Dr. Osnan Maragoto-Rodriguez and Dr. Adrian Rodriguez-Rodriguez. Last but not least, I would like to thank Prof. Dr. Thomas Aumann, Prof. Dr. Achim Schwenk and Prof. Dr. Michael Vogel for accepting to be part of the committee for my doctoral examination.

List of Figures

List of Tables

Bibliography

[1] I. Talmi and I. Unna, "Order of levels in the shell model and spin of ^{11}Be", Phys. Rev. Lett. **4**, 469–470 (1960).

[2] A. Huck, G. Klotz, A. Knipper, C. Miehé, C. Richard-Serre, G. Walter, A. Poves, H. L. Ravn, and G. Marguier, "Beta decay of the new isotopes ^{52}K, ^{52}Ca and ^{52}Sc; a test of the shell model far from stability", Phys. Rev. C **31**, 2226–2237 (1985).

[3] D. Steppenbeck, "A spectroscopic study highlights the 'doubly magic' nature of ^{54}Ca and provides direct experimental evidence for the onset of a sizable subshell closure at neutron number 34 in isotopes far from stability", Nature **502**, 207–210 (2013).

[4] R. F. Garcia Ruiz, "Unexpectedly large charge radii of neutron-rich calcium isotopes", Nature Physics **12**, 594–598 (2016).

[5] Á. Koszorús, "Charge radii of exotic potassium isotopes challenge nuclear theory and the magic character of $N = 32$", Nature Physics **17**, 439–443 (2021).

[6] M. Tanaka, M. Takechi, A. Homma, M. Fukuda, D. Nishimura, T. Suzuki, Y. Tanaka, T. Moriguchi, D. S. Ahn, A. Aimaganbetov, M. Amano, H. Arakawa, S. Bagchi, K.-H. Behr, N. Burtebayev, K. Chikaato, H. Du, S. Ebata, T. Fujii, N. Fukuda, H. Geissel, T. Hori, W. Horiuchi, S. Hoshino, R. Igosawa, A. Ikeda, N. Inabe, K. Inomata, K. Itahashi, T. Izumikawa, D. Kamioka, N. Kanda, I. Kato, I. Kenzhina, Z. Korkulu, Y. Kuk, K. Kusaka, K. Matsuta, M. Mihara, E. Miyata, D. Nagae, S. Nakamura, M. Nassurlla, K. Nishimuro, K. Nishizuka, K. Ohnishi, M. Ohtake, T. Ohtsubo, S. Omika, H. J. Ong, A. Ozawa, A. Prochazka, H. Sakurai, C. Scheidenberger, Y. Shimizu, T. Sugihara, T. Sumikama, H. Suzuki, S. Suzuki, H. Takeda, Y. K. Tanaka, I. Tanihata, T. Wada, K. Wakayama, S. Yagi, T. Yamaguchi, R. Yanagihara, Y. Yanagisawa, K. Yoshida, and T. K. Zholdybayev, "Swelling of doubly magic ^{48}Ca core in ca isotopes beyond $N = 28$", Phys. Rev. Lett. **124**, 102501 (2020).

[7] J. Bonnard, S. M. Lenzi, and A. P. Zuker, "Neutron skins and halo orbits in the sd and pf shells", Phys. Rev. Lett. **116**, 212501 (2016).

[8] A. Obertelli, "MINOS: a vertex tracker coupled to a thick liquid-hydrogen target for in-beam spectroscopy of exotic nuclei", The European Physical Journal A **50**, 8 (2014).

[9]M. Enciu, H. N. Liu, A. Obertelli, P. Doornenbal, F. Nowacki, K. Ogata, A. Poves, K. Yoshida, N. L. Achouri, H. Baba, F. Browne, D. Calvet, F. Château, S. Chen, N. Chiga, A. Corsi, M. L. Cortés, A. Delbart, J.-M. Gheller, A. Giganon, A. Gillibert, C. Hilaire, T. Isobe, T. Kobayashi, Y. Kubota, V. Lapoux, T. Motobayashi, I. Murray, H. Otsu, V. Panin, N. Paul, W. Rodriguez, H. Sakurai, M. Sasano, D. Steppenbeck, L. Stuhl, Y. L. Sun, Y. Togano, T. Uesaka, K. Wimmer, K. Yoneda, O. Aktas, T. Aumann, L. X. Chung, F. Flavigny, S. Franchoo, I. Gasparic, R.-B. Gerst, J. Gibelin, K. I. Hahn, D. Kim, Y. Kondo, P. Koseoglou, J. Lee, C. Lehr, P. J. Li, B. D. Linh, T. Lokotko, M. MacCormick, K. Moschner, T. Nakamura, S. Y. Park, D. Rossi, E. Sahin, P.-A. Söderström, D. Sohler, S. Takeuchi, H. Toernqvist, V. Vaquero, V. Wagner, S. Wang, V. Werner, X. Xu, H. Yamada, D. Yan, Z. Yang, M. Yasuda, and L. Zanetti, "Extended $p_{3/2}$ neutron orbital and the $N = 32$ shell closure in ^{52}Ca", Phys. Rev. Lett. **129**, 262501 (2022).

[10]H. N. Liu, F. Flavigny, H. Baba, M. Boehmer, U. Bonnes, V. Borshchov, P. Doornenbal, N. Ebina, M. Enciu, A. Frotscher, R. Gernhäuser, V. Girard-Alcindor, D. Goupillière, J. Heuser, R. Kapell, Y. Kondo, H. Lee, J. Lehnert, T. Matsui, A. Matta, T. Nakamura, A. Obertelli, T. Pohl, M. Protsenko, M. Sasano, Y. Satou, C. J. Schmidt, K. Schünemann, C. Simons, Y. L. Sun, J. Tanaka, Y. Togano, T. Tomai, I. Tymchuk, T. Uesaka, R. Visinka, H. Wang, and F. Wienholtz, "STRASSE: a silicon tracker for quasi-free scattering measurements at the RIBF", The European Physical Journal A **59**, 121 (2023).

[11]Y. Togano, T. Nakamura, Y. Kondo, M. Shikata, T. Ozaki, A. Saito, T. Tomai, M. Yasuda, H. Yamada, N. Chiga, H. Otsu, V. Panin, Y. Zaihong, and Y. Fujino, "New γ-ray detector CATANA for in-beam γ-ray spectroscopy with fast RI beams", Nuclear Instruments and Methods in Physics Research Section B: Beam Interactions with Materials and Atoms **463**, 195–197 (2020).

[12]R. Machleidt and F. Sammarruca, "Chiral EFT based nuclear forces: achievements and challenges", Physica Scripta **91**, 083007 (2016).

[13]A. Obertelli and H. Sagawa, *Modern nuclear physics: from fundamentals to frontiers* (Springer Singapore, 2021).

[14]E. Epelbaum, H. Krebs, and P. Reinert, "High-precision nuclear forces from chiral eft: state-of-the-art, challenges, and outlook", Frontiers in Physics **8**, 10.3389/fphy.2020.00098 (2020).

[15]H. Krebs, "Nuclear currents in chiral effective field theory", The European Physical Journal A **56**, 234 (2020).

[16]R. B. Wiringa, V. G. J. Stoks, and R. Schiavilla, "Accurate nucleon-nucleon potential with charge-independence breaking", Phys. Rev. C **51**, 38–51 (1995).

[17]R. Machleidt, "High-precision, charge-dependent bonn nucleon-nucleon potential", Phys. Rev. C **63**, 024001 (2001).

[18]S. Bogner, T. Kuo, and A. Schwenk, "Model-independent low momentum nucleon interaction from phase shift equivalence", Physics Reports **386**, 1–27 (2003).

[19]M. G. Mayer, “On closed shells in nuclei”, Phys. Rev. **74**, 235–239 (1948).

[20]M. G. Mayer, “On closed shells in nuclei. II”, Phys. Rev. **75**, 1969–1970 (1949).

[21]O. Haxel, J. H. D. Jensen, and H. E. Suess, “On the ”magic numbers” in nuclear structure”, Phys. Rev. **75**, 1766–1766 (1949).

[22]M. Mayer and J. H. D. Jensen, *Elementary theory of nuclear shell structure* (Wiley, New York, 1955).

[23]J. P. Elliott and A. M. Lane, “Evidence for two-body spin-orbit forces in nuclei”, Phys. Rev. **96**, 1160–1162 (1954).

[24]A. Navin, D. W. Anthony, T. Aumann, T. Baumann, D. Bazin, Y. Blumenfeld, B. A. Brown, T. Glasmacher, P. G. Hansen, R. W. Ibbotson, P. A. Lofy, V. Maddalena, K. Miller, T. Nakamura, B. V. Pritychenko, B. M. Sherrill, E. Spears, M. Steiner, J. A. Tostevin, J. Yurkon, and A. Wagner, “Direct evidence for the breakdown of the $N = 8$ shell closure in ^{12}Be”, Phys. Rev. Lett. **85**, 266–269 (2000).

[25]C. Thibault, R. Klapisch, C. Rigaud, A. M. Poskanzer, R. Prieels, L. Lessard, and W. Reisdorf, “Direct measurement of the masses of ^{11}Li and $^{26-32}$Na with an on-line mass spectrometer”, Phys. Rev. C **12**, 644–657 (1975).

[26]D. Guillemaud-Mueller, C. Detraz, M. Langevin, F. Naulin, M. de Saint-Simon, C. Thibault, F. Touchard, and M. Epherre, “β-decay schemes of very neutron-rich sodium isotopes and their descendants”, Nuclear Physics A **426**, 37–76 (1984).

[27]T. Motobayashi, Y. Ikeda, K. Ieki, M. Inoue, N. Iwasa, T. Kikuchi, M. Kurokawa, S. Moriya, S. Ogawa, H. Murakami, S. Shimoura, Y. Yanagisawa, T. Nakamura, Y. Watanabe, M. Ishihara, T. Teranishi, H. Okuno, and R. Casten, “Large deformation of the very neutron-rich nucleus ^{32}Mg from intermediate-energy coulomb excitation”, Physics Letters B **346**, 9–14 (1995).

[28]B. Bastin, S. Grévy, D. Sohler, O. Sorlin, Z. Dombrádi, N. L. Achouri, J. C. Angélique, F. Azaiez, D. Baiborodin, R. Borcea, C. Bourgeois, A. Buta, A. Bürger, R. Chapman, J. C. Dalouzy, Z. Dlouhy, A. Drouard, Z. Elekes, S. Franchoo, S. Iacob, B. Laurent, M. Lazar, X. Liang, E. Liénard, J. Mrazek, L. Nalpas, F. Negoita, N. A. Orr, Y. Penionzhkevich, Z. Podolyák, F. Pougheon, P. Roussel-Chomaz, M. G. Saint-Laurent, M. Stanoiu, I. Stefan, F. Nowacki, and A. Poves, “Collapse of the $N = 28$ shell closure in ^{42}Si”, Phys. Rev. Lett. **99**, 022503 (2007).

[29]A. Ozawa, T. Kobayashi, T. Suzuki, K. Yoshida, and I. Tanihata, “New magic number, N=16, near the neutron drip line”, Phys. Rev. Lett. **84**, 5493–5495 (2000).

[30]R. Kanungo, C. Nociforo, A. Prochazka, T. Aumann, D. Boutin, D. Cortina-Gil, B. Davids, M. Diakaki, F. Farinon, H. Geissel, R. Gernhäuser, J. Gerl, R. Janik, B. Jonson, B. Kindler, R. Knöbel, R. Krücken, M. Lantz, H. Lenske, Y. Litvinov, B. Lommel, K. Mahata, P. Maierbeck, A. Musumarra, T. Nilsson, T. Otsuka, C. Perro, C. Scheidenberger, B. Sitar, P. Strmen, B. Sun, I. Szarka, I. Tanihata, Y. Utsuno, H. Weick, and M. Winkler, “One-neutron removal

measurement reveals ^{24}O as a new doubly magic nucleus", Phys. Rev. Lett. **102**, 152501 (2009).

[31]K. Tshoo, Y. Satou, H. Bhang, S. Choi, T. Nakamura, Y. Kondo, S. Deguchi, Y. Kawada, N. Kobayashi, Y. Nakayama, K. N. Tanaka, N. Tanaka, N. Aoi, M. Ishihara, T. Motobayashi, H. Otsu, H. Sakurai, S. Takeuchi, Y. Togano, K. Yoneda, Z. H. Li, F. Delaunay, J. Gibelin, F. M. Marqués, N. A. Orr, T. Honda, M. Matsushita, T. Kobayashi, Y. Miyashita, T. Sumikama, K. Yoshinaga, S. Shimoura, D. Sohler, T. Zheng, and Z. X. Cao, "$N = 16$ Spherical shell closure in ^{24}O", Phys. Rev. Lett. **109**, 022501 (2012).

[32]T. Otsuka and A. Schwenk, "Shell evolution in exotic nuclei and nuclear forces", Nuclear Physics News **22**, 12–17 (2012).

[33]O. Sorlin, "Shell evolutions and nuclear forces", EPJ Web of Conferences **66**, `10.1051/epjconf/20146601016` (2014).

[34]T. Otsuka, A. Gade, O. Sorlin, T. Suzuki, and Y. Utsuno, "Evolution of shell structure in exotic nuclei", Rev. Mod. Phys. **92**, 015002 (2020).

[35]O. Sorlin and M.-G. Porquet, "Nuclear magic numbers: new features far from stability", Progress in Particle and Nuclear Physics **61**, 602–673 (2008).

[36]T. Otsuka, T. Suzuki, R. Fujimoto, H. Grawe, and Y. Akaishi, "Evolution of nuclear shells due to the tensor force", Phys. Rev. Lett. **95**, 232502 (2005).

[37]T. Otsuka, T. Matsuo, and D. Abe, "Mean field with tensor force and shell structure of exotic nuclei", Phys. Rev. Lett. **97**, 162501 (2006).

[38]*Nudat 3.0*, `https://www.nndc.bnl.gov/nudat3/` (visited on 09/01/2022).

[39]H. N. Liu, A. Obertelli, P. Doornenbal, C. A. Bertulani, G. Hagen, J. D. Holt, G. R. Jansen, T. D. Morris, A. Schwenk, R. Stroberg, N. Achouri, H. Baba, F. Browne, D. Calvet, F. Château, S. Chen, N. Chiga, A. Corsi, M. L. Cortés, A. Delbart, J.-M. Gheller, A. Giganon, A. Gillibert, C. Hilaire, T. Isobe, T. Kobayashi, Y. Kubota, V. Lapoux, T. Motobayashi, I. Murray, H. Otsu, V. Panin, N. Paul, W. Rodriguez, H. Sakurai, M. Sasano, D. Steppenbeck, L. Stuhl, Y. L. Sun, Y. Togano, T. Uesaka, K. Wimmer, K. Yoneda, O. Aktas, T. Aumann, L. X. Chung, F. Flavigny, S. Franchoo, I. Ga špari ć, R.-B. Gerst, J. Gibelin, K. I. Hahn, D. Kim, T. Koiwai, Y. Kondo, P. Koseoglou, J. Lee, C. Lehr, B. D. Linh, T. Lokotko, M. MacCormick, K. Moschner, T. Nakamura, S. Y. Park, D. Rossi, E. Sahin, D. Sohler, P.-A. Söderström, S. Takeuchi, H. Törnqvist, V. Vaquero, V. Wagner, S. Wang, V. Werner, X. Xu, H. Yamada, D. Yan, Z. Yang, M. Yasuda, and L. Zanetti, "How robust is the $N = 34$ subshell closure? first spectroscopy of ^{52}Ar", Phys. Rev. Lett. **122**, 072502 (2019).

[40]J. Prisciandaro, P. Mantica, B. Brown, D. Anthony, M. Cooper, A. Garcia, D. Groh, A. Komives, W. Kumarasiri, P. Lofy, A. Oros-Peusquens, S. Tabor, and M. Wiedeking, "New evidence for a subshell gap at $N = 32$", Physics Letters B **510**, 17–23 (2001).

[41]A. Goldkuhle, C. Fransen, A. Blazhev, M. Beckers, B. Birkenbach, T. Braunroth, E. Clément, A. Dewald, J. Dudouet, J. Eberth, H. Hess, B. Jacquot, J. Jolie, Y.-H. Kim, A. Lemasson, S. M. Lenzi, H. J. Li, J. Litzinger, C. Michelagnoli, C. Müller-Gatermann, B. S. Nara Singh, R. M. Pérez-Vidal, D. Ralet, P. Reiter, A. Vogt, N. Warr, K. O. Zell, A. Ata ç, D. Barrientos, C. Barthe-Dejean, G. Benzoni, A. J. Boston, H. C. Boston, P. Bourgault, I. Burrows, J. Cacitti, B. Cederwall, M. Ciemala, D. M. Cullen, G. De France, C. Domingo-Pardo, J.-L. Foucher, G. Fremont, A. Gadea, P. Gangnant, V. González, J. Goupil, C. Henrich, C. Houarner, M. Jean, D. S. Judson, A. Korichi, W. Korten, M. Labiche, A. Lefevre, L. Legeard, F. Legruel, S. Leoni, J. Ljungvall, A. Maj, C. Maugeais, L. Ménager, N. Ménard, R. Menegazzo, D. Mengoni, B. Million, H. Munoz, D. R. Napoli, A. Navin, J. Nyberg, M. Ozille, Z. Podolyak, A. Pullia, B. Raine, F. Recchia, J. Ropert, F. Saillant, M. D. Salsac, E. Sanchis, C. Schmitt, J. Simpson, C. Spitaels, O. Stezowski, C. Theisen, M. Toulemonde, M. Tripon, J.-J. Valiente Dobón, G. Voltolini, and M. Zieli ńska (AGATA Collaboration), "Lifetime measurements in ^{52,54}Ti to study shell evolution toward $N = 32$", Phys. Rev. C **100**, 054317 (2019).

[42]D. Steppenbeck, S. Takeuchi, N. Aoi, P. Doornenbal, M. Matsushita, H. Wang, H. Baba, S. Go, J. D. Holt, J. Lee, K. Matsui, S. Michimasa, T. Motobayashi, D. Nishimura, T. Otsuka, H. Sakurai, Y. Shiga, P.-A. Söderström, S. R. Stroberg, T. Sumikama, R. Taniuchi, J. A. Tostevin, Y. Utsuno, J. J. Valiente-Dobón, and K. Yoneda, "Structure of ^{55}Sc and development of the $N = 34$ subshell closure", Phys. Rev. C **96**, 064310 (2017).

[43]P. Koseoglou, V. Werner, N. Pietralla, P.-A. Söderström, P. Doornenbal, A. Obertelli, N. Achouri, H. Baba, F. Browne, D. Calvet, F. Château, S. Chen, N. Chiga, A. Corsi, M. L. Cortés, A. Delbart, J.-M. Gheller, A. Giganon, A. Gillibert, C. Hilaire, T. Isobe, T. Kobayashi, Y. Kubota, V. Lapoux, H. Liu, T. Motobayashi, I. Murray, H. Otsu, V. Panin, N. Paul, W. Rodriguez, H. Sakurai, M. Sasano, D. Steppenbeck, L. Stuhl, Y. L. Sun, Y. Togano, T. Uesaka, K. Wimmer, K. Yoneda, O. Aktas, T. Aumann, L. X. Chung, F. Flavigny, S. Franchoo, I. Gasparic, R.-B. Gerst, J. Gibelin, K. I. Hahn, D. Kim, T. Koiwai, Y. Kondo, J. Lee, C. Lehr, M. Lettmann, B. D. Linh, T. Lokotko, M. MacCormick, K. Moschner, T. Nakamura, S. Y. Park, D. Rossi, E. Sahin, D. Sohler, S. Takeuchi, H. Toernqvist, V. Vaquero, V. Wagner, S. Wang, X. Xu, H. Yamada, D. Yan, Z. Yang, M. Yasuda, and L. Zanetti, "Spectroscopy of neutron-rich scandium isotopes", Journal of Physics: Conference Series **1555**, 012026 (2020).

[44]L. Lalanne, O. Sorlin, A. Poves, M. Assié, F. Hammache, S. Koyama, D. Suzuki, F. Flavigny, V. Girard-Alcindor, A. Lemasson, A. Matta, T. Roger, D. Beaumel, Y. Blumenfeld, B. A. Brown, F. D. O. Santos, F. Delaunay, N. de Séréville, S. Franchoo, J. Gibelin, J. Guillot, O. Kamalou, N. Kitamura, V. Lapoux, B. Mauss, P. Morfouace, J. Pancin, T. Y. Saito, C. Stodel, and J.-C. Thomas, $N = 16$ *Magicity revealed at the proton drip-line through the study of* ^{35}*Ca*, 2023.

[45]A. Gade, R. V. F. Janssens, D. Bazin, R. Broda, B. A. Brown, C. M. Campbell, M. P. Carpenter, J. M. Cook, A. N. Deacon, D.-C. Dinca, B. Fornal, S. J. Freeman, T. Glasmacher, P. G. Hansen, B. P. Kay, P. F. Mantica, W. F. Mueller, J. R. Terry, J. A. Tostevin, and S. Zhu, "Cross-shell excitation in two-proton knockout: structure of ^{52}Ca", Phys. Rev. C **74**, 021302 (2006).

[46]S. Chen, J. Lee, P. Doornenbal, A. Obertelli, C. Barbieri, Y. Chazono, P. Navrátil, K. Ogata, T. Otsuka, F. Raimondi, V. Somà, Y. Utsuno, K. Yoshida, H. Baba, F. Browne, D. Calvet, F. Château, N. Chiga, A. Corsi, M. L. Cortés, A. Delbart, J.-M. Gheller, A. Giganon, A. Gillibert, C. Hilaire, T. Isobe, J. Kahlbow, T. Kobayashi, Y. Kubota, V. Lapoux, H. N. Liu, T. Motobayashi, I. Murray, H. Otsu, V. Panin, N. Paul, W. Rodriguez, H. Sakurai, M. Sasano, D. Steppenbeck, L. Stuhl, Y. L. Sun, Y. Togano, T. Uesaka, K. Wimmer, K. Yoneda, N. Achouri, O. Aktas, T. Aumann, L. X. Chung, F. Flavigny, S. Franchoo, I. Ga špari ć, R.-B. Gerst, J. Gibelin, K. I. Hahn, D. Kim, T. Koiwai, Y. Kondo, P. Koseoglou, C. Lehr, B. D. Linh, T. Lokotko, M. MacCormick, K. Moschner, T. Nakamura, S. Y. Park, D. Rossi, E. Sahin, D. Sohler, P.-A. Söderström, S. Takeuchi, H. Törnqvist, V. Vaquero, V. Wagner, S. Wang, V. Werner, X. Xu, H. Yamada, D. Yan, Z. Yang, M. Yasuda, and L. Zanetti, "Quasifree neutron knockout from ^{54}Ca corroborates arising $N = 34$ neutron magic number", Phys. Rev. Lett. **123**, 142501 (2019).

[47]J. Lee, M. B. Tsang, and W. G. Lynch, "Neutron spectroscopic factors from transfer reactions", Phys. Rev. C **75**, 064320 (2007).

[48]D. Steppenbeck, S. Takeuchi, N. Aoi, P. Doornenbal, M. Matsushita, H. Wang, Y. Utsuno, H. Baba, S. Go, J. Lee, K. Matsui, S. Michimasa, T. Motobayashi, D. Nishimura, T. Otsuka, H. Sakurai, Y. Shiga, N. Shimizu, P.-A. Söderström, T. Sumikama, R. Taniuchi, J. J. Valiente-Dobón, and K. Yoneda, "Low-lying structure of ^{50}Ar and the $N = 32$ subshell closure", Phys. Rev. Lett. **114**, 252501 (2015).

[49]M. L. Cortés, W. Rodriguez, P. Doornenbal, A. Obertelli, J. D. Holt, J. Menéndez, K. Ogata, A. Schwenk, N. Shimizu, J. Simonis, Y. Utsuno, K. Yoshida, L. Achouri, H. Baba, F. Browne, D. Calvet, F. Château, S. Chen, N. Chiga, A. Corsi, A. Delbart, J.-M. Gheller, A. Giganon, A. Gillibert, C. Hilaire, T. Isobe, T. Kobayashi, Y. Kubota, V. Lapoux, H. N. Liu, T. Motobayashi, I. Murray, H. Otsu, V. Panin, N. Paul, H. Sakurai, M. Sasano, D. Steppenbeck, L. Stuhl, Y. L. Sun, Y. Togano, T. Uesaka, K. Wimmer, K. Yoneda, O. Aktas, T. Aumann, L. X. Chung, F. Flavigny, S. Franchoo, I. Ga špari ć, R.-B. Gerst, J. Gibelin, K. I. Hahn, D. Kim, T. Koiwai, Y. Kondo, P. Koseoglou, J. Lee, C. Lehr, B. D. Linh, T. Lokotko, M. MacCormick, K. Moschner, T. Nakamura, S. Y. Park, D. Rossi, E. Sahin, P.-A. Söderström, D. Sohler, S. Takeuchi, H. Toernqvist, V. Vaquero, V. Wagner, S. Wang, V. Werner, X. Xu, H. Yamada, D. Yan, Z. Yang, M. Yasuda, and L. Zanetti, "$N = 32$ Shell closure below calcium: low-lying structure of ^{50}Ar", Phys. Rev. C **102**, 064320 (2020).

[50]F. Wienholtz, D. Beck, K. Blaum, C. Borgmann, M. Breitenfeldt, R. B. Cakirli, S. George, F. Herfurth, J. D. Holt, M. Kowalska, S. Kreim, D. Lunney, V. Manea, J. Menéndez, D. Neidherr, M. Rosenbusch, L. Schweikhard, A. Schwenk, J. Simonis, J. Stanja, R. N. Wolf, and K. Zuber, "Masses of exotic calcium isotopes pin down nuclear forces", Nature **498**, 346–349 (2013).

[51]M. Rosenbusch, P. Ascher, D. Atanasov, C. Barbieri, D. Beck, K. Blaum, C. Borgmann, M. Breitenfeldt, R. B. Cakirli, A. Cipollone, S. George, F. Herfurth, M. Kowalska, S. Kreim, D. Lunney, V. Manea, P. Navrátil, D. Neidherr, L. Schweikhard, V. Somà, J. Stanja, F. Wienholtz, R. N. Wolf, and K. Zuber, "Probing the $N = 32$ shell closure below the magic proton

number $Z = 20$: mass measurements of the exotic isotopes ^{52,53}K", Phys. Rev. Lett. **114**, 202501 (2015).

[52]X. Xu, M. Wang, Y.-H. Zhang, H.-S. Xu, P. Shuai, X.-L. Tu, Y. A. Litvinov, X.-H. Zhou, B.-H. Sun, Y.-J. Yuan, J.-W. Xia, J.-C. Yang, K. Blaum, R.-J. Chen, X.-C. Chen, C.-Y. Fu, Z. Ge, Z.-G. Hu, W.-J. Huang, D.-W. Liu, Y.-H. Lam, X.-W. Ma, R.-S. Mao, T. Uesaka, G.-Q. Xiao, Y.-M. Xing, T. Yamaguchi, Y. Yamaguchi, Q. Zeng, X.-L. Yan, H.-W. Zhao, T.-C. Zhao, W. Zhang, and W.-L. Zhan, "Direct mass measurements of neutron-rich ^{86}Kr projectile fragments and the persistence of neutron magic number N=32 in Sc isotopes*", Chinese Physics C **39**, 104001 (2015).

[53]E. Leistenschneider, M. P. Reiter, S. Ayet San Andrés, B. Kootte, J. D. Holt, P. Navrátil, C. Babcock, C. Barbieri, B. R. Barquest, J. Bergmann, J. Bollig, T. Brunner, E. Dunling, A. Finlay, H. Geissel, L. Graham, F. Greiner, H. Hergert, C. Hornung, C. Jesch, R. Klawitter, Y. Lan, D. Lascar, K. G. Leach, W. Lippert, J. E. McKay, S. F. Paul, A. Schwenk, D. Short, J. Simonis, V. Somà, R. Steinbrügge, S. R. Stroberg, R. Thompson, M. E. Wieser, C. Will, M. Yavor, C. Andreoiu, T. Dickel, I. Dillmann, G. Gwinner, W. R. Plaß, C. Scheidenberger, A. A. Kwiatkowski, and J. Dilling, "Dawning of the $N = 32$ shell closure seen through precision mass measurements of neutron-rich titanium isotopes", Phys. Rev. Lett. **120**, 062503 (2018).

[54]S. Michimasa, M. Kobayashi, Y. Kiyokawa, S. Ota, D. S. Ahn, H. Baba, G. P. A. Berg, M. Dozono, N. Fukuda, T. Furuno, E. Ideguchi, N. Inabe, T. Kawabata, S. Kawase, K. Kisamori, K. Kobayashi, T. Kubo, Y. Kubota, C. S. Lee, M. Matsushita, H. Miya, A. Mizukami, H. Nagakura, D. Nishimura, H. Oikawa, H. Sakai, Y. Shimizu, A. Stolz, H. Suzuki, M. Takaki, H. Takeda, S. Takeuchi, H. Tokieda, T. Uesaka, K. Yako, Y. Yamaguchi, Y. Yanagisawa, R. Yokoyama, K. Yoshida, and S. Shimoura, "Magic nature of neutrons in ^{54}Ca: first mass measurements of $^{55--57}$Ca", Phys. Rev. Lett. **121**, 022506 (2018).

[55]D.-C. Dinca, R. V. F. Janssens, A. Gade, D. Bazin, R. Broda, B. A. Brown, C. M. Campbell, M. P. Carpenter, P. Chowdhury, J. M. Cook, A. N. Deacon, B. Fornal, S. J. Freeman, T. Glasmacher, M. Honma, F. G. Kondev, J.-L. Lecouey, S. N. Liddick, P. F. Mantica, W. F. Mueller, H. Olliver, T. Otsuka, J. R. Terry, B. A. Tomlin, and K. Yoneda, "Reduced transition probabilities to the first 2^+ state in ^{52,54,56}Ti and development of shell closures at $N = 32, 34$", Phys. Rev. C **71**, 041302 (2005).

[56]A. Bürger, T. Saito, H. Grawe, H. Hübel, P. Reiter, J. Gerl, M. Górska, H. Wollersheim, A. Al-Khatib, A. Banu, T. Beck, F. Becker, P. Bednarczyk, G. Benzoni, A. Bracco, S. Brambilla, P. Bringel, F. Camera, E. Clément, P. Doornenbal, H. Geissel, A. Görgen, J. Grębosz, G. Hammond, M. Hellström, M. Honma, M. Kavatsyuk, O. Kavatsyuk, M. Kmiecik, I. Kojouharov, W. Korten, N. Kurz, R. Lozeva, A. Maj, S. Mandal, B. Million, S. Muralithar, A. Neußer, F. Nowacki, T. Otsuka, Z. Podolyák, N. Saito, A. Singh, H. Weick, C. Wheldon, O. Wieland, and M. Winkler, "Relativistic coulomb excitation of neutron-rich ^{54,56,58}Cr: on the pathway of magicity from N=40 to N=32", Physics Letters B **622**, 29–34 (2005).

[57]R. Broda, J. Wrzesi ński, A. Gadea, N. M ărginean, B. Fornal, L. Corradi, A. M. Stefanini, W. Królas, T. Pawłat, B. Szpak, S. Lunardi, J. J. Valiente-Dobón, D. Mengoni, E. Farnea, M. P. Carpenter, G. De Angelis, F. Della Vedova, E. Fioretto, B. Guiot, R. V. F. Janssens, P. F. Mantica, P. Mason, G. Montagnoli, D. R. Napoli, R. Orlandi, I. Pokrovskiy, G. Pollarolo, E. Sahin, F. Scarlassara, R. Silvestri, S. Szilner, C. A. Ur, M. Trotta, and S. Zhu, "Proton-hole states in the $N = 30$ neutron-rich isotope ^{49}K", Phys. Rev. C **82**, 034319 (2010).

[58]J. Papuga, M. L. Bissell, K. Kreim, C. Barbieri, K. Blaum, M. De Rydt, T. Duguet, R. F. Garcia Ruiz, H. Heylen, M. Kowalska, R. Neugart, G. Neyens, W. Nörtershäuser, M. M. Rajabali, R. Sánchez, N. Smirnova, V. Somà, and D. T. Yordanov, "Shell structure of potassium isotopes deduced from their magnetic moments", Phys. Rev. C **90**, 034321 (2014).

[59]Y. Sun, A. Obertelli, P. Doornenbal, C. Barbieri, Y. Chazono, T. Duguet, H. Liu, P. Navrátil, F. Nowacki, K. Ogata, T. Otsuka, F. Raimondi, V. Somà, Y. Utsuno, K. Yoshida, N. Achouri, H. Baba, F. Browne, D. Calvet, F. Château, S. Chen, N. Chiga, A. Corsi, M. Cortés, A. Delbart, J.-M. Gheller, A. Giganon, A. Gillibert, C. Hilaire, T. Isobe, T. Kobayashi, Y. Kubota, V. Lapoux, T. Motobayashi, I. Murray, H. Otsu, V. Panin, N. Paul, W. Rodriguez, H. Sakurai, M. Sasano, D. Steppenbeck, L. Stuhl, Y. Togano, T. Uesaka, K. Wimmer, K. Yoneda, O. Aktas, T. Aumann, L. Chung, F. Flavigny, S. Franchoo, I. Gašparić, R.-B. Gerst, J. Gibelin, K. Hahn, D. Kim, T. Koiwai, Y. Kondo, P. Koseoglou, J. Lee, C. Lehr, B. Linh, T. Lokotko, M. MacCormick, K. Moschner, T. Nakamura, S. Park, D. Rossi, E. Sahin, D. Sohler, P.-A. Söderström, S. Takeuchi, H. Törnqvist, V. Vaquero, V. Wagner, S. Wang, V. Werner, X. Xu, H. Yamada, D. Yan, Z. Yang, M. Yasuda, and L. Zanetti, "Restoration of the natural E($1/2^+_1$) - e($3/2^+_1$) energy splitting in odd-K isotopes towards N = 40", Physics Letters B **802**, 135215 (2020).

[60]I. Angeli and K. Marinova, "Table of experimental nuclear ground state charge radii: an update", Atomic Data and Nuclear Data Tables **99**, 69–95 (2013).

[61]K. Kreim, M. Bissell, J. Papuga, K. Blaum, M. De Rydt, R. Garcia Ruiz, S. Goriely, H. Heylen, M. Kowalska, R. Neugart, G. Neyens, W. Nörtershäuser, M. Rajabali, R. Sánchez Alarcón, H. Stroke, and D. Yordanov, "Nuclear charge radii of potassium isotopes beyond N=28", Physics Letters B **731**, 97–102 (2014).

[62]W. Nörtershäuser and C. Geppert, "Nuclear charge radii of light elements and recent developments in collinear laser spectroscopy", in *The euroschool on exotic beams, vol. iv*, edited by C. Scheidenberger and M. Pfützner (Springer Berlin Heidelberg, Berlin, Heidelberg, 2014), pp. 233–292.

[63]W. Nörtershäuser and I. D. Moore, "Nuclear charge radii", in *Handbook of nuclear physics*, edited by I. Tanihata, H. Toki, and T. Kajino (Springer Nature Singapore, Singapore, 2020), pp. 1–70.

[64]W. H. King, "Isotope shifts in x-ray spectra", in *Isotope shifts in atomic spectra* (Springer US, Boston, MA, 1984), pp. 55–61.

[65]P. Brix and H. Kopfermann, “Neuere ergebnisse zum isotopieverschiebungseffekt in den atomspektren”, in *Festschrift zur feier des zweihundertjährigen bestehens der akademie der wissenschaften in göttingen: i. mathematisch-physikalische klasse* (Springer Berlin Heidelberg, Berlin, Heidelberg, 1951), pp. 17–49.

[66]F. Sommer, K. König, D. M. Rossi, N. Everett, D. Garand, R. P. de Groote, J. D. Holt, P. Imgram, A. Incorvati, C. Kalman, A. Klose, J. Lantis, Y. Liu, A. J. Miller, K. Minamisono, T. Miyagi, W. Nazarewicz, W. Nörtershäuser, S. V. Pineda, R. Powel, P.-G. Reinhard, L. Renth, E. Romero-Romero, R. Roth, A. Schwenk, C. Sumithrarachchi, and A. Teigelhöfer, “Charge radii of ^{55,56}Ni reveal a surprisingly similar behavior at $N = 28$ in ca and ni isotopes”, Phys. Rev. Lett. **129**, 132501 (2022).

[67]A. J. Miller, K. Minamisono, A. Klose, D. Garand, C. Kujawa, J. D. Lantis, Y. Liu, B. Maaß, P. F. Mantica, W. Nazarewicz, W. Nörtershäuser, S. V. Pineda, P.-G. Reinhard, D. M. Rossi, F. Sommer, C. Sumithrarachchi, A. Teigelhöfer, and J. Watkins, “Proton superfluidity and charge radii in proton-rich calcium isotopes”, Nature Physics **15**, 432–436 (2019).

[68]P. Campbell, I. Moore, and M. Pearson, “Laser spectroscopy for nuclear structure physics”, Progress in Particle and Nuclear Physics **86**, 127–180 (2016).

[69]G. Ewald, W. Nörtershäuser, A. Dax, S. Götte, R. Kirchner, H.-J. Kluge, T. Kühl, R. Sanchez, A. Wojtaszek, B. A. Bushaw, G. W. F. Drake, Z.-C. Yan, and C. Zimmermann, “Nuclear charge radii of ^{8,9}Li determined by laser spectroscopy”, Phys. Rev. Lett. **93**, 113002 (2004).

[70]A. Antognini, F. Kottmann, and R. Pohl, “Laser spectroscopy of light muonic atoms and the nuclear charge radii”, SciPost Phys. Proc., 021 (2021).

[71]R. Pohl, F. Nez, L. M. P. Fernandes, F. D. Amaro, F. Biraben, J. M. R. Cardoso, D. S. Covita, A. Dax, S. Dhawan, M. Diepold, A. Giesen, A. L. Gouvea, T. Graf, T. W. Hänsch, P. Indelicato, L. Julien, P. Knowles, F. Kottmann, E.-O. L. Bigot, Y.-W. Liu, J. A. M. Lopes, L. Ludhova, C. M. B. Monteiro, F. Mulhauser, T. Nebel, P. Rabinowitz, J. M. F. dos Santos, L. A. Schaller, K. Schuhmann, C. Schwob, D. Taqqu, J. F. C. A. Veloso, A. Antognini, and T. C. Collaboration, “Laser spectroscopy of muonic deuterium”, Science **353**, 669–673 (2016).

[72]A. Knecht, A. Skawran, and S. M. Vogiatzi, “Study of nuclear properties with muonic atoms”, The European Physical Journal Plus, `10.1140/epjp/s13360-020-00777-y` (2020).

[73]G. Fricke, C. Bernhardt, K. Heilig, L. Schaller, L. Schellenberg, E. Shera, and C. Dejager, “Nuclear ground state charge radii from electromagnetic interactions”, Atomic Data and Nuclear Data Tables **60**, 177–285 (1995).

[74]J. W. A. Den Herder, H. P. Blok, E. Jans, P. H. M. Keizer, L. Lapikas, E. N. M. Quint, G. Van Der Steenhoven, and P. K. A. De Witt Huberts, “Single Particle Properties of ^{51}V and ^{90}Zr Studied With the $(e, e'P)$ Reaction”, Nucl. Phys. A **490**, 507–555 (1988).

[75]B. Frois, J. Cavedon, D. Goutte, M. Huet, P. Leconte, C. Papanicolas, X.-H. Phan, S. Platchkov, S. Williamson, W. Boeglin, and I. Sick, "A precise determination of the 3s proton orbit", Nuclear Physics A **396**, 409–418 (1983).

[76]S. Shlomo, I. Talmi, M. R. Anders, and G. Bonasera, "Effect of short-range correlations on the single proton $3s_{1/2}$ wave function in ^{206}Pb", Journal of Physics: Conference Series **966**, 012013 (2018).

[77]Y. Togano, T. Nakamura, Y. Kondo, J. Tostevin, A. Saito, J. Gibelin, N. Orr, N. Achouri, T. Aumann, H. Baba, F. Delaunay, P. Doornenbal, N. Fukuda, J. Hwang, N. Inabe, T. Isobe, D. Kameda, D. Kanno, S. Kim, N. Kobayashi, T. Kobayashi, T. Kubo, S. Leblond, J. Lee, F. Marqués, R. Minakata, T. Motobayashi, D. Murai, T. Murakami, K. Muto, T. Nakashima, N. Nakatsuka, A. Navin, S. Nishi, S. Ogoshi, H. Otsu, H. Sato, Y. Satou, Y. Shimizu, H. Suzuki, K. Takahashi, H. Takeda, S. Takeuchi, R. Tanaka, A. Tuff, M. Vandebrouck, and K. Yoneda, "Interaction cross section study of the two-neutron halo nucleus ^{22}C", Physics Letters B **761**, 412–418 (2016).

[78]T. Aumann, C. A. Bertulani, F. Schindler, and S. Typel, "Peeling off neutron skins from neutron-rich nuclei: constraints on the symmetry energy from neutron-removal cross sections", Phys. Rev. Lett. **119**, 262501 (2017).

[79]W. Horiuchi, Y. Suzuki, and T. Inakura, "Probing neutron-skin thickness with total reaction cross sections", Phys. Rev. C **89**, 011601 (2014).

[80]W. Horiuchi, S. Hatakeyama, S. Ebata, and Y. Suzuki, "Extracting nuclear sizes of medium to heavy nuclei from total reaction cross sections", Phys. Rev. C **93**, 044611 (2016).

[81]A. Trzcińska, J. Jastrzębski, P. Lubiński, F. J. Hartmann, R. Schmidt, T. von Egidy, and B. Kłos, "Neutron density distributions deduced from antiprotonic atoms", Phys. Rev. Lett. **87**, 082501 (2001).

[82]T. Aumann, W. Bartmann, O. Boine-Frankenheim, A. Bouvard, A. Broche, F. Butin, D. Calvet, J. Carbonell, P. Chiggiato, H. De Gersem, R. De Oliveira, T. Dobers, F. Ehm, J. F. Somoza, J. Fischer, M. Fraser, E. Friedrich, A. Frotscher, M. Gomez-Ramos, J.-L. Grenard, A. Hobl, G. Hupin, A. Husson, P. Indelicato, K. Johnston, C. Klink, Y. Kubota, R. Lazauskas, S. Malbrunot-Ettenauer, N. Marsic, W. F. O Müller, S. Naimi, N. Nakatsuka, R. Necca, D. Neidherr, G. Neyens, A. Obertelli, Y. Ono, S. Pasinelli, N. Paul, E. C. Pollacco, D. Rossi, H. Scheit, M. Schlaich, A. Schmidt, L. Schweikhard, R. Seki, S. Sels, E. Siesling, T. Uesaka, M. Vilén, M. Wada, F. Wienholtz, S. Wycech, and S. Zacarias, "Puma, antiproton unstable matter annihilation", The European Physical Journal A **58**, 88 (2022).

[83]C. J. Horowitz, S. J. Pollock, P. A. Souder, and R. Michaels, "Parity violating measurements of neutron densities", Phys. Rev. C **63**, 025501 (2001).

[84]D. Adhikari, H. Albataineh, D. Androic, K. Aniol, D. S. Armstrong, T. Averett, C. Ayerbe Gayoso, S. Barcus, V. Bellini, R. S. Beminiwattha, J. F. Benesch, H. Bhatt, D. Bhatta Pathak, D. Bhetuwal, B. Blaikie, Q. Campagna, A. Camsonne, G. D. Cates, Y. Chen, C. Clarke, J. C.

Cornejo, S. Covrig Dusa, P. Datta, A. Deshpande, D. Dutta, C. Feldman, E. Fuchey, C. Gal, D. Gaskell, T. Gautam, M. Gericke, C. Ghosh, I. Halilovic, J.-O. Hansen, F. Hauenstein, W. Henry, C. J. Horowitz, C. Jantzi, S. Jian, S. Johnston, D. C. Jones, B. Karki, S. Katugampola, C. Keppel, P. M. King, D. E. King, M. Knauss, K. S. Kumar, T. Kutz, N. Lashley-Colthirst, G. Leverick, H. Liu, N. Liyange, S. Malace, R. Mammei, J. Mammei, M. McCaughan, D. McNulty, D. Meekins, C. Metts, R. Michaels, M. M. Mondal, J. Napolitano, A. Narayan, D. Nikolaev, M. N. H. Rashad, V. Owen, C. Palatchi, J. Pan, B. Pandey, S. Park, K. D. Paschke, M. Petrusky, M. L. Pitt, S. Premathilake, A. J. R. Puckett, B. Quinn, R. Radloff, S. Rahman, A. Rathnayake, B. T. Reed, P. E. Reimer, R. Richards, S. Riordan, Y. Roblin, S. Seeds, A. Shahinyan, P. Souder, L. Tang, M. Thiel, Y. Tian, G. M. Urciuoli, E. W. Wertz, B. Wojtsekhowski, B. Yale, T. Ye, A. Yoon, A. Zec, W. Zhang, J. Zhang, and X. Zheng (PREX Collaboration), "Accurate determination of the neutron skin thickness of ^{208}Pb through parity-violation in electron scattering", Phys. Rev. Lett. **126**, 172502 (2021).

[85] S. Abrahamyan, Z. Ahmed, H. Albataineh, K. Aniol, D. S. Armstrong, W. Armstrong, T. Averett, B. Babineau, A. Barbieri, V. Bellini, R. Beminiwattha, J. Benesch, F. Benmokhtar, T. Bielarski, W. Boeglin, A. Camsonne, M. Canan, P. Carter, G. D. Cates, C. Chen, J.-P. Chen, O. Hen, F. Cusanno, M. M. Dalton, R. De Leo, K. de Jager, W. Deconinck, P. Decowski, X. Deng, A. Deur, D. Dutta, A. Etile, D. Flay, G. B. Franklin, M. Friend, S. Frullani, E. Fuchey, F. Garibaldi, E. Gasser, R. Gilman, A. Giusa, A. Glamazdin, J. Gomez, J. Grames, C. Gu, O. Hansen, J. Hansknecht, D. W. Higinbotham, R. S. Holmes, T. Holmstrom, C. J. Horowitz, J. Hoskins, J. Huang, C. E. Hyde, F. Itard, C.-M. Jen, E. Jensen, G. Jin, S. Johnston, A. Kelleher, K. Kliakhandler, P. M. King, S. Kowalski, K. S. Kumar, J. Leacock, J. Leckey, J. H. Lee, J. J. LeRose, R. Lindgren, N. Liyanage, N. Lubinsky, J. Mammei, F. Mammoliti, D. J. Margaziotis, P. Markowitz, A. McCreary, D. McNulty, L. Mercado, Z.-E. Meziani, R. W. Michaels, M. Mihovilovic, N. Muangma, C. Muñoz-Camacho, S. Nanda, V. Nelyubin, N. Nuruzzaman, Y. Oh, A. Palmer, D. Parno, K. D. Paschke, S. K. Phillips, B. Poelker, R. Pomatsalyuk, M. Posik, A. J. R. Puckett, B. Quinn, A. Rakhman, P. E. Reimer, S. Riordan, P. Rogan, G. Ron, G. Russo, K. Saenboonruang, A. Saha, B. Sawatzky, A. Shahinyan, R. Silwal, S. Sirca, K. Slifer, P. Solvignon, P. A. Souder, M. L. Sperduto, R. Subedi, R. Suleiman, V. Sulkosky, C. M. Sutera, W. A. Tobias, W. Troth, G. M. Urciuoli, B. Waidyawansa, D. Wang, J. Wexler, R. Wilson, B. Wojtsekhowski, X. Yan, H. Yao, Y. Ye, Z. Ye, V. Yim, L. Zana, X. Zhan, J. Zhang, Y. Zhang, X. Zheng, and P. Zhu (PREX Collaboration), "Measurement of the neutron radius of ^{208}Pb through parity violation in electron scattering", Phys. Rev. Lett. **108**, 112502 (2012).

[86] C. M. Tarbert, D. P. Watts, D. I. Glazier, P. Aguar, J. Ahrens, J. R. M. Annand, H. J. Arends, R. Beck, V. Bekrenev, B. Boillat, A. Braghieri, D. Branford, W. J. Briscoe, J. Brudvik, S. Cherepnya, R. Codling, E. J. Downie, K. Foehl, P. Grabmayr, R. Gregor, E. Heid, D. Hornidge, O. Jahn, V. L. Kashevarov, A. Knezevic, R. Kondratiev, M. Korolija, M. Kotulla, D. Krambrich, B. Krusche, M. Lang, V. Lisin, K. Livingston, S. Lugert, I. J. D. MacGregor, D. M. Manley, M. Martinez, J. C. McGeorge, D. Mekterovic, V. Metag, B. M. K. Nefkens, A. Nikolaev, R. Novotny, R. O. Owens, P. Pedroni, A. Polonski, S. N. Prakhov, J. W. Price, G. Rosner, M. Rost,

T. Rostomyan, S. Schadmand, S. Schumann, D. Sober, A. Starostin, I. Supek, A. Thomas, M. Unverzagt, T. Walcher, L. Zana, and F. Zehr (Crystal Ball at MAMI and A2 Collaboration), "Neutron skin of ^{208}Pb from coherent pion photoproduction", Phys. Rev. Lett. **112**, 242502 (2014).

[87]H. Okuno, N. Fukunishi, and O. Kamigaito, "Progress of RIBF accelerators", Progress of Theoretical and Experimental Physics **2012**, 03C002, 10.1093/ptep/pts046 (2012).

[88]T. Kubo, "In-flight RI beam separator BigRIPS at RIKEN and elsewhere in Japan", Nuclear Instruments and Methods in Physics Research Section B: Beam Interactions with Materials and Atoms **204**, 14th International Conference on Electromagnetic Isotope Separators and Techniques Related to their Applications, 97–113 (2003).

[89]T. Kubo, D. Kameda, H. Suzuki, N. Fukuda, H. Takeda, Y. Yanagisawa, M. Ohtake, K. Kusaka, K. Yoshida, N. Inabe, T. Ohnishi, A. Yoshida, K. Tanaka, and Y. Mizoi, "BigRIPS separator and ZeroDegree spectrometer at RIKEN RI Beam Factory", Progress of Theoretical and Experimental Physics **2012**, 03C003, 10.1093/ptep/pts064 (2012).

[90]N. Fukuda, T. Kubo, T. Ohnishi, N. Inabe, H. Takeda, D. Kameda, and H. Suzuki, "Identification and separation of radioactive isotope beams by the BigRIPS separator at the RIKEN RI Beam Factory", Nuclear Instruments and Methods in Physics Research Section B: Beam Interactions with Materials and Atoms **317**, XVIth International Conference on ElectroMagnetic Isotope Separators and Techniques Related to their Applications, December 2–7, 2012 at Matsue, Japan, 323–332 (2013).

[91]H. Kumagai, T. Ohnishi, N. Fukuda, H. Takeda, D. Kameda, N. Inabe, K. Yoshida, and T. Kubo, "Development of parallel plate avalanche counter (PPAC) for BigRIPS fragment separator", Nuclear Instruments and Methods in Physics Research Section B: Beam Interactions with Materials and Atoms **317**, 717–727 (2013).

[92]*Experimental-area*, https://ribf.riken.jp/SAMURAI/index.php?experimental_area (visited on 09/01/2022).

[93]T. Kobayashi, N. Chiga, T. Isobe, Y. Kondo, T. Kubo, K. Kusaka, T. Motobayashi, T. Nakamura, J. Ohnishi, H. Okuno, H. Otsu, T. Sako, H. Sato, Y. Shimizu, K. Sekiguchi, K. Takahashi, R. Tanaka, and K. Yoneda, "SAMURAI spectrometer for RI beam experiments", Nuclear Instruments and Methods in Physics Research Section B: Beam Interactions with Materials and Atoms **317**, XVIth International Conference on ElectroMagnetic Isotope Separators and Techniques Related to their Applications, December 2–7, 2012 at Matsue, Japan, 294–304 (2013).

[94]*MINOS*, http://minos.cea.fr/ (visited on 09/01/2022).

[95]C. Santamaria, A. Obertelli, S. Ota, M. Sasano, E. Takada, L. Audirac, H. Baba, D. Calvet, F. Château, A. Corsi, A. Delbart, P. Doornenbal, A. Giganon, A. Gillibert, Y. Kondo, Y. Kubota, C. Lahonde-Hamdoun, V. Lapoux, D. Leboeuf, C. Lee, H. Liu, M. Matsushita, T. Motobayashi, M. Niikura, M. Kurata-Nishimura, H. Otsu, A. Peyaud, E. Pollacco, G. Prono, H.

Tokieda, T. Uesaka, and J. Zenihiro, “Tracking with the MINOS time projection chamber”, Nuclear Instruments and Methods in Physics Research Section A: Accelerators, Spectrometers, Detectors and Associated Equipment **905**, 138–148 (2018).

[96] S. Takeuchi, T. Motobayashi, Y. Togano, M. Matsushita, N. Aoi, K. Demichi, H. Hasegawa, and H. Murakami, “DALI2: A NaI(Tl) detector array for measurements of γ rays from fast nuclei”, Nuclear Instruments and Methods in Physics Research Section A: Accelerators, Spectrometers, Detectors and Associated Equipment **763**, 596–603 (2014).

[97] S. Agostinelli, J. Allison, K. Amako, J. Apostolakis, H. Araujo, P. Arce, M. Asai, D. Axen, S. Banerjee, G. Barrand, F. Behner, L. Bellagamba, J. Boudreau, L. Broglia, A. Brunengo, H. Burkhardt, S. Chauvie, J. Chuma, R. Chytracek, G. Cooperman, G. Cosmo, P. Degtyarenko, A. Dell’Acqua, G. Depaola, D. Dietrich, R. Enami, A. Feliciello, C. Ferguson, H. Fesefeldt, G. Folger, F. Foppiano, A. Forti, S. Garelli, S. Giani, R. Giannitrapani, D. Gibin, J. Gómez Cadenas, I. González, G. Gracia Abril, G. Greeniaus, W. Greiner, V. Grichine, A. Grossheim, S. Guatelli, P. Gumplinger, R. Hamatsu, K. Hashimoto, H. Hasui, A. Heikkinen, A. Howard, V. Ivanchenko, A. Johnson, F. Jones, J. Kallenbach, N. Kanaya, M. Kawabata, Y. Kawabata, M. Kawaguti, S. Kelner, P. Kent, A. Kimura, T. Kodama, R. Kokoulin, M. Kossov, H. Kurashige, E. Lamanna, T. Lampén, V. Lara, V. Lefebure, F. Lei, M. Liendl, W. Lockman, F. Longo, S. Magni, M. Maire, E. Medernach, K. Minamimoto, P. Mora de Freitas, Y. Morita, K. Murakami, M. Nagamatu, R. Nartallo, P. Nieminen, T. Nishimura, K. Ohtsubo, M. Okamura, S. O’Neale, Y. Oohata, K. Paech, J. Perl, A. Pfeiffer, M. Pia, F. Ranjard, A. Rybin, S. Sadilov, E. Di Salvo, G. Santin, T. Sasaki, N. Savvas, Y. Sawada, S. Scherer, S. Sei, V. Sirotenko, D. Smith, N. Starkov, H. Stoecker, J. Sulkimo, M. Takahata, S. Tanaka, E. Tcherniaev, E. Safai Tehrani, M. Tropeano, P. Truscott, H. Uno, L. Urban, P. Urban, M. Verderi, A. Walkden, W. Wander, H. Weber, J. Wellisch, T. Wenaus, D. Williams, D. Wright, T. Yamada, H. Yoshida, and D. Zschiesche, “Geant4—a simulation toolkit”, Nuclear Instruments and Methods in Physics Research Section A: Accelerators, Spectrometers, Detectors and Associated Equipment **506**, 250–303 (2003).

[98] K. Boretzky, I. Gašparić, M. Heil, J. Mayer, A. Heinz, C. Caesar, D. Kresan, H. Simon, H. Törnqvist, D. Körper, G. Alkhazov, L. Atar, T. Aumann, D. Bemmerer, S. Bondarev, L. Bott, S. Chakraborty, M. Cherciu, L. Chulkov, M. Ciobanu, U. Datta, E. De Filippo, C. Douma, J. Dreyer, Z. Elekes, J. Enders, D. Galaviz, E. Geraci, B. Gnoffo, K. Göbel, V. Golovtsov, D. Gonzalez Diaz, N. Gruzinsky, T. Heftrich, H. Heggen, J. Hehner, T. Hensel, E. Hoemann, M. Holl, A. Horvat, Á. Horváth, G. Ickert, D. Jelavić Malenica, H. Johansson, B. Jonson, J. Kahlbow, N. Kalantar-Nayestanaki, A. Kelić-Heil, M. Kempe, K. Koch, N. Kozlenko, A. Krivshich, N. Kurz, V. Kuznetsov, C. Langer, Y. Leifels, I. Lihtar, B. Löher, J. Machado, N. Martorana, K. Miki, T. Nilsson, E. Orischin, E. Pagano, S. Pirrone, G. Politi, P. M. Potlog, A. Rahaman, R. Reifarth, C. Rigollet, M. Röder, D. Rossi, P. Russotto, D. Savran, H. Scheit, F. Schindler, D. Stach, E. Stan, J. Stomvall Gill, P. Teubig, M. Trimarchi, L. Uvarov, M. Volknandt, S. Volkov, A. Wagner, V. Wagner, S. Wranne, D. Yakorev, L. Zanetti, A. Zilges, and K. Zuber, “NeuLAND: The high-resolution neutron time-of-flight spectrometer for R3B

at FAIR", Nuclear Instruments and Methods in Physics Research Section A: Accelerators, Spectrometers, Detectors and Associated Equipment **1014**, 165701 (2021).

[99]T. Nakamura and Y. Kondo, "Large acceptance spectrometers for invariant mass spectroscopy of exotic nuclei and future developments", Nuclear Instruments and Methods in Physics Research Section B: Beam Interactions with Materials and Atoms **376**, Proceedings of the XVIIth International Conference on Electromagnetic Isotope Separators and Related Topics (EMIS2015), Grand Rapids, MI, U.S.A., 11-15 May 2015, 156–161 (2016).

[100]*Smsimulator5.4*, `http://be.nucl.ap.titech.ac.jp/~nebula/simulator.php` (visited on 09/01/2022).

[101]M. Rejmund, S. Bhattacharyya, A. Navin, W. Mittig, L. Gaudefroy, M. Gelin, G. Mukherjee, F. Rejmund, P. Roussel-Chomaz, and C. Theisen, "Shell evolution and the $N = 34$ "magic number"", Phys. Rev. C **76**, 021304 (2007).

[102]B. Fornal, R. V. F. Janssens, R. Broda, N. Marginean, S. Beghini, L. Corradi, M. P. Carpenter, G. D. Angelis, F. D. Vedova, E. Farnea, E. Fioretto, A. Gadea, B. Guiot, M. Honma, W. Królas, T. Lauritsen, S. Lunardi, P. F. Mantica, P. Mason, G. Montagnoli, D. R. Napoli, T. Otsuka, T. Pawłat, G. Pollarolo, F. Scarlassara, A. M. Stefanini, D. Seweryniak, S. Szilner, C. A. Ur, M. Trotta, J. J. Valiente-Dobón, J. Wrzesi ński, and S. Zhu, "Yrast structure of the neutron-rich $N = 31$ isotones ^{51}Ca and ^{52}Sc", Phys. Rev. C **77**, 014304 (2008).

[103]F. Perrot, F. Maréchal, C. Jollet, P. Dessagne, J.-C. Angélique, G. Ban, P. Baumann, F. Benrachi, U. Bergmann, C. Borcea, A. Bu ţ ă, J. Cederkall, S. Courtin, J.-M. Daugas, L. M. Fraile, S. Grévy, A. Jokinen, F. R. Lecolley, E. Liénard, G. L. Scornet, V. Méot, C. Miehé, F. Negoi ţ ă, N. A. Orr, S. Pietri, E. Poirier, M. Ramdhane, O. Roig, I. Stefan, and W. Wang, "β-decay studies of neutron-rich k isotopes", Phys. Rev. C **74**, 014313 (2006).

[104]R. Taniuchi, *PhD thesis, Department of Physics, Graduate School of Science, The University of Tokyo* (2018).

[105]N. S. Chant and P. G. Roos, "Distorted-wave impulse-approximation calculations for quasifree cluster knockout reactions", Phys. Rev. C **15**, 57–68 (1977).

[106]T. Wakasa, K. Ogata, and T. Noro, "Proton-induced knockout reactions with polarized and unpolarized beams", Progress in Particle and Nuclear Physics **96**, 32–87 (2017).

[107]G. JACOB and T. A. J. MARIS, "Quasi-free scattering and nuclear structure", Rev. Mod. Phys. **38**, 121–142 (1966).

[108]G. JACOB and T. A. J. MARIS, "Quasi-free scattering and nuclear structure. II.", Rev. Mod. Phys. **45**, 6–21 (1973).

[109]K. Yoshida, "Bound state properties studied by the knockout reaction", Few-Body Systems **62**, `10.1007/s00601-021-01615-2` (2021).

[110]T. Aumann, C. Barbieri, D. Bazin, C. Bertulani, A. Bonaccorso, W. Dickhoff, A. Gade, M. Gómez-Ramos, B. Kay, A. Moro, T. Nakamura, A. Obertelli, K. Ogata, S. Paschalis, and T. Uesaka, "Quenching of single-particle strength from direct reactions with stable and rare-isotope beams", Progress in Particle and Nuclear Physics **118**, 103847 (2021).

[111]M. A. Franey and W. G. Love, "Nucleon-nucleon t-matrix interaction for scattering at intermediate energies", Phys. Rev. C **31**, 488–498 (1985).

[112]M. Toyokawa, K. Minomo, and M. Yahiro, "Mass-number and isotope dependence of local microscopic optical potentials for polarized proton scattering", Phys. Rev. C **88**, 054602 (2013).

[113]K. Amos, P. J. Dortmans, H. V. von Geramb, S. Karataglidis, and J. Raynnal, "Nucleon-nucleus scattering: a microscopic nonrelativistic approach", in *Advances in nuclear physics*, edited by J. W. Negele and E. Vogt (Springer US, Boston, MA, 2000), pp. 276–536.

[114]K. Bennaceur and J. Dobaczewski, "Coordinate-space solution of the skyrme– hartree–fock– bogolyubov equations within spherical symmetry. the program hfbrad (v1.00)", Computer Physics Communications **168**, 96–122 (2005).

[115]M. Ahmad, J. Watson, D. Devins, B. Flanders, D. Friesel, N. Chant, P. Roos, and J. Wastell, "Neutron-knockout reactions from ^{2}H, ^{40}Ca and ^{48}Ca", Nuclear Physics A **424**, 92–120 (1984).

[116]F. Nowacki, A. Poves, E. Caurier, and B. Bounthong, "Shape coexistence in ^{78}Ni as the portal to the fifth island of inversion", Phys. Rev. Lett. **117**, 272501 (2016).

[117]J. Bartel, P. Quentin, M. Brack, C. Guet, and H.-B. Håkansson, "Towards a better parametrisation of skyrme-like effective forces: a critical study of the skm force", Nuclear Physics A **386**, 79–100 (1982).

[118]Y. Dong and H. Junde, "Nuclear data sheets for A = 52", Nuclear Data Sheets **128**, 185–314 (2015).

[119]K. Kasinski, A. Rodriguez-Rodriguez, J. Lehnert, W. Zubrzycka, R. Szczygiel, P. Otfinowski, R. Kleczek, and C. Schmidt, "Characterization of the STS/ MUCH-XYTER2, a 128-channel time and amplitude measurement IC for gas and silicon microstrip sensors", Nuclear Instruments and Methods in Physics Research Section A: Accelerators, Spectrometers, Detectors and Associated Equipment **908**, 225–235 (2018).

[120]A. Frotscher, *PhD thesis, Institut für Kernphysik, Technische Universität Darmstadt* (2021).

[121]W. Zabolotny, A. Byszuk, D. Dementyev, D. Emschermann, M. Gumiński, M. Kruszewski, P. Miedzik, K. Pozniak, R. Romaniuk, C. Schmidt, and M. Shitenkov, "GBTX emulator for development and special versions of GBT-based readout chains", (2021).

[122]C. G. Larrea, K. Harder, D. Newbold, D. Sankey, A. Rose, A. Thea, and T. Williams, "IPbus: a flexible Ethernet-based control system for xTCA hardware", Journal of Instrumentation **10**, C02019 (2015).

[123]K. Kasinski, W. Zabolotny, J. Lehnert, C. J. Schmidt, W. F. J. Müller, and R. Szczygiel, "STS-HCTSP, an STS Hit and Control Transfer Synchronous Protocol", in *Scientific report 2014*, Vol. 2015-1, GSI Report (GSI Helmholtzzentrum für Schwerionenforschung, Darmstadt, 2015), 78–79 p.

[124]*Peli air cases*, `https://www.peli.com/eu/en/products/cases/air-cases` (visited on 12/30/2022).

[125]*Cryo.transmit*, `https://cryo.transmit.de/en/who-we-are` (visited on 09/01/2022).

[126]R. Kersevan and M. Ady, "Recent Developments of Monte-Carlo Codes Molflow+ and Synrad+", in Proc. 10th international particle accelerator conference (ipac'19), melbourne, australia, 19-24 may 2019 (June 2019), pp. 1327–1330.

[127]D. Schultheiß, *Dissertation zur Erlangung des Doktorgrades der Mathematisch- Naturwissenschaftlichen Fakultät der Universität Augsburg* (2007).

[128]P. A. Redhead, "Hydrogen in vacuum systems: an overview", AIP Conference Proceedings **671**, 243–254 (2003).

Academic CV

Mădălina Enciu
Birth name: Mădălina Răvar

Education

2020-2023 (doctoral studies)
Technische Universität Darmstadt (Darmstadt, Germany)
Institute of nuclear physics
Thesis: "Extended $p_{3/2}$ neutron orbital and the N=32 shell closure in ^{52}Ca".

2018-2020 (M.Sc.)
University of Cologne (Köln, Germany)
Primary specialization: Nuclear and Particle physics
Secondary specialization: Astrophysics
Master thesis: "The study of the 3α-decay of 0_2^+ in ^{12}C using the Lund-York-Cologne CAlorimeter".

2015-2018 (B.Sc.)
University of Bucharest, Department of Physics (Măgurele, Romania)
Specialization: Physics (English)
Bachelor thesis: "The ^{12}C(^{13}C,p)^{24}Na cross section at very low energy via an activation method".

2011-2015 (High School)
„Gh. Lazăr" High School (Sibiu, Romania)
Specialization: Natural Science (bilingual English)

Publications

"Extended $p_{3/2}$ neutron orbital and the N=32 shell closure in ^{52}Ca", M. Enciu et al. Phys. Rev. Lett. **129**, 262501 (2022). [9]

"STRASSE: a silicon tracker for quasi-free scattering measurements at the RIBF", H. N. Liu et al. The European Physical Journal A **59**, 121 (2023). [10]